THE UNIVERSITY *of* EDINBURGH

Scattering Studies of Magnetism in Non-centrosymmetric Systems

Jana Pásztorová

Doctor of Philosophy
The University of Edinburgh
June 2019

Lay Summary

In the history of mankind, inventions and discoveries have improved people's quality of life. Milestones in history like the steam engine, understanding of electromagnetism or the very recent discovery of superconductivity. These and many others have formed the modern world as we know it nowadays. What is very often omitted is the fact that there is a long path from the idea or unusual behaviour to applications.

In our modern society, one of the main problems is the energy consumption. Energy loss in electric circuits mainly comes from unwanted heating of the components. For many years, scientists have been working on development and understanding of materials that could solve this problem. Two possible paths out of several are - superconductors and mutiferroic materials. The resistivity of materials is responsible for unwanted heating in electric circuits. Superconductors are really promising materials, as they show zero resistivity. Another path is represented by multiferroic materials and these will be discussed in this thesis mostly. Recently, they have gained lot of attention. The idea of multiferroics is that several properties of material are coupled together. This means that we can tune one property with another. Imagine that we would be able to manipulate ferromagnetic materials with electric fields. The electric control of such a system could have significantly less power consumption than magnetic field control, as it is necessary to have electric current to generate the magnetic field. It can also lead to better and smaller designs of electrical devices.

It is very important to continue the research on the structure and dynamic properties as they can provide answers for better material and technological designs in future.

Abstract

With there being a strong connection between the underlying structure of materials and their properties, understanding this inherent coupling will lead to more efficient materials. This thesis studies three non-centrosymmetric compounds $MnSb_2O_6$, $Cu_3Nb_2O_8$ and $CeRhSi_3$ with the goal of understanding the coupling between the structure and the underlying magnetic and electronic properties. All three materials lack an inversion centre and this thesis investigates how this constraint influences the underlying interactions and therefore properties of these compounds.

$MnSb_2O_6$ is predicted to be multiferroic - a group of materials that has drawn considerable attention these days. One of the most interesting aspects of multiferroics is the so-called magnetoelectric coupling. Whereas in ferroics, one can tune magnetization with magnetic field, polarization with electric field, elasticity with stress, the idea behind multiferroics is that one can tune the electric polarization by the magnetic field (or vice versa). In terms of applications, the idea of electric-field control of magnetism is particularly exciting and it could lead to smaller and more effective devices. In the first part of this thesis, I discuss single crystal preparation based on three different methods in an attempt to obtain high quality single crystals for neutron inelastic scattering studies. Improvement in the size of single crystals was achieved using the flux method. This turned out to be an important step for inelastic experiment with the total mass of 1.3 g single crystals (approximately 150 sealed ampoules). Moreover, polycrystalline sample of $MnSb_2O_6$ has been prepared successfully with the hydrothermal method. To the best of our knowledge, this process of preparation has not been published before. The second part of the $MnSb_2O_6$ study is focused on neutron experiments and following analysis. The experiment on triple axis spectrometer RITA-II mapped behaviour of spins in horizontal magnetic field. Critical exponent β was estimated with discussion on properties of this system. Obtained results

were compared with complementary experiment on BT4 spectrometer with same results. The magnetic and structural chirality was tested with polarized neutrons on instrument D3. Whereas, magnetic chirality in compound has a dominant domain, we were not able to confirm the same for the structural chirality. The last part of this section is discussing another interesting aspect of $MnSb_2O_6$ - it's noncollinear magnetic structure within triangular lattice is making it an ideal candidate to study so called multimagnon processes. The classical picture of magnon as non-interacting and long-lived excitation has been questioned by recent studies of classical systems with measured multimagnon excitations. Whereas existing spin wave theory can explain these excitations for quantum systems ($S = 1/2$), it doesn't provide an answer for their existence in classical systems.

$Cu_3Nb_2O_8$ compound belongs to type-II multiferroics, which means that electric polarization emerges at a magnetic order temperature. I prepared a poly-crystalline sample that was measured on the time-of-flight instrument MARI. Experiments revealed excitations around 30 meV that it is not expected for system with spin $S = 1/2$. We close this study with the discussion about origin of these excitations - seems like they do result from localised clusters of spins (coupled triplet) rather than individual Cu^{2+} ions.

Whereas for elements and some alloys, magnetism and superconductivity are in an antagonistic relation, several non-centrosymmetric heavy fermion compounds have been reported, where superconductivity and magnetism do coexist together. This is also the case of $CeRhSi_3$ (superconducting at high pressures). For these systems, it is not unusual to see transitions between localized and itinerant (delocalized) magnetism. We describe neutron inelastic experiment focused on study of magnetic fluctuations in the normal state at ambient conditions. This has been followed by the experiment in magnetic field, in respect to define their antiferromagnetic or ferromagnetic character. The study contains also a heuristic description and therefore possible models that can be used as an interpretation of our measured data.

This thesis also provides an example of two different types of magnetism - Mn atoms in $MnSb_2O_6$ are d elements with characteristic localized magnetism and L-S coupling, whereas Ce atoms in $CeRhSi_3$ are f elements which typically displays itinerant magnetism and j-j coupling. I discuss the framework on how to describe these two types of magnetism and also discuss various implications to $4d$ and $5d$ transition metal ions.

Declaration

I declare that this thesis was composed by myself, that the work contained herein is my own except where explicitly stated otherwise in the text, and that this work has not been submitted for any other degree or professional qualification except as specified.

Parts of this work have been published in *Physical Review B* **99** 125144 (2019) [1]. Chapter about crystal growth is under the preparation and should be submitted to *Acta Crystallographica B*.

(*Jana Pásztorová, June 2019*)

Acknowledgements

Foremost, I would like to express my sincere gratitude to my supervisor Dr. Chris Stock. The world of neutrons and scattering was pretty new to me when I started my PhD and I am very thankful for all his patience, time and immense knowledge in this field. His guidance helped me all the time in research, presentations at conferences and writing of this thesis. I was able to discuss my questions with him pretty much anytime (whatever it was background science, different instruments, laboratory techniques or principles of analysis), which I do appreciate a lot.

Besides my supervisor, I would like to convey my gratitude to the instrument scientists at various neutron facilities - Jose Garcia and Peter Gehring at NIST, Franz Demmel and Duc Le at ISIS, Christof Niedermayer at PSI, and Navid Qureshi, Bachir Ouladdiaf and Karin Schmalzl at ILL. Despite busy schedules of instrumental scientists, they were all very helpful and willing to answer my questions.

I would also like to thank to postdoctoral researcher Manila Songvilay for helpful advice on some parts of data analysis. My gratitude belong to other members of Stock's group too - Paul, Irene, Chris, Katherine and Nathan. In particular, I would like to thank Paul for all fierce discussions about science and life. It is great when your work colleague is also your friend with whom you can joke, laugh and smile.

Having a great tutors is admittedly important for the professional growth. But I believe that above all of that stands your friends and family. Its their support that did help me to overcome problems or difficult periods. My first thanks is dedicated to my childhood friend Szabi that I've known since I was seven. She is my true soulmate and understands me as no one else. I can't possibly express enough gratitude for all her support, all skype calls, crazy jokes, but also deep conversations.

I would like to acknowledge also my two amazing flatmates - Joe and Ant. I am grateful for all inside jokes that we have built over three years in the Best House Ever (BHE™). Which reminds me that I should not omit Ronnie. Joe - thank you for all interesting discussions on various topics, guitar solos, movie nights and book suggestions. I always enjoyed our conversations. Ant - you are a very good friend and one can rely on you.

Moving to a new place and country is rarely an easy thing. I would like to thank Irene for making it so much more easier. Thank you so much for all great time that we've had together, all your support and hugs. It did mean a lot to me. I can not skip Isa as I did spend lot of time with her - discovering new places and restaurants in Edinburgh. And I haven't even mentioned memories from Skye and Cuba. Thank you so much. I would like to convey many thanks to other friends from work - Izzy, Julia, Sarah, Becca, Chris, Dan, Kenny, Jöel, Nia, Ellen, Veronika, Miriam, Elise and Jacky. You probably don't know but your warm welcome was so important for me. And special thanks to Izzy for all bike rides and fun.

Last but not least, I would like to express my gratitude to my parents, grandmother and brother. Thanks for all support and comforting family atmosphere every time that I did come home for a visit. Especially to my mum, who's enthusiasm for teaching biology and mathematics, I always find very inspiring.

Contents

List of Figures

List of Tables

Chapter 1

Introduction

1.1 Interest in non-centrosymmetric compounds

In recent years, there has been interest in the study of multiferroic materials. Let's start with explanation of this term first. A ferroic is a material that adopts a spontaneous, switchable internal alignment [5]. For example - in a ferromagnetic material, the alignment of spins can be switched by a magnetic field. If it is ferroelectric material, the electric dipole moment can be switched by electric field. In the case of ferroelasticity, strain alignment can be induced by stress. A multiferroic combines any two or more of the primary ferroic ordering in the same phase [32], for example ferroelectric and ferroelastic properties present in a material makes it ideal candidate for piezoelectric application.

One of the most interesting aspects of multiferroics is magnetoelectric coupling. Whereas in ferroics, one can tune magnetization with magnetic field, polarization with electric field, elasticity with stress (see Fig. 1.1), the idea behind multiferroics is that a magnetic field can tune electric polarization (or vice versa). In terms of applications, the idea of electric-field control of magnetism is particularly exciting and it could lead to smaller and more effective devices - electric control of magnetic spins would consume significantly less power than magnetic-field control, which requires electric currents to generate the magnetic fields [5]. Magneto-electric coupling can also have application in information storage industry. In principle, this coupling could permit data to be written electrically and read magnetically [27].

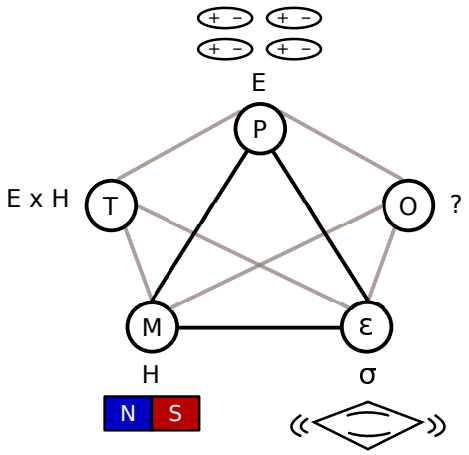

Figure 1.1 *The primary ferroic ordering - ferroelectricity (**P**), ferromagnetism (**M**) and ferroelasticity ϵ that can be switched by their conjugate electric (**E**), magnetic (**H**) and stress (σ) fields respectively. There is also promising new ferroic ordering of torroidal moments (**T**) or switchable orbital ordering (**O**), vortices and chiralities.*

Particularly impressive were measurements of properties in the rare-earth manganites Tb(Dy)MnO_3 and Tb(Dy)Mn_2O_5 that have shown high magnetic tuneability of electric polarization and dielectric constant [2, 33–35]. In applied magnetic fields, Tb(Dy)MnO_3 shows a spin-flop transition, at which the polarization vector rotates by 90° and the dielectric constant ε in $DyMnO_3$ increases by $\sim$ 500% in a narrow field range, creating a colossal magneto-dielectric effect [4], see Fig. 1.2.

These results are really impressive. Of course, going from laboratory measurement to industrial use requires the search for the optimal material. And in the case of multiferroics, it's not an easy task at all. Surprisingly, there are not so many multiferroic materials. Therefore, it is good to ask - why is it like that?

In the ideal case, ferroelectrics do show a hysteretic response of polarisation to an applied electric field (and similarly, ferromagnets do show a hysteretic response of magnetisation to an applied magnetic field). Still, ferroelectrics and ferromagnetics are quite different. The fundamental understanding of ferroelectric has been built on perovskite structures. Let's take an example of perovskite structure ABO_3 - A and B are two types of cations that differ in size. The unit cell of ABO_3 has 4 large A cations sitting in corners of the cube and 1 smaller B cation that sits in a centre of this cubic unit cell surrounded by an octahedron of oxygen anions. The theoretical studies showed that below the Curie temperature, there is a structural distortion towards to a lower symmetry phase

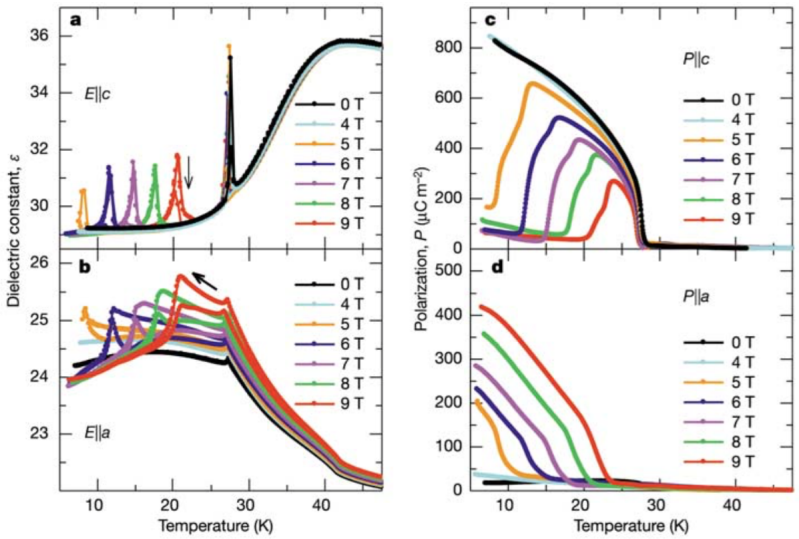

Figure 1.2 *Electric polarization flop induced by magnetic field in single crystal of $TbMnO_3$. Plots a) and b) shows temperature profiles of dielectric constant at 10kHz. c) and d) shows the electric polarization along c and a axes at various magnetic fields [2]. The onset of ferroelectricity in $TbMnO_3$ clearly correlates with the appearance of spiral magnetic ordering at $\sim$ 28 K [3]*

accompanied by the shift off-centre of the smaller cation B. The spontaneous polarisation derives largely from the electric dipole moment created by this shift [36]. Whereas, in the high temperature phase, short-range repulsion between ions is the dominant force, going to lower temperatures, forces associated with polarization of the ions start to become stronger than repulsion forces. This makes the polarized state more stable, even in the absence of an applied field. In ferroelectric systems, one deals with charge that is invariant to time-reversal symmetry, but does change in a case of spatial-inversion operation of symmetry. The ferromagnets must have unpaired localized electrons in *d* shell. Each electron carries a magnetic moment (spin), which in principle leads to 4 main types of ordering of the magnetic dipoles in materials - paramagnetic, ferromagnetic, antiferromagnetic and ferrimagnetic. Unlike the charge, magnetic moment does change after applying time-reversal symmetry. But doesn't change in a case of spatial-inversion operation, see Fig. 1.3. Another argument that is often used in papers as an explanation for the small number of multiferroics is the problem of insulating vs conducting metal. By the definition, ferroelectrics are insulators. Otherwise, an applied electric field would induce an electric current to flow, rather than causing an electric polarization [36]). On the other hand, ferromagnets are usually conducting metals. This is not necessary the reason, as we do know

examples of magnetic materials that are insulators.

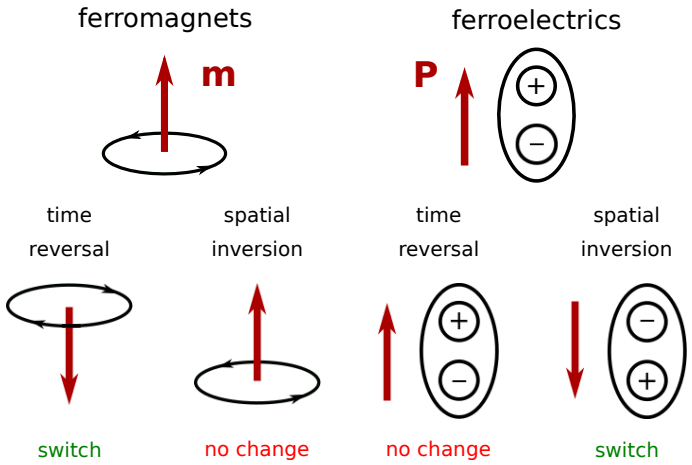

Figure 1.3 *Time-reversal and spatial-inversion symmetry in ferroics. The local magnetic moment in ferromagnets might be represented by charge that is orbiting. With time-reversal symmetry, the direction of this movement will be opposite and therefore* $\boldsymbol{m}$ *is pointing down. The spatial-inversion produces no change. It's the opposite case in ferroelectrics. The polarization* $\boldsymbol{P}$ *is invariant for time-reversal symmetry, but situation does change after applying spatial-inversion symmetry.*

Even though we do have some hints of what can or cannot constrain the material from being good multiferroic, we still don't understand the mechanism too well. The *d*-electron occupancy on the transition metal seems to be a critical variable, together with a number of competing factors. This brings us to one promising path - frustrated magnets, where the competing interactions can lead to a much more complex distortion of the lattice, which causes unconventional ferroelectricity in the material. Naturally, that puts lower constraints on the coexistence with magnetism. In fact, materials with electric dipoles induced by magnetic ordering are the best candidates for useful multiferroics, because such a dipoles are highly tunable by applied magnetic fields [4].

Characteristic	Spatial-inversion	Time-reversal
Ferroelastic	Yes	Yes
Ferroelectric	No	Yes
Ferromagnetic	Yes	No
Multiferroic	No	No

Table 1.1 *Spatial-inversion and time-reversal symmetry in ferroics [27]*

Therefore, a very important role in the search for materials with magnetically induced ferroelectricity is played by frustrated magnets (however, we do know

about cases when this can be achieved also in collinear magnetic structures). The frustrated magnetic materials have more complicated magnetic structures due to the competing interactions between spins. The role of frustration in materials is to induce spatial variations of magnetisation. Let's move to an example of a spin chain with a ferromagnetic interaction $J < 0$ between neighbouring spins and an antiferromagnetic next-nearest-neighbour interaction $J' > 0$. This second interaction J' frustrates previously simple ordering and when it is sufficiently strong, see Fig. 1.4, it does stabilize a spiral magnetic state:

$$\boldsymbol{S}_n = S[\boldsymbol{e}_1 \cos Qx_n + \boldsymbol{e}_2 \sin Qx_n], \tag{1.1}$$

where $\mathbf{e}_1$ and $\mathbf{e}_2$ are two orthogonal unit vectors and wavevector $\mathbf{Q}$ is given by:

$$\cos\left(\frac{Q}{2}\right) = -\frac{J'}{4J}. \tag{1.2}$$

Like any other magnetic ordering, the magnetic spiral spontaneously breaks time-reversal symmetry. In addition, it breaks inversion symmetry, because the change of the sign of all coordinates inverts the direction of the rotation of spins in the spiral [4]. The direction of this rotation is coupled to a sign of electric polarization. In contrast, the sinusoidal ordering can not induce ferroelectricity, as it is invariant on inversion, $x_n \to -x_n$.

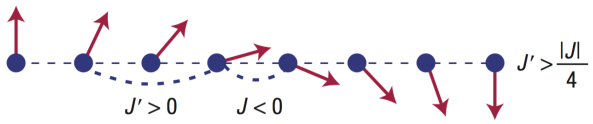

Figure 1.4 *Frustrated spin chain with ferromagnetic interaction J between neighbouring spins and an antiferromagnetic next-nearest-neighbour interaction J'. If $J'/|J| > 1/4$, the ground state is a magnetic spiral [4].*

One possible mechanism that induces ferroelectricity in material with spiral magnetic structure might be antisymmetric Dzyaloshinskii-Moriya (DM) interaction $\mathbf{D} \cdot \mathbf{S}_1 \times \mathbf{S}_2$. In fact, this interaction is relativistic correction to the usual superexchange and it's strength is proportional to the spin-orbit coupling. The DM interactions favour non-collinear spin ordering [4].

Moreover, the coupling between electric and magnetic dipoles in multiferroics also gives rise to unusual dynamics effects [4].

Let us shortly discuss several materials that have been investigated as potential multiferroics. Perovskites represent one group of these materials. The compound bismuth ferrite $BiFeO_3$ contains a cation Fe^{3+} with five $3d$ electrons which are responsible for magnetism. The Bi^{3+} cation provides the ferroelectricity via the structural distortion. A similar situation is in $BiMnO_3$ compound. However, even if magnetization and electric polarization are reasonably large [37–39], it doesn't make the compound a useful multiferroic. The dielectric constant ε is fairly insensitive to magnetic fields.

Another ferroelectric mechanism results from the fact that noncentrosymmetric magnetic ordering causes polarization [5]. Even in the case that atomic structure is centrosymmetric. This is also our motivation behind studying noncentrosymmetric compounds $MnSb_2O_6$ and $CeRhSi_3$. The idea was first introduced in the 1970s by Robert Newnham and coworkers, who recognized that the noncentrosymmetric, spiral-antiferromagnetic ground state of chromium chrysoberyl Cr_2BeO_4 results in small ferroelectric polarization.

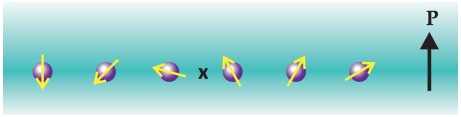

Figure 1.5 *Spiral arrangement of magnetic moments in Cr_2BeO_4 - atoms are arranged symmetrically about the point $\boldsymbol{x}$, but the spins are not, which leads to polarization. Apart from Newnham, there are several other teams that observed magneto-electric coupling from weak spin-orbit interactions (Y. Tokura, M. Mostovoy, D. Vanderbilt) [5]*

Noncentrosymmetric ordering also explains the stronger multiferroicity discovered by Cheong in $TbMn_2O_5$ and Ca_3CoMnO_6. However, in this case the multiferroics behaviour arises from strong superexchange, not weak spin-orbit interactions. The magnetoelectric coupling in these compounds lead to exciting behaviours - like electric-field control of spin chirality as demonstrated by Tokura's group [5].

Another route provides geometric ferroelectric - layered compounds with unusual polar tilts and rotations of the sublattice. Fig. 1.6 shows change from a centrosymmetric nonpolar phase to the noncentrosymmetric ferroelectric phase in $BaNiF_4$.

It would be a great achievement for solid state physics to identify a mechanism of coupled magnetism and polarization at room temperatures, which seems to be a challenge comparable with searching for usable room-temperatures superconductors.

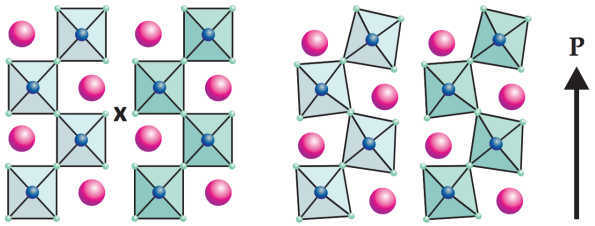

Figure 1.6 *The structural change in $BaNiF_4$ - from a centrosymmetric nonpolar phase to the noncentrosymmetric ferroelectric phase [5]*

1.2 Magnetism of d and f elements

1.2.1 Selection of quantum numbers or what is a good quantum number?

To understand any quantum mechanical system, the main goal is to formulate a Complete Set of Commuting Observables (CSCO) and hence also what defines the "good" quantum numbers of the system. A given set of operators $A, B, C, ...$ is called a complete set of commuting observables if (i) all the observables commute by pairs and (ii) specifying the eigenvalues of all of the operators determines a unique common eigenvector. We note that an observable is an operator with real eigenvalues and also the eigenvectors of an observable form a basis in state space. We also note that property that commuting observables share eigenvectors. Therefore, once a CSCO is established and the eigenvalues known, the eigenvectors can be uniquely defined.

1.2.2 Central force problem and the hydrogen atom

In order to formulate a CSCO to describe the magnetic states of an ion, we first consider the central force problem of an electron and a proton or the Hydrogen atom. This analysis ignores the presence of spin which we will outline changes the physics as one needs to consider an extra spin-orbit term in Hamiltonian $\mathcal{H}$. This also changes what we choose as our CSCO in describing a magnetic ion. We will show the spin-orbit coupling increases with the atomic number Z of the atom as Z^4 by applying classical theory and show we can the divide elements in periodic table into those with small Z (L-S coupling) and those with large Z (j-j coupling).

Starting with arguably the simplest case of the hydrogen atom that has an electron circling a proton (isotope ^{1}H which has no neutrons). The mass of proton is much bigger than that of electron with rest mass energies of $m_p c^2 =$ 938 MeV and $m_e c^2 = 0.5$ MeV. We can cast the problem in terms of reduced mass μ of two particles, in this case it is proton m_p and electron m_e that are attracted by a force [40], can be written as:

$$\mu = \frac{m_e m_p}{m_e + m_p}. \tag{1.3}$$

The eigenvalue problem is represented by the following equation:

$$\mathcal{H}_0|\psi\rangle = E|\psi\rangle, \tag{1.4}$$

which in a position representation (note that $\psi(\mathbf{r}) \equiv \langle r|\psi\rangle$) gives the following partial differential equation:

$$\left(-\frac{\hbar^2}{2\mu}\nabla^2 - \frac{Ze^2}{r} \right)\psi(\mathbf{r}) = E\psi(\mathbf{r}), \tag{1.5}$$

where e is the electron charge, $\mathbf{r}$ is the position of the electron with respect to the proton, μ is the reduced mass and ∇ is the Laplace operator. Physically, the first term on the left hand side represents the kinetic energy and the second the Coulomb potential energy. The potential electrostatic term will be important later on for crystalline electric field theory.

The Laplace operator in Cartesian coordinates has a form:

$$\nabla^2 = \frac{\partial^2}{\partial x^2} + \frac{\partial^2}{\partial y^2} + \frac{\partial^2}{\partial z^2}. \tag{1.6}$$

It's more practical to use spherical coordinates, where the Laplace operator looks like:

$$\nabla^2 = \frac{1}{r^2}\frac{\partial}{\partial r}\left(r^2 \frac{\partial}{\partial r} \right) + \frac{1}{r^2 \sin\theta}\frac{\partial}{\partial \theta}\left(sin\theta \frac{\partial}{\partial \theta} \right) + \frac{1}{r^2 \sin^2\theta}\frac{\partial^2}{\partial \phi^2}. \tag{1.7}$$

Where $\psi = \psi(r, \theta, \phi)$. This differential equation can be solved by separating variables giving differential equations in terms of r and angular coordinates (θ, ϕ). Solving the radial part gives the energy eigenvalues of hydrogen atom:

$$E_n = -\frac{\mu e^4}{32\pi^2 \varepsilon_0^2 \hbar^2}\left(\frac{1}{n^2}\right) \sim \frac{-13.6eV}{n^2}. \tag{1.8}$$

The energy eigenvalues depend on principal quantum number n.

Solving the angular differential equation and applying the boundary conditions that $|\psi\rangle$ must be both continuous and square integrable results in two more quantum numbers l, m. These are the eigenvalues of the orbital angular momentum L^2 and the z-axis projection L_z outlined above for generalised angular momentum operators. The Schrödinger equation, in position representation, can then be summarised as,

$$\mathcal{H}_0 \psi_{n,l,m}(r, \theta, \phi) = E_n \psi_{n,l,m}(r, \theta, \phi), \tag{1.9}$$

with the coordinate separated wavefunction consisting of radial $R_{n,l}$ and angular term $Y_{l,m}$:

$$\psi_{n,l,m}(r, \theta, \phi) = R_{n,l}(r) Y_{l,m}(\theta, \phi). \tag{1.10}$$

Therefore each eigenstate can be uniquely defined by the quantum numbers n, l and m, where principal quantum number n is related with energy and l and m are the eigenvalues of the orbital angular momentum operator L^2 and L_z respectively and discussed above in general times. For completeness, we write the angular operators,

$$L^2 = -\hbar^2\left[\frac{1}{\sin\theta}\frac{\partial}{\partial\theta}\left(\sin\theta\frac{\partial}{\partial\theta}\right) + \frac{1}{\sin^2\theta}\left(\frac{\partial^2}{\partial\phi^2}\right)\right], \tag{1.11}$$

$$L_z = -i\hbar\frac{\partial}{\partial\phi}. \tag{1.12}$$

The operators $\mathcal{H}_0$, L^2 and L_z commute and formulate complete set of commuting observables for the hydrogen atom. Knowing their eigenvalues allows us to

uniquely define the eigenvector.

1.2.3 Spin-orbit coupling

One thing this analysis ignores is the presence of spin discovered through the Stern-Gerlach experiment resulting in an extra operator S^2. Hence we need forth quantum number - spin quantum number s that has value $1/2$, where m_s can gain values $+1/2$ or -1/2 (spin up or spin down) as electron behaves as spinning in either clockwise or counter-clockwise fashion. In the case of hydrogen atom, we might consider the set of observables $\mathcal{H}_0$, L^2, L_z, S^2 and S_z as CSCO. However, the presence of spin introduces other terms in the energy expression and hence our Hamiltonian discussed above. While this can be formulated in general terms from Dirac's equation, we apply classical theory in this section to derive additional terms in the Hamiltonian.

In the history of physics, spectroscopic measurements have often pointed out inconsistencies in theory. That was also the case of spectroscopic measurements of the hydrogen atom. Considering the Bohr model, after the hydrogen atom is excited to the $n = 2$ orbital and then falls back to $n = 1$, one should see the so called Lyman - α line - therefore one singlet at certain frequency in spectroscopic data, see Fig. 1.7. However, a doublet has been observed instead. This is mainly due to the spin-orbit coupling that we would discuss here.

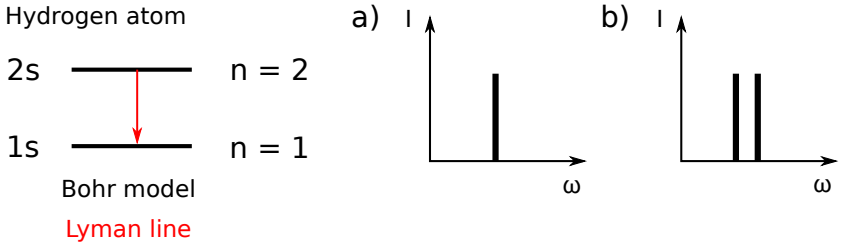

Figure 1.7 *Lyman line for electron of hydrogen atom going from excited $n = 2$ orbital to $n = 1$. Theory predicted a) as a result for spectroscopic measurement - singlet at certain frequency ω. However, doublet b) has been measured. This is mainly due to the spin-orbit coupling. This process has been explained in more details later.*

For simplicity, we would use the Bohr model, even though we know it is incorrect, but it gives an answer that is pretty close to the correct relation (that includes quantum considerations) for the spin-orbit coupling. The situation is the following - an electron is circling around the nucleus and simultaneously rotating around it's own axis, see Fig. 1.8:

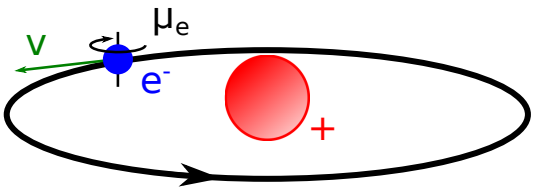

Figure 1.8 *Bohr model of hydrogen atom. Electron with intrinsic magnetic moment $\boldsymbol{\mu}_e$ is orbiting around nucleus. This movement generates magnetic field with orbital momentum that interacts with spin momentum, which results in spin-orbit coupling. $\boldsymbol{v}$ is tangential velocity of the electron.*

The electron has an intrinsic magnetic moment μ_e, which is a result of its angular momentum (spin):

$$\boldsymbol{\mu}_e = -g\frac{\mathbf{s}}{\hbar}\mu_B, \tag{1.13}$$

where g is the electron g-factor and μ_B is Bohr magneton that is defined as:

$$\mu_B = \frac{e\hbar}{2m_e}, \tag{1.14}$$

m_e is mass of the electron. An electron orbiting around a nucleus has also angular momentum $\mathbf{l}$:

$$\begin{aligned} \mathbf{l} &= \mathbf{r} \times \mathbf{p}, \\ \mathbf{p} &= m_e\mathbf{v}, \\ \mathbf{l} &= \mathbf{r} \times m_e\mathbf{v}, \end{aligned} \tag{1.15}$$

here $\mathbf{p}$ is momentum, $\mathbf{v}$ is the tangential speed of electron and $\mathbf{r}$ is position vector of electron from nucleus. Movement of the electron generates the magnetic field $\mathbf{B}$:

$$\mathbf{B} = \frac{Ze\mu_0}{4\pi}\frac{\mathbf{v} \times \mathbf{r}}{r^3}, \tag{1.16}$$

where μ_0 is permeability of free space and Z is the atomic number. Knowing the

relations for $\mathbf{l}$, Eq. (1.16) can be rewritten as:

$$\mathbf{B} = \frac{Ze\mu_0}{4\pi m_e r^3}\mathbf{l}. \tag{1.17}$$

This magnetic field $\mathbf{B}$, coming from the orbital movement, and spin, that is carried by the electron, interact with each other in similar way as two magnetic dipoles. The potential energy V associated with the interaction between the intrinsic magnetic moment of the electron and orbital momentum is then:

$$V = -\boldsymbol{\mu}_e \cdot \mathbf{B}. \tag{1.18}$$

By combining equations (1.13) with (1.14) and (1.17), the Eq. (1.18) becomes:

$$V_{SO} \propto \frac{Z}{r^3}\mathbf{s} \cdot \mathbf{l}. \tag{1.19}$$

We used proportional in equation, which comes down to the fact that energy for spin-orbit coupling must be corrected by relativistic factor of 1/2, known also as the Thomas precession factor. We discussed the case of hydrogen atom, however, for more electrons, we can add up s_i to get the total $\mathbf{S}$:

$$\mathbf{S} = \sum_{i=1}^{n} \mathbf{s}_i, \tag{1.20}$$

similarly for $\mathbf{L}$:

$$\mathbf{L} = \sum_{i=1}^{n} \mathbf{l}_i. \tag{1.21}$$

Usually, Eq. (1.19) is written in a form $\lambda \mathbf{L} \cdot \mathbf{S}$, where λ is the spin-orbit constant. However, it is interesting to note that this result is wrong by exactly a factor of 1/2 due to precession and can be understood in classical and also relativistic arguments. Putting this all together, we can write a complete Hamiltonian including Coulomb and spin orbit coupling,

$$\mathcal{H} = \mathcal{H}_0 + V_{SO}. \tag{1.22}$$

This introduces a problem and inconsistency, because L_z and S_z do not commute with $\mathcal{H}$. Therefore, the CSCO created above is no longer valid and approximations need to be made to formulate a CSCO.

1.2.4 L-S (small Z) and j-j (large Z) coupling

Given the failure of the Hydrogen Hamiltonian to give a general description in terms of a CSCO owing to spin-orbit coupling, approximations need to be made. Previously, we found the eigenvalues for Hamiltonian of hydrogen atom as $E = -13.6eV/n^2$ in the absence of spin-orbit coupling. Calculations show that the energy difference resulting from the spin-orbit coupling term is $\sim 10^{-4}eV$. In a case of hydrogen atom, the spin-orbit coupling represents just a small perturbation. However, result $\langle r^k \rangle \propto 1/Z^k$ which means that the strength of spin-orbit coupling grows quickly with the atomic number as Z^4.

In the case of $3d$-elements, atoms with small Z, the spin-orbit coupling is usually weak and can be neglected as a term in the approximate Hamiltonian. The main energy is determined by the electrostatic interactions and therefore L^2, L_z, S^2, and S_z form a complete set of commuting observabes. Therefore, the state vector can be written as $|l, m_l, s, m_s\rangle$ for describing the magnetic state, see Fig. 1.9 . This is known as L-S coupling (also as Russell-Saunders coupling).

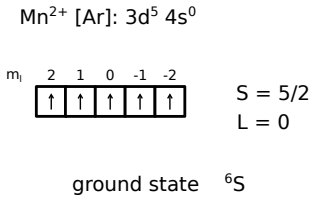

Figure 1.9 *Ground state of Mn^{2+} ion applying Hund's rules, L-S coupling*

On the other hand, f-elements (larger Z) have strong spin-orbit coupling. In this case, the spin-orbit term of Hamiltonian dominates over the electrostatic terms. In this case, the total angular momentum, defined by $\mathbf{J} = \mathbf{L} + \mathbf{S}$, squared and the z-axis projection, denoted as J^2 and J_z can be considered to form the CSCO. The state vector can be written as $|j, m_j\rangle$, see Fig. 1.10. This is known as $j - j$ coupling. The spin and orbital angular momentum of each electron couple separately [6].

In summary, L-S and j-j divide the periodic table into two segments. The smaller atomic number Z elements have Hamiltonians dominated by electrostatic

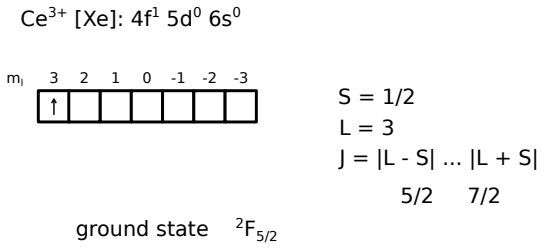

Figure 1.10 *Ground state of Ce^{3+} ion applying Hund's rules, j-j coupling*

interactions and spin-orbit coupling can be considered a perturbation. For large Z elements, the opposite is the case with spin orbit coupling dominating and electrostatic interactions a perturbation.

1.2.5 Determining L, S, and J using Hunds Rules

A typical atom does not contain just one electron, but many. A lot of them have fully filled electron shells, which means that they have no net angular momentum. However, some atoms don't have fully filled shells and therefore we need to deal with non-zero spin and orbital angular momentum. Thus an atom has total orbital angular momentum $\hbar\mathbf{L}$ and total spin angular momentum $\hbar\mathbf{S}$. These two can combine in [6]:

$$(2L+1)(2S+1) \tag{1.23}$$

ways. The upper relation can be interpreted as total number of choices of the z component of $\mathbf{L}$ multiplied by the total number of choices of the z component of $\mathbf{S}$. Different combinations of orbital and spin angular momentum gives different energies (or in other words - different states will cost different amount of energy). Spin angular momentum influences the spatial part of the wave function, whereas orbital angular momentum effects how electrons travel around nucleus. Both of them act on the way how electrons move in atom, how they avoid each other, which has influence on electrostatic repulsion energy.

Usually, the energy of atom is determined by the values of $\mathbf{S}$ and $\mathbf{L}$ through electrostatics considerations. Therefore, energy eigenstates can be labelled with values of $\mathbf{S}$ and $\mathbf{L}$. However, orbital and spin angular momentum are not always independent. They do weakly couple via so called spin-orbit interactions.

Estimates of minimal energy of the system can be done by using Hund's rules.

Their order indicates their importance, so one needs to fulfil first rule then move to second one and so on.

1. The total spin S must be maximized. This rules means that each shell will be filled with one spin rather than paired up spins. Moreover, the Pauli exclusion principle prevents spins to fill shell with two parallel spins, which would increase Coulomb repulsion between electrons.

2. If first rule is satisfied, then maximize total orbital momentum L. In other words, first spin goes to shell with the biggest m_l. This means that electrons in orbit rotating in the same direction can avoid each other more effectively and minimize energy of the system.

3. The third rule for estimate of ground state is not always needed. It arises from spin-orbit coupling. Spin-orbit coupling is strong in case of rare earth elements, but can occur in case of d-elements sometimes too. If it is the case, then J is found using $J = |L - S|$ if the shell is less than half full and $J = |L + S|$ if it is more than half full.

With all values for S, L and J, the ground state can be written using a term symbol ${}^{2S+1}L_J$. Where L is written not as a number, but a letter following this table:

L	
0	S
1	P
2	D
3	F
4	G
5	H
⋮	⋮

and $2S + 1$ is the spin multiplicity.

Hund's rules provide information about ground state, but tell us nothing about excited states or even - how close they are to ground state.

In next chapters we will discuss $3d$ and $4f$ elements as these are important in many magnetic systems. In Fig.1.11 it's possible to see application of Hund's

rules to $3d$ and $4f$ ions. S rises and becomes a maximum in the middle of each group. L and J have maxima at roughly the quarter and three-quarter positions, although for J there is an asymmetry between these maxima which reflects the differing rules for being in a shell which is less than or more than half full [6].

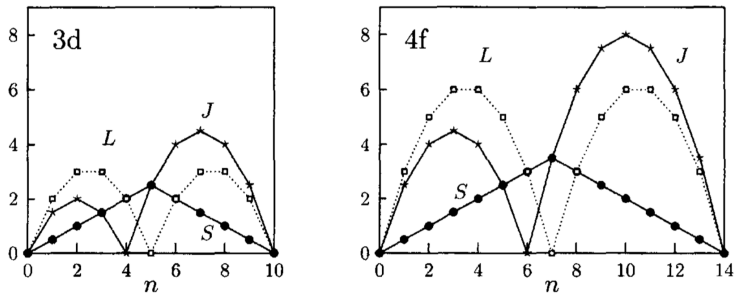

Figure 1.11 *S, L and J for 3d and 4f elements. Letter n represents number of electrons in subshell [6]*

1.2.6 Introduction to Crystal Field Theory

In many crystals containing rare earth elements, the consideration that rare earth ions behave like free ions without interacting with their surrounding, is completely fine and it works well. However, these interactions for magnetic ions in certain crystals cannot be neglected and their effect is quite large and significant [6]. The crystal field theory discusses interactions between an atom and its surroundings.

The crystal field is an electric field derived from neighbouring atoms in the crystal. In crystal field theory (CEF), the neighbouring orbitals are modelled as negative point charges. The important fact is that the size and nature of crystal field effects depend crucially on the symmetry of local environment [6]. In transition metal compounds, it is quite common that metal ion sits in centre of octahedron (for example) surrounded by other ions (quite often oxygen ions).

In many textbooks, the introduction to crystal field theory starts with description of d orbitals straight away. What about other types? An s orbital is of no great interest since it is nondegenerate. A p orbital does not split in a octahedral field, because all three orbitals are part of T_{1u} representation of cubic group. In a field of lower symmetry, splitting must occur. However, we don't apply crystal field theory to p electrons because they participate so strongly in bonding processes. In case of d orbitals, the effect of crystal field is really strong. The only other orbitals, where CEF can be used with profit are f orbitals [41]. The crystal

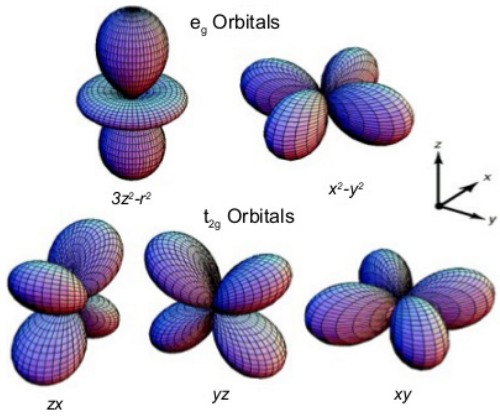

Figure 1.12 *The angular distribution of d orbitals. This figure only shows the angular part of wave function, but there is also a radial part. Only s orbitals are spherically symmetric, the others have an angular dependence. This is important as the local environments are often not spherically symmetric. The d orbitals in octahedral and tetrahedral field falls into two classes - first - t_{2g} orbitals, d_{xy}, d_{xy} and d_{xy} (these orbitals point between x, y and z axis) - and then - e_g orbitals are d_{z^2} and $d_{x^2-y^2}$ (these orbitals point along x, y and z axis).*

field contribution differs in the way it is applied as a perturbation because of its relative magnitude. In the $4f$ group, its energy is small compared with spin-orbit coupling energy, so that it is applied as a perturbation to the manifold of (2J+1) states for a given term J of the free ion [42]. As it has been mentioned several times, in the $3d$ group the crystal field energy is larger than spin-orbit coupling, and comparable with electrostatic interactions within the ion which gives rise to L-S coupling.

Let's concentrate on d orbitals as those provide a very nice explanation of basic principles of the CEF. Suppose a cation containing ten d electrons placed in the centre of a sphere with certain radius (the sphere is negatively charged). The repulsion is distributed equally in space and all d orbitals are degenerate. The sphere has an infinite number of symmetry operations. As we move to the fields with lower symmetries (meaning - with less symmetry operations), the splitting must appear. We can see quickly how this will change if surrounding atoms are placed into six corners of a octahedron (octahedral field) or four corners of a tetrahedron (tetrahedral field). The strength of repulsion between certain orbitals of transition ion in centre and surrounding ions will depend on orientation of these orbitals in a space. Therefore, they will be lowered or raised in energy.

The CEF can be explained from electrostatic charge distribution point of view

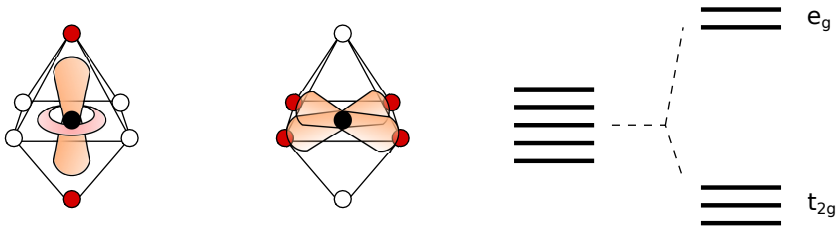

Figure 1.13 *The octahedral field - the repulsion coming from overlap of orbitals of surrounding atoms, placed in corners of an octahedron, with d_{z^2} and $d_{x^2-y^2}$ orbitals of the central ion is bigger than electronic repulsion for d_{xy}, d_{xy} and d_{xy} orbitals, which results into two levels splitting, where d_{z^2} and $d_{x^2-y^2}$ orbitals are energetically more costly.*

- let's assume octahedral field - central ion surrounded by six point charges in the corners of a octahedron. The field generated by six point charges can be represented by an expansion in spherical harmonics about the central ion as an origin. Two important assumptions must be made here - that the d orbitals of the ion do not overlap the charges and the potential obeys Laplace's equation. The potential is:

$$V = \frac{2e_i}{R}\Big[3 + \frac{35}{8R^4}\Big(x^4 + y^4 + z^4 - \frac{3r^4}{5} + ...\Big)\Big], \tag{1.24}$$

where R is the distance from ion to charges. x, y and z are coordinates of the electron and e_i is the charge at each external point [41].

Let's write a more general equation for the CEF part of Hamiltonian that is added to the Hamiltonian of the free ion as a perturbation term:

$$\mathcal{H}_{CEF}(\mathbf{r}) = \sum_j \frac{q_j}{|\mathbf{R}_j - \mathbf{r}|}, \tag{1.25}$$

where $\mathbf{R}_j$ are the positions of the ions (considered as point charges here) with charge q_j. If we take a point at $\mathbf{r}$ such that $|\mathbf{r}| < |\mathbf{R}|$, the following expansion can be made:

$$\mathcal{H}_{CEF}(\mathbf{r}) = \sum_j q_j \frac{1}{R_j} \sum_{n=0}^{\infty} \Big(\frac{r}{R_j}\Big)^n P_n(cos(\theta)), \tag{1.26}$$

here $P_n cos(\theta)$ are Legendre polynomials and the angle θ is defined such that

$|\mathbf{r}_j - \mathbf{R}_j|^2 = r^2 - 2rRcos(\theta) + R^2$. This expression can be rewritten in terms of tesserial harmonics by noting the relation:

$$P_n(cos(\theta)) = \frac{4\pi}{2n+1} \sum Z_{n\alpha}(\mathbf{r}) Z_{n\alpha}(\mathbf{R}), \tag{1.27}$$

$Z_{n\alpha}$ are normalized spherical harmonics. Substituting gives the following:

$$V(\mathbf{r}) = V(r,\theta,\phi) = \sum_j q_j \sum_{n=0}^{\infty} \frac{r^n}{R_j^{n+1}} \sum_{\alpha} \Big[\frac{4\pi}{2n+1} Z_{n\alpha}(\theta_j,\phi_j) Z_{n\alpha}(\theta,\phi) \Big]. \tag{1.28}$$

The expression above allows to separate terms involving $\mathbf{R}_j = (R_j, \theta_j, \phi_j)$ and $\mathbf{r} = (r,\theta,\phi)$. It can be condensed into following form:

$$V(\mathbf{r}) = V(r,\theta,\phi) = \sum Z_{n\alpha} \sum_{\alpha} r^n \gamma_{n\alpha} Z_{n\alpha}(\theta,\phi) = \sum_{n,\alpha} \gamma_{n\alpha} H, \tag{1.29}$$

where:

$$\gamma_{n\alpha} = \sum_j \frac{4\pi}{2n+1} q_j \frac{Z_{n\alpha}(\theta_j,\phi_j)}{R_j^{n+1}}. \tag{1.30}$$

The entire analysis has been done assuming that $r < R$, which will be the case within lattice. In an interpretation of CEF, the $\gamma_{n\alpha}$ are treated as constants that can be determined by experiment. The real charge distribution in crystals are quite complicated in fact. Despite this acknowledgement, the distributions of point charges are useful for gaining a qualitative understanding of the behaviour of the various terms in complicated potential functions [41].

If we now assume that the crystalline electric field is a perturbation on our good eigenstates (spin-orbit Hamiltonian with quantum numbers j and m), and note that the Z's transform the same way as the angular momentum operator J, we can apply the Wigner-Eckart theorem and state that the operators:

$$\mathbf{R} \propto \mathbf{J}. \tag{1.31}$$

As an example, we can make the following relationship based on this for a specific Z:

$$\sum_i (3z_i^2 - r_i^2)r^2 = \alpha\big[3J_z^2 - J(J+1)\big]\langle r^2\rangle, \tag{1.32}$$

where α is a number. we can further condense this expression (and similar ones) by rewriting it as

$$Z_{20} = \sum_i (3z_i^2 - r_i^2)r^2 = \alpha\big[3J_z^2 - J(J+1)\big]\langle r^2\rangle = \alpha_j\langle r^2\rangle O_2^0, \tag{1.33}$$

therefore:

$$V = \sum_i \gamma_{n\alpha} H_{n\alpha} = \sum_{l,m} B_l^m O_l^m. \tag{1.34}$$

Here, B_l^m are the Steven's coefficients and B_l^m are the Steven's operators. Going through all steps again - first, we rewrite the Hamiltonian (based on Coulomb potentials) in terms of a series of expansion of Legendre polynomials. Then we wrote this expression in terms of Z's - so we are working with cartesian coordinates rather than spherical (or angular) coordinates. This allows us to use perturbation theory and assume that spin-orbit eigenstates remain good eigenstates under the perturbation of the crystalline electric field. Then we can use the Wigner-Eckart theorem and state that the coordinates $(x, y, z) \propto (J_x, J_y, J_z)$ allowing us to write the crystalline electric field Hamiltonian in terms of angular momentum operators. We finally condensed the expression into one involving Steven's coefficients and operators.

Using angular momentum operators for crystalline electric field Hamiltonian is beneficial, because we can calculate eigenstates and eigenvalues relatively easily. The Steven's coefficients B_l^m can be considered experimental parameters, though they can also be calculated using the expression written above for $\gamma_{n\alpha}$. The coefficients can be approximated assuming point charges (as written above) or the expression can be generalized using charge densities. The calculation for $\gamma_{n\alpha}$ depends on terms involving $1/R_n$ and generally few terms in the sum need to be included to get good numerical convergence. This expression also shows that the nearest neighbours play a key role in consider the Coulomb potential from

nearest neighbour ions.

As it has been mentioned before, in an octahedral field, energy levels split into triply degenerate $|t_{2g}\rangle$ and doubly degenerate $|e_g\rangle$ states, see Fig. 1.14. Both, the $|t_{2g}\rangle$ and $|e_g\rangle$ are linear combination of the d atomic orbitals given by $|l = 2, m_l\rangle$ in the $|l, m_l\rangle$ basis. The gap between $|t_{2g}\rangle$ and $|e_g\rangle$ states Δ_o is often denoted as $10Dq$ which is equivalent to $120B_4$, where the Stevens parameter B_4 parametrises the crystal field Hamiltonian for an undistorted octahedron given by:

$$\mathcal{H}_{CEF} = B_4(O_4^0 + 5O_4^4), \tag{1.35}$$

in the Stevens formalism that we defined in this chapter before. It's possible to get energy scale of $|t_{2g}\rangle$ and $|e_g\rangle$ states in terms of Dq as:

$$\begin{aligned} E_t &= -4Dq, \\ E_e &= 6Dq. \end{aligned} \tag{1.36}$$

Which can be shown in the diagram nicely:

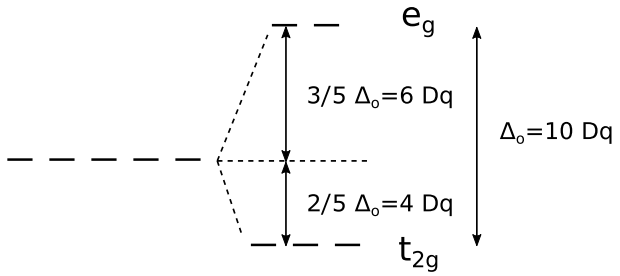

Figure 1.14 *Energy scale of t_{2g} (d_{xy}, d_{yz}, d_{zx} orbitals) and e_g (d_{z^2}, $d_{x^2-y^2}$ orbitals) states in terms of Dq in the octahedral field. Splitting Δ_o corresponds to 10 Dq.*

There is also relation among the size of orbital splitting Δ for fields of different symmetry (point charge model):

$$\begin{aligned} \Delta_t &= -\frac{4}{9}\Delta_o = -0.44\Delta_o, \\ \Delta_c &= -\frac{8}{9}\Delta_o = -0.88\Delta_o, \end{aligned} \tag{1.37}$$

where Δ_t is splitting in tetrahedral field (see Fig. 1.15) and Δ_c in cubic field. Very similar values have been confirmed by experiment. The most significant

result is the small value of Δ_t for tetrahedral fields.

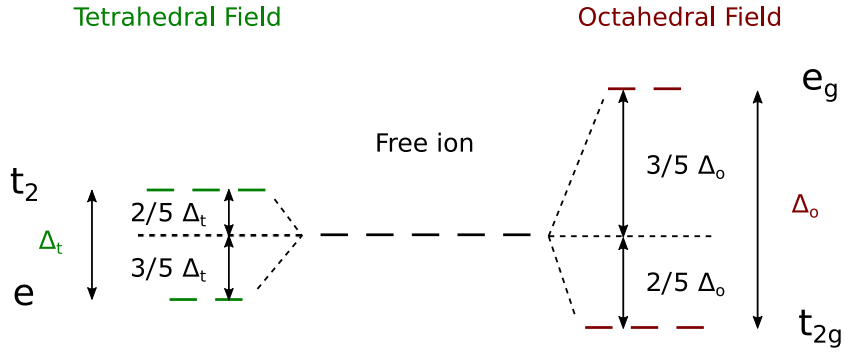

Figure 1.15 *Splitting of d orbitals in tetrahedral and octahedral field, the energy gap of splitting for tetrahedral field Δ_t is significantly smaller than the splitting in octahedral field Δ_o, $\Delta_t = -0.44\Delta_o$. In tetrahedral case, the t_2 level is triple degenerated (d_{xy}, d_{yz}, d_{zx} orbitals) and is energetically higher than e level.*

1.2.7 Weak and Strong Crystal Fields, Tanabe-Sugano Diagrams

Starting with an example, the Fe^{2+} ion has 6 valence electrons in $3d$ orbitals. It has been observed that there are two ways how the electrons occupy orbitals, which seemed to be connected with type of ligands bounded with the central atom. A simple sketch might be useful, 1.16:

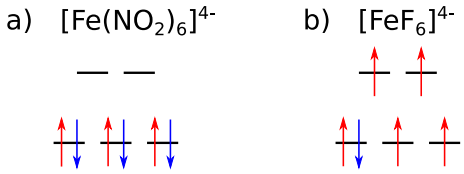

Figure 1.16 *Occupancy of electrons in orbitals for two complex ions $[Fe(NO_2)_6]^{4-}$ and $[FeF_6]^{4-}$. In a) electrons occupy just the t_{2g} level. In b) single electron enters each orbital first, following Hund's rules.*

In a first case, electrons will pair in orbitals and fill lower t_{2g} levels, rather than occupy free, energetically higher, e_g orbitals. Another way can be that one fills each orbital with one electron first, following Hund's rules, then the second electrons can be added.

Priority of one approach over another is given by the fact if it is energetically favourable for the system - it's a competition between crystal field energy and

Coulomb energy cost of putting two electrons in the same orbital, which is known as a pairing energy. If the ligand field energy is lower than the pairing energy (known as weak-field case), so electrons will first singly occupy each orbital before any orbital becomes doubly occupied. On the other hand, if the ligand field is larger than the pairing energy (the strong field case), electrons will doubly occupy lower energy orbitals before they move to energetically more costly higher energy orbitals [6].

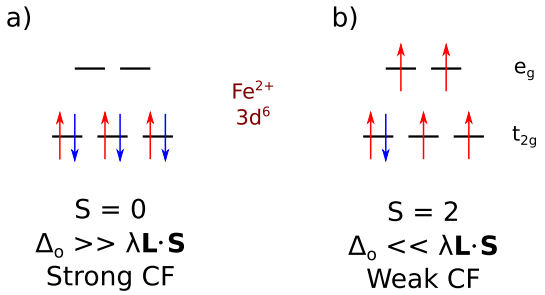

Figure 1.17 *Effect of the strong crystal field on the left and weak crystal field on the right. When $\triangle_o \gg \lambda \boldsymbol{L} \cdot \boldsymbol{S}$, only lowest orbitals are occupied with electrons, if $\triangle_o \ll \lambda \boldsymbol{L} \cdot \boldsymbol{S}$, electrons fill orbitals in respect of Hund's rules.*

Tanabe-Sugano diagrams show transition from weak field to strong field for various number of electrons in d orbitals. They can be also used to predict the size of the crystal field necessary to cause high-spin to low-spin transitions (diagram approximates the value of 10Dq - the ligand field splitting energy). The results of Tanabe-Sugano diagrams might be compared with experimental spectroscopic data. Starting reference point is the ground state and is taken to be zero, whereas the energies of all other terms and their components are plotted with respect to the ground term. In Fig. 1.18, the energy is in units of B, which we will discuss in next paragraph in more details. The abscissa is Dq/B. The ground state is always the abscissa line. A change in ground state is indicated by vertical line at the value of Dq/B where the change occurs. These diagrams do not show the complete transition from weak to strong fields, but they are carried far enough ($Dq/B = 4$), so that the states occur in same order as in a strong field.

Let's discuss the B parameter a bit more. It's one of the so called Racah parameters (A, B, C) - these are used for free-ion solution for $3d$ ions (in the absence of a crystal electric field). For example - 3 lowest-energy states for Co^{2+}

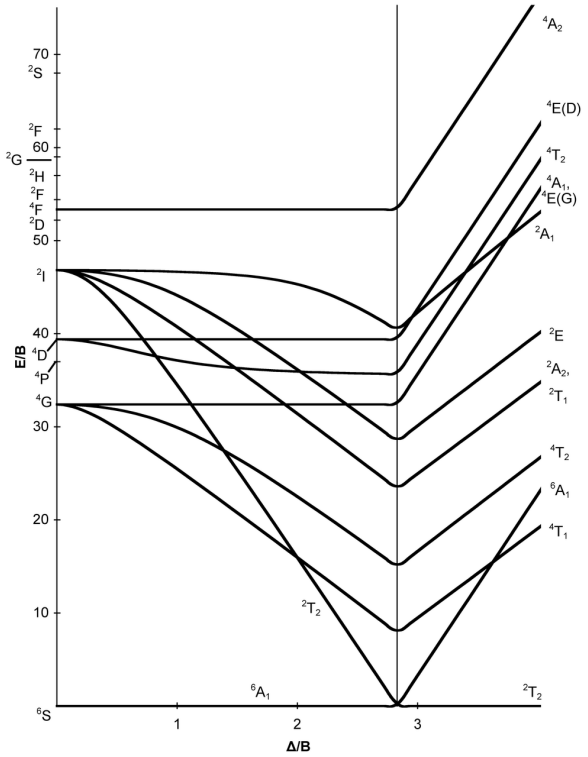

Figure 1.18 *Tanabe-Sugano diagram for octahedral complexes and d^5 electron configuration. The ground state of this configuration is ^6S. Scaling of the axis can differ - here the horizontal axis is Δ/B ($10Dq/B$).*

have the energies:

$$\begin{aligned} E(^4P) &= 3A, \\ E(^4F) &= 3A - 15B, \\ E(^2G) &= 3A - 11B + 3C. \end{aligned} \tag{1.38}$$

Physically, the terms B and C represent the effect of interactions between the electrons in the $3d$ orbitals. It has been proven that the ratio $\gamma \equiv C/B$ is close to a constant value ~ 4.6 for the $3d$ ions and therefore - Racah parameter B is taken as a parameter quantifying electron correlations [43].

Racah parameters are another way how to write results that can be derived from Slater integrals. Therefore, the Racah parameters can be recast in terms of the

Slater integrals as:

$$\begin{aligned} A &= F_0 - 49F_4, \\ B &= F_2 - 5F_4, \\ C &= 35F_4. \end{aligned} \tag{1.39}$$

However, there is also another notation for the Slater terms that it is commonly used. Let's recall these relations:

$$\begin{aligned} F_0 &= F^0, \\ F_2 &= \frac{1}{49}F^2, \\ F_4 &= \frac{1}{448}F^4. \end{aligned} \tag{1.40}$$

So far, we mentioned two ways to parametrise electron-electron interactions - original theory by Slater, which was followed by Racah. More recently, this theory has been cast in terms of the Hubbard model [43]. It seems to be natural to introduce a single parameter that can capture the effect of electron correlations that characterizes the intraorbital exchange. The intraorbital exchange can be defined as parameter which describes the attraction of parallel spins in different d orbitals [44]:

$$J(dd) = \frac{1}{14}(F^2 + F^4). \tag{1.41}$$

Previous discussion indicates that this expression can be written in terms of Slater integrals (F^i) or Recah parameters (B, C). The standard notation of horizontal axis $10Dq/B$ in Tanabe-Sugano diagrams (see Fig. 1.18) can be recalculated as $10Dq/J(dd)$. $10Dq/J(dd)$ represents two energy scales - crystal electric field and intraorbital exchange (interaction of two parallel spins in different d orbitals). High value of $J(dd)$ indicates high-spin configuration or simply - the configuration with few spins that are parallel to each other. This means that intraorbital exchange is bigger than effects of crystal field, which brings us to left side of Tanabe-Sugano diagram and therefore to the region of weak crystal field. This configuration is also given by Hund's rules. On the other hand - small $J(dd)$ means low-spin configuration and crystal field term becomes dominant - which moves system to the right side of Tanabe-Sugano diagram known as a strong

crystal field.

An important feature of the diagrams is the change from ground state given by Hund's rule to a different ground state in strong fields. This change occurs, for example, in the configurations d^4, d^5, d^6 and d^7 when in octahedral fields.

1.2.8 Jahn-Teller Distortion

So far we were discussing the behaviour of orbitals dependence on symmetry of the local environment. Sometimes, however, it is favourable for the system to influence the symmetry of local environment. Octahedral crystal environment splits degenerated d orbitals into e_g and t_{2g} levels. If octahedron spontaneously distort, the energy cost of increased elastic energy is balanced by a electronic energy saving due to the distortion, see Fig. 1.19.

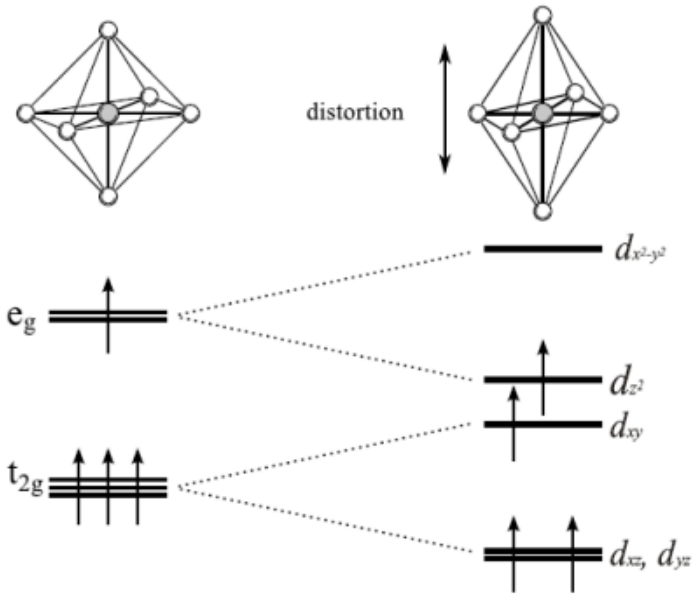

Figure 1.19 *The Jahn-Teller effect for Mn^{3+}. An octahedron can distort, thus splitting the e_g and t_{2g} levels. The distortion lowers the energy, because a single occupied e_g level is lowered in energy. The saving in energy from the lowering of the d_{xz} and d_{yz} levels is exactly balanced by the raising of the d_{xy} level [6].*

If we think about Jahn-Teller distortion in terms of overlapping orbitals, then stretching octahedron along z-axis would mean smaller overlap of d_{z^2} orbital of central atom with, for example, p orbitals of ligand atoms in corners of octahedron along z-axis. In contrast - overlap of p orbitals of other ligands with $d_{x^2-y^2}$ orbital

will be increased - therefore energetically more costly. We can quickly see that stretching octahedron along the z-axis will raise energy of $d_{x^2-y^2}$ and lower energy of d_{z^2} level. Squeezing the octahedron along z-axis will raise d_{z^2} and lower $d_{x^2-y^2}$ level, see Fig. 1.20.

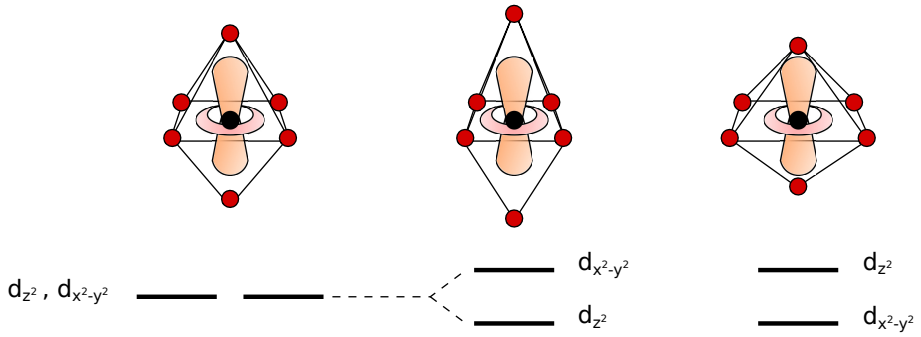

Figure 1.20 *Simple scheme of split of energy levels d_{z^2} and $d_{x^2-y^2}$ if the octahedron is deformed along z-axis - elongated or compressed.*

1.2.9 Single ion anisotropy and short discussion about Kramers doublets

Since the crystal field Hamiltonian is a real function, its eigenstates can be also expressed with real functions. On the other hand - the total orbital angular momentum $\mathbf{L}$ is pure imaginary. Since $\mathbf{L}$ is a Hermitian operator, the diagonal matrix element must be real. From this we see that the expectation value of the angular momentum over a nondegenerate eigenstate must be zero - especially, for nondegenerate ground state $|0\rangle$

$$\langle 0|\mathbf{L}|0\rangle = 0. \tag{1.42}$$

This means that orbital momentum is quenched in a nondegenerate ground state and it can be easily done by crystal field splitting. The quenched orbital angular momentum is partially restored by L-S coupling, as we are going to show.

Let E_n and $|n\rangle$ be the energy level and the corresponding eigenfunction due to the crystal field splitting. The orbital state of ion is the ground state $|0\rangle$, in which the orbital angular momentum is quenched, and the spin $\mathbf{S}$ is completely free with (2S +1)-fold degeneracy; in this case the magnetic moment of the ion is given exclusively by the spin. The free spin couples to the lattice only when we

take into account the L-S coupling. Let us treat the L-S coupling and Zeeman energy [45]:

$$V = \lambda \mathbf{L} \cdot \mathbf{S} + \mu_B \mathbf{H} \cdot (2\mathbf{S} + \mathbf{L}), \tag{1.43}$$

as a perturbation. Since the spin wave function is independent of the orbital part, the spin $\mathbf{S}$ is left as an operator in this perturbation calculation. Because of the quenching of $\mathbf{L}$, first order perturbation theory leads to:

$$\Delta E^{(1)} = 2\mu_B \mathbf{H} \cdot \mathbf{S}, \tag{1.44}$$

now, we will introduce $\Lambda_{\mu\nu}$ that has the definition:

$$\Lambda_{\mu\nu} = \sum_n \frac{\langle 0|L_\mu|n\rangle\langle n|L_\nu|0\rangle}{E_n - E_0}, \tag{1.45}$$

and we obtain second order energy as:

$$\Delta E^{(2)} = -\sum_{\mu\nu} [\lambda^2 \Lambda_{\mu\nu} S_\mu S_\nu + 2\lambda\mu_B \Lambda_{\mu\nu} H_\mu S_\nu + \mu_B^2 \Lambda_{\mu\nu} H_\mu H_\nu], \tag{1.46}$$

where μ and ν represent x, y or z. Adding $\Delta E^{(1)}$ and $\Delta E^{(2)}$, we get:

$$\mathcal{H}_S = \sum_{\mu\nu} [2\mu_B H_\mu (\delta_{\mu\nu} - \lambda\Lambda_{\mu\nu}) S_\nu - \lambda^2 S_\mu \Lambda_{\mu\nu} S_\nu - \mu_B^2 H_\mu \Lambda_{\mu\nu} H_\nu], \tag{1.47}$$

as we know that effective Hamiltonian for nondegenerate ground state splits off by crystal field. The first term in the previous equation represents an effective Zeeman energy, where g value has been replaced by the g tensor:

$$g_{\mu\nu} = 2(\delta_{\mu\nu} - \lambda\Lambda_{\mu\nu}). \tag{1.48}$$

Here the additional tensor -2 $\lambda\Lambda_{\mu\nu}$ is the induced orbital moment, which arises from the mixing with high-energy orbital states due to the L-S coupling and is expressed as a change of the magnetic moment accompanied with the spin $\mathbf{S}$.

The second term in Eq. (1.47) represents an anisotropic spin Hamiltonian - anisotropy energy for the spin direction. The third term will be discussed at the end of this chapter. Let us take main axes of the crystal x, y or z and express the components of Λ as Λ_x, Λ_y or Λ_z. Then the anisotropy spin Hamiltonian can be written as:

$$\begin{aligned}\mathcal{H}_{aniso} = &-\lambda\Big\{\frac{1}{3}(\Lambda_x+\Lambda_y+\Lambda_z)S(S+1)\\ &+\frac{1}{3}\Big[\Lambda_z-\frac{1}{2}(\Lambda_x+\Lambda_y)\Big][3S_z^2-S(S+1)]\\ &+\frac{1}{2}(\Lambda_x-\Lambda_y)(S_x^2-S_y^2)\Big\}.\end{aligned} \tag{1.49}$$

The anisotropy Hamiltonian lifts the (2S+1)-fold degeneracy of the spin. Omitting the constant term, we obtain:

$$\mathcal{H}_{aniso} = DS_z^2 + E(S_x^2 - S_y^2). \tag{1.50}$$

Let's inspect this equation in more details. Splitting of energy levels depends on the fact if the system has integer S or half-odd integer S.

Integer S

$S = 3$

$S_z = \pm S, \pm (S - 1), ..., \pm 1$ and 0

$S_z = \underbrace{\pm 3, \pm 2, \pm 1}_{\text{double degenerate}}, 0$

Half-odd Integer S

$S = 3/2$

$S_z = \pm S, \pm (S - 1), ..., \pm 1$

$S_z = \underbrace{\pm 3/2, \pm 1/2}_{\text{double degenerate}}$

$\mathcal{H}_{aniso} = DS_z^2 + E(S_x^2 - S_y^2)$

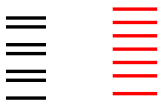

second term of $\mathcal{H}_{aniso}$ lifts the degeneracy

Kramers doublets
no additional splitting

In the case of the integer S, first term of Eq. (1.50) creates double degenerate S levels $S_z = \pm S, \pm(S-1), ..., \pm 1$ and nondegenerate level $S_z = 0$. The second term lifts the double degeneracy by the anisotropy Hamiltonian. However, for half-odd

integer S, one gets only doubly degenerate levels and this degeneracy remains due to the first term. It's the case of systems with an odd number of electrons, where the crystal field can not lift the degeneracy completely and therefore - leaving the energy levels double degenerate. This is known as Kramers theorem.

The Kramers theorem says that, in a system with odd number of electrons, two-fold degeneracy must remain in the absence of a magnetic field. This pair of states, Kramers doublets, can be split by a magnetic field, but not by an electric field. As electron configuration of Ce^{3+} ion has an odd number of electrons in the 4f shells, it qualifies as a Kramers ion. And the ground state of Ce^{3+} (and other similar systems) is a doublet.

The Kramers theorem is a general result which can be derived when the Hamiltonian for the electron system is invariant in time reversal. Under time reversal the orbital and spin angular momenta change signs; therefore the Kramers degeneracy is lifted first by the Zeeman energy (which changes sign under time reversal).

The lowest Kramers doublet can be described as fictitious spin with magnitude 1/2. The exchange interactions in this case are obtained by projecting the original isotropic exchange interaction onto two-dimensional subspace. The projected exchange interaction can be written as an anisotropic exchange interaction in terms of fictitious spins and gives rise to the magnetic anisotropy.

The third term in Eq. (1.47) is not related to L-S coupling; it comes rather from second order perturbation of the Zeeman energy. It gives anisotropic paramagnetic susceptibility, which is called Van Vleck orbital paramagnetism and non-negligible contribution when the energy of excited states is not too high.

In the case of cubic symmetry, the change of the effective g value and the orbital paramagnetism are finite and isotropic, since the anisotropy Hamiltonian in second order is merely a constant. In this case the anisotropy shows up in fourth-order perturbation; the anisotropy Hamiltonian is usually written as:

$$\mathcal{H}_S = \frac{a}{6}\Big\{S_x^4 + S_y^4 + S_z^4 - \frac{1}{5}S(S+1)[3S(S+1)-1]\Big\}. \tag{1.51}$$

The second order terms are constatnt for $S = 1/2$ even when the crystal field has a low symmetry. Similarly, Eq. (1.51) vanishes for $S < 2$. In such a situation, the anisotropy hamiltonian comes from the anisotropic interaction. The anisotropy

Hamiltonian in Eq. (1.51) becomes important for ions Mn^{2+} and Fe^{3+}, which have $S = 5/2$ and $L = 0$ [45].

1.2.10 Exchange Interactions

Considering simple magnetic orientation (we won't consider spiral magnetic structures for now), magnetic moments on magnetic ions in crystals can orient in two ways - parallel and antiparallel to each other. This ordering usually happens at low temperatures and means transition from disordered non-magnetic state to magnetically ordered state.

Nowadays, it is very well known that antiferromagnetism and ferromagnetism originate from the interactions between spins of magnetic ions. These interactions are called exchange interactions and they come from quantum exchange term of the Coulomb interactions between d electrons of neighbouring ions. Heissenberg supossed that direct exchange interactions are responsible for ferromagnetism. In fact, it has been proven that there are very few materials (CrO_2 and $CrBr_3$) in which the ferromagnetism arises from direct exchange interactions. The reason is that very often the overlap between neighbouring magnetic orbitals is insufficient. In the case of f orbitals, electrons are strongly localized and lie very close to the nucleus, so there is small probability of fluctuations of the electron density between atoms. However, the $3d$ electrons can not be treated as localized spins, in this chapter, we will discuss the case of magnetic ions in ionic crystals in which electrons are localized mainly [45]. The Hamiltonian for Heissenberg model, that considers direct exchange interactions, has a general form:

$$\mathcal{H}_{dir} = -\sum_{ij} J_{ij} \mathbf{S}_i \cdot \mathbf{S}_j. \tag{1.52}$$

In many magnetic materials it is necessary to consider other (indirect) types of interactions. There are several - superexchange interactions in ionic solids, double exchange, RKKY interactions in metals. Another perturbation comes from the presence of anisotropy in the system. We mentioned previously that the spin hamiltonian of one-ion anisotropy, is the energy that arises from the fact that orbital moments, introduced by the L-S coupling, depend on the direction of the spin $\mathbf{S}$ with respect to crystal axis [45]. Very similar effect arise when we consider the situation of two spins with anisotropic interactions.

Let us consider two magnetic ions with no orbital degeneracy in the ground state. Then the perturbation term of Hamiltonian would consist of two L-S coupling terms for two ions and the exchange interaction V_{exch}:

$$\mathcal{H}' = \lambda(\mathbf{L}_1 \cdot \mathbf{S}_1) + \lambda(\mathbf{L}_2 \cdot \mathbf{S}_2) + V_{exch}. \tag{1.53}$$

The process consists of three steps - the first one is excitation of a ion 1 to the state ψ_{n_1}, then there is exchange interaction between first excited ion and ion 2 in ground state, and finally $\mathbf{L}_1 \cdot \mathbf{S}_1$ returns the ion 1 to its ground state. By this process the following energy is derived:

$$\Delta E_3 = -\sum_{\mu\nu}[S_{1\mu}\Gamma^{(1)}_{\mu\nu}(\mathbf{S}_1 \cdot \mathbf{S}_2)S_{1\nu} + S_{2\mu}\Gamma^{(2)}_{\mu\nu}(\mathbf{S}_1 \cdot \mathbf{S}_2)S_{2\nu}], \tag{1.54}$$

where $\Gamma^{(1)}_{\mu\nu}$:

$$\Gamma^{(1)}_{\mu\nu} = 2\lambda^2 \sum_{n_1 n_1^{'}} \frac{\langle g_1|L_\mu|n_1\rangle J(n_1 g_2, n_1^{'} g_2)\langle n_1^{'}|L_\nu|g_1\rangle}{(E_{n_1} E_{g_1})(E_{n_1^{'}} E_{g_1})}, \tag{1.55}$$

$J(n_1 g_2, n_1^{'} g_2)$ is the exchange integral between excited state of ion 1 and ground state of ion 2. Off diagonal terms of state of ion 1 are generally present and are included in Eq. (1.55). Here comes also biggest difference if we compare it with relations for single ion anisotropy - single ion $\Lambda_{\mu\nu}$ does not include $J(n_1 g_2, n_1 g_2)$. However, $\Gamma^{(1,2)}_{\mu\nu}$ of the spin pair does and this anisotropy does not disappear, not even if the crystal field has cubic symmetry.

If $S = 1/2$, the Hamiltonian can be written as:

$$\mathcal{H}_{aniso} = -\frac{1}{4}\sum_{\mu\nu}\sum_{i=1,2}[(\Gamma^{(i)}_{\mu\nu} + \Gamma^{(i)}_{\nu\mu}) - \delta_{\mu\nu}(\Gamma^{(i)}_{xx} + \Gamma^{(i)}_{yy} + \Gamma^{(i)}_{zz})]S_{1\mu}S_{2\nu}. \tag{1.56}$$

This equation can be considered as an anisotropic exchange interaction and also as a generalisation of the usual magnetic-dipole interaction; thus is called the presudo-dipole interaction. If we assume that $J(n_1 g_2, n_1 g_2)$ is of the same order as the exchange integral in the ground state, the order of the interaction is estimated

as [45]:

$$\mathcal{H}_{aniso} \sim \frac{\lambda^2 J}{(\Delta E)^2} \sim (\Delta g)^2 J. \tag{1.57}$$

Here Δg is the shift of the electron g-factor from 2 (~ 0.2) and ΔE is the energy splitting. This can be also linked to Kramers doublet that we've discussed already in Chap. 1.2.9.

So far, we considered mainly diagonal terms with respect to the orbital states and were ignoring off diagonal terms mostly. If we do consider all terms, then different processes from those described above can happen - for example - there is process where both ions are excited simultaneously by the exchange interaction $J(g_1 g2, n_1 n_2)$ and then L-S coupling returns each ion to its ground state. Obviously, the diagonal terms are the dominant ones.

Taking into account the off diagonal terms of the exchange interaction with respect to the orbital state, we obtain, as second-order term in the perturbation:

$$\begin{aligned}\mathcal{H}_{DM} = &-\lambda\Big(\sum_{n_1} \frac{\langle g_1|\mathbf{L}_1\mathbf{S}_1|n_1\rangle\langle n_1 g_2|V_{exch}|g_1 g_2\rangle}{E_{n_1}E_{g_1}} \\ &+ \sum_{n_1} \frac{\langle g_1 g_2|V_{exch}|n_1 g_2\rangle\langle n_1|\mathbf{L}_1\cdot\mathbf{S}_1|g_1\rangle}{E_{n_1}E_{g_1}} \\ &+ \text{term with 1 and 2 exchanged}\Big).\end{aligned} \tag{1.58}$$

We've used the exchange interactions and L-S coupling in expression above. this can be rewritten as:

$$\begin{aligned}\mathcal{H}_{DM} =&2\lambda\sum_{\mu}\Big(\sum_{n_1} \frac{J(n_1 g_2, g_1 g_2)\langle g_1|L_{1\mu}|n_1\rangle[S_{1\mu}(\mathbf{S}_1\cdot\mathbf{S}_2)]}{E_{n_1}E_{g_1}} \\ &+ \sum_{n_2} \frac{J(g_1 n_2, g_1 g_2)\langle g_2|L_{2\mu}|n_2\rangle[S_{2\mu}(\mathbf{S}_1\cdot\mathbf{S}_2)]}{E_{n_2}E_{g_2}}\Big),\end{aligned} \tag{1.59}$$

where μ represents axis x, y and z. Using the relation:

$$[\mathbf{S}_1, (\mathbf{S}_1\cdot\mathbf{S}_2)] = -i\mathbf{S}_1\times\mathbf{S}_2, \tag{1.60}$$

we can write antisymmetric interaction between spins, where antisymmetric part comes from the cross product:

$$\mathcal{H}_{DM} = \mathbf{D} \cdot \mathbf{S}_1 \times \mathbf{S}_2. \tag{1.61}$$

This type of antisymmetric interaction was pointed out by Dzyaloshinsky first - based on symmetry analysis of the crystal structure. The microscopic derivation of the interaction has been done by Moriya - that's why it is called antisymmetric exchange interaction of Dzyaloshinsky-Moriya (DM).

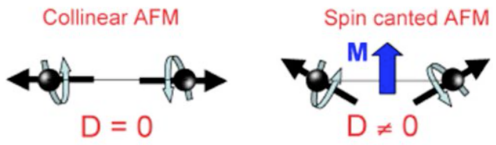

Figure 1.21 *The presence of the DM interactions ($\boldsymbol{D} \neq 0$) leads to a slight canting of the magnetic moments and resulting net magnetization $\boldsymbol{M} \neq 0$ in an otherwise collinear antiferromagnet.*

Let us do a small discussion about vector $\mathbf{D}$. It is strongly connected with presence or absence of inversion symmetry in respect to the center between the two magnetic ions. It has form:

$$\begin{aligned}\mathbf{D} = &-2i\lambda\Big[\sum_{n_1}\frac{\langle g_1|L_{1\mu}|n_1\rangle}{E_{n_1}E_{g_1}}J(n_1g_2, g_1g_2)\\ &-\sum_{n_2}\frac{\langle g_2|L_{2\mu}|n_2\rangle}{E_{n_2}E_{g_2}}J(g_1n_2, g_1g_2)\Big].\end{aligned} \tag{1.62}$$

The vector $\mathbf{D}$ clearly vanishes if surrounding crystal field has inversion symmetry with respect to the centre between the two magnetic ions.

1.2.11 Brief overview of other types of exchange interactions

Apart from all that we mentioned before, there are also other types of interactions that can be present in compounds. Let us discuss those briefly.

In the case of direct exchange, one assumes the interaction between nearest neighbour ions. However, in 1949, Shull and Smart have observed (using neutron diffraction) that the MnO compound ordered antiferromagnetically. This type of

magnetic order has been proposed by Néel just one year earlier. Moreover, Mn^{2+} ions were not next nearest neighbours, but there was a nonmagnetic oxygen atom O^{2-} between them.

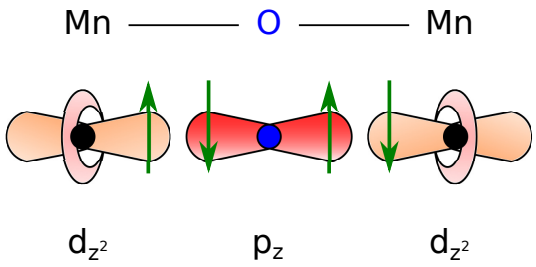

Figure 1.22 *Superexchange interactions in MnO crystal - two magnetic Mn ions interact with each other via nonmagnetic O atom between them.*

Scientists correctly deduced that there must be another type of exchange present. Usually, the exchange interactions are short-ranged. It is pretty clear that in this case, the interaction must be long-ranged and in some sense *super* - that's why we use term *superexchange interactions*, see Fig. 1.22. It was proposed by Henrik Kramers first, then refined by Phillip Anderson. Anderson pointed out that there are two terms that needs to be considered. The first is the repulsive Coulumb interaction preventing hopping of electron from one metal ion to unoccupied site of another metallic atom - it would increase the energy as is often denoted as U. The second term, denoted as t may be considered as a kinetic hopping term. In Anderson's approach, the first order term in the perturbation theory results in the usual Heisenberg ferromagnetic Hamiltonian, whereas the second order term gives an antiferromagnetic exchange:

$$\mathcal{H}_{1,2} = 4\frac{t^2}{U}\mathbf{S}_1 \cdot \mathbf{S}_2 \equiv 2J_{12}\mathbf{S}_1 \cdot \mathbf{S}_2. \tag{1.63}$$

At the same period as Anderson, John B. Goodenough and Junjiro Kanamori developed empirically also a set of rules for determining the sign and relative strength of the superexchange interactions. These rules include the effects of orbital symmetry, orbital overlaps and orbital filling. For example - if we have two half-filled $3d$ orbitals of magnetic ions interacting via an overlapping O^{2-} ligand and the angle of M-O-M is 180°, they will exhibit strong antiferromagnetic superexchange. In the contrast, similar situation, just with 90° angle between M-O-M predicts weaker ferromagnetic superexchange. In short - one needs to consider electron configuration and bonding geometry too.

Another type of exchange is called *double exchange* - it differs from superexchange

interactions in following way - electrons are itinerant (delocalized), see Fig. 1.23. Therefore, electrons are highly mobile and these itinerant electrons hop from one metal centre to another metal centre. This results in displaying of magnetic exchange coupling as well as metallic conductivity. This type of exchange has been discovered by Clarence Zener in 1950's.

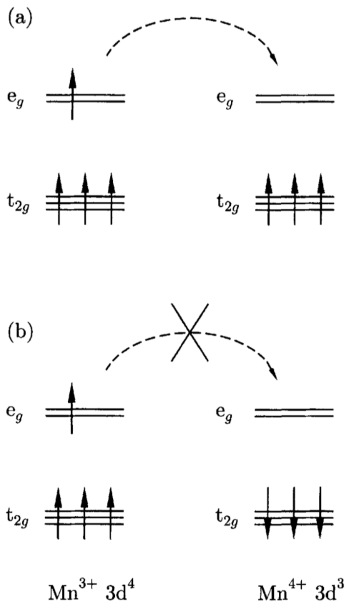

Figure 1.23 *Double exchange mechanism gives ferromagnetic coupling between Mn^{3+} and Mn^{4+} ions in $La_{1-x}Sr_xMnO_3$ compound ($0 \leq x \leq 1$). The exchange interaction favours hopping if neighbouring ions are ferromagnetically aligned (a) and not antiferromagnetically aligned (b) [6].*

It usually appears in compound with mixed valency of magnetic ions, for example $La_{1-x}Sr_xMnO_3$ compound ($0 \leq x \leq 1$) that has a perovskite structure. Mn ion can exist in oxidation state 3 or 4, so as Mn^{3+} or Mn^{4+}. Whereas, the limits give an antiferromagnetic insulator, if $x = 0$ or $x = 1$ (therefore the system is ruled by superexchange), if we dope the system with Sr atoms, it becomes ferromagnetic and shows metallic properties too. This ferromagnetic alignment is due to double exchange, see Fig. 1.23.

The last type of interaction, we would discuss here is *RKKY interaction* - indirect exchange in metals. This interaction is mediated by conduction electrons - a localized magnetic moment spin-polarizes the conduction electrons and this polarization in turn couples to a neighbouring localized magnetic moment a distance r away [6]. The name RKKY is formed from initial letters of surnames of the discoverers - Ruderman, Kittel, Kasuya and Yosida. The coupling takes

the form of an r-dependent exchange interaction J_{RKKY} given by:

$$J_{RKKY}(r) \propto \frac{\cos(2k_F r)}{r^3}, \tag{1.64}$$

where k_F is radius of spherical Fermi surface [6].

Chapter 2

Experimental

This chapter will discuss experimental techniques that we used for our study. The main part is dedicated to neutrons, then two shorter chapters talk about x-ray diffraction that has been very important for all powder and crystal synthesis that have been done. The last part explains principles of SQUID device (Superconducting QUantum Interference Device).

2.1 Neutrons

In 1919 Rutherford had discovered the proton and the picture of an atom changed to that of a nucleus with positively charged protons and circling electrons. However, even Rutherford had noticed that the atomic number of elements was smaller than the atomic mass of the element. For example, a helium atom has an atomic mass of 4, but an atomic number (or positive charge) of 2. The mass of electrons is negligible in comparison with mass of the proton. There were several theories at that time, Rutherford himself proposed an idea that there is another particle present in nucleus that has no charge, but has a mass. The confirmation came from his student James Chadwick in 1932 using different method for tracking particles (most of them were based on tracking the charged particles at that time). He has succeeded in finding the neutral particle with the same mass as a proton, but with zero charge. This particle has been named neutron. Scientists very quickly realise that the neutron had several remarkable properties. The first neutron experiments were carried out in 1945 by E. O.

Wollan that was shortly joined by C. Shull. They were using a Graphite Reactor at Oak Ridge (US) and established the basics of this new technique.

Let's mention some properties of neutrons now. The neutron is a nuclear particle with a mass m_n:

$$m_n = 1.675 \cdot 10^{-27}\text{kg}, \tag{2.1}$$

which is very close to the value of mass ot the proton. Neutron doesn't stay in the free form, but decays into a proton, an electron, and an anti-neutrino. The neutron lifetime τ is 886 s, which is time longer than the time a neutron spends within a scattering experiment and therefore the decay can typically be neglected in experiments.

The neutron doesn't have an electric charge, but does have magnetic moment, which is so important for neutron scattering experiments. The magnetic moment:

$$\mu = \gamma\mu_N, \tag{2.2}$$

where γ is the neutron magnetogyric ratio and the nuclear magneton μ_N is given by:

$$\mu_N = \frac{e\hbar}{2m_p} = 5.051 \cdot 10^{-27}\text{J/T}. \tag{2.3}$$

The neutron magnetic moment is coupled antiparallel to its spin, which has the value $s = 1/2$. The neutron interacts with nuclei via the strong nuclear force and with magnetic moments of electrons via electromagnetic force.

From a quantum mechanic point of view, it's important to keep in mind that particle-wave duality applies for neutrons too - we think about neutrons as particles when they're created, then as interfering waves in the scattering process and then again as particles in the detection process. Therefore, particle moving with constant velocity v can be described by a corresponding de-Broglie wavelength, given by:

$$\lambda = \frac{2\pi\hbar}{mv}, \tag{2.4}$$

where the neutron wave number k is:

$$k = \frac{2\pi}{\lambda}. \tag{2.5}$$

This can be also written as wave vector $\mathbf{k}$:

$$\mathbf{k} = \frac{m_n \mathbf{v}}{\hbar}, \tag{2.6}$$

$\mathbf{k}$ has the same direction as velocity $\mathbf{v}$. The wavelength is standardly expressed in units of Å (10^{-10} m) and wave number in Å^{-1}. Very useful is also conversion into the energy scale, considering neutron to be non-relativistic. Its kinetic energy is given by:

$$E = \frac{\hbar^2 k^2}{2m_n}. \tag{2.7}$$

This energy E is measured in eV or meV, where:

$$1\text{eV} = 1.602 \cdot 10^{-19}\text{J}. \tag{2.8}$$

Using Eq. (2.4), we can show one big advantage of neutrons in comparison with x-rays - neutrons in equilibrium at temperatures of 0°C and 100°C have wavelengths 1.55 Å and 1.33 Å respectively. This corresponds to inter-atomic distances in solids and therefore neutrons can be used for study of the structure. In terms of energy, it's around 20 meV, similar to elementary excitations in solids. One can thus obtain simultaneous information on the structure and dynamics of materials (measure dispersion relations of excitations in solids).

Another important property of neutrons is that their cross section doesn't depend on atomic number, which is the case of x-rays. The cross section of neutrons varies in a seemingly random fashion between elements and even between different isotopes of the same element. This gives neutrons an advantage for study of light isotopes or hydrogen that is almost invisible for x-rays. For example, there is a big difference in scattering of isotope ^1H and ^2D - these two can be used in biological samples and highlight the importance of selected groups within big molecule.

Neutrons can penetrate the sample deeper than x-rays (where one works with

charged particles), so they don't probe just surface but bulk of the material. The quantitative comparison of neutron scattering data and theoretical models is much better.

The strenght of penetration of neutrons is useful for experiments using different sample environment - cryostats, magnets, pressure cells etc.

Last point is the study of magnetism - magnetic moments of neutrons interact with magnetic moments in sample. Whereas unpolarized neutrons can give us information about periodicity and magnitude of the magnetic order, spin-polarized neutrons can reveal the direction of the atomic magnetic moments.

After this list of advantages, we shouldn't forget to mention a warning too. Although neutron scattering is a great technique, it is time consuming, very expensive and there are few large international facilities providing neutrons. Therefore, neutron experiment should be provided only when there is no other probe available.

2.1.1 Neutron Production

There are two methods to produce neutrons - with nuclear reactors or high energy particle accelerators.

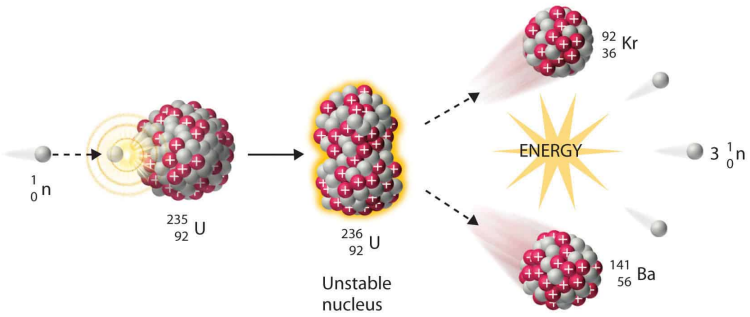

Figure 2.1 *Fission process of producing neutrons in nuclear reactors [7]*

In case of nuclear reactors, neutrons are produced as one of the products of nuclear fission of ^{235}U. This nuclear fission produces 2 or 3 neutrons, two daughter nuclei and releases energy (in order of 200 MeV), see Fig. 2.1. Research reactors use compact cores, which differentiate from power plans that have much larger core. Traditionally, nuclear reactors provide continuous stream of neutrons. However, there is one exception - the source in Dubna (Russia) - where 2 large wheels give short bursts of neutrons.

The continuous stream of neutrons in nuclear reactors must be reduced to a monochromatic beam - this is usually done by single crystal of highly reflective material - such as pyrolitic graphite, germanium or copper - called a monochromator. How does it actually work? The incoming neutrons have a wide band of different wavelengths. A crystal is chosen characteristic spacing of reflective planes of atoms, d, and scattering angle 2θ, will satisfy the Bragg law for some wavelengths and only these are transmitted in the direction of experiment. Obviously, changing the scattering angle, we can change wavelength of transmitted neutrons.

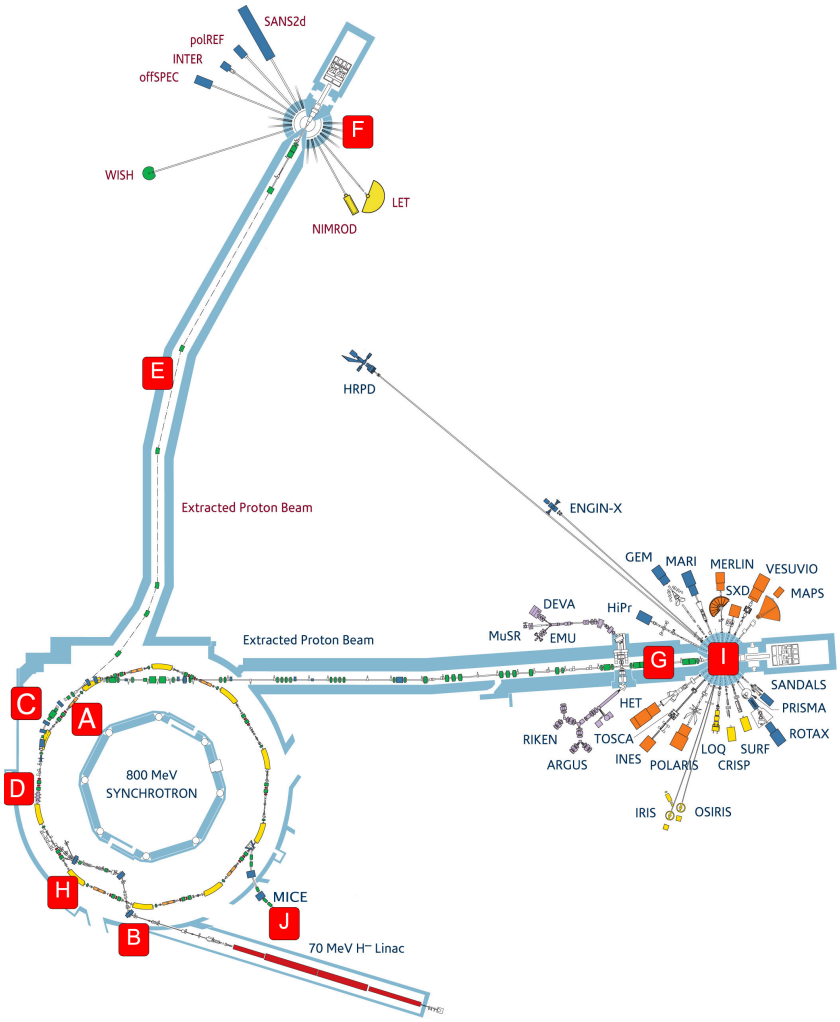

Figure 2.2 *ISIS neutron and muon facility belongs to pulsed sources. Current layout with the synchrotron ring [8].*

High energy particle accelerators use a different principle. We can divide accelerators into three groups - linacs, cyclotrons and synchrotrons. As name suggests, linacs accelerate particles in a straight line - example - the linear accelerator at Stanford (SLAC). Linacs can accelerate heavy ions to speeds

that can not be achieved with ring-type accelerators. Unlike linacs, cyclotrons accelerate particles along an outward spiral path and are held in that path by a static electromagnetic field perpendicular to the spiral path [46]. Cyclotron beam is used for medical purposes all over the world (beam can penetrate patience's body to kill tumor with minimal harm to the person), the largest is located at UC Berkeley. Synchrotrons, like cyclotrons, are cyclic accelerators. That means synchrotrons send particles into a closed-loop path, increasing their speed with each revolution. The main difference between these two is that synchrotron's loop is not a spiral. Due to versatile purposes of use, synchrotron's loop can be a circle, oval or even a polygon with rounded corners. One drawback of synchrotrons is they cannot accelerate protons for other particles from standstill, they must already be moving - a task handled by another accelerator [46].

For purposes of this thesis, synchrotrons will be discussed more as they are part of spallation neutron sources. Particles (usually protons, but it is possible to use electrons too, however they are less effective) are accelerated in synchrotron ring and then they hit a heavy target witch neutron rich nuclei (see Fig. 2.2), usually made of tungsten or tantalum (solid targets, for liquid metal target a lead or mercury can be used). Energies of the protons fluctuate around 1-3 GeV. After collision, approximately 10-20 neutrons are released per proton. Spallation sources are typically pulsed, but again, there is departure from the rule - SINQ at Paul Scherrer Institute PSI (Switzerland), which has status of pseudo-continuous neutron source [28].

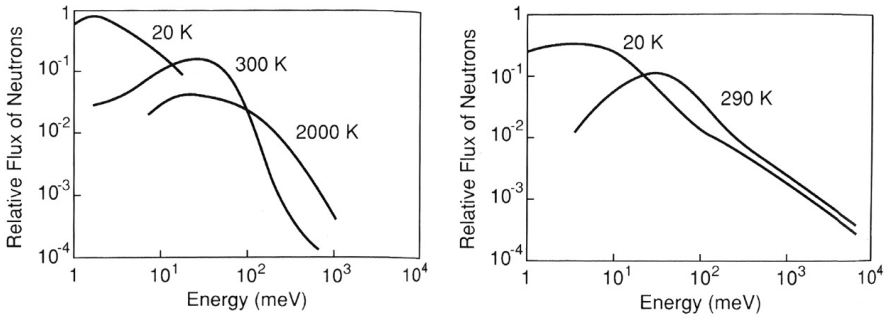

Figure 2.3 *The relative flux of neutrons as a function of energy for the high-flux reactor (ILL, France), on the left. The curves show the distribution of neutrons emerging from moderators at temperatures of 20, 300 and 2000 K. On the right is similar distribution of curves for neutrons generated at LANSCE (Los Alamos, USA) by moderators at temperature of 20 and 290 K [9].*

One advantage of spallation sources is that they produce small amound of energy ($\sim$ 27 MeV) per neutron, which is 4 or 5 times less than energy released in nuclear

reactors. On the other hand - electricity costs for accelerating particles are not small. There is also difference in the energy spectrum of moderated neutrons produced in spallation and nuclear sources. First one has bigger percentage of higher energy neutrons as it is possible to see in Fig. 2.3.

Moderators

Produced neutrons have energies up to tens or even hundreds of MeV and the corresponding wavelengths are not suitable for investigation of condensed matter problems. Therefore we need something that will slow down neutrons or in other words - longer wavelengths.

There are several types of moderators. The most common moderator is water that produces so called *thermal* neutrons. A tank with a moderator has volume from a deciliter to ten tens of liters and it is placed close to the neutron source. Neutrons collide with the atoms of moderator and lose energy until they reach thermal equilibrium with the tank of water (temperature 300 K). Knowing relations, we can quickly calculate that T = 300 K corresponds to energy 25 meV and wavelength of 1.8 Å. Certain temperature gives us certain energy. What to do if we would like to use lower energies? We know that:

$$E = k_B T, \tag{2.9}$$

where k_B is Boltzman constant. We can easily see that we need to decrease the temperature. Hence, the moderators used for lower energies are hydrogen H_2 (30 K) or solid methane CH_4 (100 K). Neutrons moderated in this way use term *cold* neutrons and if they go through hydrogen moderator, their energy is around 2.5 meV with corresponding wavelength 5.7 Å. At ILL, there is even a hot moderator consisting of graphite at 2000 K.

Neutrons moderated at temperature T will have a distribution of velocities v given by the Maxwellian distribution of velocities. We can look at neutron emission from moderator source as a effusion process, where the intensity behaves as:

$$I(v) = I_0 v^3 \exp\Big(- \frac{m_n v^2}{2 k_B T} \Big), \tag{2.10}$$

where I_0 is a constant proportional to the source power. Faster particles have

higher probability of leaving the moderator quicker. The velocity distribution reaches maximum at $v_{max} = \sqrt{3k_BT/m_n}$.

Denotation	Wavelength (Å)	Energy	Moderator
hot	0.3-0.6	1 eV-200 meV	graphite at 2000 K
thermal	0.6-2.4	200 meV-14 meV	H_2O at 300 K
cold	2.4-40	14 meV-0.05 meV	H_2 at 30 K

Table 2.1 *Traditional classification of neutrons within certain energy ranges [28].*

2.1.2 Elastic and Inelastic Neutron Scattering

With neutrons, it's possible to study the structure of materials (diffraction experiments) or dynamics - study of excitations (spectroscopic experiments). Diffraction experiments measure neutrons that have been scatterred elastically from a sample, ie. energy has not been exchanged between the neutron and the sample. Spectroscopic measurements are inelastic scattering experiments, where there is a change in energy after neutron scatters from the sample. This can be related to the atomic dynamics of the sample. Therefore, instruments at large facilities can be grouped into two main categories - diffractometers and spectrometers.

In any scattering experiment one always measures the properties of the incident (i) and final (f) neutron beams and infers the momentum and energy transferred to the sample. All diffraction and scattering experiments are governed by the laws of momentum and energy conservation:

$$\mathbf{Q} = \mathbf{k_f} - \mathbf{k_i}, \tag{2.11}$$

$$\hbar\omega = E_i - E_f. \tag{2.12}$$

The principal aim of neutron scattering experiments is the determination of probability that neutron with wave vector $\mathbf{k}_i$ is scattered into the state with wave vector $\mathbf{k}_f$. The intensity of scattered neutrons is thus measured as a function of the momentum transfer [47].

Therefore there are two basic types of the neutron scattering - elastic and inelastic. For elastic scattering in a crystalline solid is valid such that $|\mathbf{k}_i| = |\mathbf{k}_f| = k$. To understand diffraction and scattering measurements, it is necessary to deal with the reciprocal lattice of the solid. The dots in Fig. 2.4 represent a reciprocal lattice for a two-dimensional crystalline solid, with each point corresponding to a reciprocal-lattice vector. If we plot a circle with radius k on this diagram such that it passes through two points on the circle, one of which is the origin of reciprocal space, the condition for Bragg scattering from the crystal is satisfied. The circle is called the Ewald circle in two dimensions, or the Ewald sphere in three dimensions. In the diagram, $\mathbf{k}_i$ is the direction of the incident beam relative to the crystal and $\mathbf{k}_f$ is the direction of the diffracted beam. For the case satisfying the Bragg condition:

$$\mathbf{Q} = \mathbf{G} = \mathbf{k_f} - \mathbf{k_i}, \tag{2.13}$$

where $\mathbf{G}$ is a reciprocal-lattice vector.

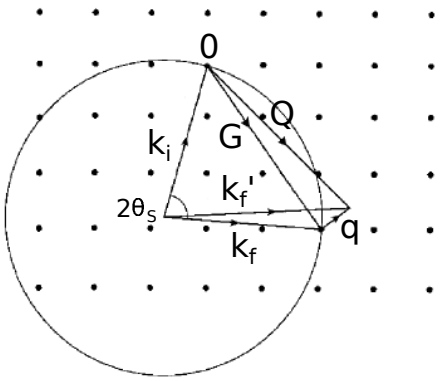

Figure 2.4 *Two-dimensional representation of reciprocal space showing the Ewald circle and the vector representation for elastic and inelastic scattering. Here* $\boldsymbol{G}$ *is a reciprocal-lattice vector and* $\boldsymbol{q}$ *the momentum transfer within the first Brillouin zone [10]*

Using equation

$$|\mathbf{Q}| = k_i^2 + k_f^2 - 2k_i k_f \cos\theta_S,$$

and Fig. 2.4 we can see that

$$|\mathbf{Q}| = |\mathbf{G}| = 2|\mathbf{k_i}| \sin\theta_S, \tag{2.14}$$

where $2\theta_S$ is the angle between the incident and the final beam for the Bragg condition. This is the well-known Braggs law, which can also be written in the more familiar form

$$\lambda = 2d \sin \theta_S, \tag{2.15}$$

by noting that the magnitude of the reciprocal-lattice vector $|\mathbf{G}| = 2\pi/d$ where d is an inter-planar spacing.

In a diffraction experiment, the magnitude of $\mathbf{Q}$ is controlled by adjusting the angle $2\theta_S$ between $\mathbf{k}_i$ and $\mathbf{k}_f$. The orientation of $\mathbf{Q}$ within the reciprocal lattice is set by rotating the sample. Thus, any point in reciprocal space can be measured by an appropriate choice of $\mathbf{k}_i$, $2\theta_S$, and the orientation ϕ of the sample relative to $\mathbf{k}_i$.

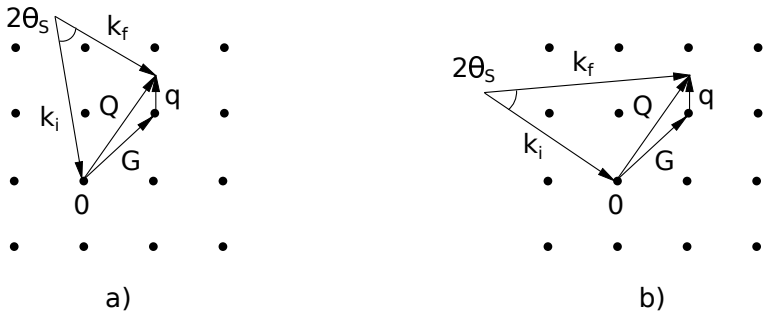

Figure 2.5 *Vector diagrams of inelastic scattering for a) neutron energy loss ($k_f < k_i$), b) neutron energy gain ($k_f > k_i$). 0 represents the origin of reciprocal space, **G** a reciprocal-lattice vector, and **q** the momentum transfer within a zone [10]*

For inelastic neutron scattering, the situation is more complicated. In this case $|\mathbf{k}_i| \neq |\mathbf{k}_f|$ since a difference is needed in order to transfer energy to the sample. In an experiment, one typically holds one wave vector (k_i or k_f) constant while varying the other. For a single-crystal sample, energies depend only on the relative momentum $\hbar\mathbf{q}$ defined within a Brillouin zone; hence, it is convenient to reference the momentum transfer to the nearest reciprocal lattice vector, i.e.,

$$\mathbf{Q} = \mathbf{G} + \mathbf{q}, \tag{2.16}$$

as illustrated in Fig. 2.5. The measured spectrum can be interpreted straightforwardly if $\mathbf{Q}$ is held constant while the energy transfer is varied. Figure 2.5 shows two cases where k_i is kept constant and k_f varies. In the first situation, Fig.

2.5 a) with $k_i > k_f$ and $\hbar\omega > 0$, energy is transferred from the incident neutron to the sample and an excitation is created; this is equivalent to Stokes scattering in optical spectroscopy. In the second example, Fig. 2.5 b) with $k_i < k_f$ and $\hbar\omega < 0$, so that the sample gives up a quantum of energy to the neutron beam. An excitation is annihilated and we have neutron energy gain (or anti-Stokes scattering).

In order to keep $\mathbf{Q}$, and thus $\mathbf{q}$, constant while varying k_f, the scattering angle must change as well as the relative orientation of the crystal with respect to k_i. The schematic in Fig. 2.5 shows the lattice staying fixed and $\mathbf{k}_i$ moving. In practice, it is the other way around: $\mathbf{k}_i$ is kept fixed in space while the crystal is rotated.

2.1.3 Neutron Cross Section

As we pointed out previously, the absence of charge in the case of neutrons allow them to penetrate deeper into the sample. Neutrons don't interact just with unpaired electrons but also the nucleus. In the next paragraphs, we will discuss the neutron cross section for scattering from nucleus.

In a scattering experiment, a beam of neutrons (with wave vector $\mathbf{k}_i$ and flux $\phi(k_i)$) is shot at the sample. Neutrons can be represented by a plane wave that is given by:

$$\Psi_i = e^{ikz}, \tag{2.17}$$

where k is the wave number $k = 2\pi/\lambda$. When they reach the sample, neutrons scatter and this new wave would have spherical symmetry described by:

$$\Psi_f = -\frac{b}{r}e^{ikr}, \tag{2.18}$$

where r is the distance of the point of measurement from the origin where the nucleus is considered to be rigidly fixed. the quantity b is so called scattering length and it's a complex quantity $b = \alpha + i\beta$. However, the imaginary part of scattering length b becomes important only for few elements with high absorption coefficient - like cadmium or boron. Coming back to the scattering process, the

resultant neutron wave will be given by:

$$\begin{aligned} \Psi &= \Psi_i + \Psi_f, \\ \Psi &= e^{ikz} - \frac{b}{r} e^{ikr}. \end{aligned} \tag{2.19}$$

Important information for an experimentalist is what is the rate of this scattering and it has a notation σ - the scattering cross section. Suppose we set up a neutron counter and measure neutrons scattered into the solid angle $d\Omega$ in certain direction, which we will specify with polar coordinates θ, ϕ. For simplicity, let's not analyse the energy of scattered neutrons. The cross section of this type of measurement is called *differential cross-section*:

$$\frac{d\sigma}{d\Omega} = \frac{\text{number of neutrons scattered per second into } d\Omega}{\Phi d\Omega}, \tag{2.20}$$

where Φ is the flux of incident neutrons. Then the *total scattering cross-section* is defined by equation:

$$\sigma_{\text{tot}} = \frac{\text{outgoing scattered neutrons}}{\text{incident neutron flux}} = \frac{\text{outgoing scattered neutrons}}{\Phi}. \tag{2.21}$$

Where by total number one means the number of neutrons scattered in all directions.

If we do consider also energy of scattered neutrons then we are interested in the rate at which neutrons are scattered into a given solid angle $d\Omega_f$, in the direction of the wave vector $\mathbf{k}_f$, with final energy between E_f and $E_f + dE_f$. This rate is the double-differential cross section, sometimes called also *partial differential cross section* [29]:

$$\frac{d^2\sigma}{d\Omega dE_f} = \frac{\text{neutrons scattered per second into } d\Omega \text{ with certain } E}{\Phi d\Omega dE_f}. \tag{2.22}$$

Let's have a closer look on units. On right hand side, we have number of neutrons per seconds [time^{-1}] divided by the flux which is [area^{-1} time^{-1}], thus the dimensions of the cross section are [area], which one would expect.

We can combine above equations for cross section to formulate [29]:

$$\frac{d\sigma}{d\Omega} = \int_0^\infty \left(\frac{d^2\sigma}{d\Omega dE_f} \right) dE_f, \tag{2.23}$$

$$\sigma_{\text{tot}} = \int_{\text{all directions}} \left(\frac{d\sigma}{d\Omega} \right) d\Omega. \tag{2.24}$$

If the scattering is axially symmetric, so it depends only on θ and not on ϕ, the last formula has a form:

$$\sigma_{\text{tot}} = \int_0^\pi \frac{d\sigma}{d\Omega} 2\pi \sin\theta d\theta. \tag{2.25}$$

Coming back to the differential cross section , it's important to mention that the cross section consists of coherent and incoherent parts:

$$\frac{d\sigma}{d\Omega_f} = \left. \frac{d\sigma}{d\Omega_f} \right|_{\text{coh}} + \left. \frac{d\sigma}{d\Omega_f} \right|_{\text{inc}}. \tag{2.26}$$

This is due to the fact that a monoatomic sample might contain nuclei with varying scattering lengths b. Most elements have a significant coherent cross section, but there are a few examples, such as hydrogen and vanadium for which the incoherent scattering is large and dominant (see Tab. 2.2).

Isotopes of the same element have different scattering lengths. Moreover, for an isotope with a nuclear spin, the scattering length varies depending on whetever the neutron and nuclear spins are parallel or antiparallel. Therefore, the scattering length b varies due to the presence of isotopes, nuclear spin or both. Suppose that there is distinct isotope or nuclear spin with scattering length b_i and occurs with frequency f_i. Where it's true that:

$$\sum_i f_i = 1. \tag{2.27}$$

If there are no correlations between the values of scattering length b of any two

nuclei, then the average value of b for the system is:

$$\overline{b} = \sum_i f_i b_i, \tag{2.28}$$

and the average value for b^2:

$$\overline{b^2} = \sum_i f_i b_i^2. \tag{2.29}$$

If there are no correlation between scattering lengths b between different nuclei, we can write down:

$$\overline{b_j b_{j'}} = \begin{cases} (\overline{b})^2 & \text{for} \quad j \neq j', \\ \overline{b^2} & \text{for} \quad j = j'. \end{cases} \tag{2.30}$$

The simplest case - when the scattering consists just of a coherent part - is when scattering system has a single isotope with zero nuclear spin. Then all scattering lengths b are equal:

$$\sigma_{\text{coh}} = 4\pi(\overline{b})^2. \tag{2.31}$$

Total scattering would contain not just the coherent part with same scattering length, but all deviations from it:

$$\sigma_{\text{tot}} = 4\pi \sum_i f_i b_i^2 = 4\pi\overline{b^2}. \tag{2.32}$$

Knowing these two relations, we can easily express the incoherent part of scattering σ_{incoh}:

$$\begin{aligned} &\sigma_{\text{incoh}} = \sigma_{\text{tot}} - \sigma_{\text{coh}}, \\ &\sigma_{\text{incoh}} = 4\pi\overline{b^2} - 4\pi(\overline{b})^2 = 4\pi\Big(\overline{b^2} - (\overline{b})^2\Big). \end{aligned} \tag{2.33}$$

Physically, the incoherent scattering arises from the random distribution of deviations of the scattering lengths from their mean value [29].

	Z	σ_{coh}	σ_{incoh}
^{1}H	1	1.8	80.2
^{2}H	1	5.6	2.0
C	6	5.6	0.0
O	8	4.2	0.0
Al	13	1.5	0.0
V	23	0.02	5.0
Fe	26	11.5	0.4
Co	27	1.0	5.2

Table 2.2 *Values of σ_{coh} and σ_{incoh} in $10^{-28}m^2$ units for different elements [29].*

It is convenient to express the differential cross section as a sum of coherent and incoherent parts:

$$\frac{d^2\sigma}{d\Omega_f dE_f} = \left.\frac{d\sigma}{d\Omega_f}\right|_{\text{coh}} + \left.\frac{d\sigma}{d\Omega_f}\right|_{\text{inc}} + \left.\frac{d^2\sigma}{d\Omega_f dE_f}\right|_{\text{coh}} + \left.\frac{d^2\sigma}{d\Omega_f dE_f}\right|_{\text{incoh}}. \tag{2.34}$$

In general terms, the coherent part provides information about the cooperative effects among different atoms, such as elastic Bragg scattering or inelastic scattering by phonons or magnons, whereas the incoherent part is proportional to the time correlation of an atom with itself and provides information about individual particle motion, such as diffusion [10].

2.1.4 Nuclear Scattering

Before we start to talk about nuclear scattering, let's do a quick revision about unit cell and reciprocal lattice. Primitive vectors of three dimensional lattice can be defined as $\mathbf{a}_1$, $\mathbf{a}_2$ and $\mathbf{a}_3$. Then volume of unit cell v_0 is defined as:

$$v_0 = \mathbf{a}_1 \cdot (\mathbf{a}_2 \times \mathbf{a}_3). \tag{2.35}$$

In scattering experiments, one deals with reciprocal lattice, which can be defined via three reciprocal primitive vectors $\mathbf{b}_1$, $\mathbf{b}_2$ and $\mathbf{b}_3$:

$$\mathbf{G} = n_1\mathbf{b}_1 + n_2\mathbf{b}_2 + n_3\mathbf{b}_3, \tag{2.36}$$

where n_1, n_2 and n_3 are integers. Reciprocal lattice vectors can be expressed also as:

$$\begin{aligned}
\mathbf{b}_1 &= 2\pi \frac{\mathbf{a}_2 \times \mathbf{a}_3}{\mathbf{a}_1 \cdot (\mathbf{a}_2 \times \mathbf{a}_3)} = \frac{2\pi}{v_0} \mathbf{a}_2 \times \mathbf{a}_3, \\
\mathbf{b}_2 &= 2\pi \frac{\mathbf{a}_3 \times \mathbf{a}_1}{\mathbf{a}_2 \cdot (\mathbf{a}_3 \times \mathbf{a}_1)} = \frac{2\pi}{v_0} \mathbf{a}_3 \times \mathbf{a}_1, \\
\mathbf{b}_3 &= 2\pi \frac{\mathbf{a}_1 \times \mathbf{a}_2}{\mathbf{a}_3 \cdot (\mathbf{a}_1 \times \mathbf{a}_2)} = \frac{2\pi}{v_0} \mathbf{a}_1 \times \mathbf{a}_2.
\end{aligned} \tag{2.37}$$

The volume of the unit cell in the reciprocal lattice v_r is:

$$v_r = \mathbf{b}_1 \cdot (\mathbf{b}_2 \times \mathbf{b}_3) = \frac{(2\pi)^3}{v_0}. \tag{2.38}$$

From above equations, we can also see that:

$$\mathbf{a}_i \cdot \mathbf{b}_j = 2\pi\delta_{ij} \quad \delta_{ij} = \begin{cases} 0 & \text{if} \quad i \neq j, \\ 1 & \text{if} \quad i = j. \end{cases} \tag{2.39}$$

In the elastic scattering experiment $\mathbf{Q} = \mathbf{G} = \mathbf{k}_f - \mathbf{k}_i$ as it has been mentioned previously. The situation is different for the inelastic experiment when $\mathbf{Q} = \mathbf{G}+\mathbf{q}$, where $\mathbf{q}$ is the wave vector.

In general, there are different type of nuclei at each atomic position in a crystal, therefore the mean value of scattering length b (see Eq. 2.31), then the coherent cross section for all processes - elastic and inelastic - is:

$$\frac{d^2\sigma}{d\Omega_f dE_f} = N \frac{k_f}{k_i} (\bar{b})^2 S(\mathbf{Q}, \omega), \tag{2.40}$$

or written in a form with σ_{coh}:

$$\frac{d^2\sigma}{d\Omega_f dE_f} = N \frac{k_f}{k_i} \frac{\sigma_{\text{coh}}}{4\pi} S(\mathbf{Q}, \omega), \tag{2.41}$$

where $S(\mathbf{Q}, \omega)$ is the scattering function. This formula applies when the sample

consists of a single element. More generally, one must include the side-dependent scattering lengths in the scattering function $S(\mathbf{Q}, \omega)$. An elegant how to write the scattering function was given by Van Hove (1954) using the definition of the atomic density operator [10]:

$$\rho_{\mathbf{Q}}(t) = \sum_{l} e^{i\mathbf{Q}\cdot\mathbf{r}_l(t)}. \tag{2.42}$$

Then one can write:

$$S(\mathbf{Q}, \omega) = \frac{1}{2\pi\hbar N} \int_{-\infty}^{\infty} dt e^{-i\omega t} \langle \rho_{\mathbf{Q}}(0) \rho_{-\mathbf{Q}}(t) \rangle. \tag{2.43}$$

Elastic Nuclear Scattering

If we consider the elastic scattering only, it is obvious that there is no energy change $\hbar\omega$ and $|\mathbf{k}_f| = |\mathbf{k}_i|$. Together with some algebraic operations that are described in the Appendix J, the formula for coherent elastic scattering cross section is:

$$\left.\frac{d\sigma}{d\Omega_f}\right|_{\text{coh}}^{\text{el}} = N\frac{(2\pi)^3}{v_0}(\bar{b})^2 \sum_{\mathbf{G}} \delta(\mathbf{Q} - \mathbf{G}). \tag{2.44}$$

Until this point, we were working with assumption that our lattice is rigid. However, atoms do fluctuate from their equilibrium positions in real systems. The consequence of this can be reduced intensities at some Bragg reflections (however, the intensity of Bragg peaks can be influenced also by the structure factor). Let $\mathbf{u}$ be the instantaneous displacement of an atom from its equilibrium position $\mathbf{r}$. This new situation will result in an extra term in the equation 2.43, which is also known as Debye-Waller factor W. For small displacements:

$$W = \frac{1}{2}\langle (\mathbf{Q} \cdot \mathbf{u})^2 \rangle. \tag{2.45}$$

Let us add another condition - we were talking about system with one atom per unit cell. Usually, we are dealing with systems that have more atoms per unit cell. If the jth atom sits at position $\mathbf{d}_j$, then the coherent elastic scattering cross

section generalizes to:

$$\left.\frac{d\sigma}{d\Omega_f}\right|_{\text{coh}}^{\text{el}} = N\frac{(2\pi)^3}{v_0}\sum_{\mathbf{G}}\delta(\mathbf{Q}-\mathbf{G})|F_N(\mathbf{Q})|^2, \tag{2.46}$$

where

$$F_N(\mathbf{G}) = \sum_j \overline{b}_j e^{i\mathbf{G}\cdot\mathbf{d}_j} e^{-W_j}. \tag{2.47}$$

The nuclear structure factor F_N contains the atomic positions $\mathbf{d}_j$ within a unit cell and the mean square displacement $\langle u_{j\alpha}^2 \rangle$. To avoid the confusion, it is important to underline that $F_N(\mathbf{G}) = F_N(hkl)$. If one measures structure factors for a large number of reflections, a model for the atomic parameters can be fitted to the results; this is the standard approach of crystallography. The square of the nuclear structure factor can be obtained from a scan through a Bragg peak. The precise formula for the integrated intensity of a peak scan depends, in general, on the resolution function of the instrument; however, there are a couple of simple cases that are easily described [10].

In last paragraph of this section, we will focus on relation between F_N and integrated intensity in terms of scattering experiment on the single crystal. The incident beam has a characteristic wavelength λ and this beam is scattered through the angle 2θ if the Bragg condition is fulfilled for a particular reflection (hkl) in a scattering plane. 2θ scattering angle is relative to the incident beam. Naturally, a detector is placed at 2θ position too, so one can collect the data. Let us simplify the situation by using a double-axis spectrometer - therefore, a measurement with no analyser. As we are rotating the sample during the measurement, we are doing a scan through the particular reflection and the intensity of scattered neutrons collected on the detector will change. The area under the observed peak (integrated intensity $\mathscr{I}$) is given by:

$$\mathscr{I} = A\frac{\lambda^3|F_N(hkl)|^2}{v_0^2 \sin 2\theta}, \tag{2.48}$$

where A is a constant that depends on the incident flux, the sample volume, and the counting time. If these factors are all held fixed in a series of measurements, then A is simply an overall scale factor [10].

Inelastic Nuclear Scattering

If we subtract out the elastic contributions such as Bragg scattering, then $S(\mathbf{Q},\omega)$ corresponds to the fluctuations in a sample, as a function of momentum and frequency. An important property of the scattering function is the principle of detailed balance:

$$S(-\mathbf{Q},-\omega) = e^{-\hbar\omega/k_BT}S(\mathbf{Q},\omega), \tag{2.49}$$

where k_B is Boltzmanns constant and T is temperature. The principle of detailed balance is an important result and deserves broader explanation, which shows its physical significance.

Let us start with alternative derivation of a coherent cross section:

$$\frac{d^2\sigma}{d\Omega_f dE_f} = \frac{k_f}{k_i}\frac{\sigma_{\text{coh}}}{4\pi}\sum_{\lambda_i} p_{\lambda_i}\sum_{\lambda_f}\left|\sum_j \langle\lambda_f|e^{i\mathbf{Q}\cdot\mathbf{r}_j}|\lambda_i\rangle\right|^2 \delta(E_i - E_f + \hbar\omega), \tag{2.50}$$

where p_{λ_i} is the probability that the scattering system is in the state λ_i and its given by the Boltzmann distribution. If the temperature of the scattering system is T, then $p_{\lambda_i} = 1/Z\exp(-E_i\beta)$, here Z is the partition function. Then the scattering function can be written as:

$$S(\mathbf{Q},\omega) = \frac{1}{NZ}\sum_{\lambda_i\lambda_f} e^{-E_i\beta}\left|\sum_j \langle\lambda_f|e^{i\mathbf{Q}\cdot\mathbf{r}_j}|\lambda_i\rangle\right|^2 \delta(E_i - E_f + \hbar\omega). \tag{2.51}$$

To make the discussion, let ω be a positive quantity, i.e. let the neutron lose energy in a scattering process (meaning also that the scattering system will gain energy). Therefore for every transition that contributes to $S(\mathbf{Q},\omega)$, the initial state has a smaller energy than the final state (by $\hbar\omega$).

Consider now the function $S(-\mathbf{Q},-\omega)$, where ω is the same positive quantity. This represents a process in which the neutron gains energy. The transitions of the system are between the same pairs of levels as for the previous process, but

now λ_f is the initial state and λ_i is the final state [29]. Thus:

$$S(-\mathbf{Q},-\omega)=\frac{1}{NZ}\sum_{\lambda_i\lambda_f}e^{-E_f\beta}\left|\sum_j\langle\lambda_i|e^{-i\mathbf{Q}\cdot\mathbf{r}_j}|\lambda_f\rangle\right|^2\delta(E_f-E_i-\hbar\omega), \tag{2.52}$$

when we compare Eq. 2.51 and 2.52, we realise that it is possible to rewrite the last equation in the form:

$$S(-\mathbf{Q},-\omega)=e^{-(E_f-E_i)\beta}\frac{1}{NZ}\sum_{\lambda_i\lambda_f}e^{-E_i\beta}\left|\sum_j\langle\lambda_f|e^{i\mathbf{Q}\cdot\mathbf{r}_j}|\lambda_i\rangle\right|^2\delta(E_i-E_f+\hbar\omega), \tag{2.53}$$

or using 2.51 and 2.52 as:

$$\begin{aligned}S(-\mathbf{Q},-\omega)&=e^{-(E_f-E_i)\beta}S(\mathbf{Q},\omega),\\ S(-\mathbf{Q},-\omega)&=e^{-\hbar\omega/k_BT}S(\mathbf{Q},\omega).\end{aligned} \tag{2.54}$$

We do have all equations to see the physical significance of principle of detailed balance now.

For a pair of states in the scattering system, probabilities that the neutron will bring about a transition in either direction are the same. The probability of the system being initially in the higher energy state is lower by the factor $\exp(-\hbar\omega\beta)$ than its probability of being in the lower energy state. Hence the function $S(-\mathbf{Q},-\omega)$ is less than $S(\mathbf{Q},\omega)$ by this factor [29].

Apart from the principle of detailed balance in inelastic processes, we should mention one more property of the scattering function. It is related to the dissipative part of a linear response function:

$$S(\mathbf{Q},\omega)=\frac{\chi''(\mathbf{Q},\omega)}{1-e^{-\hbar\omega/k_BT}} \tag{2.55}$$

where $\chi''(\mathbf{Q},\omega)$ is the imaginary part of the dynamical susceptibility. Which leads us to the formulation of total susceptibility that is actually complex and consists

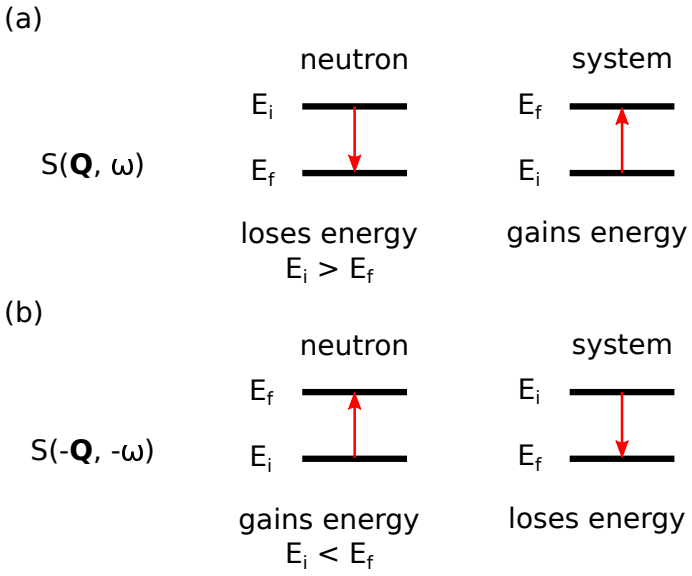

Figure 2.6 *Principle of detailed balance. The energy transfer ω was kept positive for both cases. In (a) neutron loses energy, which means that the scattering system gains energy. The probability of an opposite situation (b), meaning that system will go from energetically higher state to lower state after scattering process, is smaller by factor of* $\exp(-\hbar\omega/k_BT)$.

of real and imaginary part:

$$\chi(\mathbf{Q},\omega) = \chi'(\mathbf{Q},\omega) + \chi''(\mathbf{Q},\omega). \tag{2.56}$$

The real part of susceptibility $\chi'(\mathbf{Q},\omega)$ gives us static response and can be derived from measurements of dynamic susceptibility at $\mathbf{Q} = 0$ by extrapolating the data to larger frequencies. It can be also confirmed by probes for material characterization - measurement with SQUID and application of Curie or Curie-Weiss laws [48].

The Eq. 2.55 is quite important as it is reflecting the connection between scattering system and neutrons. In general, inelastic scattering gives us information about fluctuations in the system - whatever these are fluctuations in atomic positions (phonons) or fluctuations in processing spins in magnetic systems (magnons). Since neutrons interact only weakly with matter, the sample response is appropriately described. The response and the spontaneous fluctuation spectrum are therefore the same, meaning that in neutron scattering experiment, one measures the truly undistorted properties of the scattering system. The speed with which phonons and magnons propagate in the system

makes the neutrons the best probe for studying correlation functions [26].

2.1.5 Magnetic Scattering

As we've mentioned before, the neutron has a magnetic dipole moment that is equal to - $\gamma\mu_N\boldsymbol{\sigma}$, where γ is the gyromagnetic ratio ($\gamma = 1.913$), μ_N is nuclear magneton and $\boldsymbol{\sigma}$ is the spin operator (and can be written in form of Pauli matrices). The neutron can scatter from the magnetic moment of an atom via dipole-dipole interactions. For simplicity, we will assume that the atomic moment comes from spin purely, however, we know from section 1.2.3 in Chapter 1 that the orbital moment needs to be taken into account. The amplitude for magnetic scattering depends on so called magnetic form factor $f_M(\mathbf{Q})$. The magnetic form factor is the Fourier transform of the normalized unpaired spin density $\rho_s(\mathbf{r})$ on an atom:

$$f_M(\mathbf{Q}) = \int \rho_s(\mathbf{r}) e^{i\mathbf{Q}\cdot\mathbf{r}} d\mathbf{r}. \tag{2.57}$$

For small values of $\mathbf{Q}$, the magnetic form factor is very close to unity:

$$f_M(0) \equiv 1, \tag{2.58}$$

but it falls smoothly to zero for large scattering vectors. This can be seen in data from scattering experiments, where the strongest magnetic scattering occurs at low $\mathbf{Q}$, see Fig. 2.7.

It is important to introduce also other quantity for later discussion - the magnetic interaction vector, first introduced by de Gennes (1963) and later adopted by Moon, Riste and Koehler (1969):

$$\begin{aligned} \mathbf{S}_\perp &= \hat{\mathbf{Q}} \times (\mathbf{S} \times \hat{\mathbf{Q}}), \\ \mathbf{S}_\perp &= \mathbf{S} - \hat{\mathbf{Q}}(\hat{\mathbf{Q}} \cdot \mathbf{S}). \end{aligned} \tag{2.59}$$

where $\hat{\mathbf{Q}}$ is a unit vector along $\mathbf{Q}$. From first equation, one can see that only component of spin $\mathbf{S}$ perpendicular to the scattering vector $\mathbf{Q}$ is non-zero and

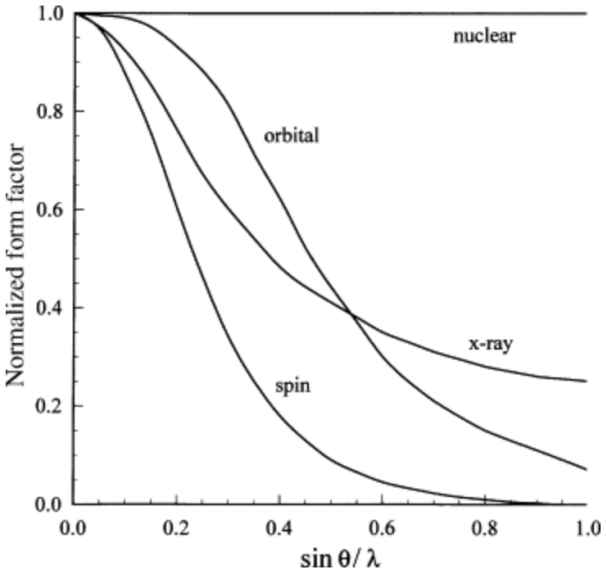

Figure 2.7 *The angular dependence of the normalized form factor for nuclear, and spin and orbital magnetic scattering for chromium metal. The comparable values for x-ray scattering are given for comparison [11].*

therefore contributes to the scattering amplitude. The spin component parallel to $\mathbf{Q}$ is invisible to neutrons. This fact is denoted by $\mathbf{S}_\perp$, it is a completely general result and is essential to all magnetic neutron scattering.

Elastic Magnetic Scattering

The coherent elastic differential cross section for magnetic scattering from a magnetically ordered crystal is given by [10]:

$$\left.\frac{d\sigma}{d\Omega_f}\right|_{\text{coh}}^{\text{el}} = N_M \frac{(2\pi)^3}{v_M} \sum_{\mathbf{G}_M} \delta(\mathbf{Q} - \mathbf{G}_M) |\mathbf{F}_M(\mathbf{G}_M)|^2, \tag{2.60}$$

where v_M and N_M refer to the volume of magnetic unit cell and number of such cells in the sample. Similarly, the sum is over the sites within the magnetic unit cell. And $\mathbf{F}_M$ is the static magnetic structure factor given by:

$$\mathbf{F}_M(\mathbf{G}_M) = \sum_j p_j \mathbf{S}_{\perp j} e^{i\mathbf{G}_M \cdot \mathbf{d}_j} e^{W_j}. \tag{2.61}$$

Except for the case of ferromagnetism, the magnetic unit cell is typically larger

than the chemical unit cell. If we compare equations for nuclear scattering 2.46 and magnetic scattering 2.60, we realise that $\mathbf{F}_N$ has been replaced by $\mathbf{F}_M$ and we are thinking in terms of new reciprocal lattice vectors $\mathbf{G}_M$. The relation between integrated intensity of a magnetic Bragg peak and $|F_M(h_M k_M l_M)|$ is the same as that for nuclear scattering [10], see equation 2.48.

However, in case of magnetic scattering we run into one problem that it is very rare for nuclear structural determinations - it is possible that different magnetic structures yield identical Bragg peaks intensities. To understand this better, we should know that magnetic structures can be divided into two categories, *collinear* and *noncollinear*. In collinear case, all magnetic spins are aligned along the same axis, either parallel or antiparallel. In some cases, a noncollinear structure yields the same Bragg intensities as a collinear model. It can be best seen in Fig. 2.8.

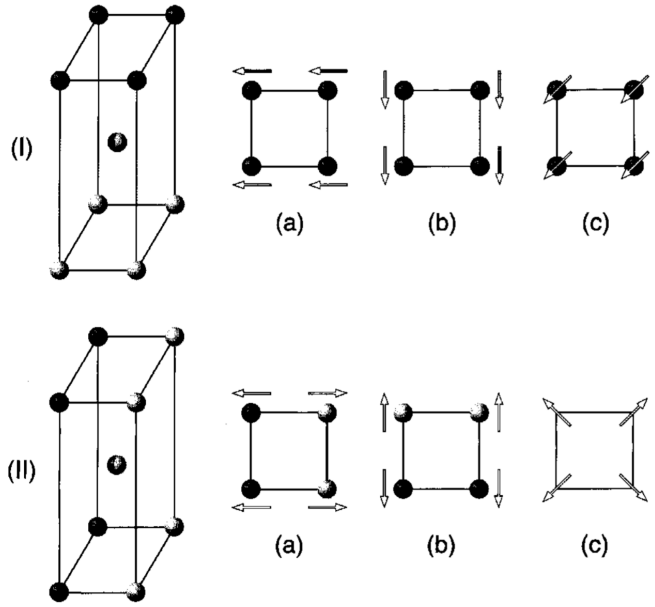

Figure 2.8 *Two fictional models of magnetic structures in a tetragonal lattice. The domain averaged Bragg intensities from (a) + (b) are identical to those given by (c) [10]. Note that I(c) is a collinear structure and II(c) is noncollinear.*

For collinear structures, one can work out explicit symmetry-dependent formulas for domain-averaged magnetic intensities. To analyze the effects of averaging over domains, it is convenient to factorize the magnetic structure factor as follows:

$$\mathbf{F}_M(\mathbf{G}_M) = \mathbf{S}_\perp \tilde{F}_M, \tag{2.62}$$

where $\mathbf{S}_\perp$ represents the component of the spin axis perpendicular to $\mathbf{Q}$, and:

$$\tilde{F}_M = \sum_j p_j e^{i\mathbf{G}_M \cdot \mathbf{d}_j} e^{W_j}, \tag{2.63}$$

with p_j now set to $+|p_j|$ or $-|p_j|$, depending on relative spin direction. Note that both $\mathbf{S}_\perp$ and $\tilde{F}_M$ depend on (hkl). The set of p_js defines the configurational symmetry of magnetic structure, which need not be the same as the *chemical* symmetry.

Magnetic Structures

Before determination of the magnetic structure, one should know the crystal structure first. The crystal structure is usually investigated by x-ray diffraction, however, in special cases, neutrons can be used too. The full characteristic of the magnetic structure consists of determining both the magnitude and the direction of all magnetic atomic moments in the magnetic unit cell. On a same basis as we can derive any crystal structure from 14 Bravais lattices, there are 36 magnetic ones. This development has been brought by Russian crystallographers mainly, who added a new operation, designated R, to the normal symmetry operations. This new operation reverses the direction of a magnetic moment. In this way the normal 230 space groups are increased by a further 1421 groups which are applicable to the structures of ferromagnetic and antiferromagnetic materials [12].

Despite the fact that the first neutron experiments were using mostly powder samples, it is necessary to say that powder data often can not provide all information needed for determination of magnetic structure (for example, magnetic reflections can overlap). Even with a single crystal, one can run into the problem of multiple domains and therefore, the problem of several solutions for the magnetic structure. Ideally, we would like to have a single crystal with a single domain, where all individual reflections can be identified separately and unambiguously. The most detailed information can be obtained by doing polarized neutron diffraction on a single domain crystal with three-dimensional polarization analysis, which can provide a unique solution. This type of experiment can also detect an unique crystallographic axis in single crystal, if it is present.

Let's start with paramagnetic materials with magnetic atoms first. The directions

of magnetic moments vary randomly from atom to atom and there is no coherent magnetic contribution to the Bragg diffraction peaks. The incoherent magnetic scattering is distributed in the background of the diffraction pattern, decreasing with increasing scattering angle θ (impact of the magnetic form factor) [12]. Unlike first paramagnetic group of materials, in second one, there are correlations present between the magnetic moments and their relative directions to each other. This leads to another classification of magnetically ordered systems - into *commensurate* and *incommensurate* structures.

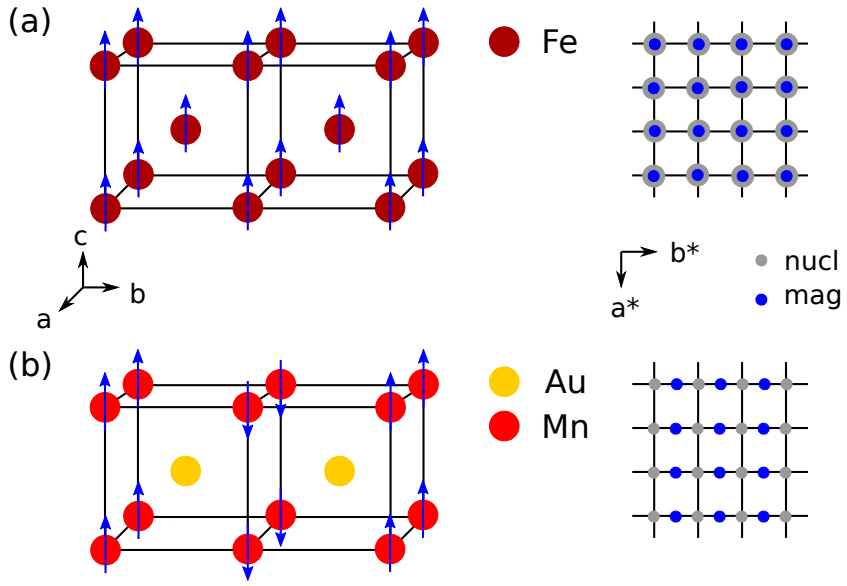

Figure 2.9 *(a) Ferromagnetic structure with wave vector* ***k****=(0, 0, 0) of body centred cubic Fe and (b) antiferromagnetic structure of AuMn with wave vector* ***k****=(0, 1/2, 0). On the right hand side are nuclear and magnetic reflections for both cases in the reciprocal space.*

Commensurate Magnetic Structures

In the simplest case of ferromagnetically ordered magnetic structure, the magnetic unit cell is the same as nuclear cell and the propagation vector is $\mathbf{k} = 0$. This means that we expect magnetic reflections superimposed on the nuclear reflections in the reciprocal space. It is possible to have also an antiferromagnetic structure with the propagation vector $\mathbf{k} = 0$. Nuclear reflections would be boosted by a magnetic component again. However, the crystal and magnetic unit cell doesn't always need to be the same. If the magnetic structure is antiferromagnetic with a propagation vector $\mathbf{k} \neq 0$, then magnetic Bragg scattering is present at positions which are different from those of nuclear Bragg reflections. Once the positions of the magnetic intensities are obtained, the next important step is to determine the periodicity of the magnetic unit cell. It is convenient to use crystal unit cell

and express the magnetic periodicity in terms of the propagation vector **k**. If **k** commensurate with the crystal unit cell, i.e. when for example **k** = (1/2, 0, 0) where the magnetic cell is $2a \times b \times c$, then the determination of propagation vector from powder data is not a very difficult task [13]. In other words - the magnetic unit cell for *commensurate* magnetic structures can be expressed in a form of integral multiple of crystal unit cell, see Fig. 2.9.

Incommensurate Magnetic Structures

If the magnetic cell is incommensurate with the nuclear cell, i.e., the components of the propagation vector cannot be expressed by simple fractions, the determination of **k** becomes more difficult. In such case, neutron diffraction investigation with a single crystal, if available, is recommended [13]. The magnetic unit cell is a superstructure of the crystal unit cell due to the large periodicity of magnetic structure in comparison with periodicity of crystal unit cell. These magnetic structures are also known as modulated, because they have some sort of modulation of the initial ferromagnetic or antiferromagnetic structure:

$$\mathbf{k} = \mathbf{k}_0 + \delta \tag{2.64}$$

where the modulation vector δ is usually small and $\mathbf{k}_0$ is the initial ferromagnetic or antiferromagnetic wave vector. Such a structure can be described by a wave vector which has in general nonrational components. The modulated magnetic structure is characterized by the appearance of satellite magnetic reflections close to the initial ferromagnetic or antiferromagetic reflections, see Fig. 2.10. The number of satellites in reciprocal space can be more than two if sample consists of multiple domains or has multiple **k**- magnetic structures.

We will discuss two examples of incommensurate structures - sine-wave and helimagnetic type. In a modulated magnetic structure the magnetic moment can be modulated in amplitude or orientation or in both. In a harmonically modulated magnetic structure the amplitude of the magnetic moment follows a sine-wave [13].

In helimagnetic structures, spins rotate along certain axis, creating helical spiral. This type of structure has been firstly reported in compounds $MnAu_2$ and MnO_2 and many other compounds later on. The structure of $MnAu_2$ can be seen in Fig. 2.10, which shows ferromagnetic sheets of atoms, perpendicular to the direction of y axis. In this particular case, there is a rotation about 51° between successive

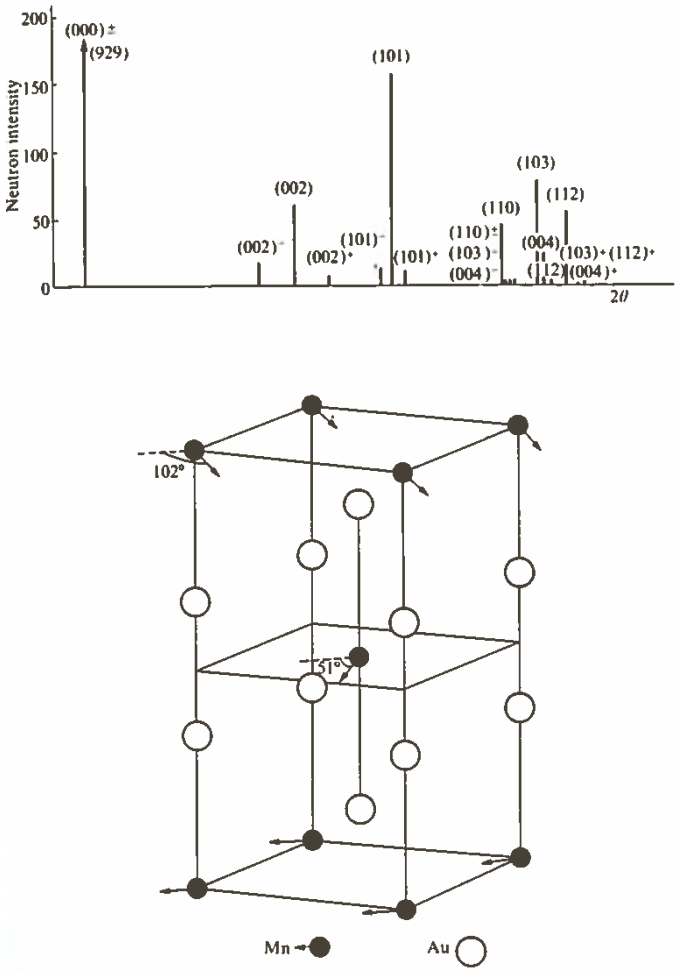

Figure 2.10 *The lower figure shows helimagnetic structure of $MnAu_2$. The direction of the moment in the manganese layers spirals around c-axis. The diffraction pattern above shows pairs of magnetic satellite reflections which accompany the nuclear reflections [12].*

sheets. In a diffraction pattern of such a material, nuclear Bragg peaks are accompanied by pairs of satellites of magnetic origin. It is possible to determine the direction of spiral axis and the magnitude of the rotation by studying the displacement of satellite peaks from the fundamental reflections.

Inelastic Magnetic Scattering

The scattering cross section for inelastic magnetic scattering depends not only on the initial and final wave vectors of the neutron, but also on the corresponding neutron spin state, $\mathbf{s}_i$ and $\mathbf{s}_f$, with $\mathbf{s} = \sigma/2$. Then differential cross section can

be written as:

$$\left.\frac{d^2\sigma}{d\Omega_f dE_f}\right|_{s_i s_f} = \frac{k_f}{k_i}\sum_{i,f} p_{\lambda_i}\left|\left\langle \lambda_f \left| \sum_l e^{i\mathbf{Q}\cdot\mathbf{r}_l} U_l^{s_i s_f} \right| \lambda_i \right\rangle\right|^2 \delta(E_i - E_f + \hbar\omega). \quad (2.65)$$

If we compare it with equation for inelastic nuclear scattering 2.50, we see that there is additional quantity $U_l^{s_i s_f}$ - the atomic scattering amplitude from the spin sate s_i to s_f for atomic site l:

$$U_l^{s_i s_f} = \langle s_f | b_l - p_l \mathbf{S}_{\perp l} \cdot \boldsymbol{\sigma} + B_l \mathbf{I}_l \cdot \boldsymbol{\sigma} | s_i \rangle, \quad (2.66)$$

where b is the nuclear coherent scattering amplitude, B is the spin dependent nuclear amplitude and $\mathbf{I}$ is the nuclear spin operator.

For unpolarized neutrons scattering from a system containing a single species of magnetic atom, the differential cross section for atomic magnetic scattering can have a form:

$$\frac{d^2\sigma}{d\Omega_f dE_f} = \frac{N}{\hbar}\frac{k_f}{k_i} p^2 e^{-2W} \sum_{\alpha,\beta} (\delta_{\alpha,\beta} - \hat{Q}_\alpha \hat{Q}_\beta) S^{\alpha\beta}(\mathbf{Q}, \omega), \quad (2.67)$$

with:

$$S^{\alpha\beta}(\mathbf{Q}, \omega) = \frac{1}{2\pi}\int_{-\infty}^{\infty} dt e^{-i\omega t} \sum_l e^{i\mathbf{Q}\cdot\mathbf{r}_l} \langle S_0^\alpha(0) S_l^\beta(t) \rangle, \quad (2.68)$$

angle brackets in this equation denote an average over configuration. Doing this derivation, we also obtain a differential cross section for magneto-vibrational scattering, where one excites phonons by scattering from ordered magnetic moments.

Integrating $S^{\alpha\beta}(\mathbf{Q}, \omega)$ over all frequencies, one obtain the Fourier transform of the instantaneous correlation function:

$$S^{\alpha\beta}(\mathbf{Q}, t = 0) = \int_{-\infty}^{\infty} d\omega S^{\alpha\beta}(\mathbf{Q}, \omega). \quad (2.69)$$

It is a definition in a form of a retarded Green's function. Without going into mathematical details, it is important to state that Green's function can describe the spin-wave spectrum (or in other words - magnetic excitations).

This gives us a nice build up for the following part - excitations in systems. Even at $T = 0$ K, atoms are not purely static. At non-zero temperature, the order is disrupted by thermally excited lattice vibrations. If it is collective behaviour on long range scale that can be quantized, we are talking about *phonons*. The behaviour of phonons is characterized by a dispersion relation, i.e. a relationship between angular frequency ω and wave vector $\mathbf{q}$. Similar situation can happen in magnetic systems. Let consider a perfectly ordered ferromagnet at $T = 0$ K. In any magnetically ordered system, neighbouring spins are correlated with each other via an exchange interaction J, therefore a violation of a spin alignment will cause collective disruption - a propagating spin wave, see Fig. 2.11. When this wavelike form is quantized, then we call it *magnon*.

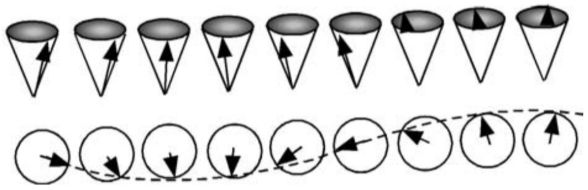

Figure 2.11 *Perspective view and view from above of a spin wave in the ferromagnetic system [13]*

There will be a series of such waves and each spin wave will posses a wavelength and a quantized energy $\hbar\omega$. The energy of the spin waves $\hbar\omega$ exhibits dispersion with respect to the wave vector $\mathbf{q}$ within a Brillouin zone. A neutron, scattering from a magnetic system, can absorb or emit one or more magnons; in this section we will consider only the single magnon processes.

For a ferromagnetic linear chain with nearest neighbour interaction this relation is given by:

$$\hbar\omega = 4JS(1 - \cos qa), \tag{2.70}$$

where a is the distance between nearest neighbouring spins. At long wavelength (low energy) $qa \ll 1$ so that:

$$(1 - \cos qa) \simeq \frac{1}{2}(qa)^2. \tag{2.71}$$

In this limit the dispersion relation for the spin wave becomes:

$$\hbar\omega \simeq 2JSa^2q^2 = Dq^2, \tag{2.72}$$

where D is called the spin wave stiffness constant. Figure 2.12 (a) shows the typical spin wave dispersion for a ferromagnet [13]. For an antiferromagnetic chain the corresponding dispersion relation is given by:

$$\hbar\omega = 4|J|S \sin qa. \tag{2.73}$$

For the long wavelength limit, the equation is reduced to:

$$\hbar\omega \simeq 4|J|Sqa. \tag{2.74}$$

The difference between the dispersion of spin waves for antiferromagnet and ferromagnet is pretty obvious. In case of ferromagnets, spin wave energy $\hbar\omega$ is proportional to q^2 for small q. In antiferromagnetic system, energy is proportional to q, the dispersion can be seen in Fig. 2.12 (b). In both cases (a) and (b) there are no gaps in the dispersion so that the energy $\hbar\omega$ is zero at $q = 0$. However, we know systems where such gaps exist - they are caused by the single ion anisotropy or the anisotropy in the exchange interaction [13].

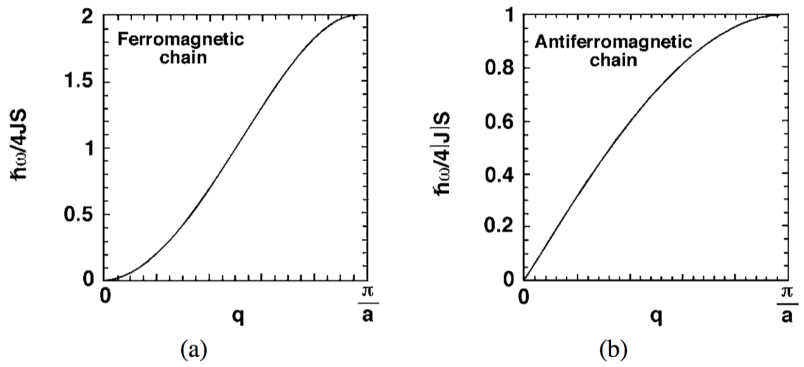

Figure 2.12 *Spin wave dispersion of a ferromagnetic chain (a) and of an antiferromagnetic chain (b) [13]*

2.1.6 Neutron Scattering Instruments

There are several different instruments that can be used for neutron scattering experiments. Every one of them has been designed for a certain purpose and therefore, it is really important to understand how they work.

In the case of inelastic experiments, it is possible to choose from 3 basic types (some of them have several subcategories) that differ in method of collecting the data - time of flight (TOF), triple-axis spectrometers (TAS) and spin-echo instruments. For purposes of this work, we are going to discuss TOF and TAS instruments in more details.

Time of flight instrument (TOF)

This technique has been refined over last 50 years and used at reactor facilities as well as pulsed sources. Obviously, pulsed sources, by their nature, are ideally suited for TOF techniques. In a case of the nuclear reactor, a continuous beam of neutrons must be chopped into pulses, which means significant loss of intensity coming from source.

The principle of the TOF technique is the time taken by a polychromatic beam of neutrons to travel from the source to the detector. As distances are known for each instrument and it's parts, it is possible to calculate the velocity of neutrons. After neutrons interact with a sample, they will gain or lose energy, which results in a velocity change. The arrival time at the counter will therefore vary [10].

One must realize that with TOF technique is not possible to determine both E_i and E_f energies. Either the initial E_i or final energy E_f must be selected by other means, typically by Bragg reflection from crystals or by chopping the beam in short time pulses close to the sample. This leads to two essentially different types of spectrometer geometries [28]:

- direct - the incoming beam of neutrons is monochromatized by a chopper system, which means fixed initial energy E_i. These neutrons hit the sample in short bursts. The final energy is determined by time of flight method,
- indirect - the sample is hit by white beam of neutrons, but only certain energy is scattered by analyzer crystals on to the detector. Therefore, in

indirect geometry, the final energy E_f is fixed and initial energy of neutrons is defined by time of flight method.

If the neutron source is a reactor, a chopper or combination of choppers define the initial pulse at time t_0. Very shortly about chopper itself - choppers are multiple collimators made from highly neutron absorbing materials rotating about an axis perpendicular to the incident beam. For example - the IN5 disk chopper TOF spectrometer (direct geometry spectrometer) at ILL (Grenoble, France), which consists of several choppers. The first two are synchronized and define the incident beam energy. The third chopper cuts unwanted neutrons - ie. neutrons that have integral multiples of desired neutron velocity (this is common issue of neutron scattering experiments - high order scattering can occur). The fourth chopper ensures that different pulses don't overlap and spins at low frequencies. It can happen that the fastest neutrons of a pulse take over the slowest neutrons of the previous pulse. After scattering process from sample, neutrons travel over a distance of about 4 meters to a number of detectors covering the angular range $-10° \leq 2\theta_S \leq 130°$.

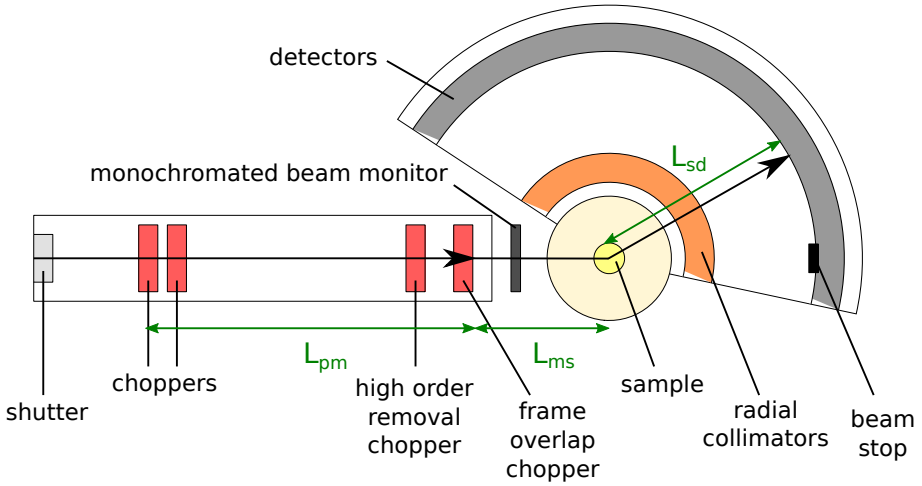

Figure 2.13 *Scheme of time of flight instrument with direct geometry, based on spectrometer IN5 at ILL*

Let's have a look on the geometry of direct TOF instrument. As it is a direct instrument, E_i must be fixed and E_f is determined by TOF method, which can be expressed in a form of the kinetic energy:

$$E_f = \frac{1}{2} m_n v_f^2 \tag{2.75}$$

After neutrons with precisely defined incident energy E_i leave the last chopper,

they fly to the sample at time t_1. After interacting with the sample, they scatter with different velocity to the detector. As we do know the length of the path of scattered neutron to detectors L_{sd} and also time that it takes t_2, we can write:

$$v_f = \frac{L_{sd}}{t_2} \tag{2.76}$$

We can see in Fig. 2.13 that the total time of neutron after it leaves the chopper consists of two parts:

$$t = \frac{L_{ms}}{v_i} + t_2 \tag{2.77}$$

where L_{ms} is distance between last chopper and sample and v_i is velocity of incident neutrons. Then our starting Eq. 2.75 can be expressed as:

$$E_f = \frac{1}{2} m_n \left(\frac{L_{sd}}{t - \frac{L_{ms}}{v_i}} \right)^2 \tag{2.78}$$

For indirect TOF spectrometers, the incident beam is polychromatic, possessing a spread in the time required for neutrons to travel from the moderator to sample (distance L_{ms}), thus defining a spread of incident energies. After a scattering process with the sample, neutrons hit analysers. Analysers are crystals that would reflect only certain energy E_f. Only those neutrons will be detected.

Indirect geometry instruments include several types - filter-detector spectrometers, crystal-analyser spectrometers and backscattering spectrometers (most of them using TOF method). The backscattering spectrometers have some of the best energy transfer resolution to present-day conventional spectrometers, approaching 1 μeV [14]. One of the examples is backscattering spectrometer OSIRIS at ISIS and we will show later, in our data anlysis, that one must work with resolution of the instrument very sensibly. The assumption - the better resolution, the better results - must be examined very carefully. For example, resolution in range of 1 μeV is not appropriate for study of very broad diffuse scattering.

Triple axis spectrometer (TAS)

Many experiments included in this thesis have been performed on triple-axis spectrometers and therefore, we will discuss the principles of this technique in more detail.

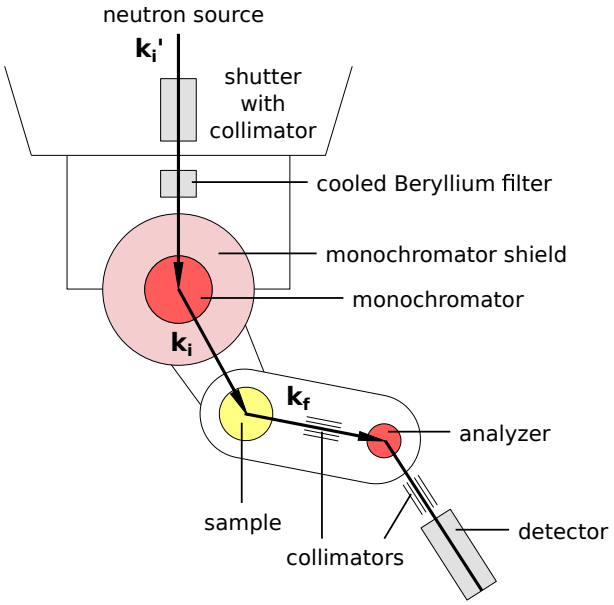

Figure 2.14 *Scheme of triple axis spectrometer.*

The three-axis instrument is the most versatile and useful instrument for use in inelastic scattering because it allows one to probe nearly any coordinates in energy and momentum space in a precisely controlled manner. This brilliant concept was developed over 40 years ago by Brockhouse (1961) at Chalk River in Canada. On instruments that uses a continuous beam of neutrons, it is necessary to directly select both E_i and E_f, in order to determine the neutron energy transfer, $\hbar\omega$. For both purposes, the Bragg diffraction from crystals is used. Such a type of instrument is denoted a triple-axis spectrometer, since the neutron changes direction by Bragg scattering three times before being detected [28]. The three axes correspond to the axes of rotation of the monochromator, the sample, and the analyser. There is a convention that 3 scattering angles, $2\theta_m$, $2\theta_s$, and $2\theta_a$, are often denoted as A2, A4, and A6, respectively. The symbol A3 denotes the sample rotation ω, while the symbols A1 and A5 denotes the rotation of monochromator and analyser crystals, respectively (these angles are also known as Bragg angles). It should be highlighted that the Bragg and the scattering angle are not necessarily related to one another by a factor of two. The modulus of momentum transfer $\mathbf{Q}$ is function of scattering angle $2\theta_s$ and not Bragg angle θ_s.

The value of θ_s represents the rotation of the sample, which is important in case of single crystals - it's used to define the orientation of specific crystallographic axes relative to $\mathbf{Q}$. This is particularly important when probing dynamics in a certain direction.

The monochromator defines the direction and magnitude of the momentum of the incident beam (see Fig. 2.14) and the analyzer performs a similar function for the scattered or final beam [10]. Choosing adequate scattering angles, one can adjust the instrument to any value of scattering vector $\mathbf{Q}$, and energy transfer $\hbar\omega$, allowed by the inelastic scattering condition. However, $\mathbf{Q}$ can only collect data within the scattering plane. This means that there are 4 free angles to determine only 3 parameters: $\hbar\omega$ and 2 dimensions of $\mathbf{Q}$. In practice, this ambiguity is solved by fixing either E_i or E_f to a predetermined value [28]. Data are usually collected along particular axis in ($\mathbf{Q}$, E) space. One can perform so called *constant energy cuts* or *constant Q cuts*.

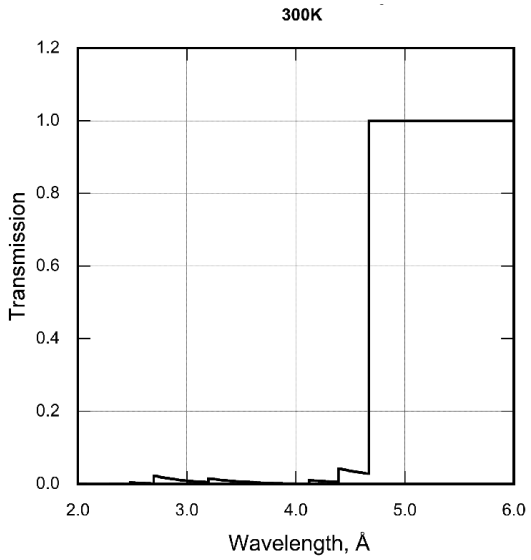

Figure 2.15 *Transmission for 10 cm of BeO filter at 300 K. A sharp cutoff is visible at wavelength 4.65 Å, which corresponds to the energy 3.78 meV. This helps to eliminate unwanted neutrons with higher energies [14].*

In order to eliminate higher order scattering and achieve passage for only a few selected energies, filters can be inserted for monochromator and/or analyser. For example one of the pyrolytic graphite (PG) filters can be used for selection of 14.7 meV neutrons. Other types of filters consist of cooled block of Be or BeO, which transmit energies below 5.2 meV and 3.8 meV, respectively. Both of them have very characteristic cutoffs at the mentioned energies, see Fig. 2.15. This

insures that neutrons that do not fulfil this condition will be scattered out of the beam, significantly reducing background.

Summary of TOF and TAS Scattering Instruments

It is important to underline that both methods are complementary. The TOF instruments can probe large regions of ($\mathbf{Q}$, E), which is a big advantage for exploratory investigations and for systems that exhibit weak dispersions. Also - TOF instruments are the best for polycrystalline samples, where the direction of $\mathbf{Q}$ is not relevant. On the other hand, it is crucial for TAS techniques, which deal with single crystals and are meant to be used for investigation of a limited range in ($\mathbf{Q}$, E) space.

2.1.7 Polarized Neutrons

The fact that the strength of the interaction between a neutron and the sample is dependent on the orientation of the neutron spin is the principle idea of polarizing neutron beams. The nuclear interaction is only neutron spin dependent, if the scattering nucleus itself has a spin and if the spins of the nuclei are ordered, which only applies to extreme conditions like very low temperatures in the mK region of very high magnetic fields. Therefore, nuclear scattering can be considered as spin independent. In contrast, electron spins are much more easily ordered leading to an important neutron spin dependence of the magnetic scattering. Polarized neutron diffraction is used to determine precise magnetic structure factors by the *flipping ratio* method. Analyzing the polarization state of the neutron after the scattering process offers the possibility to determine the type of interaction and the configuration of magnetic moments in a magnetically ordered compound [15].

The first important question is - how do we achieve a neutron beam where the majority of neutrons will have the same spin direction? There are several methods, one of them uses polarizing crystals as a monochromators. Interestingly, it is not just wavelengths that is selected (as we are used to in unpolarized scattering experiments), but also the neutron spin state. On the top of that, these compounds offer a Bragg refelections where the magnetic structure factor has the same order as the nuclear structure factor. In order to achieve this, the monochromator is placed within a permanent magnetic field $\mathbf{H}$ which produces a mono-domain state and also helps to tune the magnetic structure factor to the

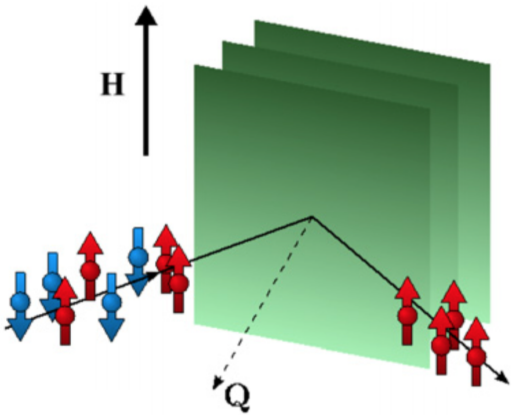

Figure 2.16 *Principle of creating a polarized beam of neutrons by polarizing crystals [15].*

correct value. The spin-dependent nature of interaction leads to the fact that only one spin state is diffracted as the cross section of the other spin state is zero [15] as can be seen in Fig. 2.16.

This can be written in terms of cross section:

$$\begin{aligned} & \frac{d\sigma}{d\Omega} = F_N^2 + 2F_N F_M + F_M^2, \\ \text{for polarized beam} \Rightarrow \quad & F_N = F_M \\ \text{spin up} \quad & \frac{d\sigma}{d\Omega} = (F_N + F_M)^2, \\ \text{spin down} \quad & \frac{d\sigma}{d\Omega} = (F_N - F_M)^2 = 0. \end{aligned} \tag{2.79}$$

Where F_N is the nuclear and F_M is the magnetic structure factor. Moreover, not only the scattering cross section is spin dependent, but also the absorption cross section. In this context the ^{3}He nucleus is ideal as it is almost transparent for one neutron spin state and highly absorbing for the other. These spin filters are pumped under a certain pressure in order to have only one ^{3}He spin state.

Once the polarized beam has been created, it is important to keep it and guide fields are used for these purposes. We are not going to discuss guide fields in this thesis, but more details can be find in ref. [15].

The polarization of the neutron beam is the average over individual polarizations

of the neutrons $\mathbf{p}_j$ [13]:

$$\mathbf{P} = \frac{1}{N} \sum_j \mathbf{p}_j, \tag{2.80}$$

with $0 \leq |\mathbf{P}| \leq 1$.

The Flipping Ratio Method

Intensity of Bragg reflections for unpolarized neutrons is given by the sum of nuclear and magnetic intensities:

$$\mathscr{I} = \mathscr{I}_{\text{nuc}} + \mathscr{I}_{\text{mag}} = (F_{\text{nuc}})^2 + (F_{\text{mag}})^2, \tag{2.81}$$

while for polarized neutrons, the amplitude depends on the polarization of the beam and is mainly given by the sum or the difference of the nuclear and magnetic amplitudes [13]:

$$\mathscr{I}^{\pm} = (F_{\text{nuc}} \pm F_{\text{mag}})^2. \tag{2.82}$$

For small F_{mag} the sensitivity is improved radically when taking advantage of polarized neutrons. To illustrate this increase of sensitivity for small magnetic amplitudes, let us take an example where $F_{\text{mag}} = 0.1F_{\text{nuc}}$. The unpolarized neutrons would be scattered with intensity:

$$\mathscr{I} = (F_{\text{nuc}})^2 + (0.1F_{\text{nuc}})^2 = 1.01(F_{\text{nuc}})^2, \tag{2.83}$$

while there are two possible direction of the polarization for polarized neutrons:

$$\begin{aligned} \mathscr{I}^{+} &= (F_{\text{nuc}} + 0.1F_{\text{nuc}})^2 = 1.21(F_{\text{nuc}})^2, \\ \mathscr{I}^{-} &= (F_{\text{nuc}} - 0.1F_{\text{nuc}})^2 = 0.81(F_{\text{nuc}})^2. \end{aligned} \tag{2.84}$$

Due to the interference term, the improvement is tremendous [13]. The simple

formula for the flipping ratio R is:

$$R(\mathbf{Q}) = \frac{\mathscr{I}^{+}}{\mathscr{I}^{-}}. \tag{2.85}$$

However, one needs to be extremely careful with this method when the studied system is non-centrosymmetric and has a chiral magnetic structure (which is the case of $MnSb_2O_6$ compound in this thesis). Several simplifications that are valid for centrosymmetric collinear systems cannot be introduced here. Formulas must be treated with special care, otherwise, the flipping ratio method would introduce erroneous results. Still, the flipping ratio method can be use for investigation of noncollinear magnetic structures if it is treated properly.

Uniaxial (Longitudinal) Polarization Analysis

In 1969 a new progress in field of polarized neutrons appeared - the uniaxial (longitudinal) polarization analysis (LPA), developed by Moon et al. [49].

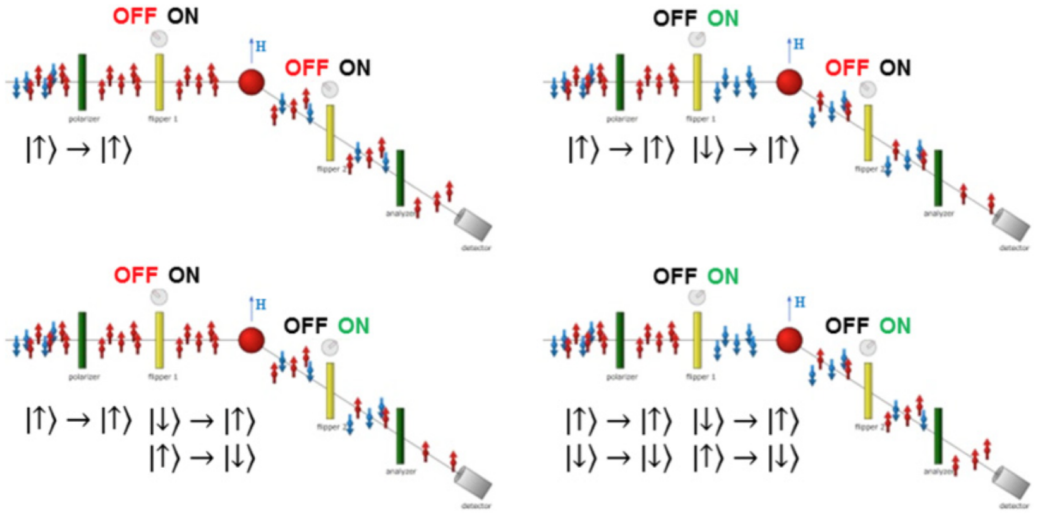

Figure 2.17 *Sketches of a polarized neutron experiment with longitudinal polarization analysis [15]. The incoming beam is polarized "up" or "down" and the scattered beam is polarized "up" or "down" before entering the detector. This allows measurement of 4 cross sections - two non-spin flip sections $(d\sigma/d\Omega)^{++}$ and $(d\sigma/d\Omega)^{--}$, two spin flip sections are $(d\sigma/d\Omega)^{+-}$ and $(d\sigma/d\Omega)^{-+}$. Green rectangles represent analysers and yellow ones flippers.*

Polarized neutrons add additional selection rules to the general law in neutron scattering (that neutrons can "see" only perpendicular part of magnetisation).

Generally, nuclear scattering is a non-spin-flip (NSF) process regardless of the initial neutron polarization state. Only magnetic components perpendicular to the scattering vector ($\mathbf{Q} \parallel \mathbf{x}$ by definition) are accessible in a neutron experiment. The components perpendicular to the polarization axis (**y** being in the scattering plane and **z** being the perpendicular axis of the instrument) contribute to the spin-flip (SF) channel, while those parallel to the axis of polarization scatter into the NSF channel. The method where the neutron spin is polarized along one axis and then analysed along the same axis is called longitudinal polarization analysis [15], nice overview can be seen in Table 2.3.

	NSF	SF
$P_0 \parallel x$	σ_N	$\sigma_{M_y} + \sigma_{M_z}$
$P_0 \parallel y$	$\sigma_N + \sigma_{M_y}$	σ_{M_z}
$P_0 \parallel z$	$\sigma_N + \sigma_{M_z}$	σ_{M_y}

Table 2.3 *Cross section of polarized neutron scattering with longitudinal polarization analysis [15]. When the initial polarization P_0 is aligned along scattering vector $\boldsymbol{Q}$, the x component σ_{M_x} of the magnetic interaction is automatically set to zero ($\boldsymbol{Q} \parallel \boldsymbol{x}$). Then the non-spin flip (NSF) is only nuclear and spin flip (SF) scattering is only magnetic.*

In the principle, there are two possibilities for uniaxial polarization analysis. When the incident beam is polarized along the scattering vector **Q**, there is a complete separation between the nuclear and the magnetic scattering - the non-spin flip scattering is only nuclear and the spin flip scattering is only magnetic. On the other hand, when the incident beam is not polarized and some polarization is found for the scattered beam, chirality exists in the magnetic system.

It can be seen that analysis of final neutron polarization is powerful tool as one can separate the nuclear and magnetic cross sections by measuring the appropriate channels. Furthermore, it is possible to extract much more detailed information about the orientation of magnetic moments too [15].

Spherical Polarization Analysis

In recent years, the method of polarization analysis was extended to the spherical (vectorial, three dimensional) polarization analysis. The concept existed already with the derivation from Maleyev et al. [50] and then Blume [51], but it was only with the ideas developed by Mezei [52, 53] in the achievement of the spin-echo spectrometer and the realisation of new instrument CryoPAD (Cryogenic

Polarization Analysis Device) by Tasset [54, 55] that a full three dimensional polarimetry experiment could be achieved [13].

The results of a polarisation analysis experiment may be expressed in terms of generalised cross-sections I^{ij}. The indices i and j each refer to one of the three orthogonal directions defined by the experiment - the first superscript gives the direction of analysis, the second the direction of polarization. In general, we can write the polarisation matrix $\mathscr{P}_{ij}$ in following form [56]:

$$\mathscr{P}_{ij} = \frac{I^{ij} - I^{-ij}}{I^{ij} + I^{-ij}}. \tag{2.86}$$

The polarization $\mathscr{P}_{ij}$ can be measured with high precision. On the top of that, spherical neutron polarimetry can provide also off diagonal terms of polarisation matrix $\mathscr{P}_{ij}$. The full polarization matrix allows one to derive information about the magnetic moment configuration in the studied system, especially chiral terms. The instrumental realization of such a task is done using the CryoPAD (Fig. 2.18).

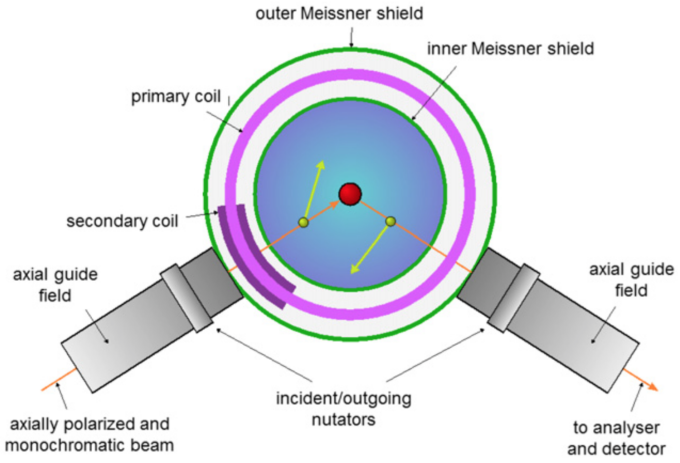

Figure 2.18 *The schematic set up of the CryoPAD [15].*

Let us have a look at this sophisticated instrument. In order to have full control of the neutron spin the sample needs to be in an absolutely magnetic field free region which is achieved by an inner Meissner shield provided by a superconducting material. In order to manipulate the neutron spin in the incident and in the scattered beam two individual magnetic fields are necessary which are supplied by a primary coil and a secondary. On the incoming and the outgoing parts of the CryoPAD nutators are positioned in which an axial guide field can be set along a direction perpendicular to the direction of motion of the neutron. The neutron spin will then adiabatically rotate towards that field direction. An outer

Meissner shield prevents the superposition of the nutator field and the coils. Due to the abrupt field change at the entrance of the CryoPAD the neutron spin will non-adiabatically rotate around the new field direction. Hereby, the magnetic field is set according to the distance the neutron will travel and its wavelength in order to control the rotation angle in such a way that the neutron spin arrives at the desired polarization axis when it enters the field-free region where it stays constant. Depending on the interaction with the sample the neutron spin might be flipped or rotated. In any case by adjusting the field in the primary coil and in the outgoing nutator the x, y or z component of the scattered neutron spin can be rotated to be parallel to the guide field between the analyzer and the sample. Similar to the LPA experiment a set of two spin flippers (after the monochromator and before the analyzer) is used to distinguish between the different spin-flip and non-spin-flip transitions [15].

Spherical neutron polarimetry (SNP) has been very successful method in determining the details of incommensurate structures as helices, cycloids and spin density waves and also in deciding between them. For this technique, it is crucial to consider orientation of crystal before experiment. It is clear that the propagation vector must lie in the scattering plane, but it is equally important to have component of moment perpendicular to the scattering plane. If both components of the moment lie in the scattering plane then magnetic interaction vector $\mathbf{S}_\perp$ is parallel to polarisation $\mathbf{y}$ for all accessible reflections. Since it is only the direction and not he magnitude of $\mathbf{S}_\perp$ which is measured by SNP when $\mathbf{k} \neq 0$ such an experiment would give no additional information [13].

The magnetic moment distribution $\mathbf{m}(\mathbf{r})$ in a sinusoidally modulated structure with propagation vector $\mathbf{k}$ can be written as:

$$\mathbf{m}(\mathbf{r}) = \sum_{\mathbf{l}} \rho(\mathbf{r} - \mathbf{l})(\hat{\mathbf{u}}\mu_u \cos(\mathbf{l} \cdot \mathbf{k}) + \hat{\mathbf{v}}\mu_v \sin(\mathbf{l} \cdot \mathbf{k})), \tag{2.87}$$

where $\hat{\mathbf{u}}$ and $\hat{\mathbf{v}}$ are unit vectors which are perpendicular to one another with μ_u and μ_v giving the amplitudes of modulations in these two directions. $\rho(\mathbf{r})$ gives the distribution of magnetic moment within a single unit cell. When either of μ_u or μ_v is zero, Eq. 2.87 describes the spin density wave; when either $\hat{\mathbf{u}}$ or $\hat{\mathbf{v}}$ is parallel to $\mathbf{k}$, it describes a cycloid and when both are perpendicular to $\mathbf{k}$, it describes a right helix. The ratio μ_u/μ_v gives the ellipticity of the cycloid or helix.

If $F_M(\mathbf{Q})$ is the structure factor for the unit cell contents [13]:

$$F_M(\mathbf{Q}) = \int_{\text{unit cell}} \rho(\mathbf{r}) e^{-i\mathbf{Q}\cdot\mathbf{r}} dr^3, \tag{2.88}$$

and $S_{\perp u}$, $S_{\perp v}$ give the projections on the plane perpendicular to $\mathbf{Q}$ of $\mu_u \hat{\mathbf{u}}$ and $\mu_v \hat{\mathbf{v}}$, respectively, the magnetic interaction vector $S_\perp$ of the reflection at $\mathbf{Q} = \mathbf{G} + \mathbf{k}$ can be written as:

$$\mathbf{S}_\perp(\mathbf{Q})_\mathbf{k} = \frac{1}{2} F_M(\mathbf{Q})(S_{\perp u} + iS_{\perp v}). \tag{2.89}$$

To see how SNP measurements determine the structure consider the case where $\hat{\mathbf{u}}$ is perpendicular to $\mathbf{k}$ and is vertical ($\parallel \mathbf{z}$) so that $\hat{\mathbf{v}}$ is in the equatorial plane. The polarization matrices $\mathscr{P}$ which would be measured for the cases: (a) $\mathbf{Q} \parallel \hat{\mathbf{v}}$; (b) $\mathbf{Q} \perp \hat{\mathbf{v}}$ [13] and (c) would be the same as first case, but for the other chirality domain:

$$\mathscr{P}(a) = \begin{pmatrix} -(1+f) & B & B \\ 0 & A & 0 \\ 0 & 0 & -A \end{pmatrix}$$

$$\mathscr{P}(b) = \begin{pmatrix} -1 & 0 & 0 \\ 0 & -1 & 0 \\ 0 & 0 & -1 \end{pmatrix}$$

$$\mathscr{P}(c) = \begin{pmatrix} -(1+f) & -B & -B \\ 0 & A & 0 \\ 0 & 0 & -A \end{pmatrix}$$

with

$$
\begin{aligned}
A &= \frac{\mu_u^2 - \mu_v^2}{\mu_u^2 + \mu_v^2}, \\
B &= \frac{2\mu_u\mu_v}{\mu_u^2 + \mu_v^2}, \\
f &= \frac{2(1-P_x)\mu_u\mu_v}{\mu_u^2 + 2P_x\mu_u\mu_v + \mu_v^2}.
\end{aligned}
\tag{2.90}
$$

It is significant that in cases (a) and (c) $\mathscr{P}_{xx}$ (element in first row and column in matrix $\mathscr{P}$) depends upon P_x through the factor f and $|\mathscr{P}_{xx}|$ may be > 1 if $|P_x| < 1$. This arises because, as mentioned earlier, the intensity scattered by a helical structure is polarisation dependent. For (b) there is no horizontal y component of $\mathbf{S}_\perp$ and so the behaviour is the same as of a collinear structure with $\mathbf{S}_\perp \parallel \mathbf{z}$. For (a) and (c) the $\mathscr{P}_{yy}$ and $\mathscr{P}_{zz}$ components give the ellipticity of the helix; the components $\mathscr{P}_{yx}$ and $\mathscr{P}_{zx}$ have opposite signs for the two chirality domains and if the two are equally populated will average to zero leading to a diagonal polarisation matrix [13].

It should be emphasized that even full polarisation matrix cannot be used in isolation to determine the magnetic structure. A prerequisite is to determine the magnetic propagation vector, so that the polarimeter can be set to record a magnetic reflection. Once the propagation vector is known, it is possible to determine the magnetic structure uniquely even with few magnetic reflections [13].

2.2 X-rays and Laue Diffraction

One can look for Bragg peaks from a single crystal of fixed orientation by using not just monochromatic beam, but one containing wavelengths from λ_1 to λ_0. Then the Ewald sphere will expand into the region contained between the two spheres determined by $\mathbf{k}_0 = 2\pi\hat{\mathbf{n}}/\lambda_0$ and $\mathbf{k}_1 = 2\pi\hat{\mathbf{n}}/\lambda_1$, where $\hat{\mathbf{n}}$ is the fixed incident direction. Bragg peaks will be observed within this region. By making the spread in wavelengths sufficiently large, one can be sure to find some reciprocal lattice points within the region. It's not good to have this region too big, containing too many Bragg reflections which will make it less easy to read.

The Laue method is probable the best suited for determining the orientation of

a single crystal whose structure is known, which is usually the case in solid state physics. When the crystal structure is not known, there is a risk that incident direction will lie along a symmetry axis of the crystal and the pattern of spots produced by the Bragg reflected rays will have the same symmetry [57].

There are essentially two methods how can be Laue diffraction performed - transmission and back-reflection, see Fig. 2.19.

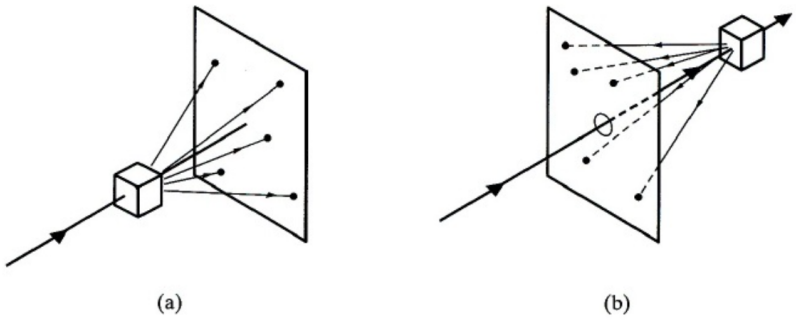

Figure 2.19 *Transmission (a) and back-reflection method (b) of performing Laue diffraction [16].*

The obtained image is linked to the structure of the crystal lattice and its symmetry properties. Usually the spots are arranged along the ellipses which are the intersection of the diffraction cones with the plane of the photographic plate [16].

2.3 SQUID

In 1911, Heike Karnerlingh Onnes observed superconductivity in mercury, the phase of material, where the electric resistance falls abruptly to the zero at critical temperature T_c. This has opened a new field for physicists and did find also practical use in devices. Very important small-scale superconducting technology was the Josephson junction, a device based on a Nobel price winning tunneling effect proposed in theory by Josephson in 1962, and observed experimentally in 1964 by Anderson and Rowell. Josephson junctions can perform as digital switching elements capable of changing states in a few picoseconds. A more common use of the Josephson junction is in a device called SQUID (Superconducting QUantum Interference Device). A SQUID consists of a closed superconducting loop including one or two Josephson junctions in the loop's current path. These thin insulating junctions interrupt superconducting loop,

but that doesn't stop the Cooper pairs of electron to quantum mechanically tunnel through the junctions. Under these conditions, a current will flow through the junction in the absence of an applied voltage (the DC Josephson effect). Because of the quantized state of the superconducting ring, and the extraordinary non-linear behaviour of the Josephson junction (see Fig. 2.20), the SQUID is capable of resolving changes in external magnetic fields that approach 10^{-15} tesla, therefore very small amount of measured material is needed. Yet can be made to operate in fields as large as 7 teslas [58].

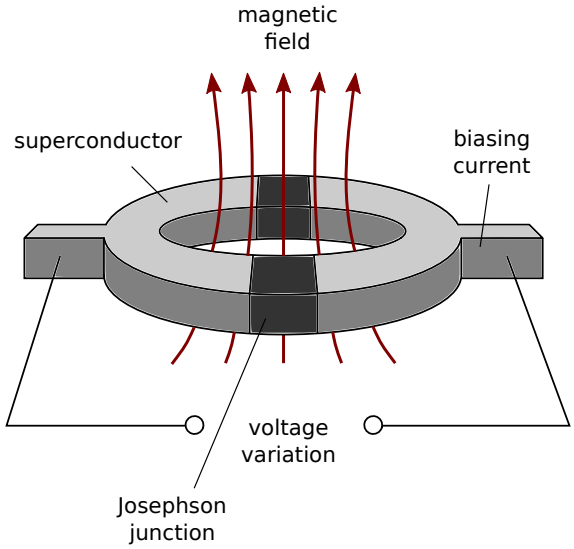

Figure 2.20 *Schematic picture of SQUID consisting of two superconductors separated by thin insulating layers to form two parallel Josephson junctions.*

The MPMS system that can be used for measurement of magnetic moment of the sample (and therefore determine its magnetization and magnetic susceptibility) consists of several parts - a superconducting magnet to generate large magnetic fields, a superconducting detection coil which couples inductively to the sample, a superconducting quantum interference device (SQUID) connected to the detection coil and a superconducting magnetic shield surrounding the SQUID. The MPMS has a temperature range from 1.9 to 400 K with a programmable applied magnetic field.

The detection principle of SQUID is that as sample moves through the system of superconducting detection coils, the magnetic moment of sample induces an electric current in coils. Detection coils are connected by superconducting wires to the SQUID. Therefore, any change of flux in detection coils will produce a change in the persistent current in the detection circuit. Since the SQUID functions as a highly linear current-to-voltage convertor [58], the changes in

detection coils produce corresponding variation in the SQUID output voltage which is proportional to the magnetic moment of the sample.

In a fully calibrated system, measurement of the voltage variations from the SQUID detector as a sample is moved through the detection coils provide a highly accurate measurements of the sample's magnetic moment. The system can be accurately calibrated using a small piece of material having a known mass and magnetic susceptibility [58].

We are not going to discuss the whole process of MPMS measurements here, however, we will point out some steps and part of data analysis. The sample is placed into plastic straw with the inside diameter of 9 mm which is maintained under low pressure with helium gas. The straw with the sample is mounted to the sample holder that is attached to the end of a rigid sample rod. The stepper-motor-controlled platform drives the sample through the detection coils in a series of discrete steps. It's been mentioned before that the SQUID is connected to the system of detection coils and as the position of sample changes, it causes a change of flux in detection coils and therefore changing the current in the superconducting circuit with SQUID. During the measurement the sample is stopped at a number of positions over the specified scan length, and at each stop, several readings of the SQUID voltage are collected and averaged. The complete scans can be repeated a number of times and the signals averaged to improve the signal-to-noise ratio [58]. The spatial (position) dependence of the ideal signal is shown in Fig. 2.21. To observe this signal requires that the sample is much smaller than the detection coil and the sample must be uniformly magnetized. If the sample is very long, it can be a problem, as its motion in the gradiometer (second order detection coils) will not be observable, since there would be no net change of the flux in the detection coil. This is the reason that a long uniform tube can be used as a sample holder.

There are two principle magnetic measurements - magnetisation as a function of temperature $\mathbf{M}(\mathrm{T})$ and magnetisation as a function of applied magnetic field $\mathbf{M}(\mathrm{H})$. By studying how the magnetisation changes, we can determine the type of magnetism and get important parameters. In terms of magnetism, materials can be sorted into several groups - paramagnetic, diamagnetic, ferromagnetic, antiferrmagnetic and ferrimagnetic materials. For the purposes of this thesis, we will discuss just paramagnetism and antiferromagnetism in more details.

Probably the simplest type of magnetism is paramagnetism. There are three key

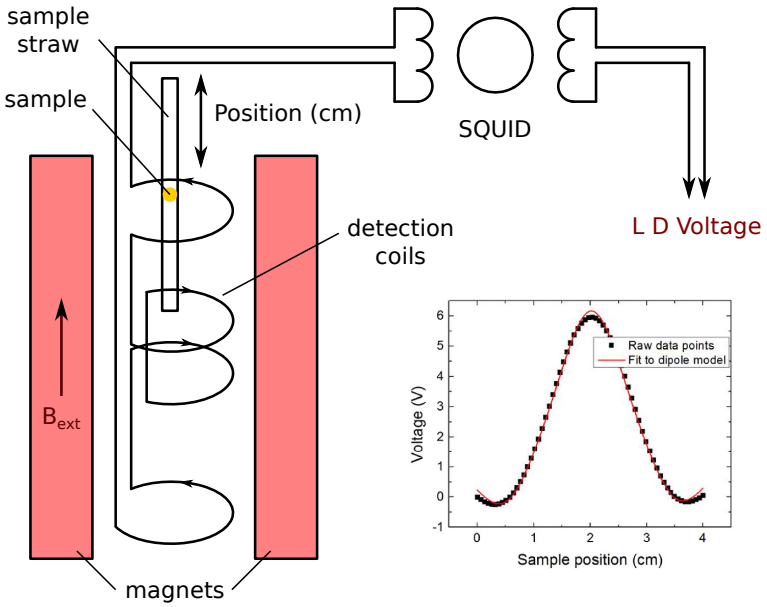

Figure 2.21 *Schematic sketch of the MPMS device. Magnetic sample moves towards detection coils, which results in change of output voltage. This voltage is plotted as function of sample position and has this very typical shape.*

features that correspond to the paramagnetic behaviour - **M** is linear function of applied magnetic field **H** (for small field, otherwise, it's not true), this linear line intersects with zero and magnetisation is reversible (so the same curve is followed if going up in field as when going down in field). Then the magnetic susceptibility χ is defined as:

$$\chi = \frac{\mathbf{M}}{\mathbf{H}} \tag{2.91}$$

Paramagnetic materials can be divided into several types, the two most important are Curie type of paramagnetism and Curie-Weiss type of paramagnetism. the Curie type of paramagnetism comes from atoms with unpaired electrons and has very characteristic temperature dependence:

$$\chi(T) = \frac{C}{T} \tag{2.92}$$

where C is the Curie constant. A plot of $1/\chi$ is very useful for characterisation of Curie paramagnetism. the slope of the curve is $1/C$ and the Curie constant is

given as:

$$C = b\mathbf{m}_{eff}^2 N \tag{2.93}$$

here, b is a universal constant, $\mathbf{m}_{eff}$ is effective magnetic moment and N is the number of magnetic atoms present. Then effective magnetic moment of magnetic atoms can be determined.

For a Curie type paramagnet, there is a force that tries to align the magnetic moments on atoms with the magnetic field ($\mathbf{m}_{eff} \cdot \mathbf{H}$). There is a constant fight between this force trying to align the moments and the heat that disrupts the alignment, leading the system to disordered state.

In the case of Curie-Weiss paramagnetism, apart from the interaction with the applied magnetic field, there is an interaction between the magnetic moments on different atoms. This exchange interaction between moments will help align moments in the same direction (driving system into ferromagnetic state) or it can help align neighboring moments in the opposite directions (driving system into antiferromagnetic state). The Curie-Weiss susceptibility is given by:

$$\chi_{cw} = \frac{C}{T - \theta} \tag{2.94}$$

and θ is called the Curie-Weiss temperature. The Curie-Weiss is related to the strength of the interaction between moments, and its sign depends on whether the interaction helps align adjacent moments in the same direction or opposite one another. Using the definition in Eq. 2.94, for $\theta > 0$ the interaction helps to align adjacent moments in the same direction (ferromagnetic interactions), and for $\theta < 0$ the interaction helps to align adjacent moments opposite each other (antiferromagnetic interactions) [58].

This paragraph will discuss antiferromagnetism, in the context of SQUID measurements, shortly. In ferromagnets, magnetic moments combine which results in enormous magnetization $\mathbf{M}$. Antiferromagnetic alignment means that magnetic moments of neighbouring atoms cancel out, resulting in very small value of $\mathbf{M}$. The $\mathbf{M}$(H) behaviour of antiferromagnet is quite different from Curie type paramagnet, since the antiferromagnetic state is a long range ordered state. The phase transition to the antiferromagnetic state is known as a Néel transition and occurs at a temperature usually denoted T_N. Above T_N an antiferromagnet is

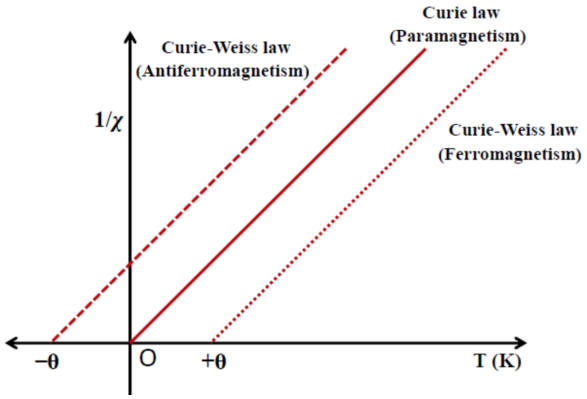

Figure 2.22 *The inverse susceptibility as a function of temperature for different systems - Curie behaviour $\chi = C/T$ and Curie-Weiss behaviour $\chi = C/(T - \theta)$. If $\theta > 0$, magnetic moments are aligned in the same direction, if $\theta < 0$ adjacent moments are aligned opposite to each other. When $\theta = 0$, the moments act completely independent of one another.*

often paramagnetic, exhibiting Curie-Weiss behaviour with $\theta < 0$. Since $\mathbf{M}$(H) curves are linear for small fields, χ remains a useful property.

Chapter 3

Crystal Growth

To date, all previous single crystals of $MnSb_2O_6$ were grown by vapour transport and high-temperature flux method. The typical reported size was varying around $2.5 \times 1.5 \times 0.5$ mm^3 [18, 59]. In ref. [18], the polycrystalline sample of $MnSb_2O_6$ was prepared using stoichiometric amount of $MnCO_4$ and Sb_2O_3. Single crystals were grown by chemical vapour transport using pre-reacted powders and a Cl_2 gas agent.

Small size of crystals limits the options of experimental probes - for example, inelastic neutron scattering, where a signal from the sample is crucial, considering the relative contribution from the background. This chapter refers about three different types of crystal growth and includes also a summary of the results. The main fraction discusses flux method, where we've done several improvements. We were able to grow crystals with average size 2-3 mm, occasionally, with size of 4-5 mm. Another two methods for preparation of $MnSb_2O_6$ - Bridgman and hydrothermal method are two new ways of preparation and to the best of our knowledge they have not been reported in scientific literature before. Hydrothermal method was proven to be successful for preparation of polycrystalline sample at temperature of 200 °C, which is significant reduction in comparison with the solid state method.

3.1 Flux Method

Flux growth is the term most commonly used to describe the growth of crystals from molten salt solvents at high temperatures. The process is analogous to crystal growth from aqueous solutions and a similar theory will apply to each case. A high temperature solvent is referred to as a flux because it permits growth to proceed at temperatures well below the melting point of the solute phase. Generally, in the growth of crystals from fluxed melts, slow cooling is required. It is also necessary to maintain the temperature at some value well above the liquid phase for roughly 12-24 hours to ensure complete dissolution of the solute. This is important since any undissolved particles will act as nucleation centres when crystallization occurs [60].

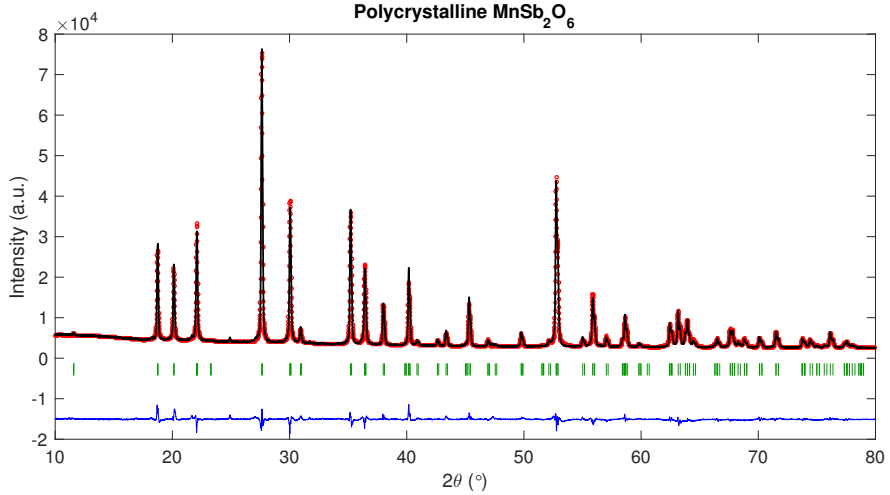

Figure 3.1 *Rietveld refinement of polycrystalline sample $MnSb_2O_6$ (χ^2 = 11.54, R_p = 15.3% and R_{wp} = 12.8%). XRD measurement was done on Bruker D2 Phaser diffractometer utilising a monochromated Cu $K_{\alpha 1,2}$ source (λ_1 = 1.5406 Å).*

The starting point was preparation of polycrystalline samples. First synthesis of polycrystalline sample repeated the procedure in paper [18], stoichiometric amounts of pure $MnCO_3$ and Sb_2O_3 were mixed together and pressed into a pellet. The pellet was heated up to 1100 ℃ . Process was repeated twice with intermediate grinding. However, following x-ray diffraction (XRD) analysis showed contribution from $Mn_2Sb_2O_7$. This problem has been solved by lowering the temperature from 1100 ℃ to 1000 ℃. Lowering temperature to 1000 ℃ helped to remove extra phase. Crystal structure was then determined by powder XRD using Bruker D2 phaser machine, Cu $K_{\alpha 1}$ radiation (λ_1=1.5406 Å). Rietveld refinement has been done with software *FullProf* and can be seen in Fig. 3.1.

Refinement just with the pcr file written for $MnSb_2O_6$ covers very well all peaks obtained from XRD experiment. We had doubts about smaller peaks at low angles (17°, 25° and 31°) until we realized interesting fact - every anode has typical wavelengths, beam consists of several characteristic wavelengths. When we deal with XRD data we usually consider wavelengths $K_{\alpha 1}$ and $K_{\alpha 2}$ (these values are also used for pcr file in *FullProf* program) - doublets that will be always present and they overlap at low angles. However, it is possible to have contribution from K_β too. It is quite rare and intensity of K_β rays is so low in comparison with K_α that we can ignore it, without bigger concerns, most of the time. In this case, when we replaced $K_{\alpha 2}$ value with K_β ($\lambda = 1.3922$ Å), we were able to refine small peaks at low angles.

Using high quality polycrystalline sample we were able to start with the single crystal growth. The polycrystalline sample is mixed with flux and heated to high temperatures where both compounds exist in liquid phase. During slow cooling process, single crystals of $MnSb_2O_6$ form, while flux is still in liquid phase as it has lower melting point. Moreover, the melting point can be lowered by adding small amount of B_2O_3.

Figure 3.2 *Sealing line in our laboratory. Gas in main horizontal tube can be pumped out by mechanical or turbo pump. Second horizontal tube works as a gas inlet. Therefore, it is possible to fill the tubes with inert gases - in our case - argon. Use of an argon atmosphere significantly improved the size of crystals. Plugs preventing quick collapse of glass walls can be seen in middle of quartz tubes.*

Starting ratios for single crystal growth were 73% of flux V_2O_5, 20% of polycrystalline sample $MnSb_2O_6$ and 7% of B_2O_3. All three compounds were finely ground, mixed together and compressed into a pellet. This pellet was then

inserted into a tube [1]. For many solid state reactions are beneficial if they run in vacuum. This can be achieved by vacuum sealing line. Air in tube is pumped out and then the tube is sealed. This way, the vacuum in tube is preserved and helps in the process of crystal growth.

For this, a customized sealing line has been built in our laboratory. The sealing line has three valves, where tubes can be inserted, see Fig. 3.2, and it is connected to the mechanical pump. The mechanical pump is the "working horse" of this system as it evacuates all impurities and small particles present in tubes. Below pressure of 1 Torr, mechanical pump is switched into the turbo pump, which can reach even lower pressures, therefore high vacuum. However, turbo pumps are very sensitive and any kind of dirt can destroy them easily. It is very important to turn turbo pump on at low pressures, when mechanical pump has done most of the work and evacuated dirt and small particles.

p (Torr)	p_{Ar} (Torr)
0.2	0.13
0.5	0.31
0.8	0.49
1	0.60
20	5.80
25	6.32
50	7.85

Table 3.1 *Table converting air pressure values p into argon pressure p_{Ar}. Black values were taken from supplementary materials for pressure gauge, blue values were interpolated, see Fig. 3.3.*

The flux method offers many possibilities for modifications in respect to get more single crystals with bigger size (as the signal from sample is stronger with greater mass), see Fig. 3.4. In this section, we will go through some modifications and their influence on size of crystals. The crucial step was use of the argon atmosphere instead of vacuum only. This idea has been taken from ref. [59] and the sealing line in our laboratory has also a gas inlet. After the quartz tubes were evacuated with the use of mechanical and turbo pumps, they were filled with an argon atmosphere up to 25 Torr. Argon was then pumped out by mechanical pump to the value 800 mTorr. After this, the turbo pump was turned on and argon was pumped down to the value 200 mTorr. This process was repeated three times (at least) and then tubes were sealed with a propane/oxygen torch. It is

[1] in our very first attempts, we tried alternative when powder was placed into a crucible and then into tube, but with no success

important to keep in mind that the pressure gauge installed on our sealing line is calibrated for measuring air pressure. Displayed values must be converted if we want to know the real value of argon pressure, see conversion Tab. 3.1.

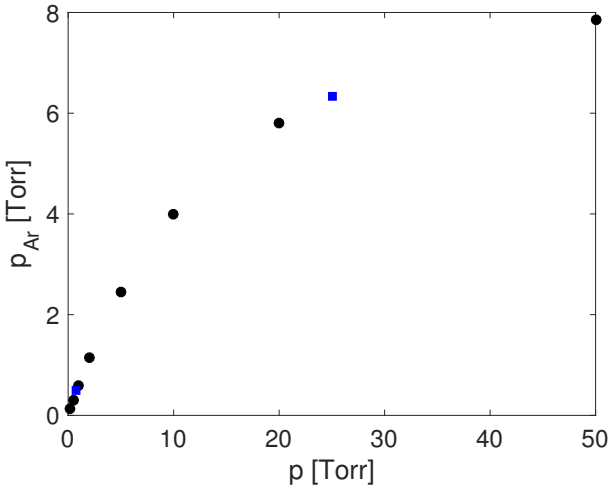

Figure 3.3 *Graphical illustration of air (p) and argon pressure (p_{Ar}) values. Blue data points were interpolated.*

The sealing process is one of the most difficult as the temperature of flame is crucial - weak flame does not melt the glass fast enough (and there is risk that glass might break), but too strong flame can heat unevenly, which results in popping of the tube and loss of vacuum. It does require a bit of training to get the flame temperature right. As this can slow down mass production of crystals, we've started to use glass plugs that prevented the glass walls from collapsing too quickly.

In last stage of the flux method growth, sealed quartz tubes were put into a box furnace. we tried several variations of heating routine, changing these parameters:

- time of dwelling at the soak temperature,
- different ratios of reactants,
- change of cooling rate.

This can be seen in Appendix D in more details. Dwelling longer at 1000 ℃ helped to grow bigger crystals (24 hours instead of 5 hours). The slower cooling rate 1 ℃/h did not affect size of the crystals. Changing ratios of reactants did not have noticeable effect on size neither. The use of an argon atmosphere came

as a biggest improvement with standard size of crystals $3 \times 2.5 \times 1$ mm^3 and bigger. Extra adjustment of sealing line with an argon inlet and possibility to use mechanical and also turbo pump was important step in the process of growing bigger single crystals.

The best heating routine was determined as following - quartz were sealed with argon atmosphere and put into the box furnace. Temperature was ramped to 1000 ℃, where it was left for 24 hours then slowly cooled down to 700 ℃ with a ramping rate 2 ℃/h. At this stage crystals had been formed during 24 h period, then the whole system was cooled down to room temperature as fast as possible.

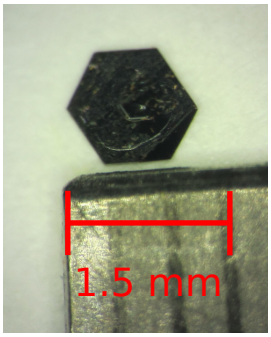

Figure 3.4 *Early stage of our $MnSb_2O_6$ single crystal attempts, flux method. Single crystals have characteristic hexagonal shape and grow in the form of platelets.*

After tubes run through the heating routine and were cooled down to the room temperature, characteristic black single crystals with hexagonal shape could be seen, immersed in flux. There are several options how to fish crystals out. One of them includes the use of acids, but this method can damage crystals. In our approach, we dissolved V_2O_5 flux in water using an ultrasonic bath. Crystals stay solid and can be fished out by filtration (Büchner funnel) combined with use of tweezers.

Improved flux method was crucial for mass production of crystals - 1.3 g of single crystals were prepared and aligned on an aluminium holder for inelastic experiment on TAS instrument MACS, see Fig. 4.20. Nice hexagonal shape of crystals helped with alignment, Laue diffractometer had been used in more questionable cases (reflections for certain scattering plane were simulated in program *SingleCrystal*). To achieve this, I sealed approximately 150 tubes over the time of 6 months.

3.2 Bridgman Method

Almost all elemental materials and some compounds can be crystallized from the melt. It does not come as a surprise that slow directional solidification of the melt is a long established method for preparation of single crystals.

The pioneering work by Bridgman was directed toward the growth of single crystals of mainly low-melting point metals required for the high pressure studies [61]. His first paper [62] described the growth of tungsten, antimony, bismuth, tellurium, cadmium, zinc and tin. Bridgman used a vertically mounted tube electric furnace to melt the sample and lowered the ampoule containing the sample through it. In general, the Bridgman technique is characterized by the translation of the crucible/ampoule containing the melt the temperature gradient in a vertical furnace. However, a horizontal configuration is also possible and does have some advantages (holds steady equilibrium between phases better).

The tube furnace used for growth can be programmed in the way that it does have several zones with different time of dwelling at certain temperature. The preparation of the sample was same as for flux method. Two tubes were filled with polycrystalline sample and flux, see Fig. 3.5, the next two contained same mixture pressed into pellets.

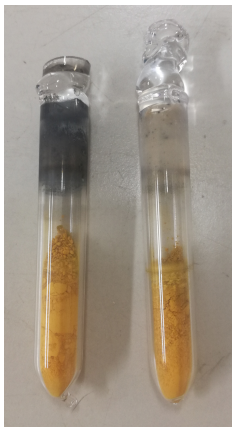

Figure 3.5 *Two tubes filled with powder for Bridgman method. Another two tubes contained powder compressed into the pellets.*

Tubes were sealed under the vacuum (argon atmosphere has not been tried for this method). Using a program specially developed by PhD student Nathan Giles-Donovan (University of Glasgow) for programming the tube furnace, temperature gradient 100 ℃ was set for 3 zones (Fig.3.6) . Later a check of the gradient showed that the furnace was able too keep just gradient 50 ℃ for higher temperatures.

Size of crystals was around $1.5 \times 1 \times 0.5$ mm^3.

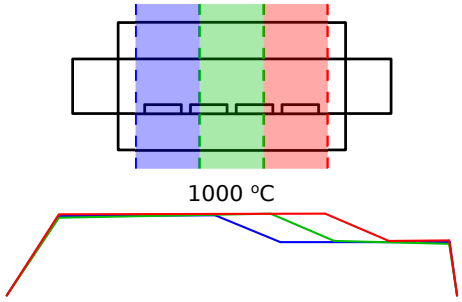

Figure 3.6 *Scheme of 3 zones with temperature gradient in the tube furnace. Image shows illustrative placement of four quarts tubes in crucibles - two with powder and two with pellets.*

Several facts in this method can be improved for obtaining bigger crystals. Controlled temperature gradient of Bridgman method can be used for growth of bigger and thicker crystals. Considering that $MnSb_2O_6$ single crystals usually grow in form of thin platelets, thicker crystals might provide opportunity to measure some material characteristics that it is not possible to investigate if sample is too thin.

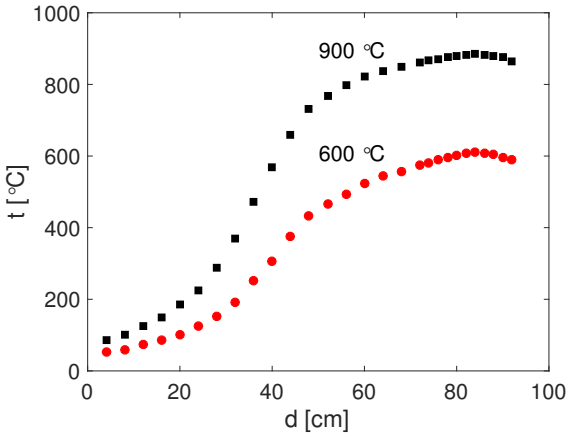

Figure 3.7 *Temperature profile of the tube furnace, Bridgman method. Two temperatures 600° and 900 °C were measured as function of distance d from coldest zone (open end) to the hottest zone (sealed) of tube furnace.*

Temperature gradient was investigated in short measurement for 600 °C and 900 °C, see Fig.3.7). From graph, one can see that zones get hotter quicker for higher temperatures. One possible solution would be to think about more efficient cooling.

3.3 Hydrothermal Method

The term *hydrothermal* was first introduced by British geologist Sir Roderick Murchison. At that time it had purely geological meaning and described the action of water at elevated temperature and pressures in the earth's crust and leading to the formation of various rocks and minerals. However, in recent years, the hydrothermal technique has been most popular, garnering interest from scientists of different disciplines, particularly since the 1990s [63]. It is well known that largest single crystal formed in nature (beryl crystal of > 1000 kg) and the largest single crystal created by man in one experimental run (quartz crystal of nearly 5000 kg at the Tokyo Communication Co. Ltd. Japan) are both of hydrothermal origin. The hydrothermal method is very important for its technological efficiency in developing bigger, purer and dislocation-free single crystals [64]. Nowadays, the term *hydrothermal* refers to any homogeneous or heterogeneous reaction in the presence of solvents above room temperature and greater than 1 atm in a closed system.

Hydrothermal technique uses pressure as an extra element that can be applied in process of crystal growth. Polycrystalline sample was prepared by mixing stoichiometric amounts of pure $MnCl_2$ and Sb_2O_3 with total mass of 0.5 g. Powder was added into Parr Acid Digestion Vessel 4744 (45 ml), see Fig. 3.8 .

Figure 3.8 *Bombs used for the hydrothermal growth. Each of metal bombs contains a plastic vessel (type - Parr Acid Digestion Vessel 4744).*

After adding 15 ml of distilled water, vessel was closed (screw-shaped parts were greased with lubricant with additional MoS_2 for easier opening) and put into oven. It was heated up to 200 ℃ (saturation pressure of water at 200 ℃ is 225

psi or 1.6 MPa, Parr tables), where it has been left for 48 hours and then cool down to room temperature at rate 50 ℃/h. Yellow polycrystalline powder (Fig. 3.9) was extracted by filtration using Büchner funnel. Remaining liquid in vessel seems to be strongly acidic, which was measured with digital pH meter.

Figure 3.9 *Polycrystalline powder of $MnSb_2O_6$ prepared by hydrothermal method.*

Structure has been checked by powder XRD, see Fig. 3.10. Even though the current refinement can be improved, Bragg reflections do appear at expected positions for $MnSb_2O_6$ structure. Work on this refinement is ongoing. Multiple annealing of the polycrystalline sample might help to improve the profile too. Another way might be also future investigation of reactants and water ratios.

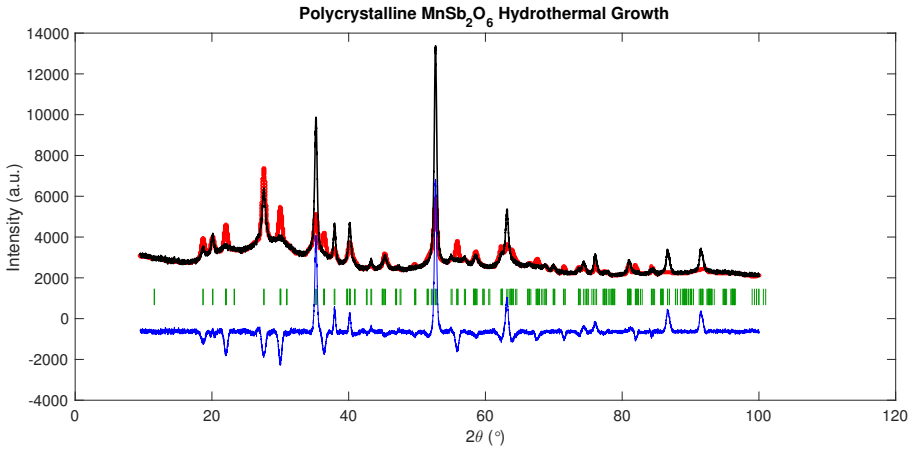

Figure 3.10 *Current Rietveld refinement of polycrystalline sample $MnSb_2O_6$ prepared by hydrothermal method (χ^2 = 42.53, R_p = 87.1% and R_{wp} = 74.5%). XRD measurement was done on Bruker D2 Phaser diffractometer utilising a monochromated Cu $K_{\alpha 1,2}$ source (λ_1 = 1.5406 Å). This refinement can be improved in future, however, Bragg reflections do appear at expected positions.*

Nevertheless, peak positions show that this might be a new way of polycrystalline synthesis that has not been reported yet. Hydrothermal method requires much

lower temperature, just 200 ℃. Whereas solid state method requires temperature as high as 1000 ℃.

We've made several attempts to growth single crystals too. Details of all attempts can be seen in the general table in Appendix E. First, the dwelling time at 200 ℃ was changed to 120 hours. Bombs were cooled down with slow rate 1 ℃/h and then left in oven for 48 hours. However, no single crystals were found after opening the hydrothermal bomb. More detailed study with use of laboratory microscope showed small black grains in polycrystalline powder, see Fig. 3.11. Unfortunately, the mass and size of these grains were so small that it wasn't possible to apply the XRD analysis.

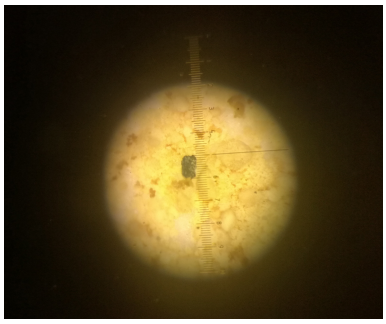

Figure 3.11 *Small black grains visible in polycrystalline powder under the microscope.*

Again, the method offers room for modifications. We tried higher dwelling temperature 225 ℃ (higher temperature means higher pressures in the hydrothermal bomb), seed crystals (can work as nucleation centres and help to start the growth) and hydrochlorid acid HCl, but without any significant improvement. For certain reactions, acids can shift balance of the reaction towards products. Another aspect for use of HCl is the fact that Sb_2O_3 is only slightly soluble in water. It does dissolve in dilute H_2SO_4 or dilute HCl (0.1 moles HCl/kg H_2O). 0.12 ml of 36% HCl was added into 14.88 ml of distilled water in the Parr Vessel 4744 (total volume - 45 ml), making total volume of 15 ml.

Chapter 4

$MnSb_2O_6$

It is undeniable that there is a connection between structure and properties of materials. Therefore, scientists are interested in studying exotic compounds with interactions between magnetic, electronic and structural degrees of freedom that can be promising for the industrial use. $MnSb_2O_6$ is predicted to be multiferroic with a unique ferroelectric switching mechanism. Its structure is a specific one as there is structural and magnetic chirality present at the same time. Moreover, the crystal structure of $MnSb_2O_6$ is non-centrosymmetric, which can bring interactions as Dzyaloshinskii-Moriya (DM) exchange into the play. We can use Skyrmion phase discovery as an example that focused attention on interactions between magnetism and crystal symmetries.

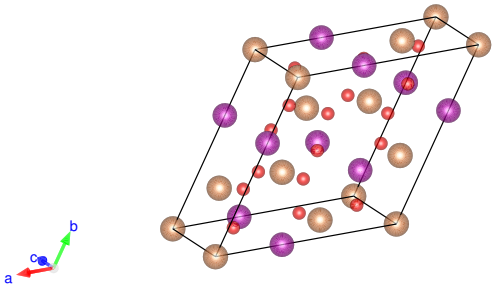

Figure 4.1 *Crystal structure of $MnSb_2O_6$ (atoms - Mn purple, Sb brown, O red).*

Before we dive more into studies that have been done on $MnSb_2O_6$, it will be very helpful to introduce another compound - langasite $Ba_3NbFe_3Si_2O_{14}$ [17, 65]. Both compounds have several common properties - they crystallize in the same

space group ($P321$), and have similar building blocks and exchange pathways. The Heisenberg exchange energies for both compounds are comparable, however, these energies are stabilized by different anisotropies. In both compounds is strong coupling between magnetic and structural chirality. How do they differ from each other? The main difference is that iron langasite belongs to group of materials with helical magnetic structure, see Fig. 4.2 , and magnetic moments in $MnSb_2O_6$ rotate like cycloids, rather than helices. It is still not clear why cycloidal magnetic structure is more preferable over a helix. One possible explanation is that single ion-anisotropy favours an out-of-plane spin rotation.

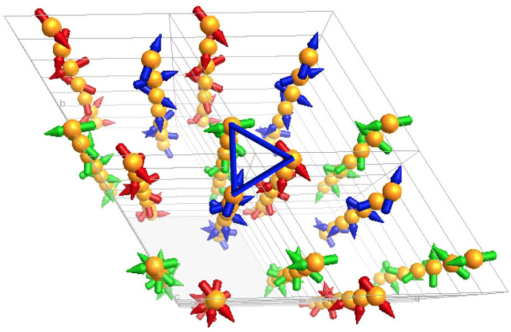

Figure 4.2 *Perspective view of the magnetic structure of iron langasite $Ba_3NbFe_3Si_2O_{14}$ with different colours for the three Bravais lattices [17]*

In the hexagonal unit cell of $MnSb_2O_6$, manganese is the only magnetic ion, and adopts a valance of 2+ giving the spin $S = 5/2$, and orbitally quenched moment $L \simeq 0$ [18]. According to previous magnetization studies [66], the magnetic interactions occur via super-exchange pathways (Mn-O-O-Mn). Magnetization data showed short-range magnetic correlations bellow $\sim$ 200 K and long-range antiferromagnetic order below $T_N = 12.5$ K [66]. Neutron powder diffraction investigations in [66] showed that manganese magnetic moments had three dimensional Heisenberg character below T_N.

The previous neutron powder diffraction results [59] showed that below $T_N = 12.5$ K (antiferromagnetic order) the manganese magnetic moments had three-dimensional Heisenberg character and rotate according to the incommensurate propagation vector $\mathbf{k} = (0.015, 0.015, 0.183)$ in a plane orthogonal to the a axis - an approximately cycloidal magnetic structure. However, the more recent neutron powder diffraction data [18] collected at 20 and 6 K showed a number of reflections evident only below T_N, which could be described with propagation vector $\mathbf{k}_{exp} = (0, 0, 0.1820)$. A calculations based upon symmetric Heisenberg exchange was performed for the three manganese sites in the unit cell. The

propagation vector $\mathbf{k}_{calc} = (k_x, k_y, k_z)$ was left free to very and minimum energy solution was found corresponding to $\mathbf{k}_{calc}$ = (0, 0, 0.166), which is in very good agreement with experimental results obtained by Johnson et al. [18].

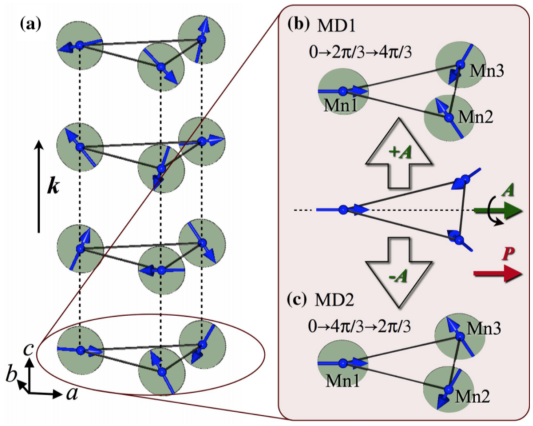

Figure 4.3 *The magnetic structure of $MnSb_2O_6$ (a) shown in single manganese triangle in the ab plane (the circular spin rotation envelopes are drawn in grey). (b) and (c) show two magnetic domains, MD1 and MD2 [18].*

The proposed cycloidal magnetic structure can be seen in Fig. 4.3. - three cycloids in the unit cell have the same polarity defined as $\mathbf{P}_m$. This arrangement could lead to net ferroelectric polarization perpendicular to c, which can be seen in many other cycloidal magnets [67]. From neutron powder diffraction data, phases between the cycloids on the three symmetry equivalent Mn atoms are either $0 \rightarrow (2/3)\ \pi \rightarrow (4/3)\ \pi$ or $0 \rightarrow (4/3)\ \pi \rightarrow (2/3)\ \pi$. Single crystal neutron diffraction experiment performed at D10 (ILL, France) did give additional information that wasn't possible to obtain from the powder data. There are two important parameters - cycloidal polarity and triangular spin arrangement. To capture these configurations, it is good to introduce vector $\mathbf{A}$:

$$\mathbf{A} = \mathbf{k} \times \mathbf{V}, \tag{4.1}$$

where $\mathbf{V}$ is known as the vector chirality defined as:

$$\mathbf{V} = \frac{1}{3}(\mathbf{S}_1 \times \mathbf{S}_2 + \mathbf{S}_2 \times \mathbf{S}_3 + \mathbf{S}_3 \times \mathbf{S}_1), \tag{4.2}$$

and $\mathbf{S}_1$, $\mathbf{S}_2$ and $\mathbf{S}_3$ are spins on the same triangle [18].

Here again, comes the striking similarity with iron langasite, for which diffraction

intensities were sensitive to the product of two scalar quantities - helicity ϵ_H (along c axis) and scalar triangular chirality ϵ_T [17]. It is important to underline that these two are scalars in the case of iron langasite and vectors for the case of $MnSb_2O_6$.

Moreover, single domain refinement showed that, unlike iron langasite that is a recemic mixture [17, 65], $MnSb_2O_6$ crystal [18] was a nonracemic mixture of two chiral structural domains (MD1 and MD2) in ratio 0.8:0.2.

Returning back to iron langasite - magnetization measurements were performed on a single crystal from 2 to 300 K under magnetic fields up to 10 T. The isotherms of the magnetization M are linear and independent of the applied field orientation, parallel $\parallel$ or perpendicular $\perp$ to the c axis (down to the ordering transition temperature). No significant anisotropy is thus detected in the paramagnetic phase as expected for an Fe^{3+} ion with a spin $S = 5/2$ and no orbital contribution [17]. In ref. [17], authors have considered a set of five exchange interactions parameters in the Heisenberg Hamiltonian - J_1-J_5 [17, 65]. For $MnSb_2O_6$, it is necessary to introduce a further two exchange pathways (J_6 and J_7), because larger manganese plaquettes give greater significance to the interactions associated with J_2 triangles. As it was mentioned several times, $MnSb_2O_6$ compound is a chiral crystal structure, which means that there are left- and right-handed diagonal exchange pathways. The left-handed interactions, J_5 and J_7 are weak compared to the right-handed interactions, J_3 and J_6. The inversion symmetry operator transforms one chiral domain into the other, also interchanges $J_3(J_6)$ with $J_5(J_7)$ [18].

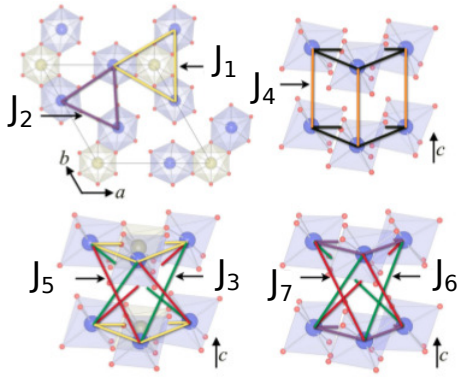

Figure 4.4 *Exchange pathways in $MnSb_2O_6$ structure [18]*

It is an interesting question why anisotropy favours the cycloidal magnetic structure in $MnSb_2O_6$ over a helix. Usually, the rotating magnetic structures are stabilized in non-centrosymmetric crystals (like MnSi [68, 69]) via the

Dzyaloshinskii-Moriya (DM) interactions, where energy may be gained through canting spins according to a vector **D** [18]:

$$\mathcal{H}_{DM} = \mathbf{D} \cdot \mathbf{S}_1 \times \mathbf{S}_2. \tag{4.3}$$

It is important to point out that when **D** lies perpendicular to a threefold rotation axis, all vectors will cancel, giving no energy gain. Johnson et al. [18] conclude that in $MnSb_2O_6$ single-ion anisotropy favour an out of plane spin rotation, breaking the three-fold symmetry.

The magnetic structure of $MnSb_2O_6$ is composed of spin cycloids that rotate in a plane along the c axis. This structure breaks the three-fold symmetry of the $P321$ paramagnetic space group. Therefore, magnetic domains must form - if the spin rotation plane contains a two-fold axis (i.e. $\mathbf{P}_m \parallel a$ axis) - three magnetic domains will form. If $\mathbf{P}_m$ lies in a more general in-plane direction, then six magnetic domains are form as can be seen in Fig. 4.5.

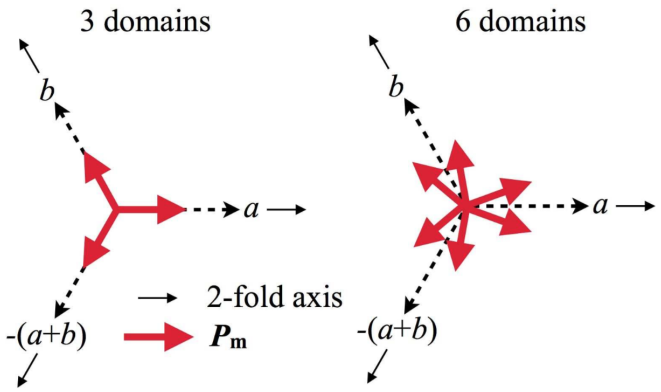

Figure 4.5 *Scheme of the two possible $\boldsymbol{P}_m$ domain configurations [18].*

Authors discuss three domains case, although, the analysis hold also for more complex case of six domains. Each magnetic domain has a magnetic polarity $\mathbf{P}_m$, which couples to the macroscopic polarization **P**. The three magnetic domains are therefore exactly equivalent to three polar domains, where the three directions of **P** are also related by three-fold symmetry [18]. Here comes the concept of special switching mechanism for $MnSb_2O_6$. Three magnetic domains, see Fig. 4.6, are represented by three colours - red, blue and green. If an external electric field **E** (greater than the ferroelectric coercive field) is applied parallel to one of the **P** domains, a single domain will form. Surprisingly, $\mathbf{P}_m$ and $-\mathbf{P}_m$ are not the same which can be seen easily using Fig. 4.6 - reversing the electric field will create a

mixed domain state with two polarities (blue and green). This domain switching mechanism can be investigated better by polarized neutrons or synchrotron x-ray experiments, where the scattering cross section is sensitive to the plane of rotation of the spins in the illuminated domains.

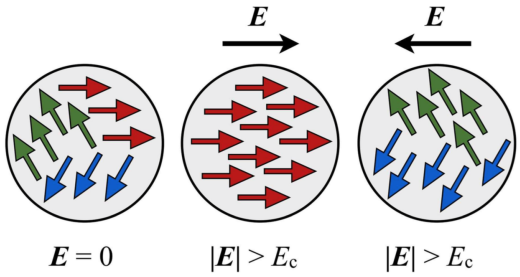

Figure 4.6 *Scheme of switching mechanism for three magnetic domains under applied electric field* $\boldsymbol{E}$ *[18].*

Same article states that a single structural enantiomer of $MnSb_2O_6$ should be ferroelectric, due to the presence of a coupling term $\lambda \mathbf{P}_m \cdot \mathbf{P}$ in the phenomenological free energy expression. The electrical polarization $\mathbf{P}$ is either parallel or antiparallel to $\mathbf{P}_m$, depending on the sign of coupling constant λ. In their DFT calculations [70], they find an electric polarization of 2 μ C m^{-2}, originating in the DM interaction, and oriented perpendicular to the c axis. Unfortunately, as the single crystal grow as a platelets, it is impossible to measure such a small, in-plane ferroelectric polarization reliably.

4.1 DC Magnetic Susceptibility Measurements

Two single crystals of $MnSb_2O_6$ were used for measurements of magnetic properties using MPMS (Magnetic Property Measurement System) device from Quantum Design. Crystals have been grown by flux method in form of thin platelets with dimensions of 3×3 mm^2 and characteristic hexagonal shape.

Temperature and field dependence of magnetisation $\mathbf{M}$ have been probed in two directions - with magnetic field $\mathbf{H} \parallel \mathbf{c}$ axis (first crystal with the mass $m_{\parallel} = 0.0021$ g) and with field $\perp$ to c axis (second crystal with the mass $m_{\perp} = 0.0087$ g). Measurements were performed with the step of 0.5 K (low temperature region, from 5 K to 40 K) and 5 K steps spaced linearly from 5 K to 300 K. From collected data, the molar susceptibility has been calculated using relation $\chi_m = \mathbf{M}/(n\mathbf{H})$, where n stands for number of moles

calculated from the known mass. Comparison for both directions can be seen in Fig. 4.7. DC susceptibility measurements for both directions indicate Curie-Weiss paramagnetic behaviour at high temperatures and undergoes an antiferromagnetic transition at 12.5 K, which is a result comparable with values in literature [18, 66].

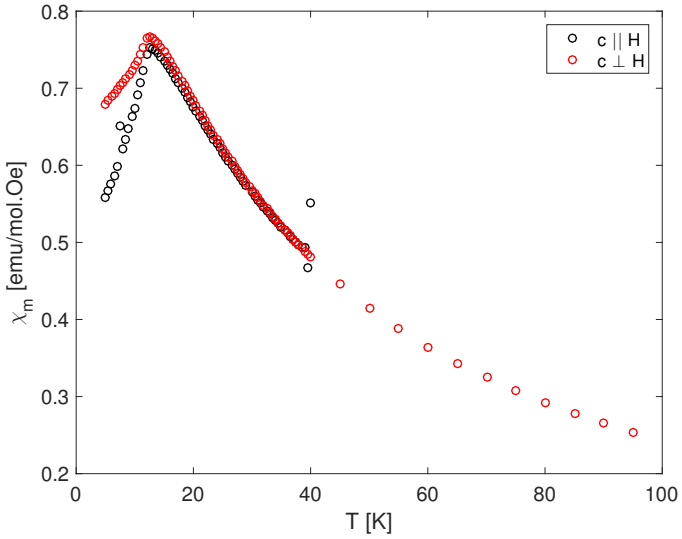

Figure 4.7 *The molar susceptibility χ_m as a function of the temperature for magnetic field $H \parallel$ and $\perp$ to the c axis ($c \equiv c*$).*

Fig. 4.8 presents a fit of the high temperature data (from 100 K to 300 K) to the Curie-Weiss law, yielding Curie-Weiss temperatures θ_{cw} of -6.1 K for $H \perp c$ axis.

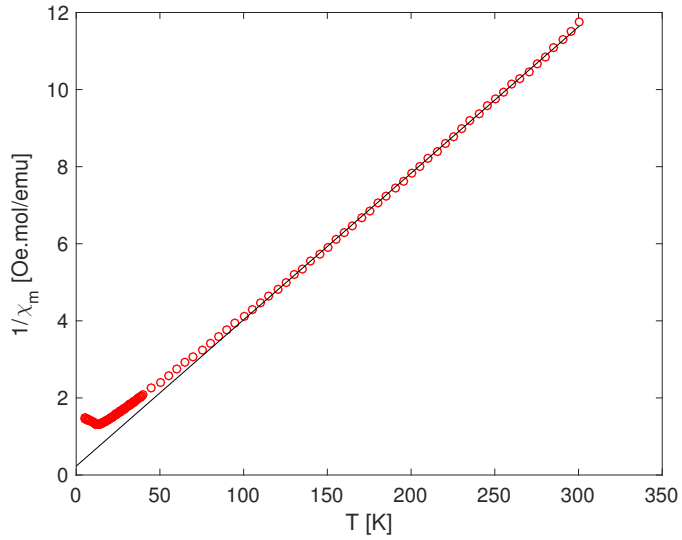

Figure 4.8 *Inverse susceptibility fitted by Curie-Weiss law for $H \perp c$ axis. θ_{cw} was estimated as -6.1 K.*

This value is smaller than previously reported θ_{cw} of -19.6 K for paramagnetic region of the powder sample [18]. It is important to underline that this value very much depends on temperature cut off - Curie-Weiss fit holds for higher temperatures. The Curie-Weiss constant for $H \parallel c$ axis hasn't been estimated as we measured magnetization $\mathbf{M}$ for this direction only for low temperatures.

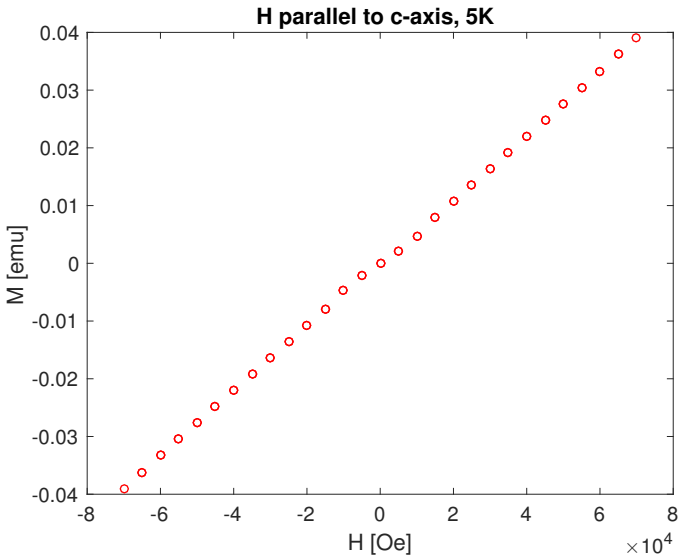

Figure 4.9 *Field dependence of magnetization for $H \parallel c$ axis.*

Last figure, Fig. 4.9 , shows field dependence of the magnetization. Linear behaviour has been observed for $H \perp c$ case too (T = 5 K).

4.2 Elastic Experiment - BT4

Our very first experiment using neutrons was an elastic experiment using the triple-axis spectrometer BT4 (NIST, USA). The centre of focus was the investigation of the wave vector. For this purpose, we were aiming to collect data sets for two different temperatures - bellow and above T_N = 12.5 K [18].

Single crystal of $MnSb_2O_6$ was aligned in the H0L scattering plane and secured on the aluminium holder (using small amount of hydrogen-free Fomblin oil and covered with aluminium foil). The experimental configuration was the following - PG002 filters were placed before the monochromator and after the sample respectively. Therefore, energy was fixed at 14.7 meV (λ = 2.4 Å). Two 80′ collimators were used, before and after the sample, see Fig. 4.10. Collimators consist of a number of thin equidistant sheets of a neutron absorbing material.

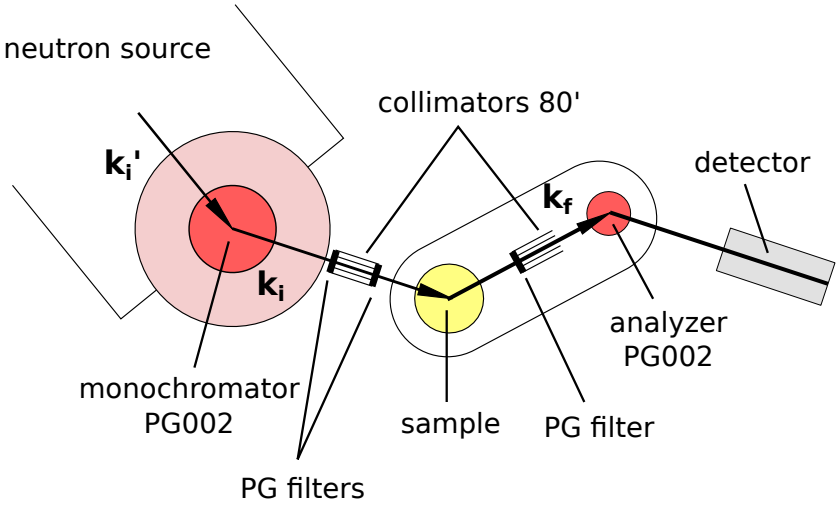

Figure 4.10 *Scheme of elastic experiment ($k_i = k_f$) on TAS instrument BT4. The energy was fixed at 14.7 meV (PG002).*

They are converging the beam of neutrons. Of course, this does come with a cost - some neutrons are absorbed and therefore the intensity of neutron beam will decrease. It is important to use reasonable collimation, so intensity is not too low. Collimators can range from 10′ to 120′, where 60′ equals to 1°.

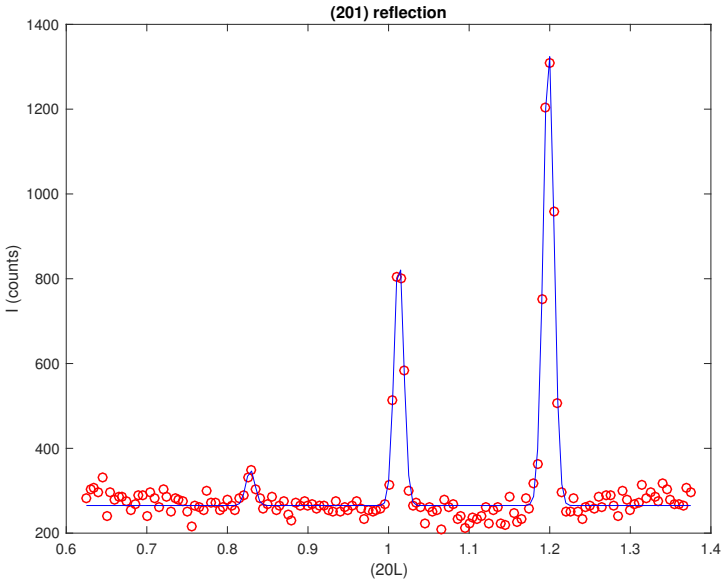

Figure 4.11 *Scan near (2, 0, 1) nuclear Bragg peak. Two magnetic reflections can be seen on sides of nuclear peak. MATLAB code with Gaussian fit has been written for all collected data.*

We started with low temperature measurement T < T_N and measured reflections around several nuclear peaks. A scan near the (0, 0, 1) nuclear Bragg peak showed no magnetic peaks (propagation vector should lie along [001], which

is consistent with previous studies [18]). The most intense incommensurate magnetic peaks were found near (2, 0, 0), (1, 0, 1) and (1, 0, 0), see Table 4.1 for more details. Scans near (0, 0, 2), (1, 0, 2) and (3, 0, 1) nuclear reflections have been contaminated with scattering from aluminium - let's not forget that sample was mounted on aluminium holder, also many parts of instrument and containers are made from aluminium. Expected positions of aluminium reflections for wavelength $\lambda = 2.4$ Å have been calculated and matched extra peaks that has occured in our data.

Unfortunately, we run into problem with motors and couldn't fully finish our experiment. Therefore, we limit our conclusions to qualitative analysis. From the collected data, it is possible to see that the direction of magnetic moments is both - within the *ab* plane and along *c*. Experiment also proved the high quality of our single crystals (single domain crystal).

Q (r.l.u.)			I (a.u.)	file
H	K	L		
0	0	1.000	0	Magpk001.bt4
1	0	-0.182	2350	Magpk002.bt4
1	0	0.825	2500	Magpk003.bt4
2	0	-0.183	150	Magpk004.bt4
2	0	0.188	2800	
2	0	-0.828	100	Magpk005.bt4
2	0	1.199	1150	
3	0	-0.181	250	Magpk006.bt4

Table 4.1 *All magnetic reflections collected on BT4 instrument, T = 3 K. Peaks were fitted with Gaussian function to obtain more detailed parameters.*

Measurement of more Bragg reflections would be sensible in the future.

4.3 Measurement in Horizontal Magnetic Field - RITA-II

The magnetic structure of $MnSb_2O_6$ has been determined as incommensurate cycloidal structure with wave vector $\mathbf{k}$ = (0, 0, 0.1820). Although, it is much more difficult to manipulate antiferromagnetically (AFM) ordered spins than ferromagnetical (FM) order, it is possible to drive AFM to FM state with use of magnetic field that it is big enough to overcome these interactions. RITA-II is

a triple axis spectrometer for cold neutrons at SINQ (PSI, Switzerland). It is a highly flexible instrument with multi-blade analyzers (see Fig. 4.12) that can be easily adjusted to the user's requirements. Furthermore, it offers possibility to use many extreme sample environments - variety of different magnets with the dilution refrigerator insert.

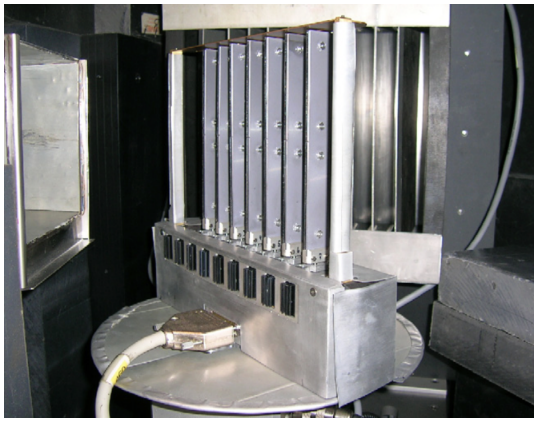

Figure 4.12 *Monochromatic dispersive mode of RITA-II with multi-blade analysers [19].*

Now, there are several facts that one needs to keep in mind before performing experiment in magnetic field - what is the propagation vector of magnetic moments in the sample and the very essential fact about neutrons that they are sensitive only to perpendicular part of the magnetisation. We know that magnetic moments propagate along *c*-axis. Our first aim was align magnetic field along this direction and see effect of field on magnetic reflections. Considering the fact that $MnSb_2O_6$ grows in a form of hexagonal platelets, it is necessary to use horizontal magnetic field for the following neutron experiment.

Moreover, tracking the behaviour of magnetic moments as a function of magnetic field and temperature, one can apply the theory of critical exponents. Theory of critical exponents offers additional information about studied system as - dimensionality, dimensionality of the order parameter, range of forces present or what type of model can be used for the best description. We will discuss the theory of critical exponents more in the section 4.3.3.

4.3.1 Alignment - MORPHEUS

Even though the single crystal on the mount is usually aligned before neutron experiment, it is good to check alignment before performing the main measurement.

SINQ facility offers their users the MORPHEUS diffractometer.

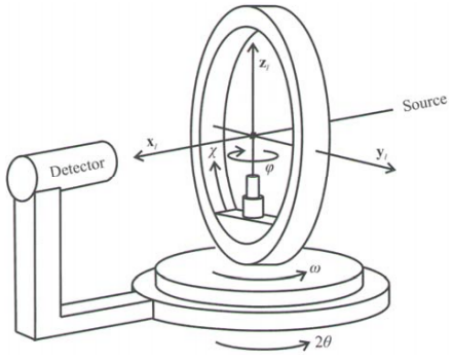

Figure 4.13 *Schematic of 4-circle diffractometer. Four circles correspond to the four angles - 2θ, χ, φ and ω.*

MORPHEUS is a versatille two axis neutron diffractometer. Single crystal diffractometers use either 3- or 4-circle goniometers. MORPHEUS has 4-circle goniometers which enable to adjust 4 angles - 2θ, χ, φ and ω. Using wavelength $\lambda = 4.99$ Å in program *PowderCell*, we've checked strong reflections for $MnSb_2O_6$. Program can calculate what 2θ angle corresponds to certain reflection. This value is then used as angle A4 for instrument and changes position of the detector. It also defines angle ω that rotates the big vertical circle with sample. Many diffraction instruments do have this angle defined as A3 and A3 = A4/2. Remaining angles χ and φ are for final adjustment, i.e. tilt of the single crystal.

Single crystal of $MnSb_2O_6$ was secured on aluminium mount and oriented in the (H, 0, L) scattering plane.

4.3.2 Experimental Details

Experiment has been carried on the instrument RITA-II using a horizontal field cryomagnet MA7 (max. field 6.8 T), see Fig. 4.14.

The initial alignment of our sample with respect to the magnetic field **H** can be seen in Fig. 4.15 . From the previous elastic neutron experiment on the BT4 instrument, we did know about magnetic reflections with highest intensities. Unlike measurements in vertical magnetic field, the horizontal magnetic field experiments are more limited. The horizontal high field cryomagnet MA7 has a restricted neutron access. There are four windows of 45° each and four dark angles - these are areas where it is not possible to measure incoming or scattered

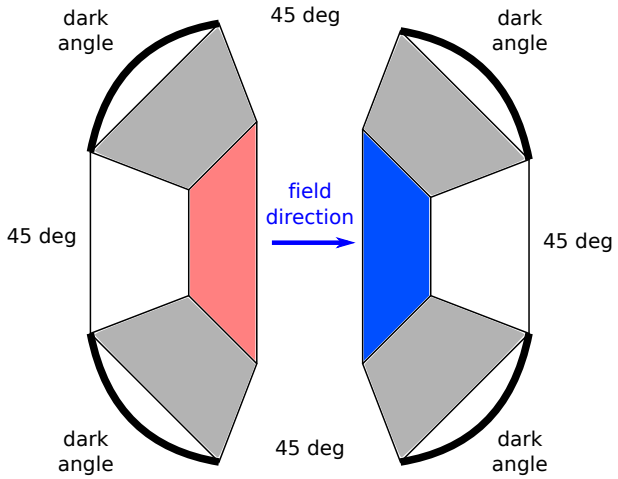

Figure 4.14 *Scheme of horizontal field cryomagnet MA7. Red part represents the left coil, blue part the right coil. The horizontal field cryomagnet has a restricted neutron access - these areas are depicted as 'dark angles'.*

neutrons. Therefore it is necessary to check which reflections are accessible. This can be done using MATLAB simulation that it is provided during the experiment.

Considering all restrictions, the magnetic reflection $\mathbf{Q} = (1, 0, 0.816)$ was chosen. Lambda was set to $\lambda = 4.9$ Å. A series of elastic scans ($E_i = E_f = 3.4$ meV) for different temperatures (from 1.7 K to 13 K) and fields (from 0 T to 5 T) have been performed. We tested two directions of the magnetic field - first one was aligned along c-axis ($c \equiv c*$), the second perpendicular to the c-axis, as can be seen in Fig. 4.15.

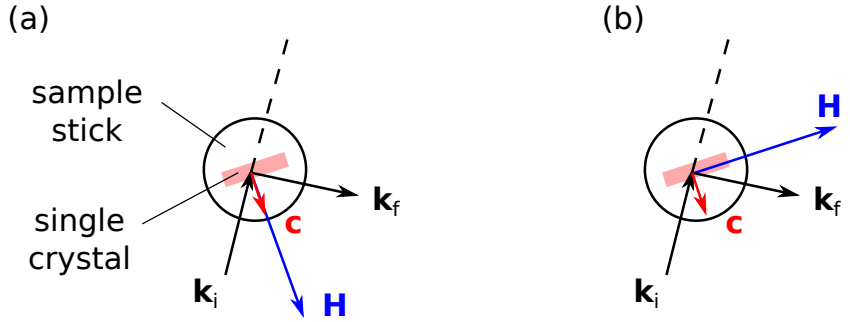

Figure 4.15 *Alignment of the magnetic in respect to the c-axis, view from above. Most measurements have been done for (a) configuration. Configuration (b) ($H \perp c$) was used at the end of experiment and showed constant behaviour of intensity as a function of the magnetic field.*

Temperature dependence measurements of (1, 0, 0.816) reflection confirmed the transition temperature to be $T_N = 12$ K. The analysis including critical exponents

will be discussed in subsection 4.3.3 in more details.

The intensity of the (1, 0, 0.816) reflection has been tracked as a function of magnetic field too. Results for different temperatures can be seen in Fig. 4.16 and show quadratic behaviour that relates to Landau theory. We can see that applied magnetic field is changing intensity of the magnetic reflection and therefore orientation of magnetic moments within sample. This is metamagnetic transition known as spin flop and it is very characteristic for AFM materials.

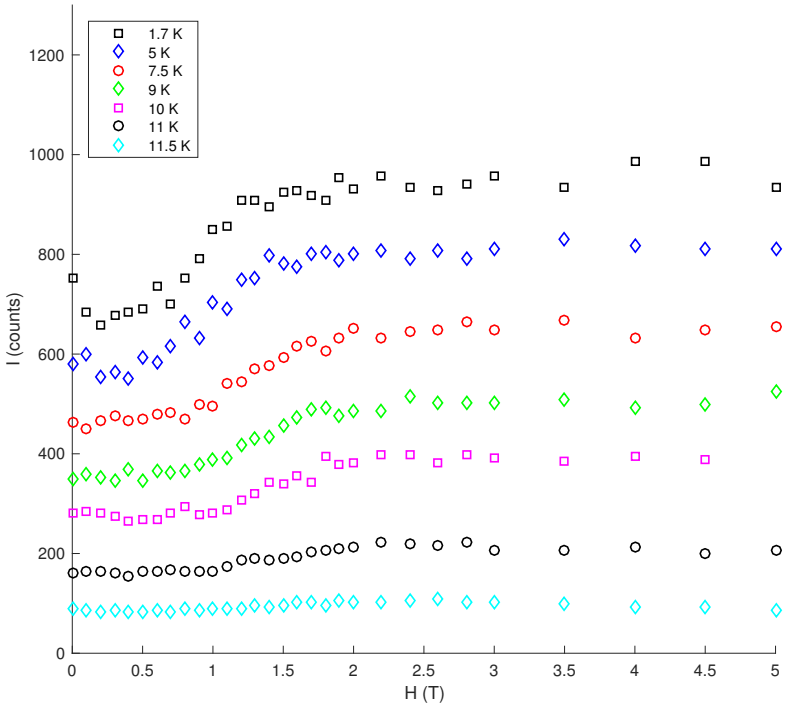

Figure 4.16 *Mapping of intensity of magnetic reflection (1, 0, 0.816) as a function of magnetic field H. Low temperature show quadratic dependence of the order parameter. This disappears as we move closer to the transition temperature $T_N \sim 12$ K. We conclude that spin flop transition is present in magnetic fields up to 5 T.*

Same as it is for a case of susceptibility, if a material has an easy axes of magnetization, it is energetically favourable for an antiferromagnet to align its magnetization perpendicular to the external field. If the anisotropy is not too big, then magnetic field can cause a rotation of the magnetic moments away from the easy axis. However, material is still largely an antiferromagnet. This type of transition is called spin flop.

Measurement of the nuclear peak **Q**=(2, 0, 1) has been done with and without

applied magnetic field with no significant change. Scan of different **Q** values (1, 0, -0.185) and (2, 0, 0.188) did not show the same behaviour and therefore highlighted the importance of (1, 0, 1) plane.

One of the last measurements included different alignment of magnetic field to the c-axis, see Fig.4.15 (b). Magnetic field was rotated by 90° and magnetic reflection (1, 0, 0.816) was scanned again. This time, intensity stayed constant for temperatures 1.7, 5 and 10 K. Therefore, experiment pointed out the importance of magnetic field direction in respect to the c-axis. All measured data with details can be found in Appendix G.

4.3.3 Critical Exponents

Before diving into the analysis of our data, it might be quite useful to do short resume here.

Spatial dimensionality and dimensionality of the order parameter are two terms often mentioned in discussions about the critical exponent analysis. We will use notation d for spatial dimensionality and D for the dimensionality of the order parameter. The term spatial dimensionality d is largely a consequence of the crystallography. Most systems correspond to the three dimensional case $d = 3$. However, there are cases of structures when interactions are particularly strong within the planes and weak between the planes - for example - graphene is considered to be two-dimensional material $d = 2$ [1], as it is a single layer of graphite [2].

Dimensionality of the order parameter refers to the anisotropy. From now on, we are going to work with magnetic systems, therefore the order parameter will refer to the ordered magnetic moments. If $D = 3$, the Hamiltonian can be described by the Heisenberg model:

$$\mathcal{H} = \sum_n \sum_i J_i (S_n^x S_{n+1}^x + S_n^y S_{n+1}^y + S_n^z S_{n+1}^z), \tag{4.4}$$

where spin is three-dimensional vector. This model applies to isotropic magnetic materials, which means that $J_z \sim J_x \sim J_y$.

[1] However, one can find papers that disagree with this classification.

[2] Graphite has strong covalent bonds within the sheets but weak Van der Waals interactions between the planes, which explains it is high cleavage along the layers.

For the case of $D = 2$, spins are arranged in effective sheets or planes, therefore, the exchange interactions within the plane are much stronger than between planes. Hamiltonian has a form of XY model:

$$\mathcal{H} = -\sum_{n}\sum_{i} J_i(S_n^x S_{n+1}^x + S_n^y S_{n+1}^y), \tag{4.5}$$

and $J_z \ll J_x \sim J_y$.

Finally, for $D = 1$, spins are distributed in a chain like arrangement with a single dominant exchange interaction, $J_z \gg J_x \sim J_y$. Such a case can be described by Ising model of Hamiltonian:

$$\mathcal{H} = -\sum_{n}\sum_{i} J_i(S_n^z S_{n+1}^z). \tag{4.6}$$

It is important to realise that d and D doesn't need to be the same. Another fact is that D can not be greater than d. For example, we can have system with spatial dimensionality $d = 2$ and the dimensionality of the order parameter could be $D = 2$ or $D = 1$.

The relative simplicity of Hamiltonians above was major driving force in study of magnetic transitions, providing opportunity to study some fundamental properties of critical phenomena. One aspect of critical phenomena includes the hypothesis of universality. The hypothesis of universality states for a continuous phase transitions, critical exponents can be calculated to describe the transition and these exponents depend on the spatial dimensionality d and the dimensionality of the order parameter D, irrelevant to the details of the microscopic interactions in the system, no matter if quantum or classical. The former is heavily dependent on the crystal structure, whilst the latter is a measure of the anisotropy in exchange Hamiltonian. The critical exponents describe the behaviour of the variables of state as one approaches a transition.

We know that $MnSb_2O_6$ system exists in paramagnetic phase above T_N, where $\langle\phi\rangle = 0$ as it's disordered phase. However, below T_N, situation does change and $\langle\phi\rangle \neq 0$. The magnetic Bragg peak intensity I is proportional to the square of the sublattice magnetization. Near the critical temperature it should vary as a

power law in reduced temperature with exponent 2β:

$$I \propto A|T - T_N|^{2\beta}, \tag{4.7}$$

where A is the constant and β is the critical exponent corresponding to the order parameter, see Tab. 4.2. In order to determine β, we have measured magnetic peak intensities as a function of temperature for $\mathbf{Q}$ = (1, 0, 0.816).

Exponent	Definition	Mean field	Ising d=3	X-Y d=3	Heisenberg d=3
α	C $\propto$ (T - T_c)$^{-\alpha}$	0	0.11	-0.01	-0.12
β	$\langle\phi\rangle \propto$ (T_c - T)$^{\beta}$	0.5	0.33	0.35	0.37
γ	$\chi \propto$ (T - T_c)$^{-\gamma}$	1	1.24	1.32	1.39
ν	$\xi \propto$ (T - T_c)$^{-\nu}$	0.5	0.63	0.67	0.78

Table 4.2 *Approximate values of critical exponents for various models (for d=3 systems), where C is specific heat, $\langle\phi\rangle$ is order parameter, χ is susceptibility and ξ is correlation length [30].*

In this chapter, we've already discussed that critical exponents can often provide additional information about the system. β has characteristic value for particular cases that differ in the spatial dimensionality, the dimensionality of order parameter or the best fitting model.

H (T)	exponent β
0	0.293
1	0.329
1.75	0.307
2.5	0.290
5	0.298

Table 4.3 *Values of exponent β for all measured magnetic fields H.*

The β exponent was approximately the same for all fields and had a value ~ 0.3 (T_N = 11.8 K), see Tab. 4.3. Systematic error was estimated around 20%. It should be emphasized that the theory of critical exponents was developed for region near the critical point and therefore only data from 6 K to 11.8 K temperature region have been considered. This value was surprising as langasite is very similar to $MnSb_2O_6$, but does belong to specific group of 2D triangular X-Y magnets for which β has characteristic value of 0.25 [65]. Similar results have been measured in $CsMnBr_3$ with $\beta = 0.21$ [71] and $CsVCl_3$ with $\beta = 0.25$ [72].

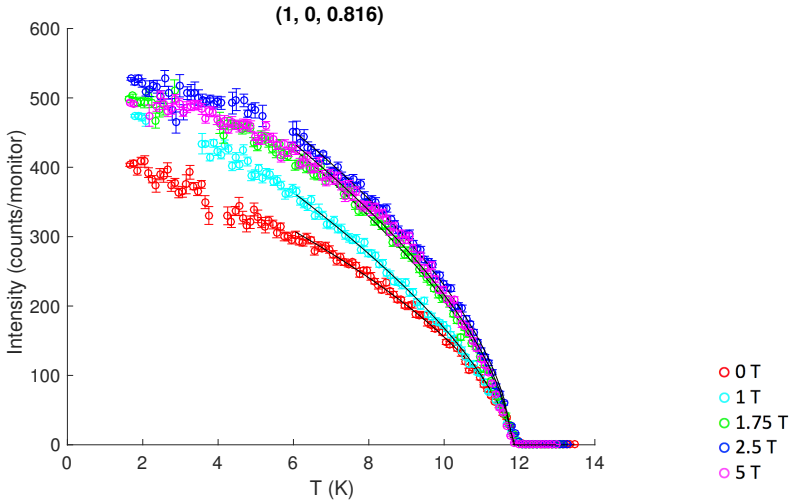

Figure 4.17 *Intensity of magnetic reflection as function of temperature. Black lines are fits following 4.7. For all five magnetic fields, the critical exponent β has value $\sim$ 0.3, which points to three dimensional character and Heisenberg model.*

We can conclude that our data didn't confirm affiliation of $MnSb_2O_6$ to specific universality class for 2D triangular X-Y magnets. Instead, it shows that system is 3D and could be described by Heisenberg model.

One might object that obtained value of critical exponent can be influenced by resolution of the instrument. For this reason, we decided to repeat the measurement of (1, 0, 0.816) magnetic Bragg peak on instrument BT4 (NIST, USA) with wavelength $\lambda = 2.4$ Å. We will discuss the results in next section.

4.4 Complementary Elastic Experiment - BT4

Similarly to our first elastic experiment on BT4 instrument, a single crystal of $MnSb_2O_6$ was aligned in the H0L scattering plane and secured on the aluminium holder. PG002 filters were placed before the monochromator and after the sample respectively, fixing the energy at 14.7 meV ($\lambda = 2.4$ Å).

The intensity of the (1, 0, 0.816) magnetic Bragg peak was measured as function of temperature with two scans - one along H direction, another along L direction - with no significant difference for value of β.

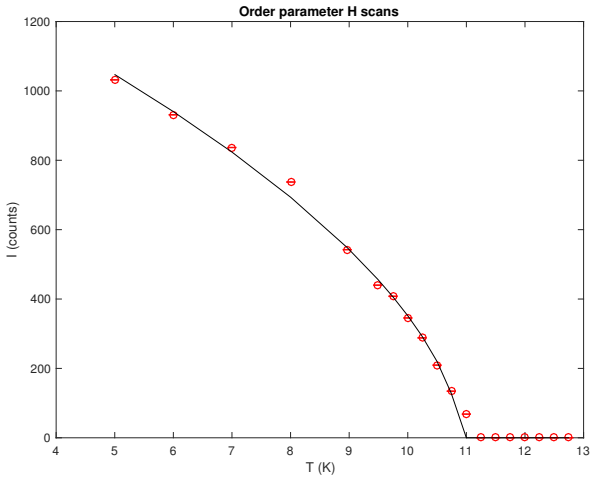

Figure 4.18 *Scan of (1, 0, 0.816) magnetic Bragg peak along H direction. Fitted value of β was $\sim$ 0.3. Data were measured on instrument BT4 (NIST, USA), λ = 2.4 Å. The difference between T_N measured on RITA-II and BT4 instrument is caused by different cooling systems used for measurements and precisions of its sensors, see following section for more details.*

4.4.1 Critical Exponents

The same procedure of fitting the intensity as function of temperature (Eq. 4.7) was applied for BT4 data too. Obtained value for β was $\sim$ 0.3.

Therefore, we can conclude that the resolution of instrument does not influence the value of critical exponent β and despite many similarities with iron langasite and other compounds, $MnSb_2O_6$ does not belong to specific universality class of 2D triangular magnets using X-Y model.

The difference between T_N measured on RITA-II (T_N = 11.8 K) and BT4 (T_N = 11 K) is caused by different cooling systems used for measurements (RITA-II - cryomagnet MA7; BT4 - Closed Cycle Refrigerator, CCR). With cryomegnet MA7, we were able to get very precise value for temperature T_N. The Closed Cycle Refrigerators (CCR) is using helium gas as the refrigerant that is driven through the 4-step cycle, see Fig. 4.19. The lowest temperature for this experiment was T = 5 K. Temperature values obtained from temperature sensors of CCR might be slightly off and this is where the difference between these two measurements comes in.

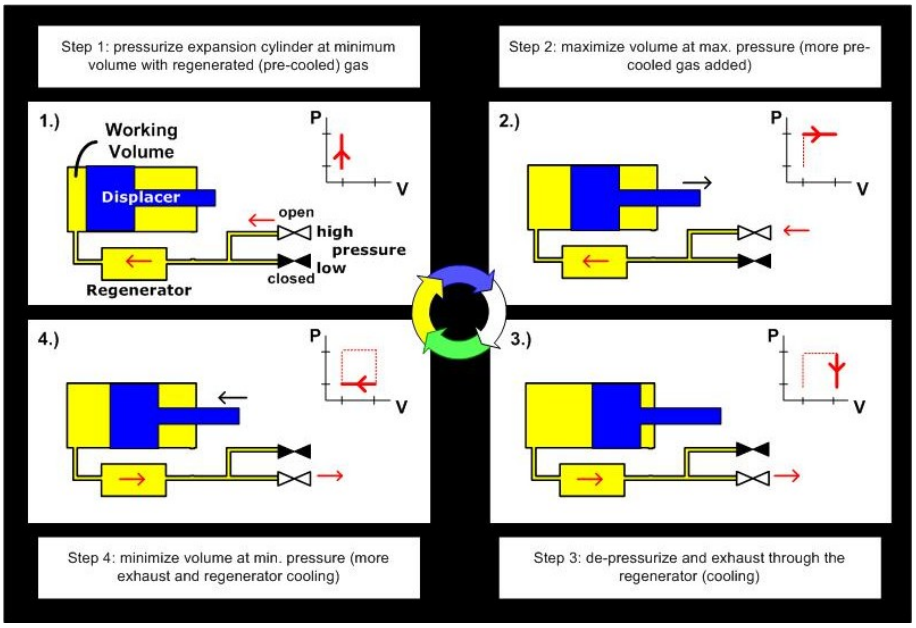

Figure 4.19 *The Closed Cycle Refrigerator (CCR) works in 4-step cycle [20].*

4.5 Inelastic experiment - MACS

According to conventional wisdom a quasiparticle is presumed well-defined until proven not to be. The textbook picture of magnons as long-lived excitations weakly interacting with each other works very well for many magnetic materials. Neverthless, in a number of recently studied spin systems magnons neither interact weakly nor remain well-defined even at zero temperature. This is due to the so-called spontaneous quasiparticle decay, a spectacular quantum-mechanical many-body effect [73].

Excitations in magnetic system can lead to creation of wave that propagates through the spins on magnetic atoms - this process is also know as single magnon excitation, or spin wave. Whereas, the theory of single magnon excitations is well known, the same can not be said about multimagnon excitations. The fundamental contribution to the theory of spin waves in magnetic insulators was made by Anderson [74], Kubo [75] and Dyson [76, 77]. These articles and following studies developed a comprehensive picture of spin waves in conventional quantum ferromagnets and antiferromagnets [78–81]. The inelastic neutron scattering spectroscopy invented in 1950s quickly became a major experimental method of investigating spin waves and other magnetic excitations in solids. Usually, the magnon-magnon interactions play a minor role at low temperatures (in the classical picture, the interaction between magnons is related to the amplitude

of spin precession and can become arbitrarily small as the amplitude decreases [73]). Therefore, the conventional picture of magnons as weakly interacting quasiparticles is fulfilled. Recently, there has been a growing body of theoretical and experimental studies that this picture is not always correct.

In fact, there are several studies and classes for magnon-magnon interactions. A nice overview with references can be find in [73]. The spin wave theory works well even for spin 1/2 systems - magnets with collinear spin structures have magnetic excitations that are weakly interacting. On the other hand, multi-magnon interactions start to be important for systems where magnetic structure becomes noncollinear. This can have multiple reasons, for example - spin canting in an applied magnetic field or presence of competing interactions in frustrated antiferromagnets.

$MnSb_2O_6$ is a classical system with spin $S = 5/2$ and a noncollinear magnetic structure in triangular lattice. Initial experiment on the polycrystalline powder (done before start of my PhD) showed promising broader excitation at approximately double value of energy transfer for single magnon excitation (spin wave). This is the value expected for appearance of multimagnon excitation. Our goal was to investigate this interesting phenomena for a single crystal case. The experiment was carried out on the MACS triple-axis spectrometer (NIST, USA).

4.5.1 Preparation and Sample Mounting

Single crystals of $MnSb_2O_6$ were synthesized using a flux technique.

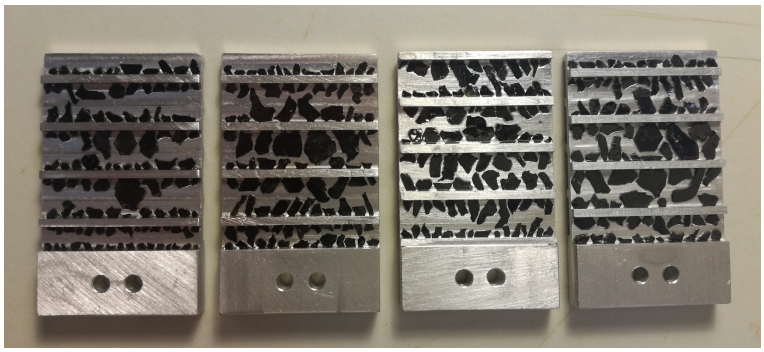

Figure 4.20 *Four aluminium plates with aligned single crystals of $MnSb_2O_6$ with total mass of 1.3 g. Both sides of each aluminium plate have been used.*

Even though the size of crystals have been improved by using our new technique,

the size was still not sufficient for inelastic experiment. One needs to keep in mind that contribution from background is large and therefore, the signal from sample must be strong. Ideally, the crystal for inelastic experiment is big enough to obtain strong signal. However, there are cases when size of crystals can not be improved any more by known techniques. In this case, one can do a little trick - align many small single crystals. I aligned several arrays of 1.3 g of single crystals in (H, H, L) scattering plane, see Fig. 4.20.

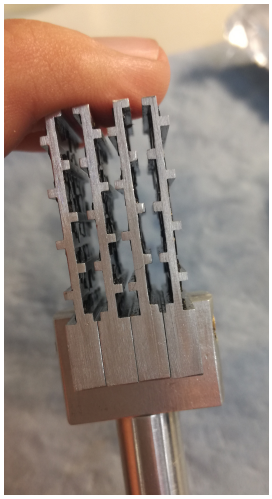

Figure 4.21 *Four aluminium plates on a sample holder. On closer inspection, aligned single crystals of $MnSb_2O_6$. For higher security, plates and holder were covered with the aluminium foil.*

Alignment by the eye was possible due to the distinctive hexagonal shape of single crystals. More disputable crystals were checked with Laue diffractometer and compared with pattern generated in the program *SingleCystal*.

The individual single crystals were secured to the plates using hydrogen-free Fomblin oil. All four plates (covered with single crystals from both sides) were stacked behind each other as can be seen in Fig. 4.21 and covered with aluminium foil that was secured with aluminium wire. Obviously, considering the alignment and the mounting, it is not possible to distinguish between $\pm c$.

4.5.2 Mosaicity - ALF experiment

Before inelastic experiments at NIST in USA, we decided to check the alignment of our single crystals using diffractometer ALF (ISIS, UK). This crystal alignment facility has a goniometer stack and a ^{3}He bank of position sensitive detectors - those can be used to check quality of single crystals or multi-crystal arrays.

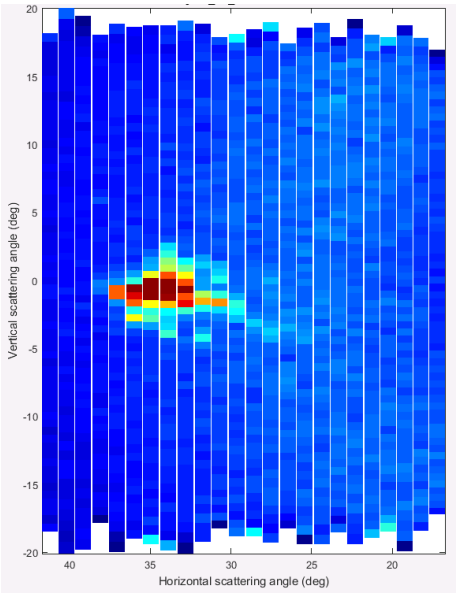

Figure 4.22 *Check of mosaicity for* $\sim$ *120 mg of* $MnSb_2O_6$ *single crystals. Bank of position sensitive detectors on instrument ALF showed mosaicity* $\sim 2°$.

We focused our attention on (1, 0, 2) reflection that we did see around $\sim$ 5 Å. We've made cut from 4.6 Å to 4.9 Å. Thanks to bank of detectors, ALF can show horizontal and also vertical scattering angle for certain reflections. This way, it is possible to see what is the mosaicity of alignment. ALF experiment was performed before main inelastic experiments at NIST and therefore, just certain fraction of single crystals was aligned on the aluminium mount at that time (with mass $\sim$ 120 mg).

In Fig. 4.22, we can see that alignment was well made with mosaicity $\sim 2°$. The ^{3}He position sensitive detectors give user an option to align single crystal (or multi arrays) easily. For comparison, user that is aligning sample on 4-circle diffractometer MORPHEUS has to work with 4 angles and especially adjusting χ and φ can be very tedious. In the case of misalignment, one needs to trace good rotation with several steps backwards. Moreover, MORPHEUS offers option to plot rocking curve only, whereas ALF with position detectors can show clear picture of specific reflections in respect to the scattering angles. On the other hand, investment into bank of ^{3}He position sensitive detectors is much higher than for simple detector of MORPHEUS diffractometer and for big research facilities with many various instruments, the improvement of detectors for diffractometers (designated for alignment of the sample) is often not top priority on the list.

4.5.3 Set Up and Investigation of Multimagnons

The MACS spectrometer was used as it can cover a broad range in momentum space. Cooled filters of beryllium and beryllium oxide were placed before the monochromator and after the sample respectively. With final energy fixed at $E_f = 3.7$ meV, we mapped energy transfers from $\Delta E = 0.2$ meV to $\Delta E = 4$ meV. Slices for different energy transfers can be seen in Fig. 4.24. Well defined excitations are fine example of localized magnetism. The excitation with high intensity at low energy transfers is a propagating spin wave. For higher energy transfers $\Delta E = 1.7$ meV, intensity falls dramatically and creates continuous areas.

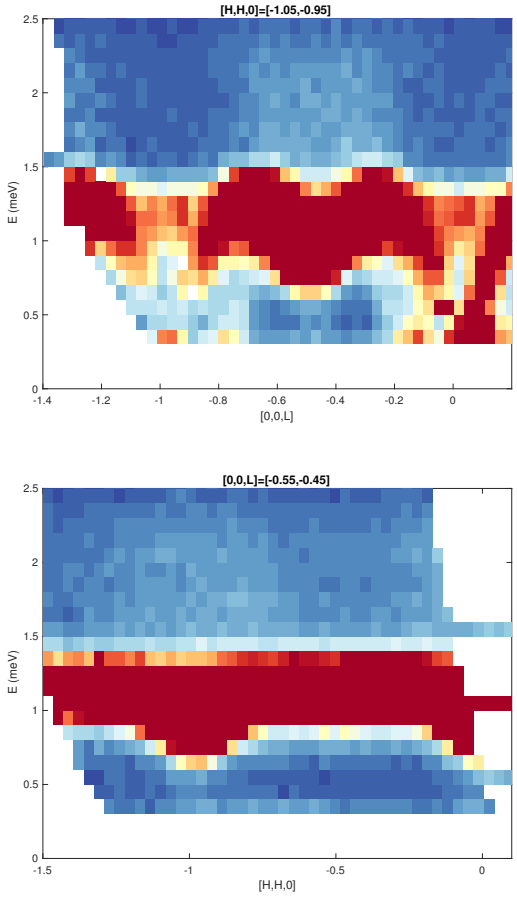

Figure 4.23 *Constant Q cuts for (H, H, 0) and (0, 0, L) scattering plane. Dispersion in both scattering planes points to the three dimensional character of this system.*

This is exactly the picture that one would expect for presence of multimagnon excitations. Two particle excitations form a continuum of states in a certain energy interval. One-magnon events occur in the spin correlations *transverse* to the ordered spin direction. Two magnon scattering events can be described in

terms of *longitudinal* fluctuations.

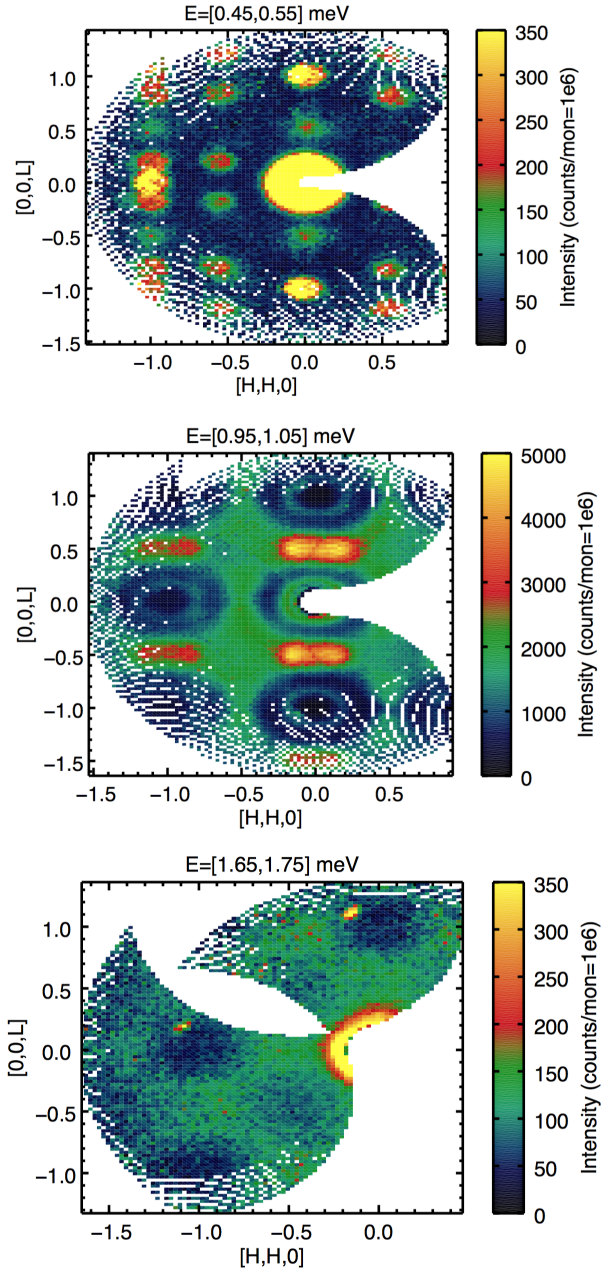

Figure 4.24 *Constant energy slices of inelastic data collected on cold triple axis spectrometer MACS. data were collected from $\Delta E = 0.2$ meV to $\Delta E = 4$ meV with final energy fixed at $E_f = 3.7$ meV.*

An understanding of how the scattering cross section is distributed between the elastic, one- and two-magnon channels can be obtained by comparing the integrated scattered intensities. Generally the two-magnon scattering starts at the higher energy of $2\times\hbar\omega_0$ than one-magnon spectrum, as it can be seen in Fig. 4.23. Sharp and intense one-magnon excitation occurs $\sim$ 1 meV, broad and less

intense two-magnon excitation can be seen above that, $\sim$ 2 meV. The intensity of the two-magnon scattering is strongest for low energies and wave vectors near the antiferromagnetic zone center.

I wrote MATLAB code that can fit both parts of multimagnon excitations, see Fig. 4.25. Parameters extracted this way can be used in following analysis. The next step would be theoretical model that can describe our system.

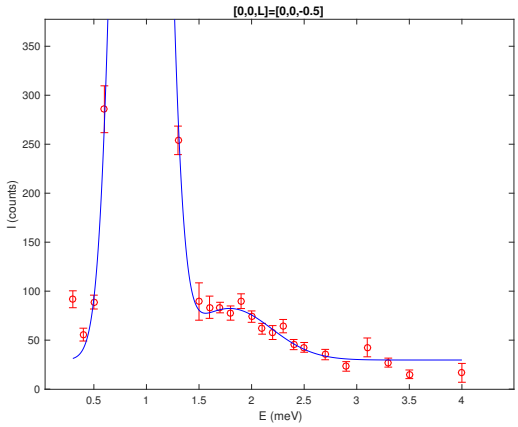

Figure 4.25 *Constant Q cut through (0, 0, L) scattering plane. Sharp intense peak represents the spin wave, the broad peak with lower intensity is multimagnon continuum.*

We can confirm the presence of multimagnon excitations in incommesurate magnetic system $MnSb_2O_6$ with spin $S = 5/2$. Further analysis can bring interesting results and be beneficial for discussions about multimagnon processes. Similar results have been measured for two-dimensional $S = 5/2$ Heisenberg antiferromagnet Rb_2MnF_4 [82].

4.6 Investigation of Chirality by Polarised Neutrons - D3

Another interesting property of this material is the coexistence of structural (see Fig. 4.27) and magnetic chirality. Chirality is the geometric property of an object according to which it exists in two distinct enantiomorphic states that are images of each other by space inversion but cannot be brought into coincidence by direct Euclidian isometry, namely, spatial proper rotation and translation, eventually combined with time reversal [83]. Structural and magnetic chiralities

are found to coexist in a small group of materials in which they produce intriguing phenomenologies.

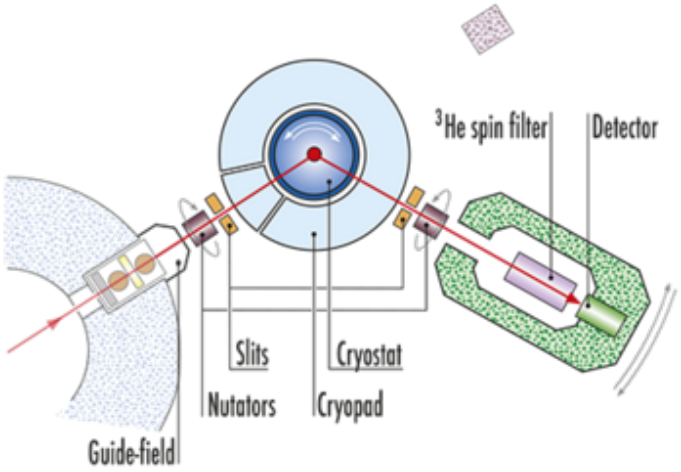

Figure 4.26 *Scheme of D3 instrument with zero-field set-up [21].*

The D3 instrument (ILL, France) is a polarised hot neutron diffractometer, see Fig. 4.26. It offers several set ups - for purposes of our work - a zero-field set up for spherical neutron polarimetry with CRYOPAD has been used. The zero-field configuration is ideal for the investigation of non-collinear magnetic structures. The CRYOgenic Polarisation Analysis Device (CRYOPAD) allow the user to do very precise measurements of neutron spin rotations occuring in the scattering process. The diffractometer uses readily exchangeable CoFe and Heusler polarising monochromators. and wavelength change is an automatic on-line operation. The scattered polarisation is analysed with a ^{3}He neutron spin filter.

In order to investigate structural and magnetic chirality present in $MnSb_2O_6$ single crystal (size $\sim$ 2 mm), we measured several reflections. Whereas the magnetic chirality likely occurs in helical or cycloidal magnetic structures, the presence of structural chirality might raise more questions. Let us discuss the magnetic chirality first. The magnetic moment distribution $\mathbf{m}(\mathbf{r})$ in a sinusoidally modulated structure with propagation vector $\mathbf{k}$ can be written as:

$$\mathbf{m}(\mathbf{r}) = \sum_{\mathbf{l}} \rho(\mathbf{r}-\mathbf{l})(\hat{\mathbf{u}}\mu_u \cos(\mathbf{l}\cdot\mathbf{k}) + \hat{\mathbf{v}}\mu_v \sin(\mathbf{l}\cdot\mathbf{k})), \tag{4.8}$$

where $\hat{\mathbf{u}}$ and $\hat{\mathbf{v}}$ are unit vectors which are perpendicular to one another with μ_u and μ_v giving the amplitudes of modulations in these two directions. When either

$\hat{\mathbf{u}}$ or $\hat{\mathbf{v}}$ is parallel to $\mathbf{k}$, it describes a cycloid. If there is a chiral domain present, then the polarization matrix should contain non-diagonal terms ($\mathbf{Q} \parallel \hat{\mathbf{v}}$):

$$\mathscr{P}(a) = \begin{pmatrix} -(1+f) & B & B \\ 0 & A & 0 \\ 0 & 0 & -A \end{pmatrix}$$

More details about these equations could be find in Chapter 2. If we rewrite this general matrix in terms of our experiment, we will get the polarization matrix in following form:

$$\mathscr{P} = \begin{pmatrix} -1 & 0 & 0 \\ 2\eta M_y M_z/M^2 & (M_y^2 - M_z^2)/M^2 & 0 \\ 2\eta M_y M_z/M^2 & 0 & (M_y^2 - M_z^2)/M^2 \end{pmatrix}. \tag{4.9}$$

We've tested several reflections. For this particular type of measurement, results come in form of matrix elements. Following polarisation matrix $\mathscr{P}_{exp}$ shows results for the magnetic reflection (1, 0, 0.818):

$$\mathscr{P}_{exp} = \begin{pmatrix} -0.938 & 0.020 & 0.049 \\ 0.394 & -0.264 & -0.018 \\ 0.408 & -0.006 & 0.252 \end{pmatrix}. \tag{4.10}$$

More about processing the polarisation data and calculation for magnetic reflection (1, 0, 0.818) can be find in Appendix F. Values correspond to expected form in Eq. 4.9. The off diagonal terms confirmed dominant magnetic chiral domain.

The structural chirality might be more difficult to imagine. To fulfil the definition, there must be certain handiness in chemical structure, which usually describes the way atoms occupy their atomic positions. An example can be seen in Fig. 4.27 - red oxygen atoms have helical handiness along c axis.

Structural chirality is connected with nuclear scattering. Swinger [84] was first who came up with the idea of spin-neutron orbit interaction, where the moving neutron magnetic moment senses the nuclear charge. The Schwinger expression for this process differs slightly for fast and slow neutrons. In case of polarized beam, the corresponding cross section can distinguish between right and left

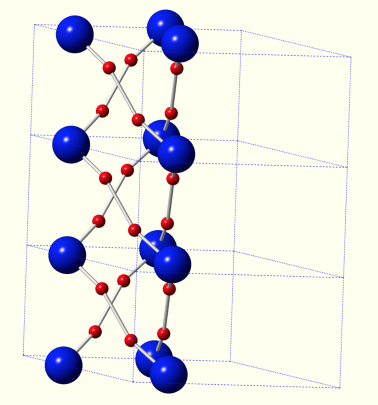

Figure 4.27 *Visualisation of structural chirality using program CrystalMaker, red atoms represent oxygen.*

handed structure with different results from the two. In fact, this does exist also in unpolarized beam, but because there is no assymetry, one can not distinguish between these two enantiomers. Distinguishing effects of structural chirality can be much more significant if imaginary part of the nuclear scattering amplitude becomes larger, which could happen in case of noncentrosymmetric crystals whose Bragg reflections exhibit complex structure factors [84]. These polarized neutron experiments should be similar to the Coster-Knol-Prins [85] experiments with x-rays.

Unlike magnetic chirality, where we were able to confirm one dominant chiral domain, our investigation of structural chirality looks more complex and seems to suggest equal structural chiral domains. This seems to be supported by polarized light measurements carried out by collaborators at Rutgers University.

As we were able to grow bigger crystals with improved flux method, we would like to repeat this part of experiment on a bigger crystal with size ~ 4 mm.

4.7 Conclusion

Even though, we were not able to finish very first elastic experiment on $MnSb_2O_6$ single crystal, collected data showed high quality of the crystal, which was important for following measurements. More data were collected on Laue diffractometer CYCLOPS and should be analysed soon.

Experiment in horizontal magnetic field on TAS instrument RITA-II ($\lambda = 4.9$Å) was focused on the investigation of *universality classes* that can describe several

properties of the system. In centre of attention was the (1, 0, 0.816) magnetic reflection that was monitored as a function of the temperature and magnetic field. Data collected for temperature dependence were fitted with power law, giving the value of critical exponent β as 0.3. This value classifies $MnSb_2O_6$ as three dimensional system (Heisenberg model), which is in agreement with ref. [18]. Value of β was confirmed with experiment on BT4 instrument (λ= 2.4 Å) with the same results and therefore, we conclude that the value of critical exponent β is not influenced by the instrument resolution.

Polarised experiment confirmed dominant magnetic domain, however, this could not proven for the structural chirality. Probably due to the small size of the single crystal. We would like to repeat this experiment with bigger sample that was successfully prepared with our improved flux method.

Inelastic experiment on instrument MACS showed broad multimagnon continuum located above sharp and intense single magnon wave. According to existing theory for magnons, this multimagnon continuum can be explained only for quantum cases, but not for classical systems like $MnSb_2O_6$. This result provides very promising path for further experimental and theoretical investigation of this phenomena.

Chapter 5

$Cu_3Nb_2O_8$

In the past few years magnetic multiferroics have been studied intensively. One group of multiferroics is represented by materials where the electrical polarization emerges at a magnetic ordering temperature. Most of these materials are cycloidal multiferroics such as $TbMnO_3$ [3, 67], $CoCr_2O_4$ [86] or $MnWO_4$ [87] with an incommensurate magnetic configuration. Coupling between magnetic and crystal structure occurs through the spin-orbit interaction, making it energetically favorable to develop local Dzyaloshinskii-Moriya (DM) vectors. These vectors are associated with local polarization.

$Cu_3Nb_2O_8$ belongs to this group of multiferroics and has triclinic centrosymmetric lattice (space group $P\bar{1}$) in the paramagnetic phase. First magnetic transition occurs at $T_N = 26$ K and it is followed by second symmetry breaking by the magnetic structure at $T_2 = 24$ K [22], see Fig. 5.1. Simultaneously, the electric polarization emerges. This magnetic phase is helicoidal with propagation vector $\mathbf{k}_m = (0.4876, 0.2813, 0.2029)$. An interesting property of this compound is the electrical polarization (with magnitude of 17.8 μC m^{-2}, [22]), which is oriented perpendiculary to the plane of rotation of spins and this fact can't be described by conventional theory developed for cycloidal multiferoics. The authors of ref. [22] therefore conclude that polarization in $Cu_3Nb_2O_8$ must arise through coupling of the chiral component of the magnetic structure with the crystal structure.

Johnson et al. propose one intuitive way to describe this phenomenon - it is well known that the direct DM effect produces a proper screw magnetic structure in structurally chiral MnSi [88]. Conversely, a magnetic structure with a screw (helical) component will induce structural chirality by the inverse DM effect [22].

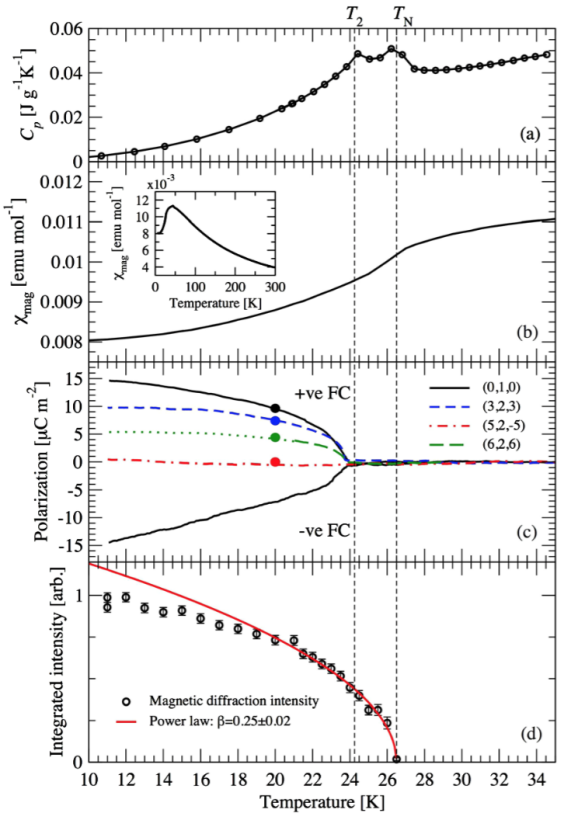

Figure 5.1 *(a) The specific heat of $Cu_3Nb_2O_8$. (b) The magnetic susceptibility of a single crystal sample, measured in a field of 1000 Oe ∥ (3, 2, 3). (c) The electric polarization determined through the integration of a pyroelectric current, measured at a warming rate of 1 K min^{-1}, having field cooled (FC) the sample with E = 2 kVcm^{-1}. (d) The temperature dependence of the neutron magnetic diffraction intensity of the fundamental reflection at d ≈ 10.4 Å. The data have been fitted with a power law [22].*

In this section I present a preliminary study of this compound using powders. We outline an unusual excitation which mimics a crystal field transition being nearly dispersionless and sharp in energy. We discuss origins of this qualitatively.

5.1 Preparation of Polycrystalline Sample

A polycrystalline sample was prepared from stoichiometric amounts of CuO and Nb_2O_5 and baked at 950 °C for 36 h in air. I ground several pellets to fine brown polycrystalline powder. Powder was checked using x-rays - Bruker D2 phaser machine, Cu $K_{\alpha 1}$ radiation (λ_1=1.5406 Å). Position of diffraction peaks was checked with Phase analysis feature of EVA Software, confirming that there

is no additional phase. More detailed Rietveld refinement has not been done.

5.2 Inelastic Experiment - MARI

In attempt to obtain more information about the energetic scale for $Cu_3Nb_2O_8$ system, we have performed inelastic neutron experiments with a powder sample. The experiments were performed on the MARI direct geometry spectrometer at ISIS.

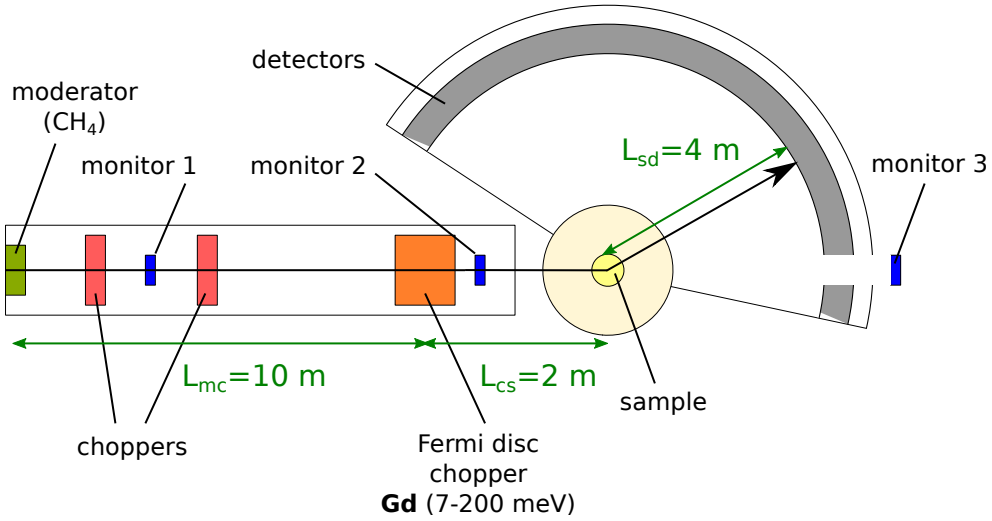

Figure 5.2 *Scheme of MARI spectrometer. MARI is a TOF instrument with direct geometry, which means that incident energy E_i is fixed by Fermi chopper. For the purposes of our experiment, we used a Fermi chopper with gadolinium slits.*

MARI is a chopper spectrometer with wide angular coverage and good resolution, making it the ideal instrument for studying crystal field excitations in magnetic materials. It is designed for studies of polycrystalline and powdered samples or liquids. Detectors consist of ^{3}He tubes that are arranged in low and high angle banks. A scheme of instrument for our experiment can be seen in Fig. 5.2 - we used G-Fermi chopper (gadolinium slits) that has the range from 7 to 200 meV. This disc Fermi chopper is used for picking the right incident energy E_i. MARI instrument offers also other types of Fermi choppers that can be used.

$Cu_3Nb_2O_8$ has spatially long range incommensurate magnetic ordering in all three reciprocal space directions below 26.5 K. The primary plan was to obtain measurements with incident energies E_i = 30 meV, 15 meV and 85 meV below the ordering temperature (we used 5 K) and then collection of data for higher

temperatures (125 K). The low temperature region in the magnetically ordered phase showed typical picture of magnons at low Q for $S = 1/2$ system with powder average dispersive excitations below $\sim$ 10 meV.

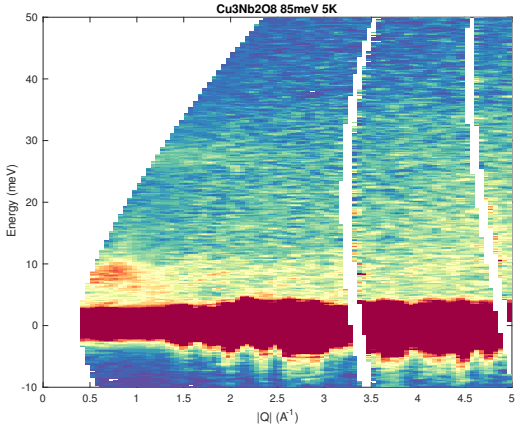

Figure 5.3 *Energy scan with visible excitation around 30 meV at 5 K.*

Unexpectedly, we found another excitation around 30 meV using an incident energy E_i = 85 meV, see Fig. 5.3. More detailed cut proves that there is clear peak around 28 meV (Fig. 5.4).

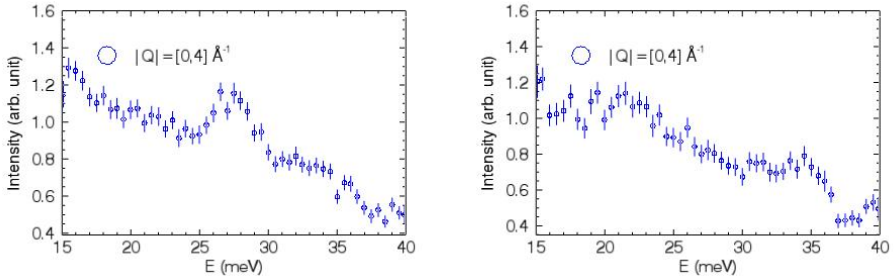

Figure 5.4 *Cuts in energy for 5 K (left) and 50 K (right) for incident energy 85 meV.*

This excitation is sharp in energy, yet well separated from the low-energy dispersive fluctuations. One possibility for the origin of this mode is a crystal field transition like a spin-orbit excitation reported in Co^{2+} materials [89]. To test the nature of this excitation, we heated system up to 50 K (above Néel temperature) as a crystal field transition will not be directly sensitive to the molecular field induced by the magnetic order. However, in this case cut doesn't show the previous peak, which might pointed to magnetic character.

Details of each run can be seen in Tab. 5.1.

run #	E_i (meV)	f (Hz)	T (K)	μAmps
21630	30	350	5	2500
21631	15	250	5	2500
21632	85	400	5	1073
21633	85	400	50	750
21634	30	350	125	1052
21635	30	350	125	998
21636	15	250	125	2000
21637	85	400	125	138

Table 5.1 *Table for all data collected on instrument MARI for $Cu_3Nb_2O_8$ compound.*

5.3 Future studies

One possibility that is currently being explored in a combined theoretical and experimental effort on single crystals is that this excitation results from localised clusters of spins. The nuclear structure is based on triplets of spins that are strongly coupled. It could be that this high energy excitation is the result of a excitation of this triplet. The magnetic Hamiltonian should then be considered as coupled triplets of spins, and not individual Cu^{2+} ions. Similar work has been done on $Cu(NO_3)_2 \cdot 2.5\ D_2O$ compound. It is antiferromagnet with spin S = 1/2 and the form of spin Hamiltonian and measurements can be find in article [90]. Another example are studies of $BaFe_2Se_3$ [91]. Given the complexity of this problem, this was not pursued as part of this thesis beyond these initial studies.

5.4 Conclusion

Polycrystalline sample of $Cu_3Nb_2O_8$ was successfully prepared in our laboratory and taken for inelastic experiment on TOF instrument MARI. Apart from expected excitations $\sim$ 10 meV, another excitation was found $\sim$ 30 meV. This excitation seems to have magnetic character as it disappears with higher temperature. The mechanism causing it is unknown and further investigation is recommended (perhaps, on single crystal).

Chapter 6

$CeRhSi_3$

The coexistence between magnetism and superconductivity is a central issue in condensed matter physics. Recently non-centrosymmetric heavy-fermion superconductors $CePt_3Si$ and UIr were reported. It is well known that magnetism and superconductivity are exclusive for elements and most alloys. Therefore, it is very interesting to see that they do coexist together in the case of heavy fermion systems. For these systems it is not unusual to see transitions between localized and itinerant (delocalized) magnetism. In principle, one should start from free electron model (conduction electrons freely moving in the system) for the itinerant magnetism. However, the coupling between magnetic moments and conduction electrons can influence lot of sample properties - like specific heat, resistance or magnetic susceptibility. For example, the linear term of specific heat for heavy fermion systems is bigger than the value expected for free electron model.

From the fundamental point of view of symmetry, the discovery of materials like $CePt_3Si$ and UIr are very surprising because there are two basic symmetries which are condsidered indispensable to form Cooper pair: time reversal symmetry and parity. The former is important for Cooper pairing in any case while the latter is mandatory for pairing in the triplet channel. Thus there is no well understood picture for the non-centrosymmetric superconductivity at present [24]. Another example of a heavy fermion system where superconductivity coexists with antiferromagnetic ordering is $CeRhSi_3$ and it has been reported by Kimura et al. [23] (see Fig. 6.1).

A group of ternary Cerium compounds with composition $CeTX_3$ (T = transition metal and X = Si or Ge), crystallizing into the teragonal $BaNiSn_3$-type (space

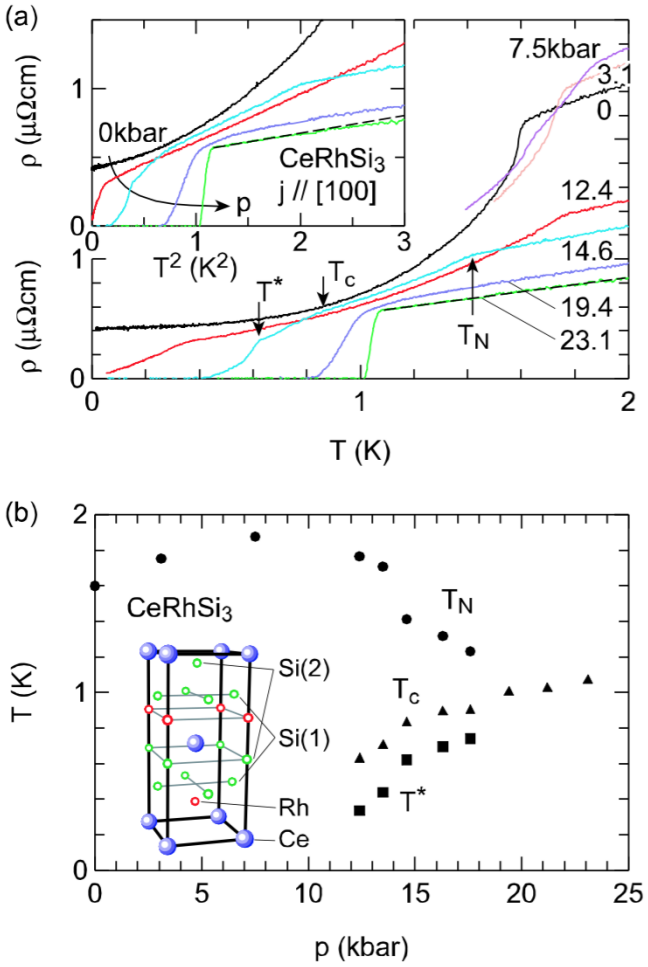

Figure 6.1 *(a) Electrical resistivity as a function of temperature for several pressures (from 0 kbar to 23.1 kbar). For the 23.1 kbar data, the broken line shows linear temperature dependence in main panel. (b) Temperature-pressure phase diagram of $CeRhSi_3$ based on resistivity measurements [23].*

group $I4mm$), see Fig. 6.2, showed interesting magnetic properties at ambient pressure [92–94]. Compounds $CeRhSi_3$ and $CeIrSi_3$ came with even more striking fact recently - heavy-fermion superconductivity under pressure. $CeRhSi_3$ has a tetragonal unit cell with lattice parameters $a = 4.269$ Å and $c = 9.738$ Å. Magnetic Ce^{3+} are located at the body center and the unit cell edges. The body center Ce^{3+} position is surrounded by a layer of Rh above and by a layer of Si below, therefore breaking inversion symmetry making $CeRhSi_3$ non centrosymmetric [1]. $CeRhSi_3$ has a comparatively high electronic specific heat coefficient of $\gamma = 110$ mJ $\cdot$ mol^{-1} $\cdot$ K^{-2}. For example, the value for antiferromagnetic $CeCoGe_3$ is $\gamma = 57$ mJ $\cdot$ mol^{-1} $\cdot$ K^{-2} [92]. Consequently, $CeRhSi_3$ is weakly antiferromagnetic with a small ordered magnetic moment $\sim 0.1\ \mu_B$ bellow temperature of $T_N = 1.6$ K (obtained

from electrical resistivity and susceptibility measurements [95]) characterized by incommensurate wave vector of ($\sim$ 0.22, 0, 0.5) [24]. Superconductivity occurs around temperature T_c = 1.1 K [23] and pressures greater than $\sim$ 12 kbar. The muon spectroscopy showed that antiferromagnetic phase coexists with superconducting until the pressures of 23.6 kbar, when antiferromagnetism is supressed, following a second order transition indicative of a quantum critical point [96].

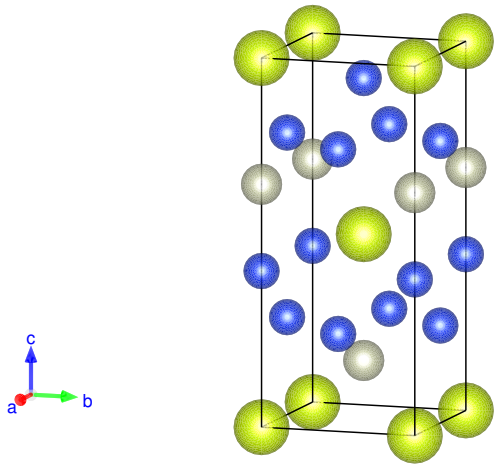

Figure 6.2 *Crystal structure of $CeRhSi_3$ (atoms - Ce green, Rh silver, Si blue)*

Moreover, a very high Kondo temperature $T_K \sim 100$ K [92] was estimated from magnetic susceptibility and electrical resistivity, such a value may be enhanced by the influence of the crystalline electric field (CEF) [92]. New research corrected the Kondo temperature using analysis of specific heat. Muro et al. obtained $T_K \sim 50$ K [97]. The previously reported value [92] turns out to be T_K enhanced by the CEF effect. In order to evaluate the CEF state, reverse value of measured susceptibility data was fitted with CEF Hamiltonian and the mean-field approximation. The CEF Hamiltonian for a Ce^{3+} ion with tetragonal symmetry is given by [97]

$$\mathcal{H}_{CEF} = B_2^0 O_2^0 + B_4^0 O_4^0 + B_4^4 O_4^4, \tag{6.1}$$

where O_n^m and B_n^m are the Steven's operators equivalents and CEF parameters, respectively.

Analyses of magnetic contribution of specific heat C_{mag} and use of CEF level scheme [97] allow to calculate Schottky contribution. Discrepancy of this contribution may be caused by strong interference between CEF and Kondo effect,

B_2^0 = -1.75 K
B_4^0 = 0.381 K
B_4^4 = 4.74 K

Table 6.1 *Steven's coefficients taken from [31]*

as often observed in some other heavy-fermion systems [98].

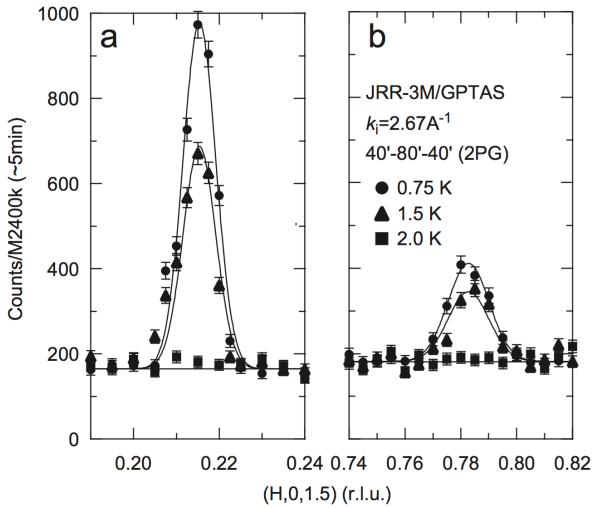

Figure 6.3 *Peak profiles through (a) Q = (0.215, 0, 1.5) and (b) Q = (0.785, 0, 1.5) that have been measured by Aso et al. [24].*

In article [24] neutron diffraction measurements are also refered. Aso et al. were looking for magnetic reflections in the major symmetry axes of three scattering planes - (H, 0, L), (H, H, L) and (H, K, 0). Only in the (H, 0, L)-zone, the magnetic reflections can be observed. Fig. 6.3 shows Bragg reflections in (H, 0, 1.5)-zone at 0.75 K and 1.5 K (below T_N) and they disappeared at 2 K, which indicate their magnetic origin.

The main aim of our research, in case of $CeRhSi_3$, was to investigate the magnetic phase using neutrons as a main probe. In next sections, we describe neutron inelastic experiment focused on study of magnetic fluctuations in the normal state at ambient conditions. The following section includes experiment in magnetic field in respect to define AFM or FM character of these fluctuations. Last section contains the heuristic description and therefore possible models that can be used as an interpretation of our measured data.

6.1 Materials Preparation and Sample Mounting

Single crystals of $CeRhSi_3$ have been prepared by the flux method by collaborators at Brookhaven National Laboratory. For inelastic experiment it is essential to have strong signal from sample as there is a big contribution from the background. Moreover, is weakly antiferromagnetic bellow $T_N = 1.6$ K [95] with value ~ 0.1 μ_B for ordered magnetic moments. Given the relatively small sample sizes, an array of 2 g of single crystals were aligned on a series of aluminium plates as can be seen in Fig. 6.4.

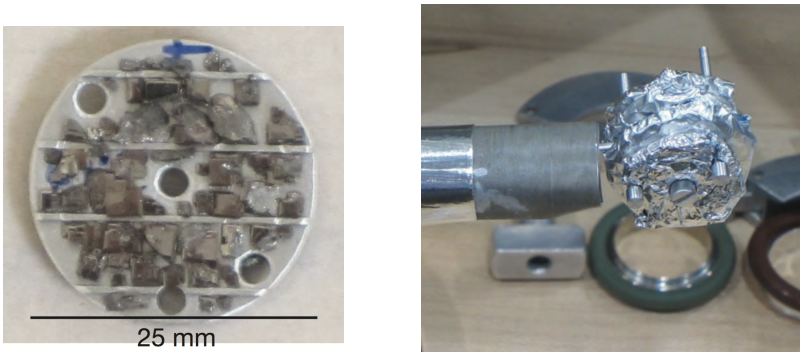

Figure 6.4 *The sample mount used for neutron inelastic scattering studies on $CeRhSi_3$. Blue arrow on the aluminium plate (figure on left) shows direction of a axis.*

The individual single crystals were secured to the aluminium plates using hydrogen-free Fomblin oil and covered with aluminium foil. The aluminium plates were shaped in circles with two pins which enable to rotate the sample and swap between the (H, 0, L) and (H, H, L) scattering planes. Given the sample mounting, our sample was on average centrosymmetric as the mounting does not distinguish between $\pm c$.

Preparatory Neutron Experiments

Before we discuss our experiments, it is good to provide a short overview of preparatory neutron experiments. I would like to underline that these experiments were performed before start of my PhD and therefore data and analysis were not part of my research. However, reader might be interested in initial experiments and conclusions taken from them.

One of them was aiming to search for a static Bragg peak using the D23 diffractometer (ILL, France). This experiment was not successful as it could not resolve the signal from background. This agrees with results for comparatively weak static moment in comparison to the inelastic scattering. All following experiments we therefore focused on studying the dynamics with spectroscopy.

Initial triple-axis measurement were carried out on the PANDA spectrometer (MLZ, Germany), where it was established that the magnetic scattering is very broad in momentum space. This was further confirmed by experiments on the SPINS spectrometer (NIST, USA).

6.2 Inelastic Experiment - OSIRIS

For the purposes of this investigation of this broad magnetic fluctuations observed before, we decided to use the indirect time of flight (TOF) spectrometer OSIRIS (ISIS, UK). As its geometry is indirect, it means that the final energy E_f is fixed. Neutrons scattered by the sample are energy analysed by means of Bragg scattering from a large-area pyrolytic graphite crystal-analyser array. The analyser is associated with 42-element ^{3}He detectors.

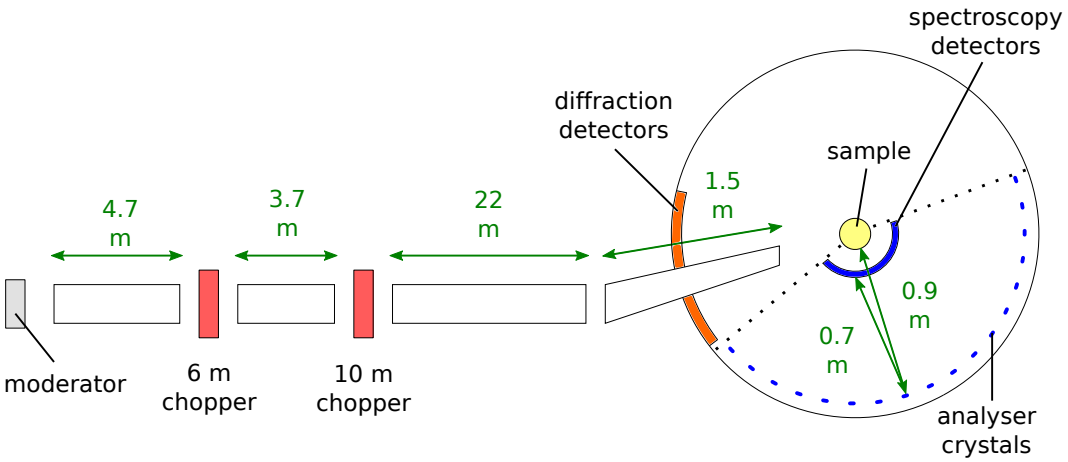

Figure 6.5 *Scheme of OSIRIS (ISIS, UK). It is TOF spectrometer with indirect geometry, which gives this spectrometer an advantage of a very good energy resolution. Final energy for experiment was fixed at E_f = 1.84 meV (PG002 filter). OSIRIS is also utilized for diffraction experiments of long wavelengths (see diffraction detector bank).*

OSIRIS is a spectrometer optimised for very low energy studies and long wavelength diffraction. One of its usages is high-resolution quasi/inelastic neutron

scattering spectroscopy. A very convenient way of building an instrument using indirect TOF method is to build it as a backscattering spectrometer. This type is very well known for high energy resolution - in case of OSIRIS - we are talking about energy resolution of 25 μeV (PG002) or 100 μeV (PG004). It's possible to access low energies too.

We had to stop the first measurement, because of the leak in outer chamber, which was followed by the failure of dilution fridge. Problems with cooling lasted in repeated experiment. The mixing chamber for ^{3}He/^{4}He was not working properly and the lowest stable temperature was just around 1 K (T_N is around 1.6 K for $CeRhSi_3$). However, it was possible to collect the data this time, one of the slices can be seen in Fig. 6.6.

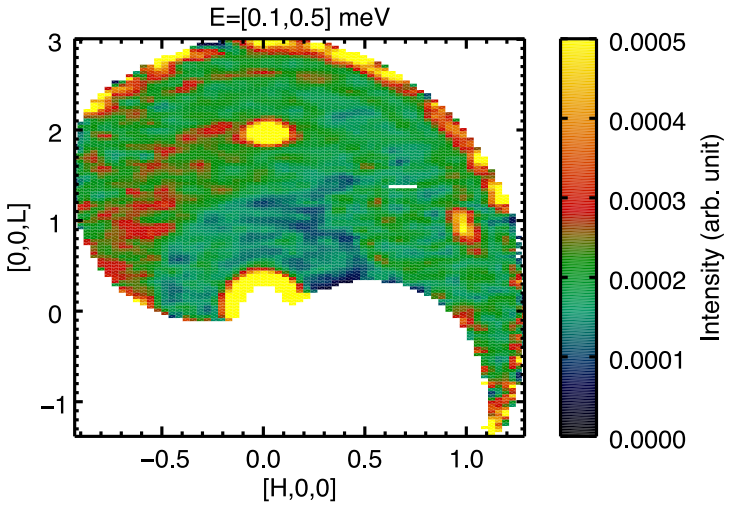

Figure 6.6 *$CeRhSi_3$ data collected with OSIRIS. Too fine resolution did not match fluctuation under study that should appear around (0, 0, ∼1.5). Ring, visible on the left from the elastic peak (0, 0, 2), is caused by high energy scattering most likely.*

Unfortunately, it was not possible to extract any useful information about magnetic fluctuations, which should appear around (0, 0, ∼1.5) position in the reciprocal space. Moreover, it seems like there was contribution from high energy scattering on the left side from elastic peak (0, 0, 2). This was the main motivation for experiment on triple axis spectrometer MACS, where filters can be placed in front of the sample and also behind it, reducing undesirable scattering of high energy neutrons or extra scattering from aluminium.

6.3 Inelastic Experiment - MACS

Our very first inelastic experiment using OSIRIS showed us that higher analysing energy is needed for seeing the magnetic fluctuation around (0, 0, ∼1.5). OSIRIS's fine energy resolution (∼ 25 μeV) proved to be too fine and could match the excitations under study. Therefore, we've decided to use cold multiple axis spectrometer MACS (NIST, USA). The MACS spectrometer has several advantages, the main are high intensity of the beam, 20 analysers providing extremely good detection and 40 He detectors. This spectrometer provides cold neutrons and the user has the possibility to add Be filters and collimators. In our case, we used two set ups - in first case with no Be filter before monochromator and in second one with Be filter. Beryllium oxide filter was placed after the sample for both cases. First set up, without the first Beryllium filter, it was found that the sample mount and Fomblin oil gave a large background making extraction of the magnetic signal difficult and unreliable. Therefore, the use of double filter configuration was found necessary. The final energy was fixed at E_f = 3.7 meV, which afforded energy transfers ΔE up to 1.3 meV. The (H0L) plane for temperatures above and below T_N has been measured.

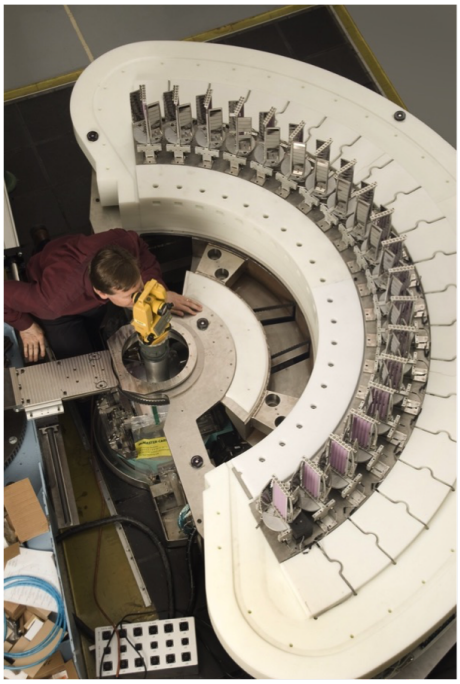

Figure 6.7 *MACS - cold multiple axis spectrometer. Design of this instrument provides ultra high sensitivity access to dynamic correlations in condensed matter on energy scales from 2.2 meV to 20 meV [25].*

6.3.1 Background Subtraction

Before we could proceed to analysis, the subtraction of background from collected data was needed. Mostly due to the fact that background scattering of neutrons from the Fomblin grease and also the Aluminium sample holder were an issue. I wrote a code in MATLAB that has been used for solving this problem for all data sets. As we underlined before, MACS has wide detector coverage that allowed us to measure inelastic signal and also a large background region where the magnetic signal was not observed.

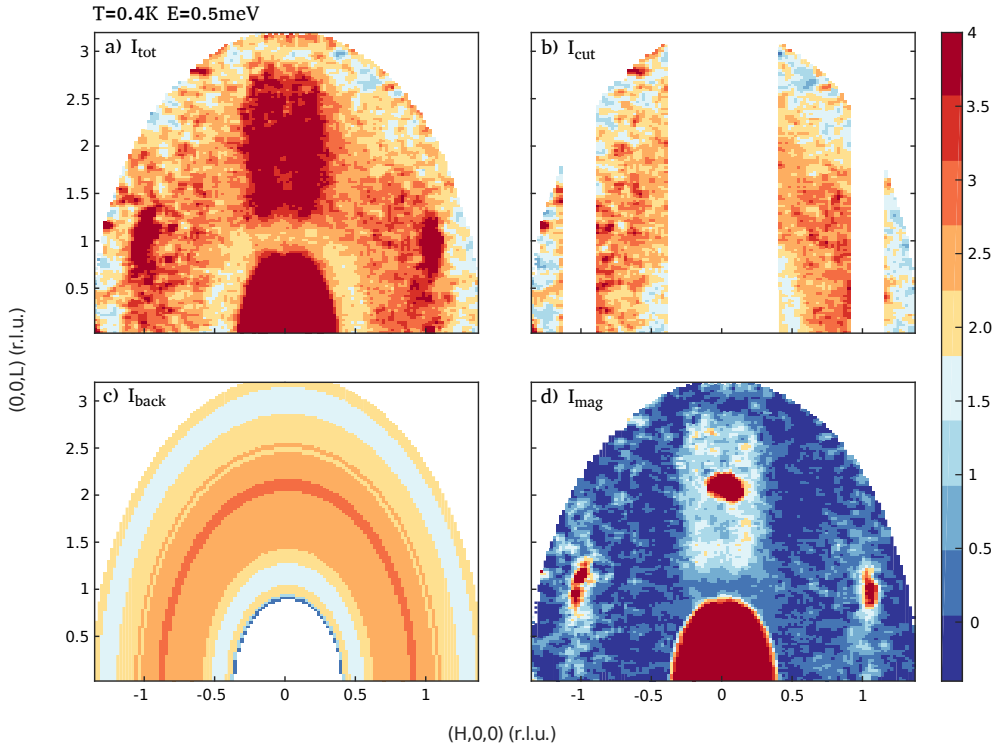

Figure 6.8 *Method used for background subtraction from measured data. (a) shows the smoothed intensity. (b) are data with cut regions that either corresponded to Bragg reflections, direct beam or broad magnetic scattering around (0, 0, 1.5) position. Figure (c) illustrates the background signal generated by finding the radial average. Last figure (d) obtains purely magnetic signal. This procedure has been repeated for different energies and temperatures as background signal changes with these variables.*

Fig. 6.8 (*a*) shows the collected data (background and inelastic signal) with smoothed intensity. The main magnetic region is surrounded by weaker scattering signal on both sides and appears as a ring of intensity in $|\vec{Q}|$. Bragg reflections near the (1, 0, 1) and (-1, 0, 1) positions are clearly visible. Broad magnetic

fluctuation occurs around (0, 0, 2) position. It is important to point out that signal from background varies with temperature and energy. Therefore, the background needed to be approximated at each temperature and energy. My first MATLAB code was written for data to cover energies E from 0.45 meV and 0.55 meV and temperatures from 0.1 K to 0.7 K. This code was later extended for other data sets. After Bragg peaks and magnetic region has been identified, we have removed strips that contained these regions, as shown in Fig. 6.8 (b). Next step was to interpolate the values of background for these cut areas. For that I plotted a graph of scattered intensity as a function of momentum transfer Q. This dependence gave us information about background in the raw data. Obtained background was then radially averaged. This averaging did not consider small angle scattering from the main beam indicated by the bright region about the origin in Fig. 6.8. Subtracting background (c) from Fig. 6.8 (a) gives the magnetic inelastic signal as it can be seen in Fig. 6.8 (d).

A similar background subtraction procedure has been applied in a recent study on MACS investigating $CeCo(In_{1-x}Hg_x)_5$ ($x = 0.01$) [99].

6.4 Experimental Results - MACS

Considering results achieved by Aso [24] - weak low temperature magnetic Bragg peak at ($\sim$ 0.2, 0, 0.5) - we focused our measurements in the (H, 0, L) scattering plane. After we applied the background subtraction method described in previous section, we focused on investigation of the temperature dependence. Fig. 6.9 shows constant energy slices ($E = 0.5$ meV) for three different temperatures $T = 0.3$ K, 6 K and 10 K.

We can see nuclear Bragg peaks at (1, 0, 1) and (-1, 0, 1) positions. The broad magnetic scattering, that it is elongated along the L direction, includes also (0, 0, 2) nuclear Bragg peak, which is an allowed crystallographic Bragg reflection. The background corrected scattering near $\mathbf{Q} = (0, 0, 2)$ in Fig. 6.9 (a) therefore contains sharp nuclear reflection and scattering extending over the entire Brillouin zone. The momentum broadened rods of scattering are elongated along L indicative of weak correlations along c. With increasing temperature, the broad scattering weakens in intensity, confirming the magnetic origin (see Figs. 6.9 ($a - c$)).

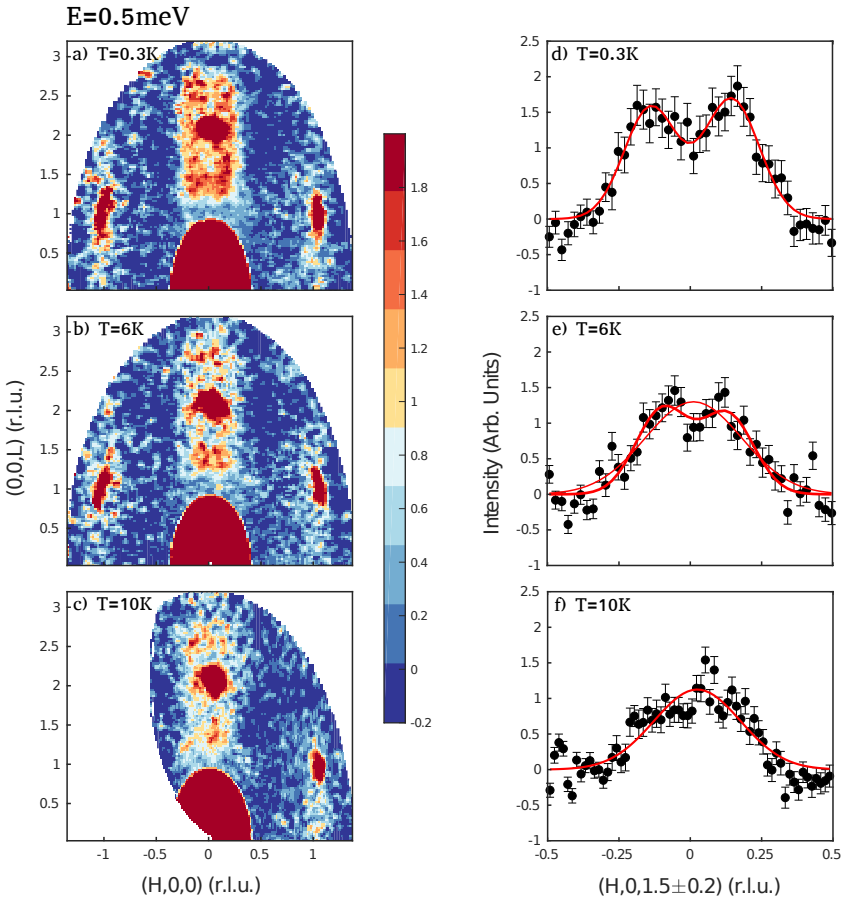

Figure 6.9 *Constant energy slices $E = 0.5$ meV taken on the MACS triple axis spectrometer for different temperatures. On the right hand side (d)-(f) are cuts along the (H, 0, 1.5 ± 0.2) direction. In panel (d), red line is a Gaussian fit illustrating two symmetrically displaced peaks. Panel (e) shows a fit to two peaks and also a single peak, it is easy to see that two peaks fit works still better than single peak. However, at temperature 10 K, the correlated scattering is very well described by a single peak centred at the $H = 0$ position.*

On the right hand side in Fig. 6.9 are cuts through these magnetic scattering regions near $\mathbf{Q} = (0, 0, 2)$ integrating along L in the (H, 0, 1.5 ± 0.2) direction. At low temperatures ($T = 0.3$ K), two symmetrically displaced peaks along H can be seen ($H_0 = 0.14 \pm 0.03$). As we were increasing temperature, we could see that incommensurate broad scattering started to move towards commensurate position. After reaching 10 K, the scattering can be well described by a commensurate peak centered at H = 0. The low-energy magnetic scattering in $CeRhSi_3$ therefore crosses over from incommensurate scattering along H to a commensurate scattering with increasing temperature.

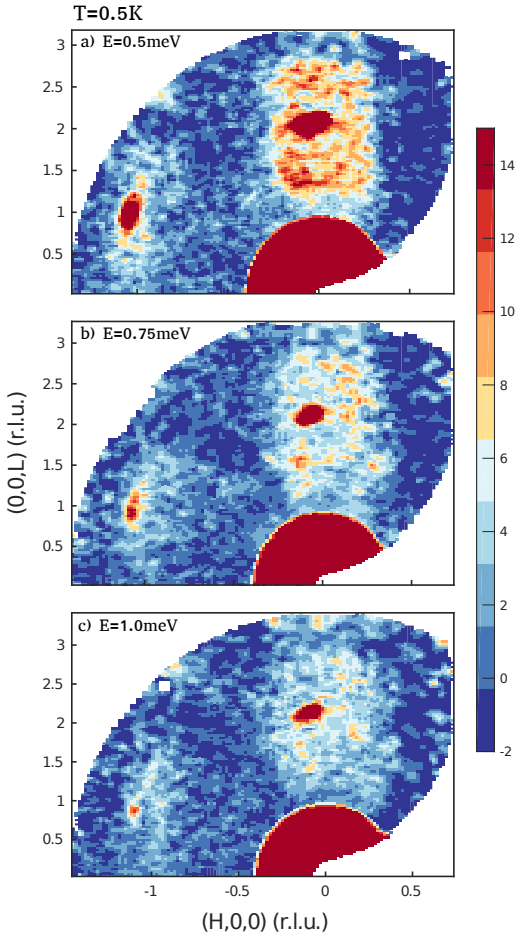

Figure 6.10 *Comparison of three different constant energy slices (a) $E = 0.5$ meV, (b) $E = 0.75$ meV and (c) $E = 1.0$ meV at $T = 0.5$ K. The correlated magnetic scattering becomes weaker and also shifts from incommensurate to the commensurate position with increasing energy transfers.*

After we analysed temperature dependence, we focused our attention to comparison of the data for different energies. Fig. 6.10 shows a series of constant energy slices taken at $T = 0.5$ K using the MACS spectrometer. Fact that the intensity is decreasing for nuclear peaks too is caused by spectrometer resolution. More details can be find in Appendix I.

At low energy transfers of $E = 0.5$ meV (Fig. 6.10 (a)), we can see broad magnetic scattering along L direction that is centered near H $= 0.14 \pm 0.03$ r.l.u. However, an increase in energy transfer from 0.75 meV to 1 meV, Figs. 6.10 (b) and (c), causes a significant decrease in scattering intensity. Moreover, the centre of this broad magnetic scattering seems to move towards commensurate position

Q = (0, 0, 2). In Fig. 6.10 (c) , the magnetic fluctuations are still quite broad, but much more centered at the commensurate position.

Conclusions from temperature and energy dependence can be made. The magnetic scattering crosses from incommensurate to commensurate response through either increasing the energy transfer or temperature.

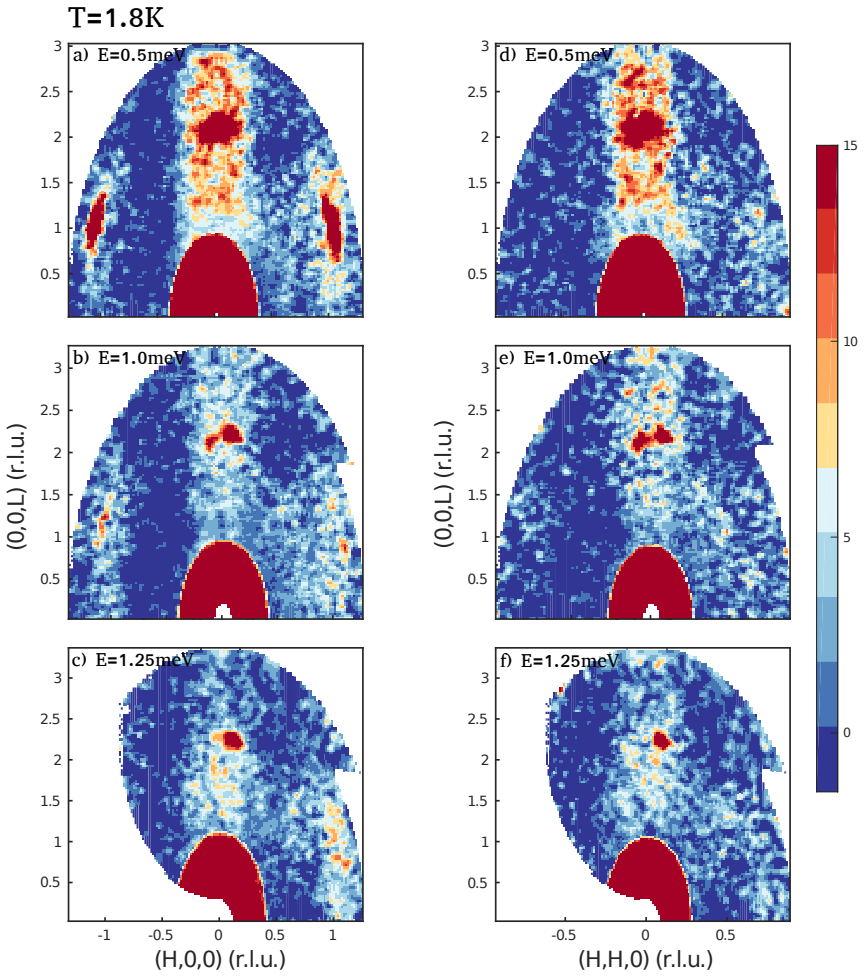

Figure 6.11 *A comparison of the magnetic scattering in the (H, 0, l), panels (a-c), and (H, H, L), panels (d-f), scattering planes.*

The experimental data has been taken in the (H, 0, L) plane mainly motivated by the discovery of a weak magnetic Bragg peak in this scattering plane. Fig. 6.11 is comparing magnetic fluctuation in the (H, 0, L) and (H, H, L) scattering planes for different energy transfers. It can be seen that with increasing energy transfer, the scattering broadens and weakens considerably near the (0, 0, 2) position in both scattering planes. Moreover, the scattering for (H, 0, L) and (H, H, L)

planes looks very similar quantitatively.

Even though similar heavy fermion compounds usually show antiferromagnetic character, it is not clear from the momentum dependence if the observed broad magnetic fluctuations are ferromagnetic or antiferromagnetic. Therefore, we performed an experiment in magnetic field to test this using the triple axis spectrometer IN12 (ILL, France).

6.5 Character of magnetic fluctuation - IN12

Ce based compounds usually show antiferromagnetic interactions between atoms, however, the magnetic scattering occurring near the commensurate (0, 0, 2) position intrigued us to do further investigation. We can mention an example of $YbRh_2Si_2$ compound [100] with an underlying ferromagnetic response. Even though the ferromagnetism in Ce based compounds is rare, it has been reported in CeRuPO [101] and also $CeSb_2$ [102]. Moreover, body centered position of Ce atoms in unit cell can easily allow ferromagnetic or antiferromagnetic alignment of spins on nearest Ce^{3+} atoms (see Fig. 6.12).

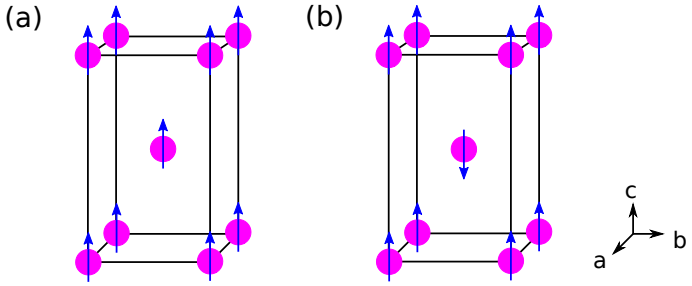

Figure 6.12 *Illustrative model of ferromagnetic and antiferromagnetic interactions between neighbouring Ce^{3+} atoms (purple) within tetragonal unit cell. In reality, orientation of spins is much more complicated as $CeRhSi_3$ magnetic structure has been reported to be incommensurate with wave vector (∼0.22, 0, 0.5) [24].*

To test this hypothesis, we have applied a vertical magnetic field in order to check for a strong response of the magnetic fluctuations. The experiment was performed on the triple axis spectrometer IN12 for cold neutrons that offers measurement at very low temperatures and use of magnetic fields up to 15 T. On the top of that, IN12 has a very low background and low higher order contamination. Recently, a new double focusing PG monochromator has been installed on IN12, composed of 11 × 11 PG(002) crystals.

In the centre of interest was the response of magnetic fluctuation after applying a vertical magnetic field. The basic idea behind the experiment was that for overcoming antiferromagnetic interactions one would need very strong field $\sim$ 100 T. In case of ferromagnetic interactions we would need much weaker field $\sim$ 10 T. Two main scans have been made - one scan along H direction - from ($\bar{1}$, 0, 1.5) to (1, 0, 1.5) and second one along L direction - from (0, 0, 0.6) to (0, 0, 1.9). Data were collected also for two different temperatures - 0.5 K and 2.5 K (T_N = 1.6 K). The final energy of TAS was fixed as E_f = 3.66 meV and initial energy as E_i = 4.16 meV. Result for a constant (H, 0, 1.5) scan at 0 and 6 T at low temperatures can be seen in Fig. 6.13. While the data is statistics limited, we do not observe a strong or significant response of magnetic fluctuations to a magnetic field aligned within the $a - b$ plane.

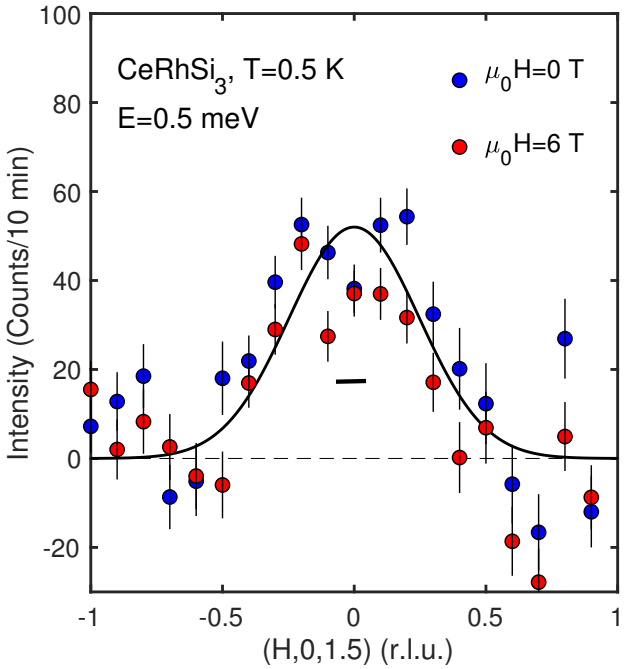

Figure 6.13 *Constant energy scan E = 0.5 meV taken at 0 and 6 T on the triple axis spectrometer IN12 (ILL, France). a temperature independent background has been subtracted from the data. No strong or significant response in magnetic field has been observed.*

The last part of measurement was additional check for a possible ferromagnetic response of nuclear peak (0, 0, 2) in magnetic field. However, no measurable change has been observed. This observation and lack of a strong change with applied field in the inelastic channel, we conclude that the underlying interaction is dominated by antiferromagnetic interactions.

6.6 Heuristic Description

The next step in our analysis was to try and understand the interplay between commensurate magnetic fluctuations at higher temperatures and energies and the incommensurate response at low temperatures and energies. First, we applied crystal field symmetry approach (CEF) and tried to explain our data through $j_{eff} = 1/2$ excitations. However, analysis in next section shows that this approach can not be used. therefore, we went for another way of explaining broad magnetic response - in terms of weakly coupled Kramers doublets through the use of the Random Phase Approximation (RPA). We found that RPA approach can reproduce our measured data qualitatively.

6.6.1 CEF

As a starting point towards understanding the neutron scattering cross section, we review the crystal field theory results and calculate matrix elements relevant for the discussion.

Ce has large Z and belongs to the f-elements. As it was mentioned in the first chapter, for these elements, s and l are no longer a good quantum numbers and one needs to consider total angular momentum j. The state vector can be written as $|j, m_j\rangle$. Total angular momentum j for Ce^{3+} ion is 5/2 meaning that system has 6 states 5/2, 3/2, 1/2, -1/2, -3/2 and -5/2 (as m_j values will be *j*, *j+1*, ..., *-j*). This can be written as:

$$
\begin{aligned}
|j, m_j\rangle &= \left|\frac{5}{2}, \frac{5}{2}\right\rangle, \\
|j, m_j\rangle &= \left|\frac{5}{2}, \frac{3}{2}\right\rangle, \\
|j, m_j\rangle &= \left|\frac{5}{2}, \frac{1}{2}\right\rangle, \\
|j, m_j\rangle &= \left|\frac{5}{2}, -\frac{1}{2}\right\rangle, \\
|j, m_j\rangle &= \left|\frac{5}{2}, -\frac{3}{2}\right\rangle, \\
|j, m_j\rangle &= \left|\frac{5}{2}, -\frac{5}{2}\right\rangle.
\end{aligned}
\tag{6.2}
$$

And each state can be expressed as a simple matrix:

$$
\left|\frac{5}{2}, \frac{5}{2}\right\rangle = \begin{bmatrix} 1 \\ 0 \\ 0 \\ 0 \\ 0 \\ 0 \end{bmatrix}. \tag{6.3}
$$

CEF Hamiltonian can have a form in terms of Stevens operators O_l^m and Stevens parameters B_l^m. This form depends on the symmetry of the unit cell and corresponding group. $CeRhSi_3$ is lacking the centre of inversion, but does have 4-fold rotation axis and 4 vertical mirror planes (see Fig. 6.2), which classifies $CeRhSi_3$ into C_{4v} group. Using table from U. Walter in Appendix C, the general CEF Hamiltonian has a form:

$$
\mathcal{H}_{CEF} = B_2^0 O_2^0 + B_4^0 O_4^0 + B_4^4 O_4^4 + B_6^0 O_6^0 + B_6^4 O_6^4, \tag{6.4}
$$

Moreover, Stevens operators O_6^0 and O_6^4 for Ce^{3+} with $j = 5/2$ are equal to zero, which simplifies Hamiltonian to:

$$
\mathcal{H}_{CEF} = B_2^0 O_2^0 + B_4^0 O_4^0 + B_4^4 O_4^4, \tag{6.5}
$$

where Stevens operators for $j = 5/2$ are defined as:

$$O_2^0 = [3J_z^2 - J(J+1)], \tag{6.6}$$

$$O_4^0 = [35J_z^4 - 30J(J+1)J_z^2 + 25J_z^2 - 6J(J+1) + 3J^2(J+1)^2], \tag{6.7}$$

$$O_4^4 = 1/2[J_+^4 - J_-^4]. \tag{6.8}$$

One can see from above equations that Stevens operators are linear combinations of angular momentum operators acting on the $|j,\, m_j\rangle$ basis. J^2, J_z, J_+ and J_- have been calculated using MATLAB code. More details about total angular momentum operators can be find in Appendix A.

Calculated J^2, J_z, J_+ and J_- give result in form of matrix with size 6x6. For J^2 and J_z, non-diagonal elements of matrix are equal to zero:

$$J^2 = \begin{bmatrix} 8.75 & 0 & 0 & 0 & 0 & 0 \\ 0 & 8.75 & 0 & 0 & 0 & 0 \\ 0 & 0 & 8.75 & 0 & 0 & 0 \\ 0 & 0 & 0 & 8.75 & 0 & 0 \\ 0 & 0 & 0 & 0 & 8.75 & 0 \\ 0 & 0 & 0 & 0 & 0 & 8.75 \end{bmatrix}, \tag{6.9}$$

$$J_z = \begin{bmatrix} 5/2 & 0 & 0 & 0 & 0 & 0 \\ 0 & 3/2 & 0 & 0 & 0 & 0 \\ 0 & 0 & 1/2 & 0 & 0 & 0 \\ 0 & 0 & 0 & -1/2 & 0 & 0 \\ 0 & 0 & 0 & 0 & -3/2 & 0 \\ 0 & 0 & 0 & 0 & 0 & -5/2 \end{bmatrix}. \tag{6.10}$$

On the other hand, J_+ and J_- do have off-diagonal terms and zero diagonal

values:

$$J_+ = \begin{bmatrix} 0 & 2.236 & 0 & 0 & 0 & 0 \\ 0 & 0 & 2.828 & 0 & 0 & 0 \\ 0 & 0 & 0 & 3.000 & 0 & 0 \\ 0 & 0 & 0 & 0 & 2.828 & 0 \\ 0 & 0 & 0 & 0 & 0 & 2.236 \\ 0 & 0 & 0 & 0 & 0 & 0 \end{bmatrix}, \tag{6.11}$$

$$J_- = \begin{bmatrix} 0 & 0 & 0 & 0 & 0 & 0 \\ 2.236 & 0 & 0 & 0 & 0 & 0 \\ 0 & 2.828 & 0 & 0 & 0 & 0 \\ 0 & 0 & 3.000 & 0 & 0 & 0 \\ 0 & 0 & 0 & 2.828 & 0 & 0 \\ 0 & 0 & 0 & 0 & 2.236 & 0 \end{bmatrix}. \tag{6.12}$$

Let's not forget that all these calculations have been done in $|j,\, m_j\rangle$ basis.

First, for being able to calculate eigenvalues of $\mathcal{H}_{CEF}$, we must transform the coordinates of the angular momentum operators from $|j,\, m_j\rangle$ basis to the basis corresponding to the eigenstates of the crystal field $\mathcal{H}_{CEF}$. Therefore, we need to know so called transformation matrix $\mathcal{C}$. This matrix can transform any operator (denoted as A) from the $|j,\, m_j\rangle$ to the $|CEF\rangle$ basis and vice versa using:

$$A_{|\phi CEF\rangle} = \mathcal{C}^{-1} A_{|j,m\rangle} \mathcal{C} \tag{6.13}$$

Second, CEF Hamiltonian goes back to the Eq. 6.5 that contains Stevens coefficients. Those were taken from Muro's paper [92] (Muro used values obtained from magnetic susceptibility measurements).

The transformation matrix $\mathcal{C}$ with columns the eigenstates in the $|j,\, m_j\rangle$ basis is

following then:

$$\mathcal{C} = \begin{bmatrix} 0 & 0.605 & 0 & 0 & 0.796 & 0 \\ 0.796 & 0 & 0 & 0 & 0 & -0.605 \\ 0 & 0 & 1.000 & 0 & 0 & 0 \\ 0 & 0 & 0 & 1.000 & 0 & 0 \\ 0 & -0.796 & 0 & 0 & 0.605 & 0 \\ -0.605 & 0 & 0 & 0 & 0 & -0.796 \end{bmatrix}. \tag{6.14}$$

$\mathcal{H}_{CEF}$ after this transformation takes the following diagonal form with elements the energy eigenvalues:

$$\mathcal{H}^{CEF}_{|\phi CEF\rangle} = \mathcal{C}^{-1}\mathcal{H}^{CEF}_{|j,m\rangle}\mathcal{C}, \tag{6.15}$$

$$\mathcal{H}^{CEF}_{|\phi CEF\rangle} = \begin{bmatrix} 8.817 & 0 & 0 & 0 & 0 & 0 \\ 0 & -13.974 & 0 & 0 & 0 & 0 \\ 0 & 0 & -13.974 & 0 & 0 & 0 \\ 0 & 0 & 0 & 8.817 & 0 & 0 \\ 0 & 0 & 0 & 0 & 5.157 & 0 \\ 0 & 0 & 0 & 0 & 0 & 5.157 \end{bmatrix}. \tag{6.16}$$

Eigenvalues of $\mathcal{H}_{CEF}$ give relative energies and their splitting for ion in the crystalline electric field. Based on the parameters above, the calculated eigenstates are 0, 19 and 23 meV. From the matrix, it is clear that degenerated orbitals split into 3 doublets in tetragonal CEF, see Fig. 6.14. This is in agreement with Kramers theorem - Ce^{3+} ion has one electron in f-shell, which means half-integer total spin, and CEF does not break time reversal symmetry - therefore, there is at least one more eigenstate with the same energy.

The crystal field scheme in Fig. 6.14 shows that the ground state doublet is separated from the next higher energy doublet by $\sim$ 19 meV = 220 K. Given the energy scale separating these two excitations, at low temperatures we would expect this doublet to be well separated from the higher energy and then to possibly behave as a $j_{eff} = 1/2$ magnet similar to the spin-orbit split levels in Co^{2+} [89] or $4d$ or $5d$ transition metal ions [43, 103–105]. In other words, total angular momentum operator J can be projected into $j_{eff} = 1/2$ manifold. This

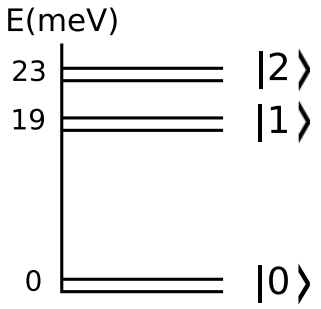

Figure 6.14 *CEF level scheme calculated from field and structure.*

projection is accomplished by a special case of the Wigner-Eckhart theorem:

$$J = \alpha j_{eff}, \tag{6.17}$$

where α is the projection factor. In this section, we investigate this point by studying the lowest energy doublets and the angular momentum operators in this two dimensional subspace.

Once again using the transformation matrix $\mathcal{C}$, we can transform the angular momentum operators between the different basis, for example J_z:

$$J^z_{|\phi CEF\rangle} = \mathcal{C}^{-1} J^z_{|j,m\rangle} \mathcal{C}. \tag{6.18}$$

Same can be written for J_x, J_y etc. Applying transformation matrix on J_z we can get $J^z_{|\phi CEF\rangle}$ that is in the CEF basis:

$$J^z_{|\phi CEF\rangle} = \begin{bmatrix} 0.034 & 0 & 0 & 0 & 0 & -1.928 \\ 0 & -0.034 & 0 & 0 & 1.928 & 0 \\ 0 & 0 & 0.500 & 0 & 0 & 0 \\ 0 & 0 & 0 & -0.500 & 0 & 0 \\ 0 & 1.928 & 0 & 0 & 1.034 & 0 \\ -1.928 & 0 & 0 & 0 & 0 & -1.034 \end{bmatrix}. \tag{6.19}$$

To determine if the ground state doublet can be projected onto a $j_{eff} = 1/2$ angular momentum operator, we consider the upper 2×2 matrix (denoted in blue) which operates on this subspace:

$$J^z_{|CEF\rangle} = \left[\begin{array}{cc|cccc} 0.034 & 0 & 0 & 0 & 0 & -1.928 \\ 0 & -0.034 & 0 & 0 & 1.928 & 0 \\ \hline 0 & 0 & 0.500 & 0 & 0 & 0 \\ 0 & 0 & 0 & -0.500 & 0 & 0 \\ 0 & 1.928 & 0 & 0 & 1.034 & 0 \\ -1.928 & 0 & 0 & 0 & 0 & -1.034 \end{array}\right]. \tag{6.20}$$

For $J^x_{|CEF\rangle}$, it would be:

$$J^x_{|CEF\rangle} = \left[\begin{array}{cc|cccc} 0 & 1.078 & 1.126 & 0 & 0.298 & 0 \\ 1.078 & 0 & 0 & -1.126 & 0 & 0.298 \\ \hline 1.126 & 0 & 0 & 1.500 & 0 & -0.856 \\ 0 & -1.126 & 1.500 & 0 & 0.856 & 0 \\ 0.298 & 0 & 0 & 0.856 & 0 & -1.078 \\ 0 & 0.298 & -0.856 & 0 & -1.078 & 0 \end{array}\right]. \tag{6.21}$$

Therefore, we can get corresponding $\tilde{A}^x$, $\tilde{A}^y$ and $\tilde{A}^z$ operators (2×2 matrix) from $J^x_{|CEF\rangle}$, $J^y_{|CEF\rangle}$ and $J^z_{|CEF\rangle}$:

$$\tilde{A}^x = \begin{bmatrix} 0 & 1.078 \\ 1.078 & 0 \end{bmatrix}, \tag{6.22}$$

$$\tilde{A}^y = \begin{bmatrix} 0 & 1.078i \\ -1.078i & 0 \end{bmatrix}, \tag{6.23}$$

$$\tilde{A}^z = \begin{bmatrix} 0.034 & 0 \\ 0 & -0.034 \end{bmatrix}. \tag{6.24}$$

However, operators $\tilde{A}^x$, $\tilde{A}^y$ and $\tilde{A}^z$ in CEF basis must obey rules of Lie algebra and it can be shown that this is not satisfied. These 2×2 matrices do not follow the canonical commutation relations summarized by $\vec{J} \times \vec{J} = i\vec{J}$ (more about commutation relations can be find in Appendix A) as satisfied by the Pauli spin matrices which belong to the SU(2) group.

On the other hand, it is possible to prove that these relations are obeyed if we consider whole 6×6 matrix. Following relation must hold:

$$[J^z_{|CEF\rangle}, J^x_{|CEF\rangle}] = i\hbar J^y_{|CEF\rangle}, \tag{6.25}$$

where

$$[J^z_{|CEF\rangle}, J^x_{|CEF\rangle}] = J^z_{|CEF\rangle} J^x_{|CEF\rangle} - J^x_{|CEF\rangle} J^z_{|CEF\rangle}. \tag{6.26}$$

For our calculations:

$$[J^z_{|CEF\rangle}, J^x_{|CEF\rangle}] = \begin{bmatrix} 0 & -1.078 & 1.126 & 0 & -0.298 & 0 \\ 1.078 & 0 & 0 & 1.126 & 0 & 0.298 \\ -1.126 & 0 & 0 & 1.500 & 0 & 0.856 \\ 0 & -1.126 & -1.500 & 0 & 0.856 & 0 \\ 0.298 & 0 & 0 & -0.856 & 0 & -1.078 \\ 0 & -0.298 & -0.856 & 0 & 1.078 & 0 \end{bmatrix},$$

and for $iJ^y_{|CEF\rangle}$ (normalized by $\hbar$):

$$iJ^y_{|CEF\rangle} = \begin{bmatrix} 0 & -1.078 & 1.126 & 0 & -0.298 & 0 \\ 1.078 & 0 & 0 & 1.126 & 0 & 0.298 \\ -1.126 & 0 & 0 & 1.500 & 0 & 0.856 \\ 0 & -1.126 & -1.500 & 0 & 0.856 & 0 \\ 0.298 & 0 & 0 & -0.856 & 0 & -1.078 \\ 0 & -0.298 & -0.856 & 0 & 1.078 & 0 \end{bmatrix}.$$

Same proof is possible to get for all pairs of $J_{|CEF\rangle}$s.

Therefore, we can conclude from previous analysis that problem can not be simplified just to the ground doublet solution. Even though the ground state at low temperatures is isolated from the next state by a big gap, $CeRhSi_3$ cannot be projected onto a $j_{eff} = 1/2$ angular momentum operator - $\tilde{A} \neq \alpha J$. From a symmetry perspective, this result is not surprising given the highly anisotropic crystalline electric field. These results lead us to the path of different solution that

could explain interplay between commensurate and incommensurate response in $CeRhSi_3$ system.

6.6.2 RPA

We've showed in previous sections that the magnetic response of $CeRhSi_3$ is widely extended in momentum and energy. This has been observed in other more localized Ce^{3+} systems such as $CeRhIn_5$ [106, 107]. That also means that excitations can not be parametrized by crystal field or well defined harmonic magnons for low energy magnetic dynamics in $CeRhSi_3$. Furthermore, as the ground state can not be projected onto a $j_{eff} = 1/2$, damped spin wave theory cannot be applied neither (it involves Heisenberg coupling of $j_{eff} = 1/2$ spins).

Our aim was therefore to come up with a theory that could interpret our energy and temperature dependence data. In particular, there are two competing effects - one can be described by a commensurate wave vector near $\mathbf{Q} = (0, 0, 2)$ and another associated with the low temperature incommensurate wave vector located near H $\sim$ 0.22. In this section, we would like to discuss whether a weakly correlated series of Kondo sites can consistently describe the commensurate scattering and the extended nature of it in momentum. We want to underline that this model is not unique and has been used in a number of materials - notably in the cuprates and pnictides with models based on band structure or stripes.

The magnetic neutron cross section is proportional to $S(\vec{Q}, \omega)$ which is related to the susceptibility by,

$$S(\mathbf{Q}, \omega) \propto [n(\omega) + 1]\chi''(\mathbf{Q}, \omega) \tag{6.27}$$

where $[n(\omega) + 1]$ is the Bose factor and $\chi''(\mathbf{Q}, \omega)$ is the imaginary part of the susceptibility. Another fact that it's worth to notice is that the extended nature of neutron cross section in momentum means weak correlations between Ce^{3+} sites. We therefore consider a single-site susceptibility describing fluctuations within the ground state Kramers doublet with a characteristic energy scale Γ set by the relaxational timescale τ via $\Gamma \sim 1/\tau$. This results in a single site susceptibility given by:

$$\chi_0(\omega) = \frac{X_0\Gamma}{\Gamma - i\omega}, \tag{6.28}$$

where X_0 is the temperature dependent single site static susceptibility. A similar approach has been used to describe the paramagnetic scattering in Uranium based heavy fermions [108–110] and also in the paramagnetic phase of the cuprates [111, 112]. To parameterize the coupling between different Ce^{3+}, we apply the random phase approximation (RPA) which gives a final susceptibility with the following form:

$$\chi(\mathbf{Q}, \omega) = \frac{\chi_0(\omega)}{1 - \chi_0(\omega)J(\mathbf{Q})}. \tag{6.29}$$

Where $J(\mathbf{Q})$ is the Fourier transform of the coupling between the magnetic sites. Let us consider a two dimensional magnet with only nearest neighbour coupling along the a and b axes, for simplicity, then:

$$J(\mathbf{Q}) = \sum_r J_r e^{i\mathbf{Q}\cdot\mathbf{r}} = 2J_{RKKY}\left[\cos(2\pi H) + \cos(2\pi K)\right] \tag{6.30}$$

If we put together all previous equations, we can express the imaginary part of the susceptibility as:

$$\chi''(\mathbf{Q}, \omega) = \frac{X_0\Gamma\omega}{\omega^2 + \Gamma^2[1 - X_0J(\mathbf{Q})]^2}. \tag{6.31}$$

More details about these derivations can be find in Appendix B. $\chi''(\mathbf{Q}, \omega)$ is proportional to the neutron cross section. Now, it is important to realize that the cross section is peaked in momentum (highest intensity of magnetic fluctuations), when $1 - X_0J(\mathbf{Q})$ is a minimum:

$$\begin{aligned} 1 - X_0J(\mathbf{Q}) &= 0, \\ X_0J(\mathbf{Q}) &= 1. \end{aligned} \tag{6.32}$$

We note that this form of χ'' is an odd function in energy required for detailed balance [29]. Given the scattering is confined along the (0,0,L) direction and extended along L indicative of short-range correlations, we have considered the cross section from in-plane fluctuations and weakly correlated Ce^{3+} spins along c. The neutron cross section can therefore be written as:

$$S(\mathbf{Q},\omega) \propto [n(\omega)+1]\chi''(\mathbf{Q},\omega)\left[1-\left(\frac{Q_{ab}}{Q}\right)^2\right] \times [1+\alpha\cos(\mathbf{Q}\cdot\mathbf{c})]\,. \tag{6.33}$$

The parameter α denotes the strength of nearest neighbor correlations along c.

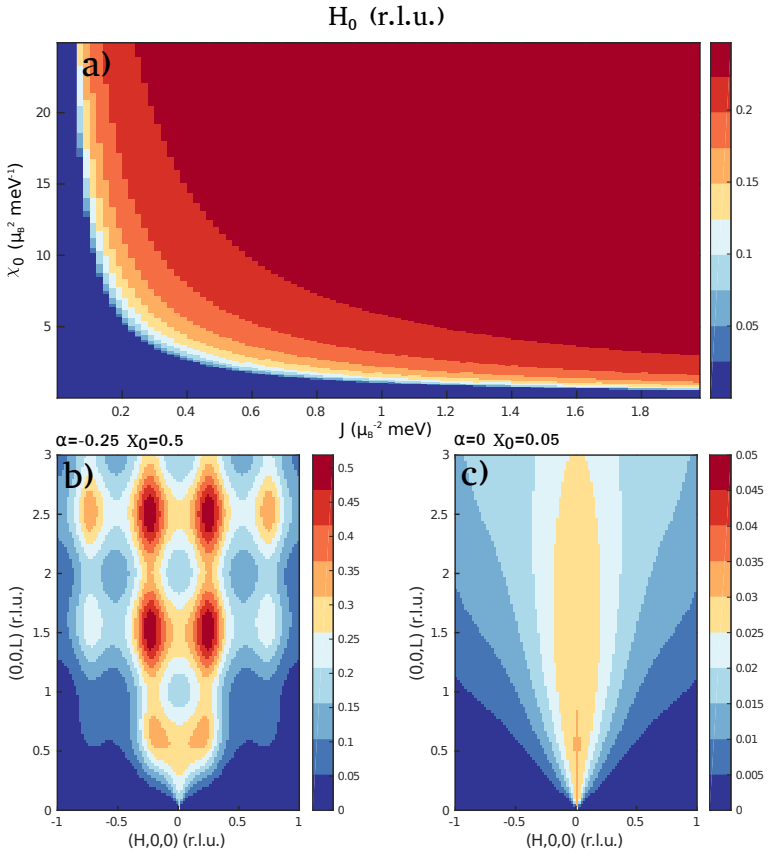

Figure 6.15 *(a) shows the maximum scattering intensity as a function of X_0 and an exchange constant J between different Ce^{3+} ions. Next two panels (b-c) shows simulated constant energy slices $E = 0.5$ meV. They differ in value of parameters X_0 and α (interlayer correlations). Smaller values of X_0 and α (c) lead to intensity that it's peaked at the commensurate position.*

Fig. 6.15 (a) illustrates the X_0 and J phase diagram with the colours indicating where in H the term in the susceptibility $(1 - X_0 J(\mathbf{Q}))$ is a minimum and

therefore where the neutron scattering cross section is maximum. The value of Γ was chosen to be 0.5 meV to match the energy range were strong magnetic fluctuations are observed on MACS. This plot shows that for small values of susceptibility X_0, a maximum in the scattering cross section occurs at the commensurate value H $\sim$ 0 where for larger values of either X_0 or J, the cross section is maximum at H = 0.25 when $2\pi H = 1/2$. This is further illustrated in Figs. 6.15 (b, c) which plots constant energy slices for the two extreme cases. Panels (b) and (c) differ in value of variables α and X_0. Panel (b) shows the case of large susceptibility X_0 and also large correlations α along c. The intensity profiles display peaks displaced along H near H = 0.25 and also L = 0.5. When the value for susceptibility X_0 is decreased (see panel (c) in 6.15), the cross section becomes peaked around the commensurate position.

This simple heuristic model can capture the main qualitative results of our experimental data. Data show a trade off in intensity between incommensurate magnetic scattering peaked near ($\sim$ 0.2, 0, 1.5) and also the commensurate (0, 0, 2) position. The maximum in the cross section shifts with increasing temperature or energy transfer. In both cases, our model says that such a change in either energy or temperature coincides with a reduction in susceptibility X_0. We note that neutron diffraction results have reported a Bragg peak near $\vec{q}_0$=($\sim$ 0.22, 0, 0.5). The displacement of the wavevector from the 0.25 position along H may be accounted for through incorporating further neighbour exchange constants resulting in a more complex form of $J(\mathbf{Q})$ discussed above.

6.7 Conclusion

Most results of $CeRhSi_3$ study were published in ref. [1]. The main inelastic experiment was performed on TAS instrument MACS that has very high flux and multiple analysers that make this instrument ideal for collecting a huge amount of data. We applied radial subtraction of background contribution in our data sets. Unlike well defined and localised excitation for $MnSb_2O_6$, $CeRhSi_3$ shows very broad magnetic fluctuations. Experiment in magnetic field confirmed their antiferromagnetic character.

As a last part of our analysis, we've decided to come up with the best heuristic description of measured data. As ground state is separated from first excited state by a big gap, our first choice was crystal field theory (CEF). In cases like

this, it is quite common to project the ground state into $j_{eff} = 1/2$. However, consideration of ground state exclusively does not obey rules of Lie algebra. These 2×2 matrices do not follow the canonical commutation relations and are fulfilled only for whole 6×6 matrix. We do think that $j_{eff} = 1/2$ projection holds better for compounds with d elements due to the more symmetric octahedral field, whereas compounds with f elements are made of less symmetric octahedrons. However, it might be interesting to test this assumption on several systems. After failure of CEF approach, we've decided to apply random phase approximation (RPA). RPA theory comes from the discussion about susceptibility. As our simulations showed, smaller values of susceptibility and variable α showed intensity peaked around commensurate positions. On the other hand, bigger values of susceptibility and α lead to intensity that was peaked at incommensurate positions. Therefore, we conclude that $CeRhSi_3$ is on the borderline between RKKY driven antiferromagnetism and Kondo-screened state.

Chapter 7

Conclusions

This thesis studies magnetism in three non-centrosymmetric compounds $MnSb_2O_6$, $Cu_3Nb_2O_8$ and $CeRhSi_3$ with the neutron scattering techniques. It also compares two different types of magnetism for d and f elements.

Chapter 3 is discussing the procedure of $MnSb_2O_6$ single crystal growth for which three different techniques have been used - flux, Bridgman and hydrothermal method. Improvement of flux method, starting from [59] paper, did bring bigger crystals. Crystals prepared this way were possible to mass-produce. The black $MnSb_2O_6$ crystals have well-defined hexagonal shape, rather thin along c-axis. Several steps have been tested and changed - time of dwelling, cooling rate, use of new sealing line with high vacuum. The most important step was use of argon atmosphere before final sealing. First crystals had size around 1 mm. Towards the end, an average size of single crystal was $\sim$ 2.5 mm. Some single crystals were even 4-5 mm big. Most crystals (total mass of 1.3 g) were aligned for inelastic experiment on spectrometer MACS. Approximately 150 tubes were sealed to achieve this. Bridgman method produced single crystals of average size reported in previous studies. As only one run has been tried, there is still room for improvement of temperature gradient and whole procedure. To the date of this thesis, $MnSb_2O_6$ have not been synthesized with use of hydrothermal method. Applying higher pressure during process of forming crystal allows to reduce the temperature of synthesis. Polycrystalline sample of $MnSb_2O_6$ has been successfully prepared at temperature 200 ℃ from $MnCl_2$ and Sb_2O_3. This represents significant reduction in comparison with solid state method where $MnSb_2O_6$ is prepared from $MnCO_3$ and Sb_2O_3 at 1000 ℃ and double baking

with intermediate grinding. Attempts for preparation of single crystals were not successful, but experiments with acidity might bring more promising results. Manuscript with all results for crystal growth is under the preparation and should be submitted into *Acta Crystallographica B*.

Chapter 4 discusses study on the $MnSb_2O_6$ compound. First elastic experiment proved high quality of prepared single crystals and expected magnetic reflections for incommensurate magnetic structure. Wave vector corresponds to value reported in previous studies [18]. Due to the problems with the instrument, the experiment was not fully finished. This could be solved with new set of data from CYCLOPS (ILL, France) that has been collected already and should be analysed soon. Realisation of experiment in horizontal magnetic field was one of the most challenging in terms of restrictions - it was important to consider the direction of $\mathbf{Q}$, the orientation of crystal and magnetic field. In some cases, system can be driven into ferromagnetically ordered state applying magnetic field that is big enough to overcome antiferromagnetic interactions. This was not possible as the upper limit of the field strength was 5 T. This transition might be possible with use of stronger magnet. This experiment was focusing mostly on magnetic reflection (1, 0, 0.816). This particular scattering plane seems to be crucial as other reflections did not show comparable results. Order parameter showed quadratic behaviour for low temperatures when measured as a function of field. For temperatures closer to the transition temperature $T_N = 12$ K, the intensity stayed constant. This could be caused by transition called spin flop, when spins are slightly tilted to certain direction. When the magnetic field was rotated by 90°, the intensity of the same reflection stayed the same for increasing magnetic field (measurements were done for 1.7, 5 and 10 K). Intensity was measured as a function of temperature too and then fitted with power law containing critical exponent β. Critical exponents can often reveal additional information about system. In this case, the value of β was calculated as 0.3 for all measured fields, which classifies $MnSb_2O_6$ as three dimensional system that could be described with Heisenberg model. Despite many similarities with iron langasite, $MnSb_2O_6$ does not belong to specific universality class of 2D triangular X-Y magnets. To rule out the influence of instrument resolution, measurement was repeated on different spectrometer BT4 with wavelength $\lambda = 2.4$ Å with same results. According to article [18], $MnSb_2O_6$ compound should be a case where structural and magnetic chirality coexist together. This was tested with polarized neutrons on instrument D3 with use of CRYOPAD. Whereas, dominant magnetic domain has been confirmed by appearance of off-diagonal terms of the polarization matrix,

the same can not be said about structural chirality. From the collected data, it seems like both domains are represented equally. Structural chirality can be tested by method known as Schwinger scattering. Improved routine for flux method enables to growth bigger crystals. It might be worth to repeat the experiment with bigger crystal. Inelastic experiment on instrument MACS was investigating another phenomena called multimagnon excitations. According to existing spin wave theory, these should not appear in classical systems. Some recent studies [82] showed that this is not always the case. $MnSb_2O_6$ ($S = 5/2$) has several prerequisites to belong to this new group of materials - has triangular lattice with incommensurate propagation vector. Energy transfers from 0.2 meV up to 4 meV were measured. Constant Q cuts for (H, H, 0) and (0, 0, L) scattering plane revealed sharp and intense spin wave and broad multimagnon excitation that occurs $\sim$ 2 meV (which is double value of single magnon wave). The next step in analysis would be a model that could describe measured data.

A short study of $Cu_3Nb_2O_8$ is included in Chapter 5. Polycrystalline sample was prepared and investigated with use of time of flight spectrometer MARI. Apart from expected magnetic excitations $\sim$ 10 meV, another excitation was found $\sim$ 30 meV. The excitation seems to have magnetic character as it disappears at higher temperatures. It is sharp in energy, yet well separated from the low-energy dispersive fluctuations. As this excitation does not come from expected energy levels for $S = 1/2$ system, it seems that there is another mechanism causing it. One option might be excitation of spin triplet, where spins are strongly coupled. Given the complexity of this problem, this was not pursued as part of this thesis beyond these initial studies.

Chapter 6 includes the study of $CeRhSi_3$ that has been published in [1]. In contrast to strictly localised magnetism of $MnSb_2O_6$ with dispersing spin waves, inelastic spectra of $CeRhSi_3$ shows broad excitations - both in energy and momentum. This is due to the delocalised character of Ce atoms. First experiment on time of flight spectrometer OSIRIS showed importance of resolution. Very fine resolution of this backscattering instrument made it impossible to observe these broad excitations. Therefore, the experiment was repeated on triple axis spectrometer MACS. This measurement was successful. As all measured data obtain contribution from the background, the background subtraction method has been designed and written in a form of a code that was used for all data. Following data analysis showed that the magnetic scattering crosses from incommensurate to commensurate response through either increasing

the energy transfer or temperature. In respect to shine some light on character of these fluctuations, an experiment in magnetic field was performed. Even though the ferromagnetism in Ce based compounds is rare, there are some cases [101, 102] when it has been reported. Experiment was done on cold triple axis spectrometer IN-12 and results for a constant (H, 0, 1.5) scan at 0 T and 6 T at low temperatures do not show strong or significant response to the magnetic field aligned within the a-b plane. Therefore, character of magnetic fluctuations is antiferromagnetic. Last section of this study includes heuristic description of measured data. First approach was using crystal field theory (CEF). As ground state is doublet separated from first excited state by a big energy gap, one might try to project this ground state into $j_{eff} = 1/2$. In fact, this can be find as an example for Ce^{3+} ions in some textbooks too. However, consideration of ground state exclusively does not obey rules of Lie algebra. These 2×2 matrices do not follow the canonical commutation relations. These relations are fulfilled in the case when whole 6×6 matrix is considered. As the CEF theory could not provide heuristic description, a different approach has been chosen. Random phase approximation (RPA) is a model used in several systems before - notably in the cuprates and pnictides. From data it is obvious that magnetic excitations are moving from incommensurate to commensurate positions for higher temperatures and energy transfers. RPA theory is based on discussion about suscpetibility. It is known fact that imaginary part of susceptibility is proportional to the neutron cross section. By choosing correct parameters, one can try to simulate similar results as those obtained in the experiment. Indeed, smaller values of susceptibility and variable α showed intensity peaked around commensurate positions. On the other hand, bigger values of susceptibility and α lead to intensity that was peaked at incommensurate positions. This is in agreement with our experimental data. In interpretation by Doniach phase diagram [113], $CeRhSi_3$ is on the borderline between RKKY driven antiferromagnetism and Kondo-screened state. Our results are consistent with a weak RKKY coupling between sides and also growing susceptibility which drives the incommensurate order. This might point to the existence of well-defined spin excitations at low energues in more localized variants such as $CeCoGe_3$. Heuristic model described in paper [1] and this thesis is based on weakly correlated relaxing and strongly Kondo screened localized Kramers doublets. Therefore, $CeRhSi_3$ is likely on borderline between RKKY antiferromagnetic phase with strong correlations and a fully Kondo screened phase where no correlations exist.

Appendix A

Short Outline of Generalized Angular Momentum Operators

For better understanding of previous chapters, a short review of generalised angular momentum relations is given. The eigenstates of the operators J can be understood in terms of the eigenvalues j (related to the total length of the angular momentum operator) of J^2, and the projection along a particular direction (z-axis) given by the eigenvalue of J_z. In terms of Dirac notation, we can summarize the eigenvalue and eigenvector problem as follows.

$$J^2|j,m\rangle = j(j+1)\hbar^2|j,m\rangle \tag{A.1}$$

$$J_z|j,m\rangle = m\hbar|j,m\rangle \tag{A.2}$$

To connect with the observables J_x and J_y, it is useful to define the operators J_+ and J_-:

$$J_+|j,m\rangle = \sqrt{j(j+1)-m(m+1)}\hbar|j,m+1\rangle \tag{A.3}$$

$$J_-|j,m\rangle = \sqrt{j(j+1)-m(m-1)}\hbar|j,m-1\rangle \tag{A.4}$$

These are often referred to as ladder operators, because they raise m (J_+) or

lower m (J_-). And it is known that:

$$J_+ = J_x + iJ_y \tag{A.5}$$

$$J_- = J_x - iJ_y \tag{A.6}$$

Values of J_x and J_y can be expressed from above equations (two unknown variables):

$$J_x = \frac{J_+ + J_-}{2} \tag{A.7}$$

$$J_y = \frac{J_+ - J_-}{2i} \tag{A.8}$$

Generalised angular momentum operators J_x, J_y and J_z can be defined through the commutation relationships must be obey. These are summarised below

$$[J_x, J_y] = i\hbar J_z \tag{A.9}$$

$$[J_y, J_z] = i\hbar J_x \tag{A.10}$$

$$[J_z, J_x] = i\hbar J_y \tag{A.11}$$

This can be compactly written as $\mathbf{J} \times \mathbf{J} = i\mathbf{J}$. Total angular momentum operator J can be written as:

$$J^2 = J_x^2 + J_y^2 + J_z^2 \tag{A.12}$$

and commutes with all three components:

$$[J^2, J_i] = 0 \quad i = x, y, z \tag{A.13}$$

The CSCO of the angular momentum problem is therefore J^2 and one projection take onto cartesian coordinates typically chosen as J_z. J^2, J_z form a CSCO as they commute and specifying the eigenvalues uniquely defines the eigenvector $|j, m\rangle$.

Appendix B

Random Phase Approximation (RPA)

This appendix show derivation of RPA method in more details. Let's think about a simple picture of Ce^{3+} ions in a chain - magnetic ions can interact with next neighbours via exchange $J(\mathbf{r})$. Moving from real to reciprocal space, interaction J undergoes Fourier transformation:

$$J(\mathbf{Q}) = \sum_r J(\mathbf{r}) e^{i\mathbf{Q}\cdot\mathbf{r}}. \tag{B.1}$$

Ce ions are in the ground state doublet as energetically lowest state with big energy gap to first excited state. It is possible to write the formula for susceptibility of single Ce atom in this chain $\chi_0(\omega)$. If the susceptibility of single atom is $\chi_0(\omega)$, then susceptibility of whole system would be simply just sum:

$$\begin{aligned}\chi(\mathbf{Q},\omega) = \chi_0(\omega) &+ \chi_0(\omega)J(\mathbf{Q})\chi_0(\omega) \\ &+ \chi_0(\omega)J(\mathbf{Q})\chi_0(\omega)J(\mathbf{Q})\chi_0(\omega) \\ &+ ...,\end{aligned} \tag{B.2}$$

that can be expressed as:

$$\begin{aligned}\chi(\mathbf{Q},\omega) = \chi_0(\omega)[1 &+ J(\mathbf{Q})\chi_0(\omega) \\ &+ J(\mathbf{Q})\chi_0(\omega)J(\mathbf{Q})\chi_0(\omega) \\ &+ ...].\end{aligned} \tag{B.3}$$

Written in one line:

$$\chi(\mathbf{Q},\omega) = \chi_0(\omega)[1 + J(\mathbf{Q})\chi_0(\omega) + J^2(\mathbf{Q})\chi_0^2(\omega) + ...]. \tag{B.4}$$

The expression in brackets can be rewritten as:

$$\frac{1}{1-x} = 1 + x + x^2 + x^3 + x^4 + ..., \tag{B.5}$$

therefore:

$$\frac{1}{1 - J(\mathbf{Q})\chi_0(\omega)} = 1 + J(\mathbf{Q})\chi_0(\omega) + J^2(\mathbf{Q})\chi_0^2(\omega) + J^3(\mathbf{Q})\chi_0^3(\omega) + ... \tag{B.6}$$

This leads to:

$$\chi(\mathbf{Q},\omega) = \chi_0(\omega)\frac{1}{1 - J(\mathbf{Q})\chi_0(\omega)}. \tag{B.7}$$

Very good example for use of this approximation can be find in [108] for U_2Zn_{17} compound. As conventional models involving crystal field can not account for the spin dynamics, RPA seems to be a way how to describe the data. Single f-like moments interact with conduction electrons via Kondo interactions and RKKY coupling. this is also the case of our studied system $CeRhSi_3$, where the crystal field description fails.

It is known from theory that frequency-dependent susceptibility for a single

Kondo impurity has the form:

$$\chi_0(\omega) = \frac{\chi_0\Gamma}{(\Gamma - i\omega)}. \tag{B.8}$$

This can be rewritten:

$$\chi_0(\omega) = \frac{\chi_0\Gamma}{(\Gamma - i\omega)}\left(\frac{\Gamma + i\omega}{\Gamma + i\omega}\right), \tag{B.9}$$

$$\chi_0(\omega) = \frac{\chi_0\Gamma(\Gamma + i\omega)}{\Gamma^2 - i^2\omega^2},$$

$$\chi_0(\omega) = \frac{\chi_0\Gamma^2 + i\omega\chi_0\Gamma}{\Gamma^2 + \omega^2}.$$

We are left with real and imaginary part of $\chi_0(\omega)$:

$$\chi_0(\omega) = \frac{\chi_0\Gamma^2}{\Gamma^2 + \omega^2} + i\frac{\omega\chi_0\Gamma}{\Gamma^2 + \omega^2}, \tag{B.10}$$

then:

$$\chi_0(\omega) = \chi_0'(\omega) + i\chi_0''(\omega), \tag{B.11}$$

so the final relation is:

$$\chi_0''(\omega) = \frac{\omega\chi_0\Gamma}{\Gamma^2 + \omega^2}. \tag{B.12}$$

Plugging $\chi_0(\omega)$ from Eq. (B.8) into relation (B.7), we get:

$$\chi(\mathbf{Q}, \omega) = \frac{\frac{\chi_0\Gamma}{(\Gamma - i\omega)}}{1 - J(\mathbf{Q})\frac{\chi_0\Gamma}{(\Gamma - i\omega)}}, \tag{B.13}$$

$$\chi(\mathbf{Q}, \omega) = \frac{\chi_0\Gamma(\Gamma - i\omega)}{[(\Gamma - i\omega) - J(\mathbf{Q})\chi_0\Gamma](\Gamma - i\omega)},$$

$$\chi(\mathbf{Q},\omega) = \frac{\chi_0\Gamma}{(\Gamma - i\omega) - J(\mathbf{Q})\chi_0\Gamma},$$

$$\chi(\mathbf{Q},\omega) = \frac{\chi_0\Gamma}{\Gamma(1 - J(\mathbf{Q})\chi_0) - i\omega},$$

$$\chi(\mathbf{Q},\omega) = \frac{\chi_0\Gamma}{\Gamma(1 - J(\mathbf{Q})\chi_0) - i\omega}\left(\frac{\Gamma(1 - J(\mathbf{Q})) + i\omega}{\Gamma(1 - J(\mathbf{Q})) + i\omega}\right),$$

$$\chi(\mathbf{Q},\omega) = \frac{\chi_0^2\Gamma^2(1 - J(\mathbf{Q})) + i\chi_0\Gamma\omega}{[\Gamma(1 - J(\mathbf{Q})\chi_0)]^2 - i^2\omega^2},$$

$$\chi(\mathbf{Q},\omega) = \frac{\chi_0^2\Gamma^2(1 - J(\mathbf{Q})) + i\chi_0\Gamma\omega}{\Gamma^2(1 - J(\mathbf{Q})\chi_0)^2 + \omega^2}. \tag{B.14}$$

Which can be written in form of a real and imaginary part:

$$\chi(\mathbf{Q},\omega) = \frac{\chi_0^2\Gamma^2(1 - J(\mathbf{Q}))}{\Gamma^2(1 - J(\mathbf{Q})\chi_0)^2 + \omega^2} + i\frac{\chi_0\Gamma\omega}{\Gamma^2(1 - J(\mathbf{Q})\chi_0)^2 + \omega^2}. \tag{B.15}$$

The imaginary part of $\chi(\mathbf{Q},\omega)$ is:

$$\chi''(\mathbf{Q},\omega) = \frac{\chi_0\Gamma\omega}{\Gamma^2(1 - J(\mathbf{Q})\chi_0)^2 + \omega^2}. \tag{B.16}$$

If we define $\Gamma_Q = \Gamma(1 - J(\mathbf{Q})\chi_0)$, then relation above can be rewritten as:

$$\chi''(\mathbf{Q},\omega) = \frac{\chi_0\Gamma\omega}{\Gamma_Q^2 + \omega^2} \tag{B.17}$$

In our analysis is important to map the magnetic fluctuation. Half width Γ of peak fit will change across the energies. Eventually, fluctuation disappears, then $\Gamma_Q = 0$:

$$0 = \Gamma(1 - J(\mathbf{Q})\chi_0) \quad \Rightarrow \quad J(\mathbf{Q})\chi_0 = 1. \tag{B.18}$$

Appendix C

The Crystal Field Parameters of 32 Point Groups

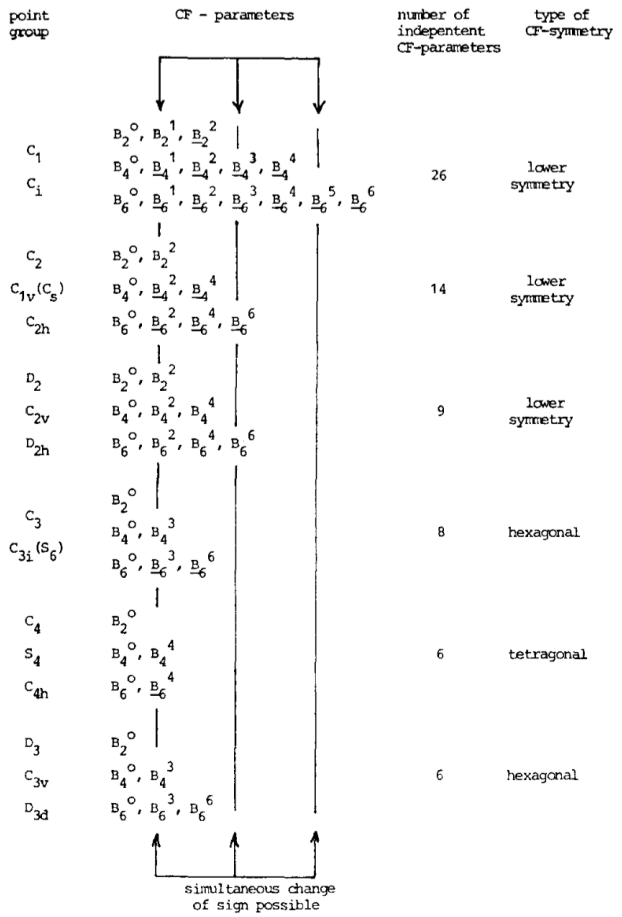

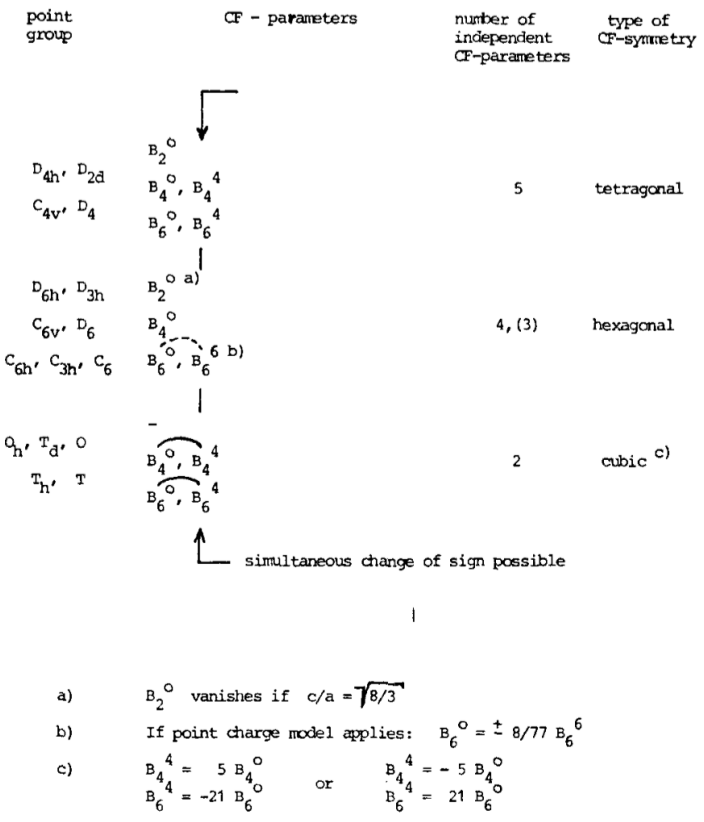

U. Walter, *J. Phys. Chem. Solids* **45**:401-408, (1984).

Appendix D

Flux Method - Heating Routines

Modifications of the heating routine (ToF = Type of furnace, NoT = Number of tubes, Atmos = Atmosphere, R = Rachmaninoff box furnace, B = Brahms box furnace, C = Chopin tube furnace).

ToF	NoT	Percentage	Heating Routine	Atmos
box (R)	2	20% $MnSb_2O_6$ 73% V_2O_5 7% B_2O_3	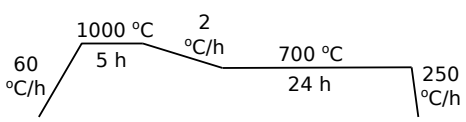	air
tube (C)	3	20% $MnSb_2O_6$ 73% V_2O_5 7% B_2O_3	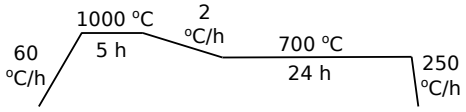	air
box (B)	1	20% $MnSb_2O_6$ 73% V_2O_5 7% B_2O_3	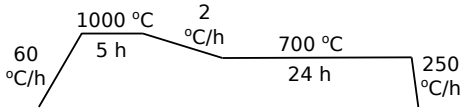	air
box (R)	3	20% $MnSb_2O_6$ 73% V_2O_5 7% B_2O_3	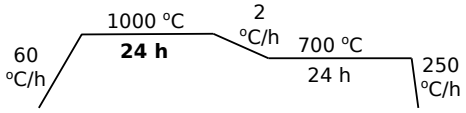	air
box (R)	3	**22**% $MnSb_2O_6$ **75**% V_2O_5 **3**% B_2O_3	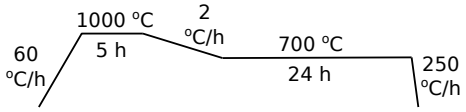	air
box (B)	3	20% $MnSb_2O_6$ 73% V_2O_5 7% B_2O_3	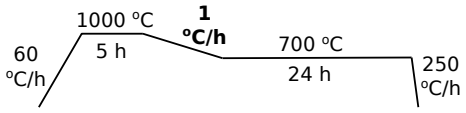	air

ToF	NoT	Percentage	Heating Routine	Atmos
box (R)	4	20% $MnSb_2O_6$ 73% V_2O_5 7% B_2O_3	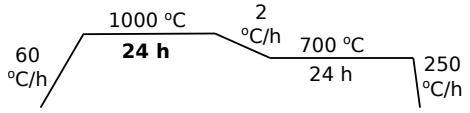	air
box (R)	3	20% $MnSb_2O_6$ 73% V_2O_5 7% B_2O_3	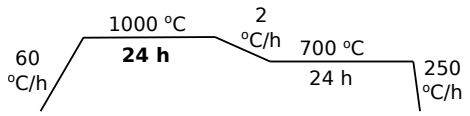	**argon** 200 mTorr
box (R)	12	20% $MnSb_2O_6$ 73% V_2O_5 7% B_2O_3	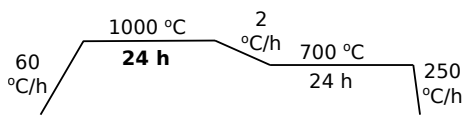	**argon** 200 mTorr
box (R)	15	20% $MnSb_2O_6$ 73% V_2O_5 7% B_2O_3	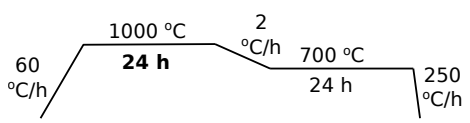	**argon** 200 mTorr
box (R)	10	20% $MnSb_2O_6$ 73% V_2O_5 7% B_2O_3	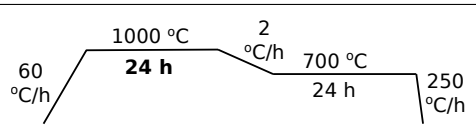	**argon** 200 mTorr
box (B)	6	20% $MnSb_2O_6$ 73% V_2O_5 7% B_2O_3	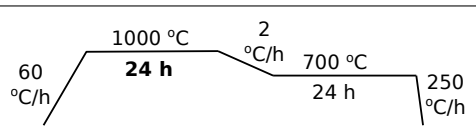	**argon** 200 mTorr
box (R)	11	20% $MnSb_2O_6$ 73% V_2O_5 7% B_2O_3	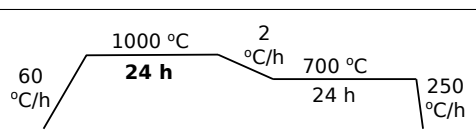	**argon** 200 mTorr
box (B)	6	20% $MnSb_2O_6$ 73% V_2O_5 7% B_2O_3	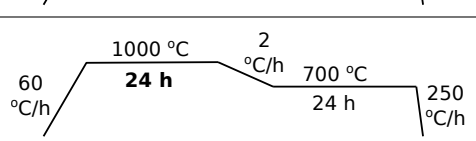	**argon** 200 mTorr
box (R)	15	20% $MnSb_2O_6$ 73% V_2O_5 7% B_2O_3	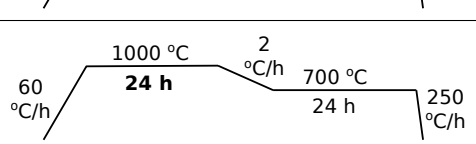	**argon** 200 mTorr
box (R)	15	20% $MnSb_2O_6$ 73% V_2O_5 7% B_2O_3	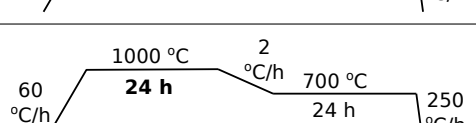	**argon** 200 mTorr
box (R)	15	20% $MnSb_2O_6$ 73% V_2O_5 7% B_2O_3	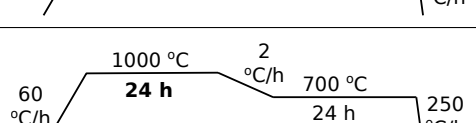	**argon** 200 mTorr
box (R)	15	20% $MnSb_2O_6$ 73% V_2O_5 7% B_2O_3	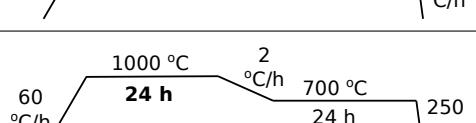	**argon** 200 mTorr
box (R)	16	20% $MnSb_2O_6$ 73% V_2O_5 7% B_2O_3	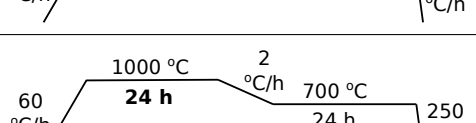	**argon** 200 mTorr

Appendix E

Hydrothermal Method - Heating Routines

Modifications of the hydrothermal procedure (NoB = Number of hydrothermal bombs, V = volume of water, molR = molar ratios of $MnCl_2$ and Sb_2O_3).

Preparation of Polycrystalline sample

NoB	mass [g]	V [ml]	molR	Heating Routine	Notes
2	0.5 0.5	30	1:1	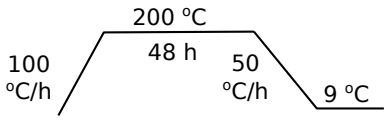	-

Single Crystals Attempts

(HCl = runs with HCl acid used V(36% HCl)=0.12 ml, CS = crystals seeds used)

NoB	mass [g]	V [ml]	molR	Heating Routine	Notes
2	0.5 0.5	30	1:1	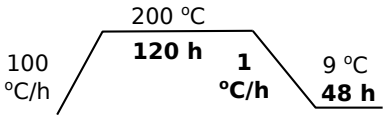	-
5	0.25 0.50 1 2 4	30	1:1	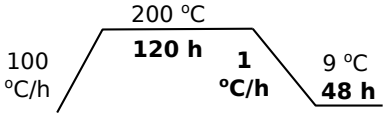	-
3	0.25 0.50 0.25	15	1:1	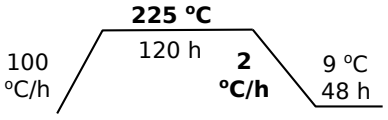	- - CS
3	0.65 0.65 0.65	15	2:1	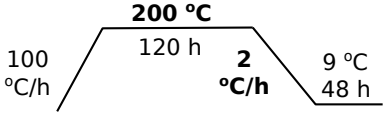	- CS B_2O_3
4	0.25 0.50 0.25 0.50	14.88	1:1	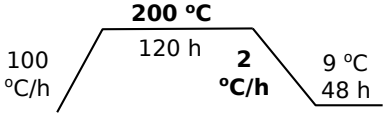	HCl HCl HCl+CS HCl+CS

Appendix F

Polarised Data Analysis

As it was mentioned in previous chapters (Chap. 2 and Chap. 4), presence of magnetic chirality can be confirmed if the polarisaton matrix has off-diagonal terms in following form:

$$\mathscr{P} = \begin{pmatrix} -1 & 0 & 0 \\ 2\eta M_y M_z/M^2 & (M_y^2 - M_z^2)/M^2 & 0 \\ 2\eta M_y M_z/M^2 & 0 & (M_y^2 - M_z^2)/M^2 \end{pmatrix}. \tag{F.1}$$

Several magnetic reflections have been tested during the experiment on D3 instrument (ILL, France). This Appendix focuses on the calculation of polarisation matrix $\mathscr{P}_{exp}$ for magnetic reflection (1, 0, 0.818) in more details. The results of a polarisation analysis experiment may be expressed in terms of generalised cross-sections I^{ij}.Each element of the matrix comes from the following definition:

$$\mathscr{P}_{ij} = \frac{I^{ij} - I^{-ij}}{I^{ij} + I^{-ij}}, \tag{F.2}$$

Easier way how to think about this expression is in terms neutrons that flipped after interaction with the sample. Denominator in Eq. F.2 is considering all neutrons, up and down. It is well known that nuclear scattering is non-spin flip, therefore one can choose appropriate nuclear Bragg peak as a reference value for the denominator. In our case it was nuclear reflection (3, 0, 3):

$$(I^{ij} + I^{-ij})_{(303)} = 0.885 \tag{F.3}$$

Numerator corresponds to magnetic scattering that is spin flip. The components

of magnetisation will change and this can be expressed numerically as a single element of the polarisation matrix $\mathscr{P}_{exp}$:

$$\mathscr{P}_{exp} = \begin{pmatrix} \frac{-0.8297}{0.885} & \frac{0.0175}{0.885} & \frac{0.043}{0.885} \\ \frac{0.3487}{0.885} & \frac{-0.2336}{0.885} & \frac{-0.0156}{0.885} \\ \frac{0.3611}{0.885} & \frac{-0.0050}{0.885} & \frac{0.2229}{0.885} \end{pmatrix}, \tag{F.4}$$

which is:

$$\mathscr{P}_{exp} = \begin{pmatrix} -0.938 & 0.020 & 0.049 \\ 0.394 & -0.264 & -0.018 \\ 0.408 & -0.006 & 0.252 \end{pmatrix}. \tag{F.5}$$

This matrix corresponds to the Eq. F.1:

$$\mathscr{P}_{exp} = \begin{pmatrix} -0.938 & 0.020 & 0.049 \\ 0.394 & -0.264 & -0.018 \\ 0.408 & -0.006 & 0.252 \end{pmatrix} \approx \begin{pmatrix} -1 & 0 & 0 \\ 0.394 & -0.264 & 0 \\ 0.408 & 0 & 0.252 \end{pmatrix}. \tag{F.6}$$

Appendix G

Table for RITA-II Data

The magnetic reflection **Q** = (1, 0, 0.816) was chosen as main one for our experiment. Few more magnetic reflections have been tested and the experiment ended with measurement where reflection was investigated in field that was rotated by 90°. Lambda was set to $\lambda = 4.9$ Å.

Type in table refers to nuclear (n) or magnetic (m) reflection.

run #	Bragg peak	type	T(K)	H(T)	monitor
2761	(2 0 1)	n	105	0	5000
2762 - 2775	(1 0 0.816)	m	1.7	0	5000
2776 - 2789	(1 0 0.816)	m	1.7	0.5	5000
2790 - 2802	(1 0 0.816)	m	1.7	0.75	5000
2803 - 2815	(1 0 0.816)	m	1.7	1	5000

run #	Bragg peak	type	T(K)	H(T)	monitor
2816 - 2828	(1 0 0.816)	m	1.7	1.25	5000
2829 - 2841	(1 0 0.816)	m	1.7	1.5	5000
2842 - 2854	(1 0 0.816)	m	1.7	1.75	5000
2855 - 2867	(1 0 0.816)	m	1.7	2	5000
2868 - 2880	(1 0 0.816)	m	1.7	2.25	5000
2881 - 2893	(1 0 0.816)	m	1.7	2.5	5000
2894 - 2899	(1 0 0.816)	m	1.6 - 12	2.5	5000
2900	(2 0 1)	n	1.7	2.5	3000
2901	(2 0 1)	n	1.7	2.5	3000
2902	(2 0 1)	n	1.7	2.5	50000
2903	(2 0 1)	n	1.7	0	50000
2904	-	-	-	-	-
2905 - 2910	(1 0 0.816)	m	1.65 - 13.5	0	10000
2911	(1 0 0.816)	m	1.7	0	10000
2912				-	
2913				0.1	
2914				0.2	
2915				0.3	
2916				0.4	

run #	Bragg peak	type	T(K)	H(T)	monitor
2917	(1 0 0.816)	m	1.7	0.5	10000
2918				0.6	
2919				0.7	
2920				0.8	
2921				0.9	
2922				1	
2923				1.1	
2924				1.2	
2925				1.3	
2926				1.4	
2927				1.5	
2928				1.6	
2929				1.7	
2930				1.8	
2931				1.9	
2932				2	
2933				2.2	
2934				2.4	
2935				2.6	
2936				2.8	
2937				3	
2938				3.5	
2939				-	
2940				4	
2941				4.5	
2942				-	
2943				5	
2944	(1 0 0.816)	m	1.7	4.5	5000
2945				4	
2946				3	
2947				2	
2948				1.9	
2949				1.8	
2950				1.7	
2951				1.6	
2952				1.5	

run #	Bragg peak	type	T(K)	H(T)	monitor
2953	(1 0 0.816)	m	1.7	1.4	5000
2954				1.3	
2955				1.2	
2956				1.1	
2957				1	
2958				0.9	
2959				0.8	
2960				0.7	
2961				0.6	
2962				0.5	
2963				0.4	
2964				0.3	
2965				0.2	
2966				0.1	
2967				0	
2968	(1 0 0.816)	m	5	0	5000
2969				0.1	
2970				0.2	
2971				0.3	
2972				0.4	
2973				0.5	
2974				0.6	
2975				0.7	
2976				0.8	
2977				0.9	
2978				1	
2979				1.1	
2980				1.2	
2981				1.3	
2982				1.4	
2983				1.5	
2984				1.6	
2985				1.7	
2986				1.8	
2987				1.9	
2988				2	

run #	Bragg peak	type	T(K)	H(T)	monitor
2989	(1 0 0.816)	m	5	2.2	5000
2990				2.4	
2991				2.6	
2992				2.8	
2993				3	
2994				3.5	
2995				4	
2996				4.5	
2997				5	
2998	(1 0 0.816)	m	10	0	5000
2999				0.1	
3000				0.2	
3001				0.3	
3002				0.4	
3003				0.5	
3004				0.6	
3005				0.7	
3006				0.8	
3007				0.9	
3008				1	
3009				1.1	
3010				1.2	
3011				1.3	
3012				1.4	
3013				1.5	
3014				1.6	
3015				1.7	
3016				1.8	
3017				1.9	
3018				2	
3019				2.2	
3020				2.4	
3021				2.6	
3022				2.8	
3023				3	
3024				3.5	

run #	Bragg peak	type	T(K)	H(T)	monitor
3025	(1 0 0.816)	m	10	4	5000
3026				4.5	
3027				5	
3028			1.7	5	
-	(1 0 0.816)	m	-		5000
3033			13		
3034	(1 0 0.816)	m	11	0	10000
3035				0.1	
3036				0.2	
3037				0.3	
3038				0.4	
3039				0.5	
3040				0.6	
3041				0.7	
3042				0.8	
3043				0.9	
3044				1	
3045				1.1	
3046				1.2	
3047				1.3	
3048				1.4	
3049				1.5	
3050				1.6	
3051				1.7	
3052				1.8	
3053				1.9	
3054				2	
3055				2.2	
3056				2.4	
3057				2.6	
3058				2.8	
3059				3	
3060				3.5	
3061				4	
3062				4.5	
3063				5	

run #	Bragg peak	type	T(K)	H(T)	monitor
3064	(1 0 0.816)	m	7.5	0	6000
3065				0.1	
3066				0.2	
3067				0.3	
3068				0.4	
3069				0.5	
3070				0.6	
3071				0.7	
3072				0.8	
3073				0.9	
3074				1	
3075				1.1	
3076				1.2	
3077				1.3	
3078				1.4	
3079				1.5	
3080				1.6	
3081				1.7	
3082				1.8	
3083				1.9	
3084				2	
3085				2.2	
3086				2.4	
3087				2.6	
3088				2.8	
3089				3	
3090				3.5	
3091				4	
3092				4.5	
3093				5	
3094	(1 0 0.816)	m	9	0	8000
3095				0.1	
3096				0.2	
3097				0.3	
3098				0.4	
3099				0.5	

run #	Bragg peak	type	T(K)	H(T)	monitor
3100	(1 0 0.816)	m	9	0.6	8000
3101				0.7	
3102				0.8	
3103				0.9	
3104				1	
3105				1.1	
3106				1.2	
3107				1.3	
3108				1.4	
3109				1.5	
3110				1.6	
3111				1.7	
3112				1.8	
3113				1.9	
3114				2	
3115				2.2	
3116				2.4	
3117				2.6	
3118				2.8	
3119				3	
3120				3.5	
3121				4	
3122				4.5	
3123				5	
3124	(1 0 0.816)	m	11.5	0	15000
3125				0.1	
3126				0.2	
3127				0.3	
3128				0.4	
3129				0.5	
3130				0.6	
3131				0.7	
3132				0.8	
3133				0.9	
3134				1	
3135				1.1	

run #	Bragg peak	type	T(K)	H(T)	monitor
3136	(1 0 0.816)	m	11.5	1.2	15000
3137				1.3	
3138				1.4	
3139				1.5	
3140				1.6	
3141				1.7	
3142				1.8	
3143				1.9	
3144				2	
3145				2.2	
3146				2.4	
3147				2.6	
3148				2.8	
3149				3	
3150				3.5	
3151				4	
3152				4.5	
3153				5	
3154			1.7	1	
-	(1 0 0.816)	m	-		
3159			12.5		
3160	(1 0 0.816)	m	1.7	1.75	
3161			1.7	1.75	
-	(1 0 0.816)	m	-		
3166			13		

Next step was to check other magnetic Bragg peaks and study their behaviour. As these are different reflections, horizontal magnet had been rotated for reaching them.

run #	Bragg peak	type	T(K)	H(T)	monitor
3167	(1 0 -0.182)	m	1.7	0	5000
3168					
3169	(2 0 0.188)	m	1.7	0	5000
3170	(2 0 0.188)	m	1.7	4	5000
3171	(1 0 -0.185)	m	1.7	4	5000
3172				3	
3173				2	
3174				1.5	
3175				1	
3176				0.5	

Last part of experiment was measurement of magnetic reflection (1, 0, 0.816) with the magnetic field rotated by 90° (magnetic field **H** aligned perpendicular to *c*-axis, see Fig. 4.15 (b)).

run #	Bragg peak	type	T(K)	H(T)	monitor
3177	(1 0 0.816)	m	1.7	0	5000
3178				0.1	
3179				0.2	
3180				0.3	
3181				0.4	
3182				0.5	
3183				0.6	
3184				0.7	
3185				0.8	
3186				0.9	
3187				1	
3188				1.1	
3189				1.2	
3190				1.3	
3191				1.4	
3192				1.5	
3193				1.6	
3194				1.7	
3195				1.8	
3196				1.9	

run #	Bragg peak	type	T(K)	H(T)	monitor
3197	(1 0 0.816)	m	1.7	2	5000
3198				2.2	
3199				2.4	
3200				2.6	
3201				2.8	
3202				3	
3203				3.5	
3204				4	
3205				4.5	
3206				5	
3207	(1 0 0.816)	m	5	0	5000
3208				0.1	
3209				0.2	
3210				0.3	
3211				0.4	
3212				0.5	
3213				0.6	
3214				0.7	
3215				0.8	
3216				0.9	
3217				1	
3218				1.1	
3219				1.2	
3220				1.3	
3221				1.4	
3222				1.5	
3223				1.6	
3224				1.7	
3225				1.8	
3226				1.9	
3227				2	
3228				2.2	
3229				2.4	
3230				2.6	
3231				2.8	
3232				3	

run #	Bragg peak	type	T(K)	H(T)	monitor
3233	(1 0 0.816)	m	5	3.5	5000
3234				4	
3235				4.5	
3236				5	
3237	(1 0 0.816)	m	10	0	5000
3238				0.1	
3239				0.2	
3240				0.3	
3241				0.4	
3242				0.5	
3243				0.6	
3244				0.7	
3245				0.8	
3246				0.9	
3247				1	
3248				1.1	
3249				1.2	
3250				1.3	
3251				1.4	
3252				1.5	
3253				1.6	
3254				1.7	
3255				1.8	

Appendix H

Calculations of Landé g-factor and Cross Section Intensities for Ce^{3+} ion in $CeRhSi_3$

Calculation of Landé g-factor:

$$g_J = g_L \frac{J(J+1) - S(S+1) + L(L+1)}{2J(J+1)} + g_S \frac{J(J+1) + S(S+1) - L(L+1)}{2J(J+1)}.$$

Where the orbital g_L is equal to 1, and under the approximation g_S=2, the above expression simplifies to:

$$g_J \approx \frac{3}{2} + \frac{S(S+1) - L(L+1)}{2J(J+1)}. \tag{H.1}$$

For Ce^{3+} ion - $S = 1/2$, $L = 3$ and $J = 5/2$, therefore:

$$g_J \approx \frac{3}{2} + \frac{\frac{1}{2}(\frac{1}{2}+1) - 3(3+1)}{2(\frac{5}{2}(\frac{5}{2}+1))} \approx \frac{6}{7}. \tag{H.2}$$

Neutron experiment can map energy levels of system with appropriate energetic scale as it can be seen from Fermi's golden rule:

$$I \propto |\langle f|V'|i\rangle|^2, \tag{H.3}$$

where I is measured intensity of signal from system. Analysing energy used for

MACS neutron experiment allows to study ground state, as one needs to keep in mind that first excited state is separated by energy gap of almost 20 meV.

$$I_{inelastic} \propto \sum_{i=x,y} |\langle -|J^i|+\rangle|^2 \mu_B^2 = 2.3\mu_B^2, \tag{H.4}$$

$$I_{elastic} \propto g_J^2 |\langle 0|J^z|0\rangle|^2 \mu_B^2 \sim 10^{-3}\mu_B^2. \tag{H.5}$$

Value of $|\langle 0|J_z|0\rangle|$ element is given in matrix. And Landé g-factor for Ce ion can be easily calculated as $g_J = 6/7$. Small value matches with experimental results on triple axis spectrometer MACS (NIST, USA) - signal from elastic scattering was weak and underlined importance of powerful triple axis spectrometer for such a measurement.

Appendix I

Spectrometer Resolution

Due to the non-zero angular spread in the collimations as well as the non-zero mosaic spread in the monochromator and analyzer, the incident and final neutron wavevectors $\mathbf{k}_i$ and $\mathbf{k}_f$ are not perfectly well defined. Neutrons will in general deviate by some amount $\Delta\mathbf{k}_i$ and $\Delta\mathbf{k}_f$ from their most probable path. The resolution function of a spectrometer is the probability of detection of neutrons as a function of $\Delta\mathbf{k}_i$ and $\Delta\mathbf{k}_f$ when the instrument has been set to measure a scattering process with wavevectors [26]. The six cartesian coordinates for $\mathbf{k}_i$ and $\mathbf{k}_f$ are not independent of each other, but this problem can be formulated in terms of only four coordinates - $\Delta\mathbf{Q}$ and $\Delta\omega$. The measured intensity is for a triple-axis spectrometer is then given by the four-dimensional integral:

$$I(\mathbf{Q},\omega) = \int R(\Delta\mathbf{Q},\Delta\omega)\Big[\frac{d^2}{d\Omega dE_f}(\mathbf{Q}-\Delta\mathbf{Q},\omega-\Delta\omega)\Big]d\Delta\mathbf{Q}d\Delta\omega \qquad \text{(I.1)}$$

where $R(\Delta\mathbf{Q},\Delta\omega)$ is the resolution function which depends on $\mathbf{Q}$, E_i, E_f, the horizontal and vertical collimations, and the mosaic spreads [26].

A computer program usually does calculate resolution function and carries out the convolution with an appropriate cross-section. The resolution function can be visualized as a four-dimensional resolution ellipsoid. As this ellipsoid "scans" through the certain feature in reciprocal space (with coordinates $\mathbf{Q}$, ω), the measured signal increases above its background level, see Fig. I.1.

Although the resolution ellipsoid is a 4D object, the vertical $\mathbf{Q}$-resolution (i.e., the resolution perpendicular to the scattering plane) is completely decoupled from the remaining three dimensions of the resolution function. In order to increase the signal, the vertical collimations are kept very coarse. As a result, the vertical

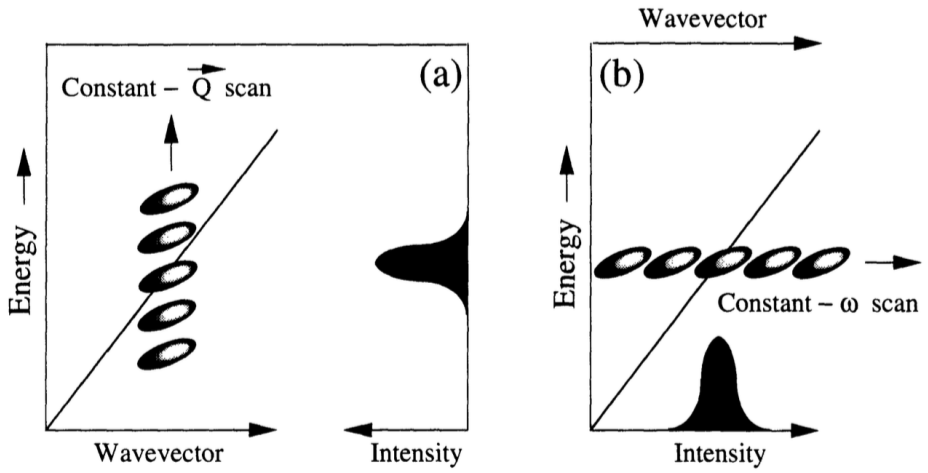

Figure I.1 *The resolution function can be visualized as a resolution ellipsoid. This ellipsoid is shown for constant* $\boldsymbol{Q}$ *and constant* ω *scans [26].*

resolution (which then only depends on E_i and E_f) is generally so large that the intrinsic scattering in this direction is automatically integrated over. It is then instructive to consider the projections of the remaining three dimensions of the resolution ellipsoid onto the scattering plane and the energy axis [26]. This is demonstrated in Fig. I.2 - this is a constant energy scan in the H-direction. Centre of interest is the rod of 2D magnetic scattering. In Figs. I.2 (a)-(d), the projections of the resolution ellipsoid onto the scattering plane are shown for different values of L. The ovals indicate the slice at $\omega = 0$ of the resolution ellipsoid.

The degree of alignment of the resolution ellipsoid with the (1, 0, L)-rod depends on the value of L. In order to optimize the signal-to- background-ratio of an inelastic scan, one generally attempts to find a spectrometer configuration that corresponds to a maximum alignment of the resolution ellipsoid with the intrinsic signal. Since the cross-section is independent of L, the highest signal-to-background-ratio for a scan in the H-direction at ω = 3meV is achieved for L = -0.55; the resolution ellipsoid is "focussed" for L = -0.55. In this case, the resolution in the H-direction (i.e., the direction of the scan) is $\sim 0.03a^* \sim 0.035\text{Å}^{-1}$, while the much coarser vertical resolution is $\sim 0.13\text{Å}^{-1}$.

Fig. I.2 (e) shows the projection (of width $\sim$ 1.3 meV) of the resolution ellipsoid onto the energy axis for L = -0.55, as seen from the reciprocal origin. Similarly, Fig. I.2 (f) shows the same projection perpendicular to **Q**. Note, that the energy projection is much larger than the width of the slice obtained from a Bragg peak

(which is a delta function in both - momentum and energy) [26].

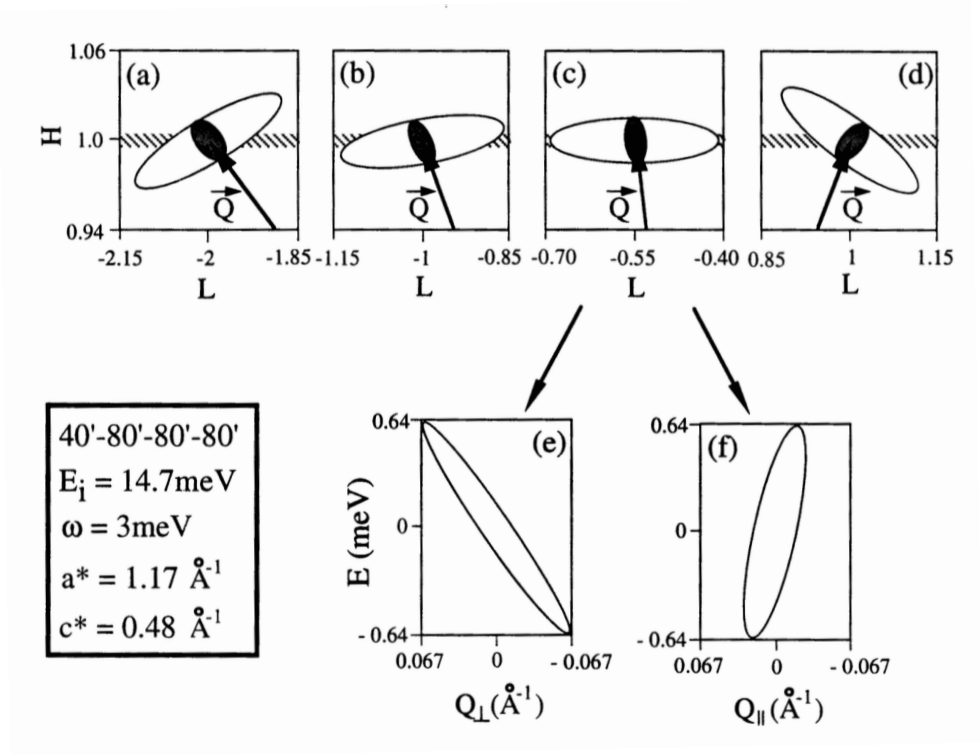

Figure I.2 *Focusing condition for a typical inelastic magnetic scan [26].*

Appendix J

Scattering Cross Section for Coherent Elastic Scattering

We present more detailed look at scattering cross section for the coherent elastic scattering. Let's start with general equation for scattering section for all processes - elastic and inelastic:

$$\frac{d^2\sigma}{d\Omega_f dE_f} = N\frac{k_f}{k_i}(\bar{b})^2 S(\mathbf{Q},\omega). \tag{J.1}$$

The scattering function $S(\mathbf{Q},\omega)$ has following form:

$$S(\mathbf{Q},\omega) = \frac{1}{2\pi\hbar N}\int_{-\infty}^{\infty} dt e^{i\omega t}\langle\rho_{\mathbf{Q}}(0)\rho_{-\mathbf{Q}}(t)\rangle. \tag{J.2}$$

This is the Fourier transform of the time dependent pair-correlation function. If system obeys Bragg conditions, it scatters neutrons in particular direction. It's very convenient to describe it by Dirac function $\delta(x)$:

$$\delta(x) = \begin{cases} x \neq 0 & \delta(x) = 0, \\ x = 0 & \delta(x) = \infty. \end{cases} \tag{J.3}$$

$$\int_{-\infty}^{\infty} \delta(x)dx = 1. \tag{J.4}$$

$\delta(x)$ is not a proper mathematical function but it is nevertheless a very useful

tool in mathematical physics. $\delta(x)$ function can be written in a form:

$$\delta(x) = \frac{1}{2\pi}\int_{-\infty}^{\infty} e^{ikx}dk. \tag{J.5}$$

Following this example, we can write:

$$\delta(\omega) = \frac{1}{2\pi}\int_{-\infty}^{\infty} e^{i\omega t}dt, \tag{J.6}$$

or in a form with $1/\hbar$:

$$\frac{1}{\hbar}\delta(\omega) = \frac{1}{\hbar}\frac{1}{2\pi}\int_{-\infty}^{\infty} e^{i\omega t}dt. \tag{J.7}$$

From definition of delta function $\delta(x)$ we know:

$$\delta(cx) = \frac{1}{c}\delta(x), \tag{J.8}$$

where c is the positive constant. Therefore:

$$\delta(\omega\hbar) = \frac{1}{2\pi\hbar}\int_{-\infty}^{\infty} e^{i\omega t}dt. \tag{J.9}$$

Then the scattering function $S(\mathbf{Q},\omega)$ (Eq. J.2) can be written in the following form:

$$S(\mathbf{Q},\omega) = \frac{1}{N}\delta(\hbar\omega)\langle\rho_{\mathbf{Q}}(0)\rho_{-\mathbf{Q}}(t)\rangle. \tag{J.10}$$

This scattering function can be rewritten in more elegant way using atomic density operator (given by Van Hore):

$$\rho_{\mathbf{Q}}(t) = \sum_{l} e^{i\mathbf{Q}\cdot\mathbf{r}_l(t)}. \tag{J.11}$$

Then for coherent, elastic nuclear scattering, we consider the time average of the density operator:

$$S(\mathbf{Q},\omega) = \frac{1}{N}\delta(\hbar\omega)\left\langle \sum_{ll'} e^{i\mathbf{Q}\cdot(\mathbf{r}_l-\mathbf{r}_{l'})} \right\rangle. \tag{J.12}$$

If we think about scattering in three-dimensional space, we need to consider

three-dimensional δ-function by:

$$\delta(\mathbf{r}) = \delta(x)\delta(y)\delta(z). \tag{J.13}$$

$$\delta(\mathbf{r}) = \begin{cases} \mathbf{r} \neq 0 & \delta(\mathbf{r}) = 0, \\ \mathbf{r} = 0 & \delta(\mathbf{r}) = \infty. \end{cases} \tag{J.14}$$

We should also keep in mind that:

$$\int_{\text{all space}} \delta(\mathbf{r}) d\mathbf{r} = 1, \tag{J.15}$$

$$\int_{\text{all space}} f(\mathbf{r})\delta(\mathbf{r} - \mathbf{r}_0) d\mathbf{r} = f(\mathbf{r}_0), \tag{J.16}$$

where d$\mathbf{r}$ is an element of volume. In the respect for the equation J.5, we can write:

$$\delta(\mathbf{r}) = \frac{1}{2\pi^3} \int_{\text{all rec. space}} e^{i\mathbf{Q}\cdot\mathbf{r}} d\mathbf{Q}, \tag{J.17}$$

here d$\mathbf{Q}$ represents an element of volume in reciprocal space. It's possible to prove that:

$$\int_{\text{cell}} e^{i(\mathbf{Q}-\mathbf{Q}')\cdot\mathbf{r}} d\mathbf{r} = v_0 \delta_{\mathbf{Q}\mathbf{Q}'}, \tag{J.18}$$

where v_0 is volume of the unit cell. Then in a reciprocal space, the following is true:

$$\int_{\text{cell}} e^{i\mathbf{Q}\cdot(\mathbf{r}-\mathbf{r}')} d\mathbf{Q} = \frac{(2\pi)^3}{v_0} \delta_{\mathbf{r}\mathbf{r}'}. \tag{J.19}$$

The last relation that we need for formulating the elastic cross section is:

$$\sum_{\mathbf{r}} e^{i\mathbf{Q}\cdot\mathbf{r}} = c \sum_{\mathbf{G}} \delta(\mathbf{Q} - \mathbf{G}), \tag{J.20}$$

where constant c is actually a volume of reciprocal unit cell $(2\pi)^3/v_0$:

$$\sum_{\mathbf{r}} e^{i\mathbf{Q}\cdot\mathbf{r}} = \frac{(2\pi)^3}{v_0} \sum_{\mathbf{G}} \delta(\mathbf{Q} - \mathbf{G}), \tag{J.21}$$

in fact, this is a different way how to write the lattice sum. If we return to our starting formula for scattering function Eq. J.2 and substitute individual parts, we will get new definition:

$$S(\mathbf{Q}, \omega) = \delta(\hbar\omega) \frac{(2\pi)^3}{v_0} \sum_{\mathbf{G}} \delta(\mathbf{Q} - \mathbf{G}). \tag{J.22}$$

Finally, we can return to our starting equation J.1 for scattering cross section for all processes. Let's write it down for better understanding of different parts:

$$\frac{d^2\sigma}{d\Omega_f dE_f} = N \frac{k_f}{k_i} (\bar{b})^2 S(\mathbf{Q}, \omega), \tag{J.23}$$

$\hbar\omega$ is change in the energy of the neutron. In elastic process, there is no change as:

$$|\mathbf{k}_f| = |\mathbf{k}_i|. \tag{J.24}$$

Therefore, we will obtain coherent elastic scattering section $\mathrm{d}\sigma/\mathrm{d}\Omega$:

$$\left.\frac{d\sigma}{d\Omega_f}\right|_{\mathrm{coh}}^{\mathrm{el}} = N \frac{(2\pi)^3}{v_0} (\bar{b})^2 \sum_{\mathbf{G}} \delta(\mathbf{Q} - \mathbf{G}) \tag{J.25}$$

Appendix K

Table of Some Neutron Research Facilities

Nuclear Sources

Institution	Country	Power (MW)
National Institute of Standards and Technology (NIST)	USA	20
Oak Ridge National Laboratory (ORNL)	USA	85
Brookhaven National Laboratory (BNL)	USA	60
Chalk River Laboratories	Canada	120
Institute Laue Langevin (ILL)	France	58
Commissariat a lEnergie Atomique (CEA)	France	14
Hahn-Meitner Institute	Germany	10
Ris National Laboratory	Denmark	10
Japanese Atomic Energy Research Institute (JAERI)	Japan	20
Australian Nuclear Science and Technology Organisation	Australia	10
Bhabha Atomic Research Centre	India	100

Spallation Sources

Institution	Country	Power (kW)
Argonne National Laboratory	USA	7
Los Alamos National Laboratory	USA	180
Rutherford-Appleton Laboratory	UK	160
Joint Institute of Neutron Research (JINR)	Russia	2000
Paul Scherrer Institute	Switzerland	1000
High-Energy Laboratory (KEK)	Japan	3
The European Spallation Source (ESS)	Sweden	5000

Bibliography

[1] Pásztorová, J. *et al.* Relaxing Kondo-screened Kramers doublets in $CeRhSi_3$. *Physical Review B* **99** (2019).

[2] Kimura, T., Goto, T. & Shintani, H. Magnetic control of ferroelectric polarization. *Nature* **426** (2003).

[3] Kenzelmann, M., Harris, A. B., Jonas, S. & Broholm, C. Magnetic inversion symmetry breaking and ferroelectricity in $TbMnO_3$. *Physical Review Letters* **95** (2005).

[4] Cheong, S.-W. & Mostovoy, M. Multiferroics: a magnetic twist for ferroelectricity. *Nature Materials* **6** (2007).

[5] Spaldin, N., Cheong, S. & Ramesh, R. Multiferroics: Past, present and future. *Physics Today* .

[6] Blundell, S. *Magnetism in Condensed Matter* (Oxford University Press, 2001), 13 edn.

[7] Nuclear fission. URL `https://www.nuclear-power.net/nuclear-power/fission/`. [online; accessed 29.01.2019].

[8] Accelerator and target developments (2007). URL `https://www.isis.stfc.ac.uk/Pages/Accelerator-and-Target-Developments.aspx`. [online; accessed 07.08.2019].

[9] Pynn, R. Neutron scattering (1990).

[10] G. Shirane, S. M. S. & Tranquada, J. M. *Neutron Scattering with Triple-Axis Spectrometer* (Cambridge University Press, 2002), 2 edn.

[11] Toperverg, B. P. & Zabel, H. Neutron scattering - magnetic and quantum phenomena. *Experimental Methods in the Physical Sciences* **48** (2015).

[12] Bacon, G. E. *Neutron Diffraction* (Oxford University Press, 1975), 3 edn.

[13] Chatterji, T. *Neutron Scattering from Magnetic Materials* (Elsevier, 2006), 1 edn.

[14] Carpenter, J. M. & Loong, C. K. *Elements of Slow-Neutron Scattering* (Cambridge University Press, 2015), 1 edn.

[15] Qureshi, N. Instrumental aspects. *EPJ Web of Conferences* **155** (2017).

[16] Laue diffraction (2018). URL `http://physicsopenlab.org/2018/01/18/laue-diffraction/`. [online; accessed 14.02.2019].

[17] Marty, K., Simonet, V., Ressouche, E. & Ballou, R. Single domain magnetic helicity and triangular chirality in structurally enantiopure $Ba_3NbFe_3Si_2O_{14}$. *Physical Review Letters* **101** (2008).

[18] Johnson, R. D., Cao, K. & Chapon, L. C. $MnSb_2O_6$: A polar magnet with a chiral crystal structure. *Physical Review Letters* **111** (2013).

[19] Lefmann, K. *et al.* Realizing the full potential of a RITA spectrometer. *Physica B* **385**.

[20] Closed cycle refrigerators (CCR) (2017). URL `https://www.nist.gov/ncnr/sample-environment/sample-environment-equipment/closed-cycle-refrigerators-ccr`. [online; accessed 16.08.2019].

[21] D3 - the spin polarised hot neutron beam facility. URL `https://www.ill.eu/users/instruments/instruments-list/d3/description/instrument-layout/`. [online; accessed 12.06.2019].

[22] Johnson, R. D., Cao, K. & Chapon, L. C. $Cu_3Nb_2O_8$: A multiferroic with chiral coupling to the crystal structure. *Physical Review Letters* **107** (2011).

[23] Kimura, N., Ito, K., Saitoh, K., Umeda, Y. & Aoki, H. Pressure-induced superconductivity in noncentrosymmetric heavy-fermion $CeRhSi_3$. *Physical Review Letters* **95** (2005).

[24] Aso, N., Miyano, H. & Yoshizawa, H. Incommensurate magnetic order in the pressure-induced superconductor $CeRhSi_3$. *Journal of Magnetism and Magnetic Materials* **310**, 602–604 (2007).

[25] The multi-analyzer crystal spectrometer (MACS) (2019). URL `https://idg.jhu.edu/instrumentation/neutron_scattering/macs-2/`. [online; accessed 05.04.2019].

[26] Greven, M. *Neutron Scattering Study of Magnetism in Insulating and Superconducting Lamellar Copper Oxides.* Ph.D. thesis, Massachusetts Institute of Technology (1995).

[27] Eerenstein, W., Mathur, N. D. & Scott, J. F. Multiferroic and magnetoelectric materials. *Nature* **442** (2006).

[28] Jensen, P. & Udby, L. Wiki neutrons (2014). URL `https://www.e-neutrons.org/wiki/`. [online; accessed 29.01.2019].

[29] Squires, G. L. *Introduction to the theory of Thermal Neutron Scattering* (Cambridge University Press, 1978), 1 edn.

[30] Chaikin, P. M. & Lubensky, T. C. *Principles of condensed matter physics* (Cambridge University Press, 1995), 1 edn.

[31] Muro, Y. *et al.* Crystalline electric field effect and magnetic properties of $CeRhSi_3$ single crystal. *Journal of the Physical Society of Japan* **76** (2007).

[32] Schmid, H. Multi-ferroic magnetoelectrics. *Ferroics* **162**, 317–338 (1994).

[33] Hur, N., Park, S. & Sharma, P. A. Electric polarization reversal and memory in a multiferroic material induced by magnetic fields. *Nature* **429** (2004).

[34] Hur, N. & Park, S. Colossal magnetodielectric effects in $DyMn_2O_5$. *Physical Review Letters* **93** (2004).

[35] Goto, T., Kimura, T., Lawes, G. & Ramirez, A. P. Ferroelectricity and giant magnetocapacitance in perovskite rare-earth manganites. *Physical Review Letters* **92** (2004).

[36] Hill, N. A. Why are there so few magnetic ferroelectrics? *The Journal of Physical chemistry B* **104** (2000).

[37] Kimura, T., Kawamoto, S. & Yamada, I. Magnetocapacitance effect in multiferroic $BiMnO_3$. *Physical Review B* **67** (2003).

[38] Son, J. Y., Kim, B. G., Kim, C. H. & Cho, J. H. Writing polarization bits on the multiferroic $BiMnO_3$ thin film using Kelvin probe force microscope. *Applied Physics Letters* **84** (2004).

[39] Yang, C. H., Koo, J., Song, C. & Koo, T. Y. Resonant x-ray scattering study on multiferroic $BiMnO_3$. *Physical Review B* **73** (2006).

[40] Pauling, L. & Wilson, E. B. *Introduction to Quantum Mechanics with Applications to Chemistry* (Dover Publications, 1963).

[41] McClure, D. S. *Electronic Spectra of Molecules and Ions in Crystals* (Academic Press, 1989), 1 edn.

[42] Abragam, A. & Bleaney, B. *Electron Paramagnetic Resonance of Transition Ions* (Oxford University Press, 2013).

[43] Cowley, R. A., Buyers, W. J. L. & Stock, C. Neutron scattering investigation of the d-d excitations below the mott gap of CoO. *Physical Review B* **88** (2013).

[44] van der Marel, D. & Sawatzky, G. A. Electron-electron interaction and localization in d and f transition metals. *Physical Review B* **37** (1988).

[45] Yosida, K. *Theory of Magnetism* (Springer, 2010), 2 edn.

[46] Mraz, S. What are the differences between linear accelerators, cyclotrons, and synchrotrons? (2017). URL `https://www.machinedesign.com/whats-difference-between/`. [online; accessed 14.08.2019].

[47] A. Furrer, J. M. & Strassle, T. *Neutron Scattering in Condensed Matter Physics* (World Scientific, 2009), 1 edn.

[48] Jackman, J. A. *Spin and Lattice Dynamics in Uranium Rocksalt Compounds*. Ph.D. thesis, The University of Guelph (1983).

[49] R. M. Moon, T. R. & Koehler, W. C. Polarization analysis of thermal-neutron scattering. *Physical Review* **181** (1969).

[50] S. V. Maleyev, V. G. B. & Suris, R. A. *Soviet Physics Solid State* **4** (1963).

[51] Blume, M. Polarization effects in the magnetic elastic scattering of slow neutrons. *Physical Review* **130** (1963).

[52] Mezei, F. *The Principles of Neutron Spin Echo* (Springer Link, 1980).

[53] Mezei, F. *Physica B* **137** (1986).

[54] Tasset, F. *Physica B* **156**.

[55] P. J. Brown, J. B. F. & Tasset, F. A study of magnetoelectric domain formation of Cr_2O_3. *Journal of Physics: Condensed Matter* **10** (1998).

[56] Qureshi, N. Mag2pol: A program for the analysis of spherical neutron polarimetry, flipping ratio and integrated intensity data `1801.08431v4`.

[57] Ashcroft, N. W. & Mermin, N. D. *Solid State Physics* (Brooks/Cole, Cengage Learning, 1976), 1 edn.

[58] McElfresh, M. Fundamentals of magnetism and magnetic measurements - featuring quantum design's magnetic property measurement system (1994).

[59] Retmers, J. N., Greedan, J. E. & Subramanian, M. A. Crystal structure and magnetism in $MnSb_2O_6$ incommensurate long-range order. *Journal of Solid State Chemistry* **79** (1989).

[60] Pamplin, B. R. *Crystal growth* (Pergamon Press, 1975), 1 edn.

[61] Hurle, D. T. J. *Handbook of crystal growth 2* (North-Holland, 1994).

[62] Bridgman, P. W. Certain physical properties of single crystals of tungsten, antimony, bismuth, tellurium, cadmium, zinc, and tin. *Proceedings of the American Academy of Arts and Sciences* **60** (1925).

[63] Byrappa, K. *Hydrothermal processing of advanced materials* (John Wiley Sons, 2005).

[64] Rudolph, P. *Bulk Crystal Growth* (Elsevier, 2015), 2 edn.

[65] Stock, C., Chapon, L. C., Schneidewind, A. & Su, Y. Helical spin waves, magnetic order, and fluctuations in the langasite compound $Ba_3NbFe_3Si_2O_{14}$. *Physical Review B* **83** (2011).

[66] Reimers, J. N., Greedan, J. E. & Subramanian, M. A. Crystal structure and magnetism in $MnSb_2O_6$: Incommensurate long-range order. *Journal of Solid State Chemistry* **79** (1989).

[67] Kimura, T. *et al.* Magnetic control of ferroelectric polarization. *Nature* **426** (2003).

[68] Kataoka, M., Nakanishi, O., Yanase, A. & Kanamori, J. Antisymmetric spin interaction in metals. *Journal of the Physical Society of Japan* **50** (1981).

[69] Grigoriev, S. V. *et al.* Magnetic structure of MnSi under an applied field probed by polarized small-angle neutron scattering. *Physical Review B* **74** (2006).

[70] King-Smith, R. D. & Vanderbilt, D. Theory of polarization of crystalline solids. *Physical Review B* **47** (1993).

[71] Mason, T. E., Gaulin, B. D. & Collins, M. F. Neutron scattering measurements of critical exponents in $CsMnBr_3$: A $Z_2 \times S_1$ antiferromagnet. *Physical Review B* **39** (1989).

[72] Kawamura, H. Critical properties of helical magnets and triangular antiferromagnets. *Journal of Applied Physics* **63** (1988).

[73] Zhitomirsky, M. E. & Chernyshev, A. L. Colloquium: Spontaneous magnon decays .

[74] Anderson, P. W. An approximate quantum theory of the antiferromagnetic ground state. *Physical Review* **86** (1952).

[75] Kubo, R. The spin-wave theory of antiferromagnetics. *Physical Review* **87** (1952).

[76] Dyson, F. J. General theory of spin-wave interactions. *Physical Review* **102** (1956).

[77] Dyson, F. J. Thermodynamic behavior of an ideal ferromagnet. *Physical Review* **102** (1956).

[78] Kranendonk, J. V. & Vleck, J. H. V. Spin waves. *Reviews of Modern Physics* **30** (1958).

[79] Mattis, D. C. *The Theory of Magnetism I* (Springer-Verlag Berlin Heidelberg, 1981), 1 edn.

[80] Majlis, N. *Quantum Theory of Magnetism* (Springer-Verlag Berlin Heidelberg, 2007), 2 edn.

[81] Ward, S. *et al.* Bound states and field-polarized Haldane modes in a quantum spin ladder. *Physical Review Letters* **118** (2017).

[82] Huberman, T., Coldea, R. & Cowley, R. A. Two-magnon excitations observed by neutron scattering in the two-dimensional spin-5/2 Heisenberg antiferromagnet Rb_2MnF_4. *Physical Review B* **72** (2005).

[83] Flack, H. Chiral and achiral crystal structures. *Helvetica Chimica Acta* **86** (2013).

[84] Shull, C. G. Neutron spin-neutron orbit interaction with slow neutrons. *Physical Review Letters* **10** (1963).

[85] Coster, D., Knol, K. S. & Prins, J. A. *Zeitschrift fur Physik* **63** (1930).

[86] Yamasaki, Y. *et al.* Magnetic reversal of the ferroelectric polarization in multiferroic spinel oxide. *Physical Review Letters* **96** (2006).

[87] Taniguchi, K., Abe, N., Takenobu, T., Iwasa, Y. & Arima, T. Ferroelectric polarization flop in frustrated magnet $MnWO_4$. *Physical Review Letters* **97** (2006).

[88] Blume, M. Magnetic scattering of x rays (invited). *Journal of Applied Physics* **57** (1985).

[89] Sarte, P. M. *et al.* Disentangling orbital and spin exchange interactions for Co^{2+} on a rocksalt lattice. *Physical Review B* **98** (2018).

[90] Xu, G., Broholm, C., Reich, D. H. & Adams, M. A. Triplet waves in a quantum spin liquid. *Physical Review Letters* **84** (2000).

[91] Mourigal, M. *et al.* Block magnetic excitations in the orbitally selective Mott insulator $BaFe_2Se_3$. *Physical Review Letters* **115** (2015).

[92] Muro, Y., Eom, D. H., Takeda, N. & Ishikawa, M. Contrasting Kondo-lattice behavior in $CeTSi_3$ and $CeTGe_3$ (T = Rh and Ir). *Journal of the Physical Society of Japan* **67** (1998).

[93] Pecharsky, V. K., Hyun, O. & Gschneidner, K. A. Unusual magnetic properties of the heavy-fermion compound $CeCoGe_3$. *Physical Review B* **47** (1993).

[94] Yamamoto, H., Ishikawa, M., Hasegawa, K. & Sakurai, J. Electrical resistivity, heat capacity and magnetic susceptibility anomalies in $Ce_{1-x}La_xIr_2Ge_2$. *Physical Review B* **52** (1995).

[95] Kimura, N., Umeda, Y., Asai, T. & Terashima, T. Fermi surfaces of $LaRhSi_3$ and $CeRhSi_3$. *Physica B* **294** (2001).

[96] Egetenmayer, N., Gavilano, J. L., Maisuradze, A., Gerber, S. & MacLaughin, D. E. Direct observation of the quantum critical point in heavy fermion $CeRhSi_3$. *Physical Review Letters* **108** (2012).

[97] Muro, Y., Ishikawa, M., Hirota, K., Hiroi, Z. & Takeda, N. Crystalline electric field effect and magnetic properties of $CeRhSi_3$ single crystal. *Journal of the Physical Society of Japan* **76** (2007).

[98] Rietschel, H., Renker, B., Felten, R., Steglich, F. & Weber, G. *Journal of Magnetism and Magnetic Materials* **76**.

[99] Stock, C. *et al.* From Ising resonant fluctuations to static uniaxial order in antiferromagnetic and weakly superconducting $CeCo(In_{1-x}Hg_x)_5$. *Physical Review Letters* **121** (2018).

[100] Stock, C. *et al.* From incommensurate correlations to mesoscopic spin resonance in $YbRh_2Si_2$. *Physical Review Letters* **109** (2012).

[101] Krellner, C. *et al.* CeRuPO: A rare example of a ferromagnetic Kondo lattice. *Physical Review B* **76** (2007).

[102] Canfield, P. C., Thompson, J. D. & Fisk, Z. Novel Ce magnetism in CeDipnictide and Di-Ce pnictide structures. *Journal of Applied Physics* **70** (1991).

[103] Stamokostas, F. L. & Fiete, G. A. Mixing of t_{2g}-e_g orbitals in 4d and 5d transition metal oxides. *Physical Review B* **97** (2018).

[104] Sakurai, J., Buyers, W. J. L., Cowley, R. A. & Dolling, G. Crystal dynamics and magnetic excitations in cobaltous oxide. *Physical Review* **167** (1968).

[105] Kanamori, J. Theory of the magnetic properties of ferrous and cobaltous oxides. *Progress of Theoretical Physics* **17** (1957).

[106] Stock, C. *et al.* Single to multiquasiparticle excitations in the itinerant helical magnet $CeRhIn_5$. *Physical Review Letters* **114** (2015).

[107] Das, P., Lin, S. Z., N. J. Ghimire, F. R., K. Huang & Janoschek, M. Magnitude of the magnetic exchange interaction in the heavy-fermion antiferromagnet $CeRhIn_5$. *Physical Review Letters* **113** (2014).

[108] Broholm, C. *et al.* Spin fluctuations in the antiferromagnetic heavy-fermion system U_2Zn_{17}. *Physical Review Letters* **58** (1987).

[109] Stock, C. *et al.* Anisotropic critical magnetic fluctuations in the ferromagnetic superconductor UCoGe. *Physical Review Letters* **107** (2011).

[110] Schrder, A., Aeppli, G., Bucher, E., Ramazashvili, R. & Coleman, P. Scaling of magnetic fluctuations near a quantum phase transition. *Physical Review Letters* **80** (1998).

[111] Yamani, Z. *et al.* Separation of magnetic and superconducting behaviour in $YBa_2Cu_3O_{6.33}$ ($T_c = 8.4$ K). *Physical Review B* **91** (2015).

[112] Stock, C. *et al.* Spin dynamics near the critical doping in weakly superconducting underdoped $YBa_2Cu_3O_{6.35}$ ($T_c = 18$ K). *Physical Review B* **77** (2008).

[113] Doniach, S. The Kondo lattice and weak antiferromagnetism. *Physica B* **91**, 231–134 (1977).